

5-2009

An On-sun parametric study of solar hydrogen production using WO₃ photoanodes

Christopher K. Halford
University of Nevada, Las Vegas

Follow this and additional works at: <https://digitalscholarship.unlv.edu/thesesdissertations>



Part of the [Applied Mechanics Commons](#), and the [Energy Systems Commons](#)

Repository Citation

Halford, Christopher K., "An On-sun parametric study of solar hydrogen production using WO₃ photoanodes" (2009). *UNLV Theses, Dissertations, Professional Papers, and Capstones*. 785.
<https://digitalscholarship.unlv.edu/thesesdissertations/785>

This Thesis is protected by copyright and/or related rights. It has been brought to you by Digital Scholarship@UNLV with permission from the rights-holder(s). You are free to use this Thesis in any way that is permitted by the copyright and related rights legislation that applies to your use. For other uses you need to obtain permission from the rights-holder(s) directly, unless additional rights are indicated by a Creative Commons license in the record and/or on the work itself.

This Thesis has been accepted for inclusion in UNLV Theses, Dissertations, Professional Papers, and Capstones by an authorized administrator of Digital Scholarship@UNLV. For more information, please contact digitalscholarship@unlv.edu.

AN ON-SUN PARAMETRIC STUDY OF SOLAR HYDROGEN PRODUCTION
USING WO₃ PHOTOANODES

by

Christopher K. Halford

Bachelor of Science
University of Nevada, Las Vegas
2002

Master of Science
University of Nevada, Las Vegas
2004

A thesis submitted in partial fulfillment
of the requirements for the

Doctor of Philosophy Degree in Mechanical Engineering
Department of Mechanical Engineering
Howard R. Hughes College of Engineering

Graduate College
University of Nevada, Las Vegas
May 2009

UMI Number: 3384003

INFORMATION TO USERS

The quality of this reproduction is dependent upon the quality of the copy submitted. Broken or indistinct print, colored or poor quality illustrations and photographs, print bleed-through, substandard margins, and improper alignment can adversely affect reproduction.

In the unlikely event that the author did not send a complete manuscript and there are missing pages, these will be noted. Also, if unauthorized copyright material had to be removed, a note will indicate the deletion.

UMI[®]

UMI Microform 3384003
Copyright 2009 by ProQuest LLC
All rights reserved. This microform edition is protected against
unauthorized copying under Title 17, United States Code.

ProQuest LLC
789 East Eisenhower Parkway
P.O. Box 1346
Ann Arbor, MI 48106-1346



Dissertation Approval
The Graduate College
University of Nevada, Las Vegas

April 17, 2009

The Dissertation prepared by

Christopher K. Halford

Entitled

An On-Sun Parametric Study of Solar Hydrogen Production
Using WO3 Photoanodes

is approved in partial fulfillment of the requirements for the degree of

Doctor of Philosophy in Engineering

Examination Committee Chair

Dean of the Graduate College

Examination Committee Member

Examination Committee Member

Graduate College Faculty Representative

Examination Committee Member

ABSTRACT

An On-Sun Parametric Study of Solar Hydrogen Production Using WO₃ Photoanodes

by

Christopher K. Halford

Dr. Robert F. Boehm, Examination Committee Chair
Professor of Mechanical Engineering
University of Nevada, Las Vegas

The solar production of hydrogen using photoactive electrodes is a topic receiving much attention in recent years. The use of thin metal oxide films as photoanodes allows the water splitting reaction to occur at a much lower applied voltage than would be necessary with a straight electrolysis process. Researchers have reported up to 18% solar to hydrogen efficiencies over short periods [1]. The University of Nevada Las Vegas in conjunction with the UK based firm Hydrogen Solar have developed a prototype of this type of cell using a WO₃ photoanode. An on-sun test facility has been constructed by the UNLV Center for Energy Research where a study is being conducted with regard to the effects various design parameters on the rate of hydrogen evolution. Parameters being studied include electrolyte temperature, electrolyte flow rate, electrolyte resistivity, applied voltage, and membrane to electrode spacing. The data collected will be used in a parametric study of the cell performance. This study will be used to establish general trends as to the effects of these parameters on the performance of the cells outside of a laboratory environment.

TABLE OF CONTENTS

ABSTRACT.....	iii
LIST OF FIGURES	vii
ACKNOWLEDGMENTS	xii
CHAPTER 1 INTRODUCTION AND LITERATURE SURVEY.....	1
<u>Historical Background</u>	1
<u>Theory of Operation</u>	2
Basic Semiconductor Theory.....	2
Oxidation and Reduction	4
Bandgap and Band Edge Requirements.....	5
<u>Testing On-Sun</u>	7
<u>Formal Statement of Proposed Study</u>	8
<u>Uniqueness of Proposed Study</u>	9
CHAPTER 2 DESIGN AND CONSTRUCTION OF ON-SUN TEST FACILITY	11
<u>Design Criteria</u>	11
<u>Location Selection</u>	12
<u>Data Acquisition Shed</u>	13
<u>Solar Tracker</u>	14
<u>Electrolyte Flow and Plumbing</u>	15
Flow Diagram and Description.....	15
Wetted Materials.....	18
<u>Data Acquisition and Control System</u>	24
CR10X Measurement and Control System.....	24
AM 16/32 Multiplexer	25
SDM-IO16 Input Output Expansion Module	26
PS100 Power Supply.....	26
Other Peripherals	27
<u>Measurement Devices</u>	29
Thermistors	29
Flowmeters.....	40
Resistivity Sensors.....	43
pH Sensor.....	47
Cell Potential.....	48
Cell Current.....	52
Integrated Solar Flux.....	53
Wind Speed.....	56

Wind Direction.....	57
Ambient Temperature and Relative Humidity.....	57
Other CR10X Measurements.....	58
Spectroradiometer.....	58
<u>Measurement and Control Program</u>	62
Input Locations.....	62
Scan Rate.....	62
Measurement Instructions.....	63
Electrode Potential Calculations.....	63
Thermistor Calculations.....	63
Temperature Control Constants.....	64
pH Calculations.....	64
Resistivity Control Constants.....	64
Resistivity Control Loop.....	64
Temperature Control Loop.....	66
Reference Cell Temperature Control Constants.....	68
Reference Cell Temperature Control Loop.....	68
Output File.....	69
Graphical User Interface (GUI).....	70
<u>Design and Construction of Other System Components</u>	71
Heat Exchanger (Cooler).....	71
Tank and Heater Assembly.....	74
<u>Finished System</u>	77
CHAPTER 3 DESIGN AND CONSTRUCTION OF CELLS.....	78
<u>Design Criteria</u>	78
<u>Photoanodes</u>	80
<u>Initial Conceptual Cell Design</u>	81
<u>Heat Bonded PEM/Cathode Attachment</u>	83
<u>First Generation Cells</u>	87
<u>Second Generation Cells</u>	90
Design.....	90
Construction and Final Units.....	100
CHAPTER 4 EXPERIMENTAL PROCEDURE.....	105
<u>Preliminary Tests</u>	105
<u>Final Test Series</u>	107
Test Structure.....	107
Formal Test Procedure.....	111
Solar Spectrum Measurements.....	114
Controlled Input Parameters.....	127
Other Input Parameters.....	132

CHAPTER 5 TEST RESULTS AND ANALYSIS.....	144
<u>Test Results</u>	144
<u>Analysis</u>	162
Quantifying Test Results.....	162
Effects of Single Parameter Variations.....	167
CHAPTER 6 CONCLUSIONS AND FUTURE WORK.....	177
<u>Test Facility</u>	178
<u>Cells</u>	180
<u>Test Procedure and Final Results</u>	182
<u>Summary</u>	185
APPENDIX A NOMENCLATURE.....	186
APPENDIX B EQUIPMENT SPECIFICATIONS.....	187
APPENDIX C MEASUREMENT UNCERTAINTY ANALYSIS.....	221
APPENDIX D COMPUTER CODE.....	On CD-ROM
REFERENCES.....	230
VITA.....	236

LIST OF FIGURES

Figure 1.	Relative band positions for the three types of materials.....	3
Figure 2.	Ideal band edge position for the water splitting reaction	5
Figure 3.	Band edge positions for several common semiconductors.....	6
Figure 4.	Finished data acquisition equipment enclosure.....	14
Figure 5.	Electrolyte flow path and measurement points for experiment.....	16
Figure 6.	Campbell Scientific CR10X datalogger	24
Figure 7.	Campbell Scientific AM 16/32 multiplexer	25
Figure 8.	Campbell Scientific SDM-IO16 pulse channel expansion module.....	26
Figure 9.	Campbell Scientific PS100 power supply	27
Figure 10.	Wiring of data acquisition components.....	28
Figure 11.	Finished data acquisition system installed in shed.....	29
Figure 12.	YSI 44032 precision thermistor.....	30
Figure 13.	Thermistor with quick disconnect plug	30
Figure 14.	Thermistor housing assembly.....	32
Figure 15.	Three wire half bridge used for thermistor measurements.....	33
Figure 16.	Configuration of thermistors during calibration.....	36
Figure 17.	West side thermistor agreement before and after calibration.....	39
Figure 18.	East side thermistor agreement before and after calibration	39
Figure 19.	Omega FTB601B ultra low flow sensor.....	40
Figure 20.	Flowmeter connection to SDMIO16 module	42
Figure 21.	Dual Foxboro 873RS resistivity analyzers installed in shed.....	43
Figure 22.	Foxboro 871CC contacting resistivity sensor installed in system.....	43
Figure 23.	Resistivity analyzer and pH sensor connections to multiplexer.....	45
Figure 24.	Corrected resistivity vs. voltage relation	46
Figure 25.	Absolute resistivity vs. voltage relation	46
Figure 26.	Omega PHE-5460-EC installed in system	47
Figure 27.	Wiring for cell potential and current measurements	49
Figure 28.	Potential of 3.8M Ag/AgCl reference electrode vs. temperature	51
Figure 29.	Finished reference cell.....	52
Figure 30.	Pyanometer, spectroradiometer integraing sphere, and tracker sensor	53
Figure 31.	Connection of weather sensors to CR10X datalogger.....	55
Figure 32.	Various weather sensors installed on tracker	56
Figure 33.	Facing the integrating sphere due South prior to calibration	60
Figure 34.	Seting the elevation angle of the integrating sphere.....	60
Figure 35.	Logic for resistivity control loop.....	65
Figure 36.	Logic for inlet temperature control loop	67
Figure 37.	Logic for reference cell temperature control loop.....	69
Figure 38.	Graphical user interface used to monitor and control system	70
Figure 39.	Construction details of shell and tube heat exchanger	71
Figure 40.	Modified air release valve used on heat exchanger.....	73
Figure 41.	Finished heat exchanger installed on system.....	73

Figure 42.	Construction details of tank and heater assembly	74
Figure 43.	Finished heater and tank assembly installed on system	76
Figure 44.	Completed test system in operation.....	77
Figure 45.	Photoanode as received from "Hydrogen Solar"	80
Figure 46.	Initial conceptual design for test cells	81
Figure 47.	PEM (Nafion® 117) after hydration and cleaning process	83
Figure 48.	Platinized titanium mesh used for cathode.....	83
Figure 49.	Setup used to heat bond PEM/cathode assembly	85
Figure 50.	Sample heat bonded PEM cathode assembly	86
Figure 51.	First generation cells and manifolds.....	87
Figure 52.	Stress cracking around threaded insert in polycarbonate cell body	88
Figure 53.	Cross section of flow channels for first generation cells.....	89
Figure 54.	Second generation cells and manifolds	91
Figure 55.	Exploded view of second generation cells	92
Figure 56.	Details of manifold attachment and tracker mount	94
Figure 57.	Details of PEM retaining clips and cell body gaskets	95
Figure 58.	PEM/Cathode assembly.....	96
Figure 59.	Details of upper and lower flow channels	97
Figure 60.	Details of anode lead attachment.....	98
Figure 61.	Details of cathode lead attachment.....	99
Figure 62.	Machining the manifolds.....	101
Figure 63.	Cathode assembly prior to anode placement.....	101
Figure 64.	Flow channels on finished cells.....	102
Figure 65.	Fully assembled cells with manifolds.....	103
Figure 66.	Finished cells with manifolds installed on tracker	104
Figure 67.	Variation of Nernst potential with pH for test high and low temperatures	110
Figure 68.	Solar intensity vs. time and wavelength for Test 1	115
Figure 69.	Solar intensity vs. time and wavelength for Test 2	115
Figure 70.	Solar intensity vs. time and wavelength for Test 3	116
Figure 71.	Solar intensity vs. time and wavelength for Test 4	116
Figure 72.	Solar intensity vs. time and wavelength for Test 5	117
Figure 73.	Solar intensity vs. time and wavelength for Test 6	117
Figure 74.	Solar intensity vs. time and wavelength for Test 7	118
Figure 75.	Solar intensity vs. time and wavelength for Test 8	118
Figure 76.	Maximum spectral mismatch for Test 1	120
Figure 77.	Maximum spectral mismatch for Test 2.....	120
Figure 78.	Maximum spectral mismatch for Test 3.....	121
Figure 79.	Maximum spectral mismatch for Test 4.....	121
Figure 80.	Maximum spectral mismatch for Test 5.....	122
Figure 81.	Maximum spectral mismatch for Test 6.....	122
Figure 82.	Maximum spectral mismatch for Test 7.....	123
Figure 83.	Maximum spectral mismatch for Test 8.....	123
Figure 84.	Maximum spectral mismatch between tests conducted on different days	125
Figure 85.	Average series spectrum compared to AM 1.5 Dir+Circ.....	126
Figure 86.	Average series spectrum compared to AM 1.5 Global Tilt.....	127
Figure 87.	Series average setpoint deviation for inlet temperature	129

Figure 88.	Series average setpoint deviation for ref cell temperature	129
Figure 89.	Series average setpoint deviation for West flow	130
Figure 90.	Series average setpoint deviation for East flow	130
Figure 91.	Series average setpoint deviation for temp corrected resistivity	131
Figure 92.	Series average setpoint deviation for cathode potential	131
Figure 93.	Series average absolute resistivity for the four cases	134
Figure 94.	Time varying series standard deviation of absolute resistivity	135
Figure 95.	Time varying series standard deviation of absolute resistivity	135
Figure 96.	Time varying series standard deviation of absolute resistivity	136
Figure 97.	Time varying series standard deviation of absolute resistivity	136
Figure 98.	Series average pH for the four cases	139
Figure 99.	Time varying series standard deviation of pH.....	140
Figure 100.	Time varying series standard deviation of pH.....	141
Figure 101.	Time varying series standard deviation of pH.....	141
Figure 102.	Time varying series standard deviation of pH.....	142
Figure 103.	Test 1 anode potential.....	145
Figure 104.	Test 1 currents for West cell (d=.8mm)	146
Figure 105.	Test 1 currents for East cell (d=1.6mm).....	146
Figure 106.	Test 2 anode potential.....	147
Figure 107.	Test 2 currents for West cell (d=.8mm)	148
Figure 108.	Test 2 currents for East cell (d=1.6mm).....	148
Figure 109.	Test 3 anode potential.....	149
Figure 110.	Test 3 currents for West cell (d=.8mm)	150
Figure 111.	Test 3 currents for East cell (d=1.6mm).....	150
Figure 112.	Test 4 anode potential.....	151
Figure 113.	Test 4 currents for West cell (d=.8mm)	152
Figure 114.	Test 4 currents for East cell (d=1.6mm).....	152
Figure 115.	Test 5 anode potential.....	153
Figure 116.	Test 5 currents for West cell (d=.8mm)	154
Figure 117.	Test 5 currents for East cell (d=1.6mm).....	154
Figure 118.	Test 6 anode potential.....	155
Figure 119.	Test 6 currents for West cell (d=.8mm)	156
Figure 120.	Test 6 currents for East cell (d=1.6mm).....	156
Figure 121.	Test 7 anode potential.....	157
Figure 122.	Test 7 currents for West cell (d=.8mm)	158
Figure 123.	Test 7 currents for East cell (d=1.6mm).....	158
Figure 124.	Test 8 anode potential.....	159
Figure 125.	Test 8 currents for West cell (d=.8mm)	160
Figure 126.	Test 8 currents for East cell (d=1.6mm).....	160
Figure 127.	Photocurrent for Test 1	162
Figure 128.	Photocurrent for Test 2.....	163
Figure 129.	Photocurrent for Test 3.....	163
Figure 130.	Photocurrent for Test 4.....	164
Figure 131.	Photocurrent for Test 5.....	164
Figure 132.	Photocurrent for Test 6.....	165
Figure 133.	Photocurrent for Test 7.....	165

Figure 134. Photocurrent for Test 8.....	166
Figure 135. Variation of PPCT between tests where only flow is changed	168
Figure 136. Variation of PPCT between tests where only temp is changed.....	170
Figure 137. Variation of PPCT between tests where only corrected res is changed	171
Figure 138. Variation of PPCT between tests where only spacing is changed.....	173
Figure 139. Average change in PPCT (mC) due to variations of the four inputs.....	175
Figure 140. Average change in PPCT (percent) due to variations of the four inputs...	176

LIST OF TABLES

Table 1.	Test matrix for final series	108
Table 2.	Integrated values for worst case spectral differences	124
Table 3.	Integrated values for series average and reference spectra.....	127
Table 4.	Maximum and time averaged mean values of avg series setpoint deviation	132
Table 5.	Maximum std deviation and time averaged mean values for abs resistivity	137
Table 6.	Maximum std deviation and time averaged mean values for pH	142
Table 7.	Total charge transfer for light and dark tests and PPCT	167
Table 8.	Changes in PPCT due to flow	169
Table 9.	Changes in PPCT due to temperature	171
Table 10.	Changes in PPCT due to corrected resistivity	172
Table 11.	Estimated residence times for four cases tested.....	174
Table 12.	Changes in PPCT due to electrode spacing	174

ACKNOWLEDGMENTS

I would like to take the time to acknowledge the people and organizations who have made this work possible. First of all, my sincere thanks to Professor Robert F. Boehm for his support and guidance, not only on this project but throughout my studies at UNLV. I would also like to recognize the other members of my committee; Dr. Samir Moujaes, Dr. Yahia Baghzouz, Dr. Yitung Chen, and Dr. Woosoon Yim. Your assistance with this project has been greatly appreciated. Additionally, my thanks go out to Dr. Jaci Battista for allowing me to use her lab facilities for this project. Next, I would like to express my gratitude to The Department of Energy (DOE), without whose financial support this project would not have been possible. Additionally, my thanks goes out to my lab-mates Rick Hurt, Suresh Sadenini, Sachin Deshmukh, as well as my close friends Isaac Mahderekal and Kumar Karpanan, for their input on many of the technical aspects of the project. Finally, this work is dedicated to my beloved mother, without whose many sacrifices over the years my education would not have been possible.

CHAPTER 1

INTRODUCTION AND LITERATURE SURVEY

Historical Background

The use of a photo-active metal oxide to drive the water-splitting reaction was first documented in 1972 by Fujishima and Honda [2], who used an n-type TiO_2 photoanode. The cell used an aqueous electrolyte of pH 4.7 and a platinum black counter electrode, with irradiation being supplied by a 500W xenon lamp. TiO_2 remains a popular choice for solar water splitting due to its low cost and stability in many types of electrolytes. Other early experiments with this type of anode are documented in [3]-[16]. One of the main drawbacks with TiO_2 which was stressed in all of the preceding references is its large bandgap. This characteristic of the material limits the portion of the solar spectrum which can be utilized to less than 10%. [10] This limitation has led researchers to investigate other suitable semiconductor materials. One possible alternative was found to be WO_3 . This material has a smaller bandgap than TiO_2 and therefore has the potential to utilize a larger portion of the solar spectrum. This is the material which will be used for the cells in this study. Some early studies involving water splitting using WO_3 as a photoanode are documented in [17] [18] [19]. One disadvantage of this material is that due to its band edge position it is incapable of producing the hydrogen reduction reaction without an externally applied bias. This concept will be explained in more detail in the subsequent sections of this writing.

Theory of Operation

The splitting of water into its elemental components can be achieved at a theoretical minimum potential difference of 1.23V. In conventional electrolysis, this energy is supplied from an external source such as a battery or solar panel. The use of thin film photoactive materials as electrodes allows for the reduction and possible eventual elimination of any external voltage source. In addition to eliminating the need for a separate power source, the photoactive material used in these types of cells is quite inexpensive when compared to photovoltaic panels. With the development of the right semiconductor material, cells could be produced to output hydrogen and oxygen with water and sun as the only inputs. To help clarify how this works a brief discussion of the basic concepts is presented here.

Basic Semiconductor Theory

The method of hydrogen production being explored here is possible due to the unique electronic structure of tungsten trioxide and many other similar materials. Compounds of these types can be loosely categorized based upon their electronic structure as semiconductors. A brief description of these unique properties and how they relate to this work is presented here.

Materials can be classed as either insulators, conductors or semiconductors depending upon the electronic structure of the molecules. In a conductor, electrons in the valence bands and conduction bands are close together, often overlapping one another. Valence electrons can be easily excited into the conduction band where they are free to move through the material. The opposite case is that of an insulator. In these materials there is a large energy difference (bandgap) between the valence and conduction energy levels.

Very large amounts of energy are necessary to promote an electron from the valence to the conduction band, so these materials are poor electrical conductors. An intermediate between these two cases is the semiconductor. In these materials there is a definite energy difference between the valence and conduction bands but this difference is much smaller than in the case of an insulator. Figure 1 shows the band structure for the three types of materials.

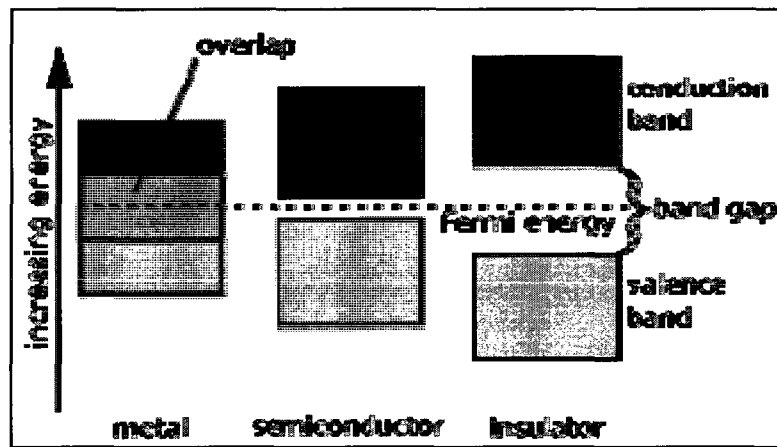


Figure 1. Relative band positions for the three types of materials

Due to the intermediate band structure shown in the preceding figure, many semiconductors can exhibit photoactive properties. This is to say that photons of sufficient energy can be absorbed by the materials and cause the promotion of valence electrons to the conduction band. This phenomenon can be used to drive an uphill chemical reaction such as water splitting. The requirement on the photon energy is expressed as.

$$h\nu \geq E_{gap} \quad (1)$$

Where ν is the frequency of the incident light, h is Planck's constant and E_{gap} is the semiconductor bandgap.

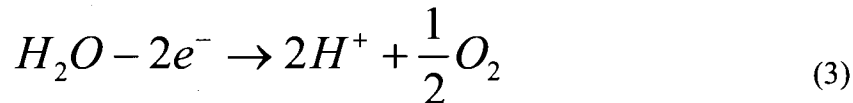
Oxidation and Reduction

In order to relate the electrochemical aspects of the water splitting reaction to the preceding discussion on semiconductors, a brief explanation of the oxidation/reduction reaction and the standard potential is presented here.

Many chemical reactions involve the loss of electrons (oxidation) of one species and the gain of electrons (reduction) of another. Reactions such as this are known as redox reactions. The splitting of water into elemental hydrogen and oxygen is such a reaction with the transfer of electrons between species occurring at the electrodes. To help clarify this, the net reaction;



May be written as two half reactions occurring at each of the electrodes of the cell. At the anode the water molecules are oxidized as;



At the cathode the hydrogen ions are reduced as;



Under standard conditions each of these half reactions occur at a known standard potential. The standard potentials for the oxidation and reduction reactions presented here are 1.23V and 0V respectively relative to the standard hydrogen electrode or SHE.

Bandgap and Band Edge Requirements

Splitting water without an externally applied potential places two limitations on the semiconductor which can be used. First, the bandgap of the material must be larger than the thermodynamic minimum potential for the reaction, in this case 1.23V. Secondly the positions of the valence and conduction bands must straddle the standard potentials for the two half reactions as shown in Figure 2.

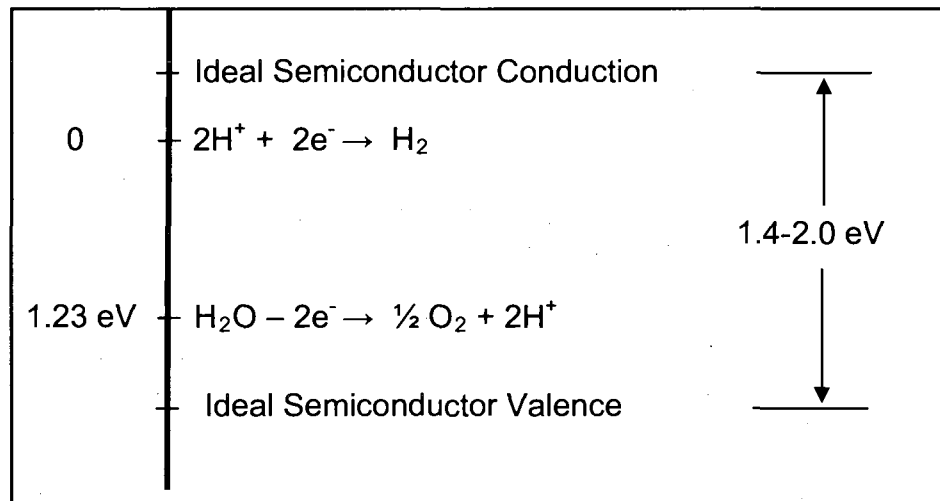


Figure 2. Ideal band edge position for the water splitting reaction

In addition to these requirements, Equation 1 dictates that the maximum portion of the solar spectrum will be utilized when the bandgap is 1.23V but no larger. That is to say that only photons of energy higher than the bandgap have the potential to cause the electron excitation required to drive the oxidation reaction. Photons of lower energy are dissipated as heat within the cell. In reality, the bandgap needs to be somewhat larger

than the theoretical minimum 1.23V to overcome the various sources of overpotential present in any real cell. Estimates of the theoretical optimum bandgap for water splitting using solar energy range from 1.4eV to 2.0eV [20]–[23]. Figure 3 shows the band edge positions for several metal oxide semiconductors.

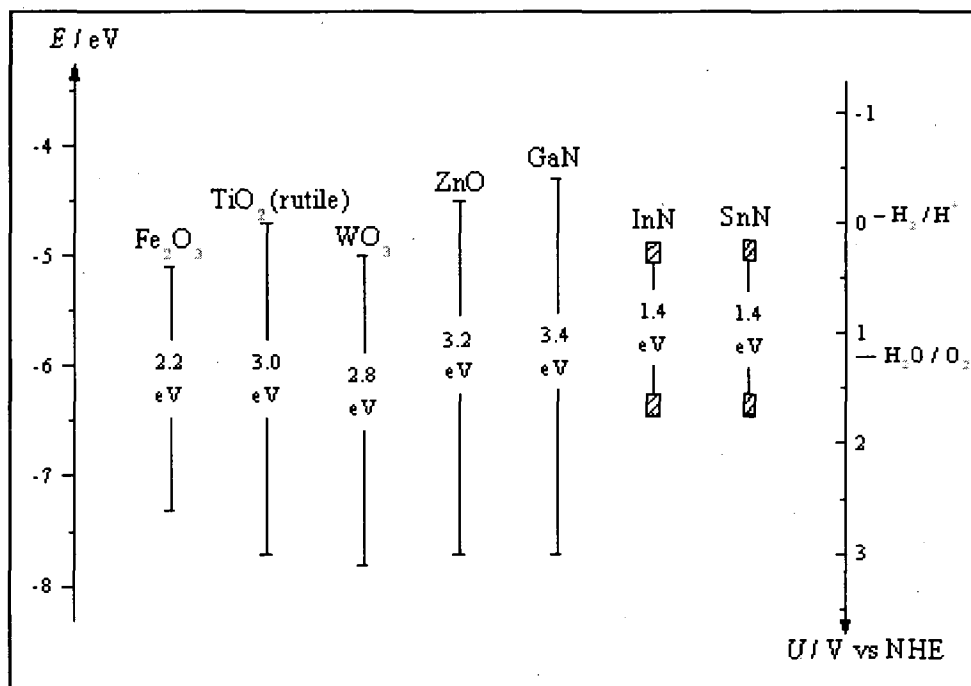


Figure 3. Band edge positions for several common semiconductors

As evident from the preceding figure, the conduction band for WO₃ is not sufficiently negative to cause the reduction of the hydrogen ions without the application of an external bias voltage. In addition to this, the bandgap, while smaller than that of TiO₂, is still too large to absorb more than a small fraction of the solar spectrum. Much of the current work with regard to water splitting using WO₃ is directed towards moving the conduction band edge to the negative side of the H₂/H⁺ couple and/or shrinking the bandgap. [24]–[45]

Testing On-Sun

As the title implies, the eventual goal of this project is the testing of semiconductor film based devices under actual solar illumination. This section seeks to explain some of the benefits of this approach as well as discuss some of the methods used to quantify the solar spectrum.

The intensity of solar radiation outside of the earth's atmosphere is relatively constant, with most researchers agreeing on a value of 1366W/m^2 for the solar constant. The spectral distribution of radiation at the surface of the earth, however, is a strong function of the thickness of the atmosphere that it must pass through. This thickness or "air mass" varies greatly over the course of a day as the sun moves across the sky. Researchers have defined the air mass as the ratio of the path length of the direct solar beam through the atmosphere and the thickness of the atmosphere. For example, an air mass or AM 1 spectrum would occur when the sun is directly overhead. Similarly an AM 0 spectrum would be measured at the top of the earth's atmosphere. Based upon this logic, the American Society for Testing and Materials has defined two standard reference spectra for the testing of photovoltaic (PV) and photoelectrochemical (PEC) type devices. The two spectra (direct plus circumsolar and global tilt) occur at an air mass of 1.5 which corresponds to a solar zenith angle of 48.2 degrees. Other specified conditions for both spectra are listed in [46]

Much work has been published with regards to the testing of photoelectrochemical cells using simulated solar illumination. Artificial light sources are convenient because they are stationary and their intensity is relatively constant over time. Testing on sun, while more difficult, has the advantage of more accurately representing the standard AM

1.5 spectrum. In [21] it is shown that use of a Xenon lamp can lead to a large overestimation of photoconversion efficiencies compared to efficiencies under the standard AM1.5 spectrum. This is mainly due to the fact that the xenon lamp emits a significant photon flux below 250nm whereas there is essentially no emission below 300nm for the AM 1.5 standard. This deviation of artificial light sources from the actual solar spectrum is also noted in [22] [47] [48].

Formal Statement of Proposed Study

For the reasons stated in the previous sections, it was proposed that a study be conducted which would allow for the testing of full size PEC hydrogen production devices under actual solar illumination. The experimental setup would allow for the control and measurement of key input parameters such as electrolyte temperature, resistivity and flowrate through the devices. Testing procedures would be developed to study the effects of changes in the photocurrent due to these parameters. The data collected will be used to determine the relative importance of each of these parameters on the overall system performance. The proposed study can be divided into the five tasks listed below.

- (1) Design and Construction of On-Sun Test Facility
- (2) Design and Construction of Cells
- (3) Development of Standard Testing Procedure
- (4) Formal Testing
- (5) Analysis and Interpretation of Test Data

Uniqueness of Proposed Study

The project being discussed here is unique for several reasons. As was mentioned previously, the focus of much of the current research is centered on shifting the band edge positions of the semiconductors to maximize solar absorption while eliminating the need for an external bias voltage. Bandgap engineering requires an extensive semiconductor background as well as a great deal of specialized equipment which is not currently available at the UNLV CER. The work being proposed here uses the WO_3 anode as supplied by the CER's industrial partner Hydrogen Solar. With the exception of the size of the anode, the university has no input as far as the design of the photoanode and no attempt were made to alter its properties in any way. Instead, this work will take an existing photoanode and attempt to create a full size experimental cell. This can then be studied outside of a laboratory environment and under conditions at which a working system would be expected to perform. The study will attempt to establish general trends regarding photocurrent and the design parameters discussed in the previous section.

In addition to facilitating the formal parametric study, the design and construction of the test cells also addresses many practical problems which would be encountered in the manufacturing of such devices. Issues such as cell body material selection, cell geometry, sealing, fasteners, electrode lead attachment, PEM attachment, are all obstacles to large scale use of these types of cells. These aspects receive little attention in the current literature but are addressed here. Additionally, the design and construction of the test facility provides a guideline for implementation of a complete working system.

An extensive search of the existing literature has found many publications regarding the experimental testing of photoactive materials for solar water splitting. Most of this

work is devoted to altering the band characteristics of the photoanode material. These studies generally work with either electrodes of very small areas (typically less than 3cm^2), or are systems consisting of photoactive particles suspended in the electrolyte. Due to the obvious differences between the suspended particle systems and the work being proposed in this document, publications involving these types of systems are excluded from the references presented in this section. References are limited to publications involving cells with solid electrodes. The cells being studied are typically open to atmospheric pressure with no flow over the electrodes. Illumination is provided by a xenon lamp or other artificial light source. Generally the cells are tested using a range of basic or acidic electrolytes. Tests of these types are documented in [1] [49]-[68]. During the tests conducted by Hydrogen Solar problems were encountered using these types of electrolytes due to corrosion of the photoanode. Because of this, the initial testing will be conducted using pure water, even though the increased resistivity is expected to keep current densities low. At this point only one reference has been found documenting tests under actual sunlight. [69] This study uses a TiO_2 photoanode to produce hydrogen using seawater as the electrolyte. Unlike the work being presented here, the photoactive material is deposited on a metal substrate instead of on conductive glass. The experiment was performed with no electrolyte movement and no attempt was made to study the effects of the parameters being investigated here.

CHAPTER 2

DESIGN AND CONSTRUCTION OF ON-SUN TEST FACILITY

Before the testing described in the previous chapter could commence, it was first necessary to construct a test platform which would allow for the control and measurement of key parameters. The purpose of this chapter is to document the design and construction of this test platform. It is worthwhile to note that in the description of the system construction, SI units are used for all dimensions with the exception of pipe and tubing size and fasteners. These items are sized and designated using English units and conversion of these dimensions to SI units serves only to add confusion.

Design Criteria

Before any construction on the test platform was commenced, a formal definition of its desired attributes and capabilities was created. This formal design criteria for the system is as follows:

- (1) Sensitive electronic equipment will be housed in a protective enclosure.
- (2) The system will allow for the tracking of at least two cells in elevation and azimuth.
- (3) The system will allow for measurement and recording of the following cell parameters
 - a. Electrolyte temperature into and out of each cell

- b. Bias voltage applied to each electrode (Relative to SHE)
- c. Current through each cell
- d. Flow rate through each cell
- e. Resistivity of electrolyte

(4) The system will allow for measurement and recording of the following weather parameters

- a. Total integrated solar flux
- b. Solar flux as a function of wavelength
- c. Ambient temperature
- d. Relative humidity
- e. Wind speed
- f. Wind direction

(5) The system will allow for control of the following parameters

- a. Electrolyte temperature at the cell inlet
- b. Bias voltage applied to each electrode
- c. Flow rate through each cell
- d. Electrolyte resistivity

Location Selection

Before construction could begin it was first necessary to select a suitable location for the project. After much research, the South side of the roof of the Thomas Beam engineering building on the UNLV campus was selected as the best site. This location provides a year round unobstructed view of the sun through the majority of the daylight

hours as well as providing relatively easy access to electrical power, communications lines, water lines and the freight elevator. A steel superstructure located directly behind the test setup can cast a shadow on the cells late in the day but it was observed on the Summer solstice (worst case) that there would be no interference with the test until at least 7:00PM. The surface of the roof is flat and covered uniformly with a white reflective coating which serves to simplify any modeling of reflection and scattering effects compared to more complex geometries.

Data Acquisition Shed

Summertime temperatures at the test site location can exceed 48 °C. Conditions such as these will quickly destroy much of the electronic equipment required for this experiment. For this reason, it is necessary to house sensitive hardware in a climate controlled enclosure. A 1.2 by 1.2 by 1.5m pressboard shed from a previous project was recycled for this purpose. The enclosure had been on the roof for many years and required some refurbishing. It was scraped down and any open seams were caulked to keep water out. The structure was then recoated with white latex paint. 10cm thick fiberglass insulation then was laid between the studs and covered with plywood sheeting to keep loose glass fibers out of the equipment. The finished enclosure was moved to the experiment site and power was run from a 20 amp breaker to a 4 socket outlet installed in the shack. Phone and data lines were also installed to facilitate remote data collection. Cooling is provided by a 2300W window-mount air conditioner. A 4m long galvanized sheet metal conduit was run from the shed to the location where the tracking unit would be installed to protect the sensor leads. Figure 4 shows the finished enclosure.

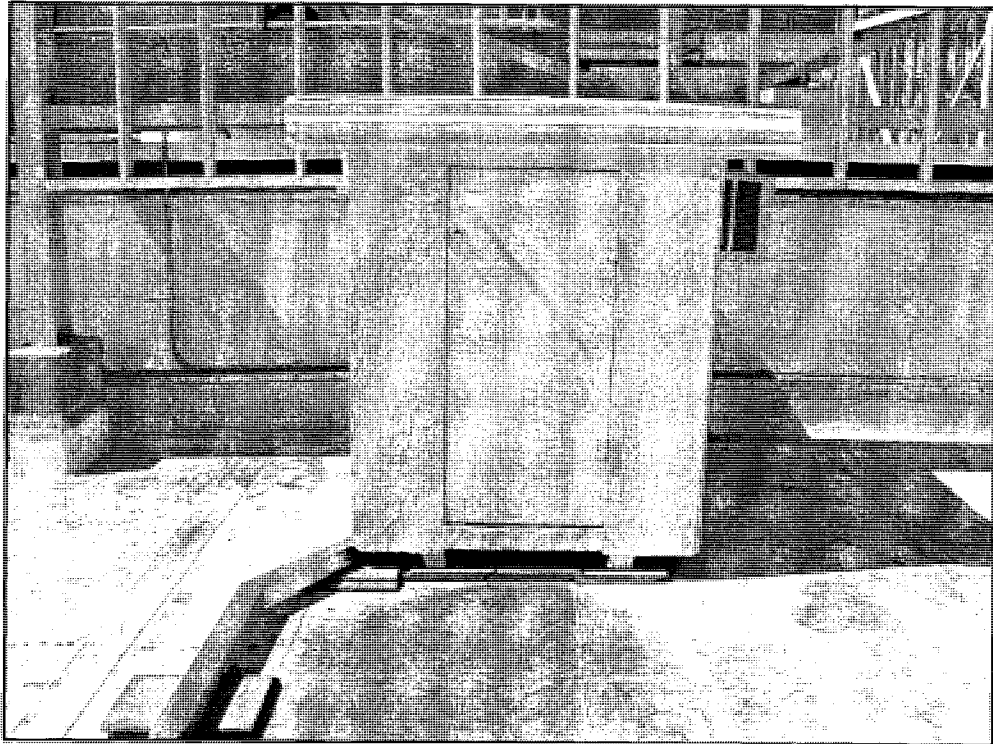


Figure 4. Finished data acquisition equipment enclosure

Solar Tracker

To simplify analysis it was decided that the cells should track the sun in elevation and azimuth. To facilitate this a Watt Sun[®] AZ-125 tracker mounted on a custom trailer was installed 10m in front (South) of the shed. This distance was selected to minimize the shading caused by the previously mentioned superstructure. It is worthwhile to mention here that it is a good idea to keep the tracker and the shack as close together as is possible. This will minimize any transients or loss of signal in the measurements caused by the longer lead lengths.

The tracker was mounted on concrete blocks and was leveled about both axes using wooden shims. The 24VDC power supply required for the controller was mounted in the shack and power leads run to the tracker through the aforementioned sheet metal channel.

For the experiment, it was desirable to have the ability to test at least two cells concurrently. To facilitate this the tracker was fitted with two perforated sheet metal trays on either side of the tracking head. The trays are painted to prevent corrosion and long enough to support the cells and any tubing required for the inlet and outlet manifolds. The perforated sheet metal allows easy attachment of the cells and tubing using plastic wire ties.

Electrolyte Flow and Plumbing

Flow Diagram and Description

As was mentioned in the previous sections, the test system was designed to allow for two cells to be tested concurrently under dynamic flow conditions. Implementation of this required that a network of plumbing be installed on and around the tracker to facilitate the flow of electrolyte through the cells as well as through the various measurement and control components of the system. The purpose of this section is to document the design and construction of this portion of the project with the basic flow path of the electrolyte for the experiment shown in Figure 5.

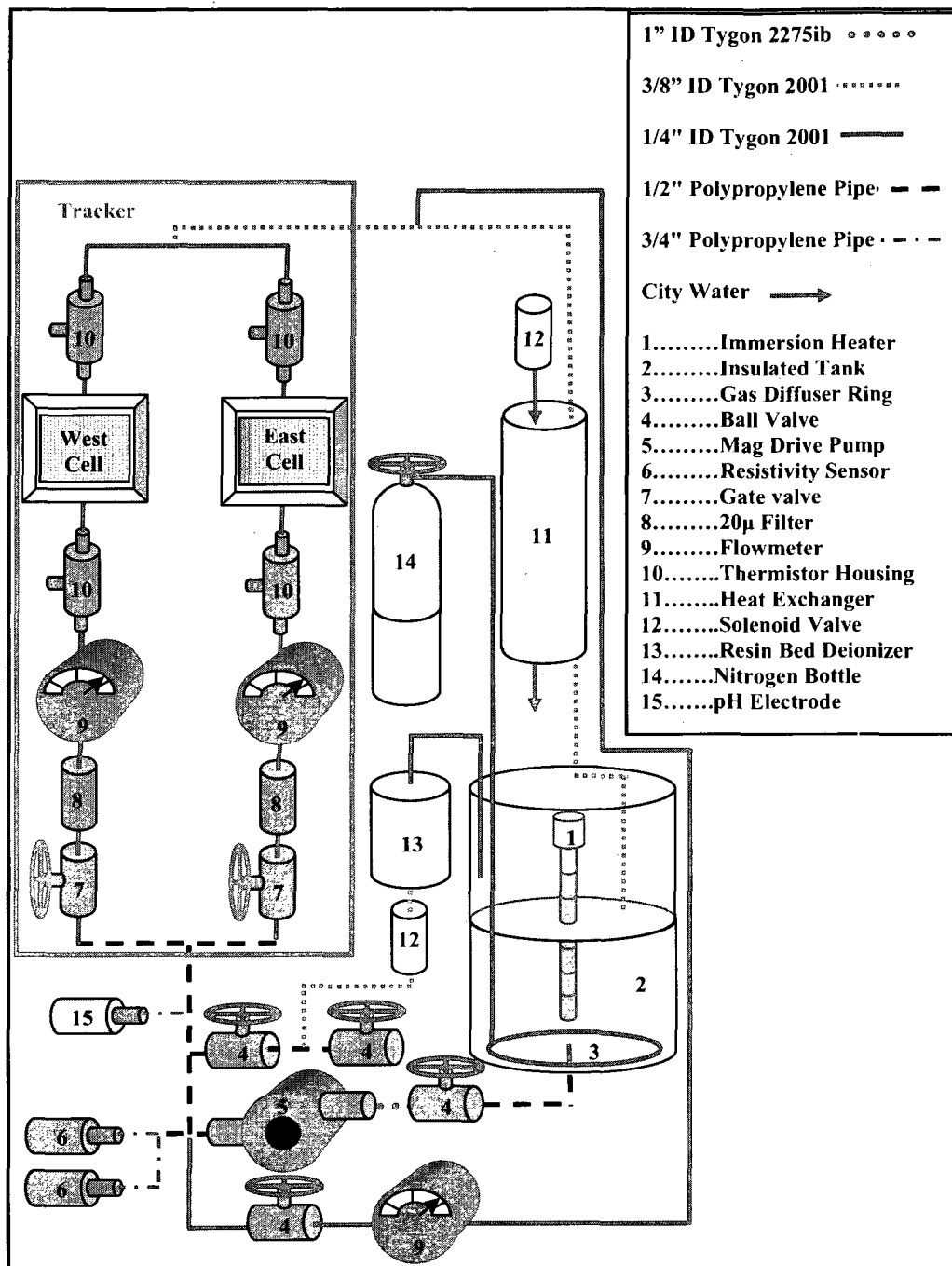


Figure 5. Electrolyte flow path and measurement points for experiment

As shown, the electrolyte leaves the insulated reservoir where heat can be added as needed using an electrical resistance heater. From here it enters the inlet of the pump. Downstream of the pump outlet two resistivity (absolute and temperature compensated)

measurements and a pH measurement are made. The flow is then split into four parallel circuits (East cell, West cell, bypass, and resistivity control). As shown, the flow through each of the two cells is regulated using a gate valve and then passed through a 20 μ filter before passing through the flowmeters and cells. The inlet and outlet temperatures for each cell are measured and the two flows are recombined downstream of the outlet temperature measurements.

A third parallel circuit bypasses the cells and flows directly into the heat exchanger. The bypass allows the cooling loop to be effective even when the flow rate through the cells is very low. Flow through the bypass is controlled with a ball valve and measured using a flowmeter as shown. Upstream of the heat exchanger, the combined flow through the cells rejoins the bypass flow. If cooling is required to maintain a specific inlet temperature, city water is run through the shell side to remove the excess heat. When cooling is not required the city water is shut off and the shell side drains. The outer walls of the heat exchanger are insulated to prevent heat loss when the cooling system is not needed. Upon exiting the heat exchanger, the combined flow from the three circuits is returned to the tank.

An additional parallel circuit is used for the resistivity control loop. This circuit bleeds off a very small portion of the flow and passes it through a resin bed de-ionization filter to increase the electrolyte resistivity as required to maintain the setpoint. A solenoid valve turns the flow on and off as dictated by the measurement and control logic. Flow rate through the deionizer when the solenoid is open is adjusted using a ball valve. Since the resistivity of the system tends to decline over time on its own, the system does not include a means to actively reduce it.

To suppress unwanted reactions, an inert gas injection system is included in the system as shown in Figure 5. This component is necessary due to the fact that the rate of hydrogen production is to be calculated based upon cell current and not directly measured. As a result of this, it becomes necessary to suppress other competing reactions which would give false results. For the case being presented here, the reduction of dissolved oxygen at the cathode is energetically favorable to the reduction of hydrogen ions, which is the desired reaction. To prevent this unwanted reaction, the electrolyte must be purged of dissolved oxygen prior to and during each test. This is accomplished by diffusing an inert gas (in this case nitrogen) through the liquid electrolyte. As shown in the figure, a cylinder of compressed nitrogen is used to bubble the gas through a circular diffuser located at the bottom of the electrolyte tank.

Wetted Materials

Water of the purity level being used in this experiment acts as an aggressive solvent when in contact with many materials. To prevent contamination of the electrolyte and cells, every effort was made to avoid introducing impurities into the process. For this reason, material selection for the various components which are in contact with the electrolyte is critical. This section gives a brief description of the system components which are in contact with the electrolyte and the materials that they are constructed from.

Rigid piping and fittings:

Where rigid piping was required black polypropylene was used. This material has good resistance to most basic or acidic electrolytes and is rated for temperatures up to 82 °C.

Barbed tube fittings:

For connections between various components and the flexible tubing or between the flexible tubing and itself, white polypropylene barbed fittings were used. This material has good resistance to most basic or acidic electrolytes and is rated for temperatures up to 90 °C.

Electrolyte tank, piston and lid:

These parts are also made from white polypropylene with the same properties listed previously.

Thermistor housings:

These parts are also made from white polypropylene with the same properties listed previously.

Flexible tubing:

When flexible tubing was required, Tygon[®] formulation 2001 was used wherever possible. This tubing is plasticizer free and is resistant to most acidic or basic electrolytes. It withstands temperatures up to 57 °C. The one place where a different formulation was used was for the run from the electrolyte tank to the pump inlet. Because this length is

under a negative pressure, the Tygon 2001 originally used tended to collapse at higher temperatures. For this reason, this section was replaced with formulation 2275ib. This tubing has similar properties as formulation 2001 but has an internal braid and is vacuum rated. It is worthwhile to mention here that neither of the two Tygon formulations used in the experiment are resistant to prolonged exposure to UV radiation. Initially the tubing was installed on the tracker without any covering. Within a month's time it was very brittle and required replacement. The new tubing was covered with flexible foam pipe insulation and wrapped with a reflective barrier material. This helps reduce system deviation from the temperature set point as well as shielding the tubing from UV rays.

Pump:

The pump selected is a 75W centrifugal, magnetic drive type used for corrosive liquids. This component has no metal parts and can withstand fluid temps of up to 93 °C. The wetted parts are carbon, ceramic, Ryton[®], and Viton[®]. These materials are resistant to most caustic and acidic electrolytes. It is worthwhile to note here that the original carbon bushings in the pump impeller wore very quickly and contaminated the process with carbon residue. Because of this, the carbon bushings were replaced with ones made of Rulon LR[®]. This is a self lubricating reinforced PTFE material with excellent wear and chemical resistance and a max temperature of 250 °C.

Flow control valves:

The flow control valves are a gate type valve with an acetal body. This material is resistant to most caustic and acidic electrolytes. The o-rings are Viton and the units are rated for temperatures up to 93 °C.

Shutoff and purge valves:

These are ball type valves with a CPVC body. The O-rings are EPDM and the seats are polyethylene. These materials are compatible with most caustic and acidic electrolytes and resist temperatures up to 82 °C.

Inline filters:

The filter body is made of acetal with a 20 μ polyester element. Acetal has been discussed previously while polyester is compatible with most acidic and weak basic solutions. Temperature data is not listed for these but no problems were encountered with sustained fluid temperatures of 70 °C.

Flowmeters:

All wetted parts of the flowmeter except for the o-rings are made of PVDF. This material is resistant to most acidic and basic electrolytes. The o-rings are made of Viton which was discussed previously. The maximum operating temperature for the units is listed as 82 °C. Detailed specifications for these units are included in Appendix B.

Solenoid valve:

The body is made of black polypropylene which was discussed previously and has Buna-N seals. Buna-N[®] has good chemical resistance and the units are rated for a maximum temperature of 49 °C.

Inline resin bed de-ionizing filter:

This unit has a polypropylene housing and is designed for pure water applications. The rated maximum temperature is 49 °C.

Thread sealing tape:

PTFE tape was applied to seal the threads of all NPT fittings. This material resists temperatures of 288 °C and is compatible with most chemicals.

Silicone sealant:

Where a liquid sealant was required, RTV silicone was used. This material resists temperatures of 200 °C and is compatible with most chemicals.

Heater:

The heater is a cartridge-style immersion type. The body is 316 stainless steel and it is rated at 405W at 120VAC. This material has excellent resistance to most caustic and acidic electrolytes and is well suited to ultra-pure water applications. It is worthwhile to note here that while many metals such as 316 ss exhibit admirable chemical resistance, generally a plastic can be found which will perform better. For this reason, metals are

used only when there is no other alternative. The only metals present in the system (including the cells) are 316 ss, titanium, gold and platinum .

Thermistor sheaths:

The thermistor sheaths were constructed of 316 ss which has been discussed previously.

Resistivity cell:

The cell body is made of Ryton with EPDM o-rings and a titanium electrode. Ryton and EPDM were discussed previously. The titanium electrode oxidizes naturally to form a chemically passive but electrically conductive surface. These electrodes are designed to work for a wide range of pH and are well suited to ultra-pure water applications. The maximum operating temperature is listed as 120 °C. Detailed specifications for these units are included in Appendix B.

pH electrode:

The cell body and housing are made of CPVC with Viton o-rings. Both of these materials have been previously discussed. Additional wetted materials are glass and polyethylene which both have excellent chemical resistance. The max operating temp is listed as 100°C. Detailed specification for this unit is included in Appendix B.

Data Acquisition and Control System

The long term testing of these types of PEC devices for this project requires that the test system be capable of operating and collecting data relatively autonomously. To facilitate this aspect of the project, a data acquisition and control system was designed based upon components manufactured by Campbell Scientific®. This section gives a brief description of the various components used and what their functions are in the finished measurement control system.

CR10X Measurement and Control System

The Campbell Scientific CR10x (Figure 6) is a fully programmable datalogger and controller with 12 single ended (6 differential) analog voltage inputs, 3 pulse inputs, 3 excitation channels, as well as 8-5V control ports. This device is the heart of the measurement and control system. Complete specifications for this and all other data acquisition hardware are included in Appendix B.

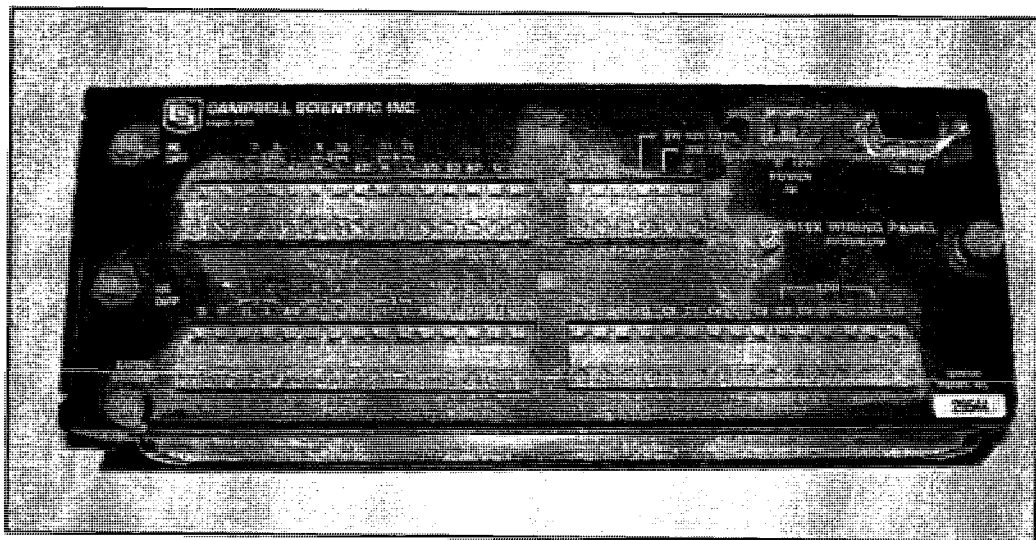


Figure 6. Campbell Scientific CR10X datalogger

AM 16/32 Multiplexer

This multiplexer, shown in Figure 7, is used to expand the number of analog voltage channels available. Using one or two (depending on whether the unit is in 2 by 32 or 4 by 16 mode respectively) analog inputs on the CR10X, a total of 32 two-wire, or 16 four-wire sensors can be measured with this device. The AM16/32 uses solid state relays to connect each sensor one at a time to the analog input on the datalogger. Once the connection is made, the CR10X makes the measurement as specified in the program and writes the value into a specified input location in the datalogger memory. This is then repeated for each sensor connected to the multiplexer with each measurement going to a different input location. The length of time that each set of contacts are closed as well as delay between closures are fully adjustable in the program. This device was added because more than six differential voltage measurements were required for the project.

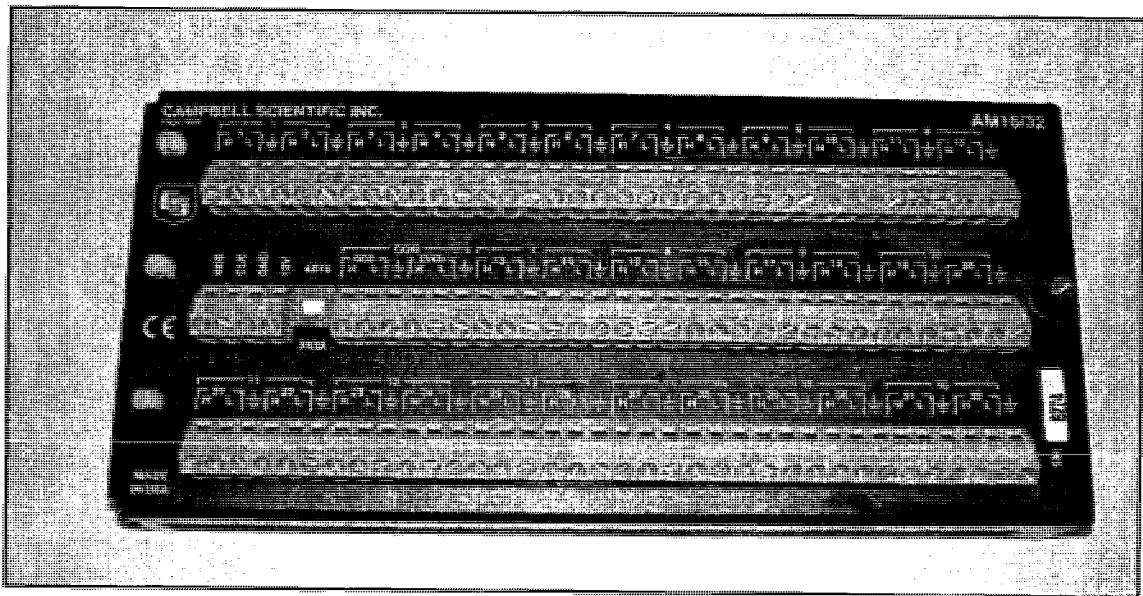


Figure 7. Campbell Scientific AM 16/32 multiplexer

SDM-IO16 Input Output Expansion Module

This unit (Figure 8) was added to the system to expand the number of pulse input sensors which can be measured. It functions similarly to the multiplexer, allowing up to 16 pulse measurements to be taken. Each port on the device can also be configured as a switchable 5V output controlled by the datalogger program.

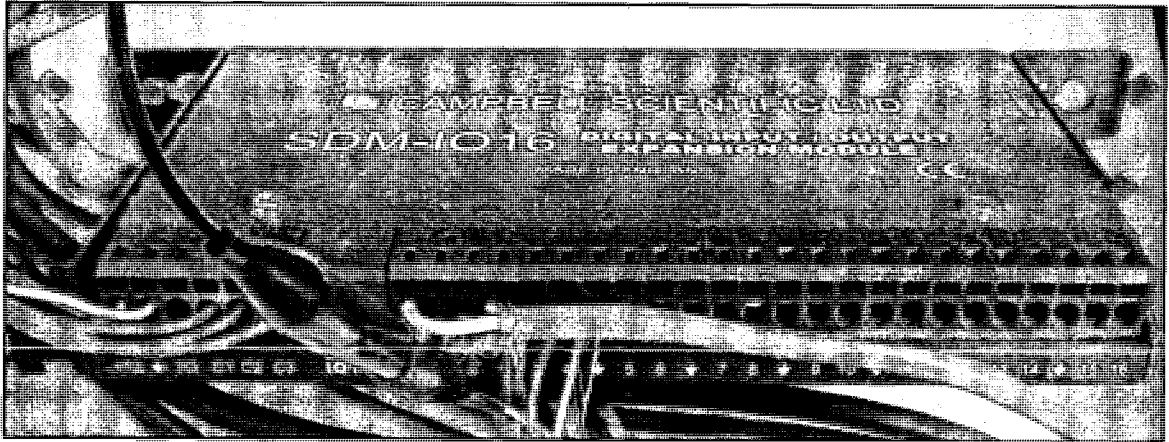


Figure 8. Campbell Scientific SDM-IO16 pulse channel expansion module

PS100 Power Supply

The data acquisition system is powered by the Campbell scientific PS100 power supply shown in Figure 9. This unit consists of a battery and charger which is powered by a 120VAC to 24VDC adapter. The device provides a relatively constant 12VDC to the logger and its peripherals. The battery allows the logger to function without AC power for several days.

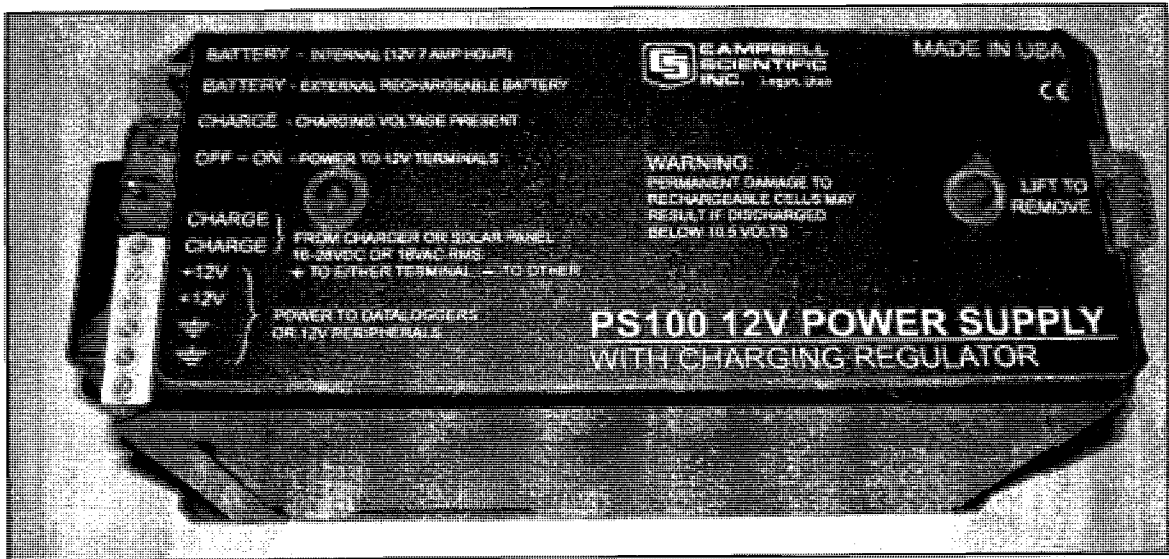


Figure 9. Campbell Scientific PS100 power supply

Other Peripherals

In addition to the aforementioned devices, a Com210 phone modem was used to provide remote access to the data and the SC532 serial interface device allows the CR10X to be connected to a Desktop or Laptop computer running the Campbell Scientific “Loggernet[®]” software package. The datalogger and its peripherals are wired as shown in Figure 10.

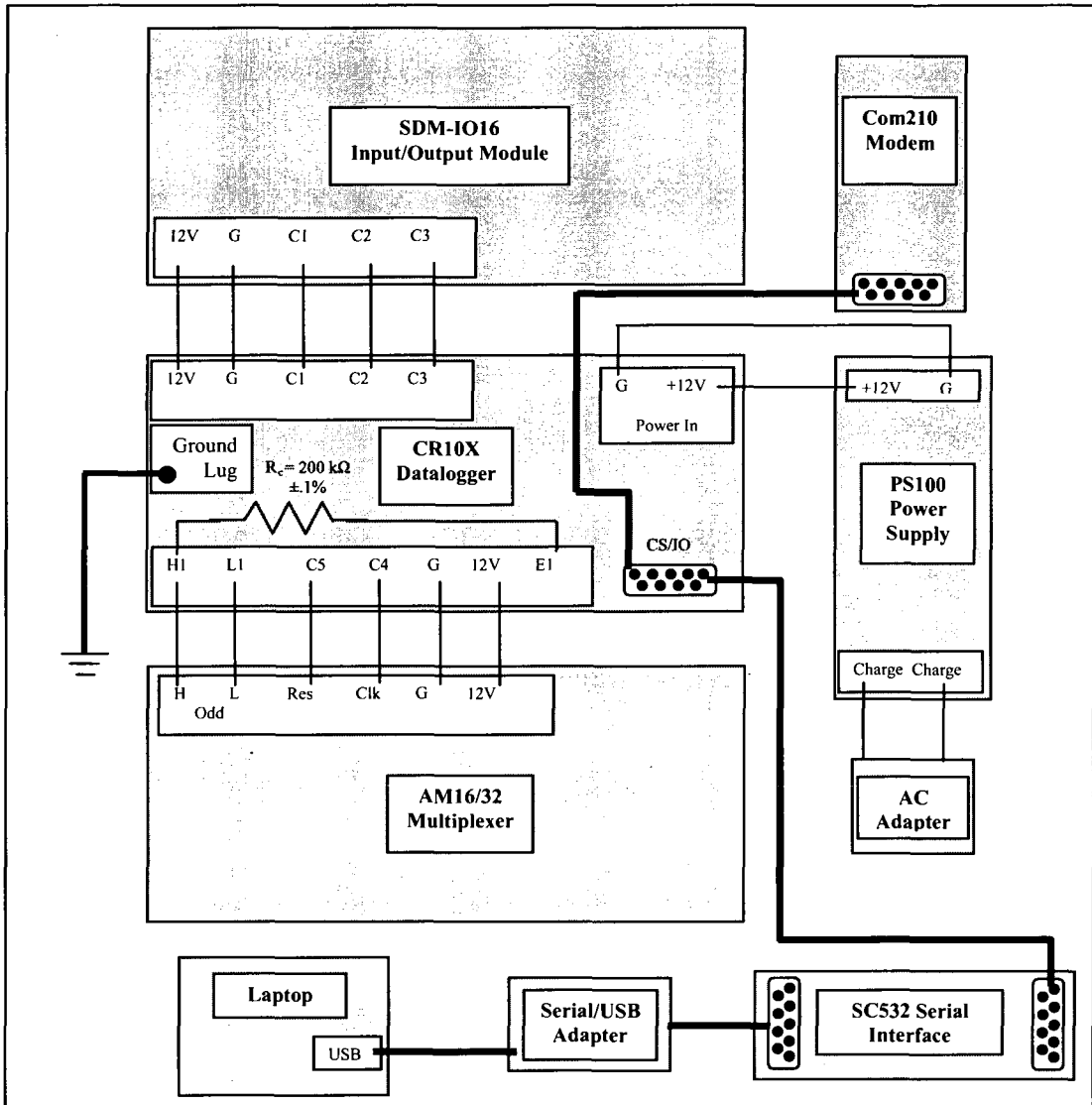


Figure 10. Wiring of data acquisition components

The computer used for this project is an IBM Thinkpad[®] T43. The machine has 1.5Gb of RAM and the processor speed is 1.6GHz. Figure 11 shows the finished data acquisition system installed in the shed.

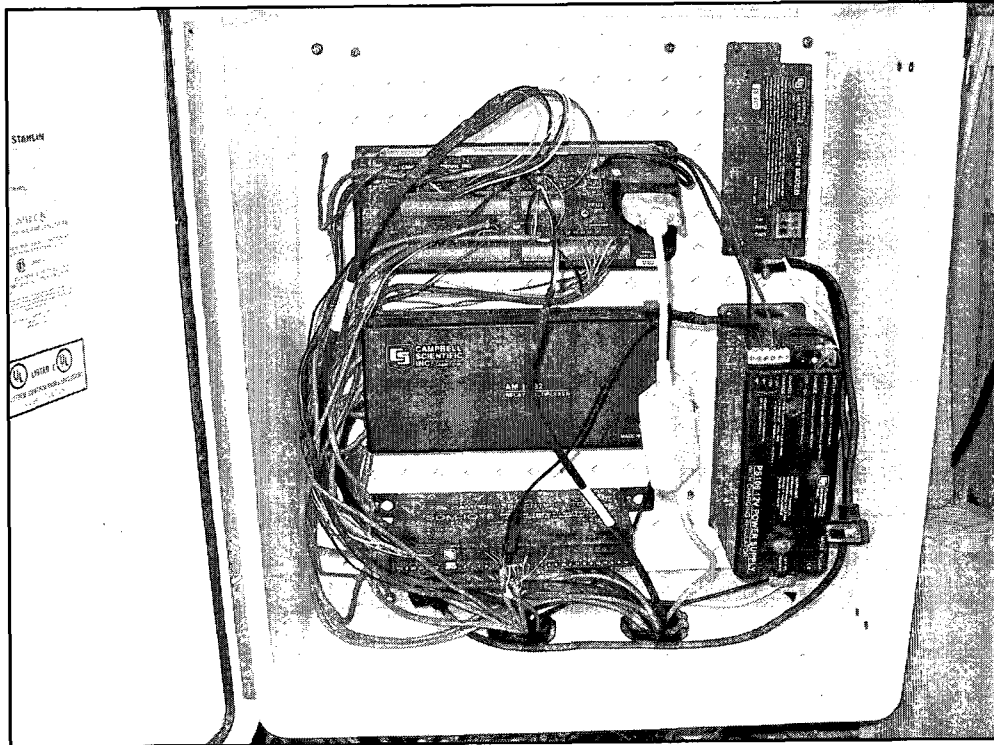


Figure 11. Finished data acquisition system installed in shed

Measurement Devices

This project uses a wide variety of measurement devices to quantify the many inputs to the system. The purpose of this section is to provide a brief description of each device used and how they are integrated into the data acquisition/control system described in the previous section.

Thermistors

Electrolyte temperatures into and out of both cells are measured using YSI 44032 precision thermistors mounted in specially constructed housings. These units are rated as being interchangeable within $.1\text{ }^{\circ}\text{C}$ in the range of $0\text{ to }70\text{ }^{\circ}\text{C}$, using the Steinhart, Hart [70] coefficients supplied by the manufacturer. Detailed specifications for the units are listed in Appendix B.

Thermistors were selected for this application because the temperature change across each cell was expected to be too small to accurately measure with a thermocouple. The units as received consist of a small bead of the resistive compound coated with epoxy, with two bare lead wires as shown in Figure 12.

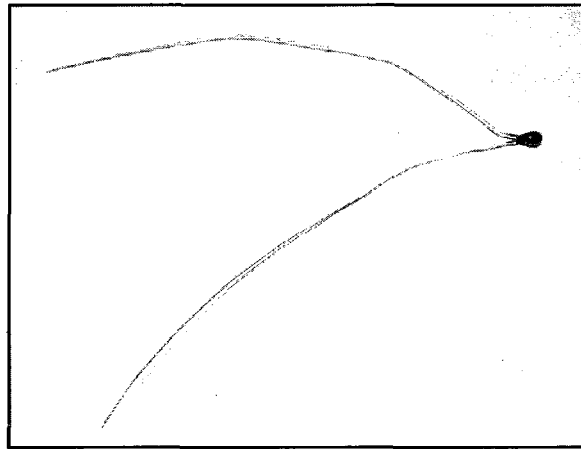


Figure 12. YSI 44032 precision thermistor

The thermistor leads were soldered to quick disconnect male stereo headphone plugs and all connections were covered with heat shrink tubing as shown. The finished sensor is shown in Figure 13.

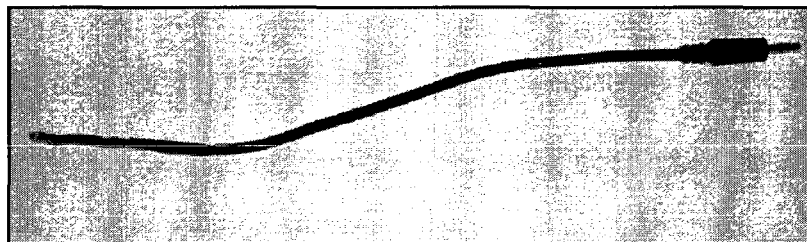


Figure 13. Thermistor with quick disconnect plug

Initially tests were made with the thermistor bead immersed directly in the water flow. This worked for short term measurements but eventually the bead would become saturated with water leading to erroneous readings. Because of this, pipe plug type sheaths were constructed of 316 stainless steel to prevent direct contact between the bead and the electrolyte. The thermistor beads were coated with Omegatherm[®] 202 grease to minimize any thermal contact resistance and then inserted into the sheath. A barbed fitting was then screwed into the top of each sheath and heat shrink tubing was shrunk over the fittings and the thermistor leads to provide strain relief. To hold the finished thermistor probes, housings were constructed of polypropylene round stock. The rod was cut to 6.5cm lengths and then bored through axially. This hole was then tapped 1/2" NPT and 1/4" barbed tubing connectors were installed at both ends. A second hole at the top of the housing was drilled and tapped 1/4" NPT to allow mounting of the thermistor probes. The external exposed parts of the probe assembly were then covered with foam pipe insulation to minimize errors caused by changing ambient conditions. Figure 14 shows the finished sensor/housing assembly.

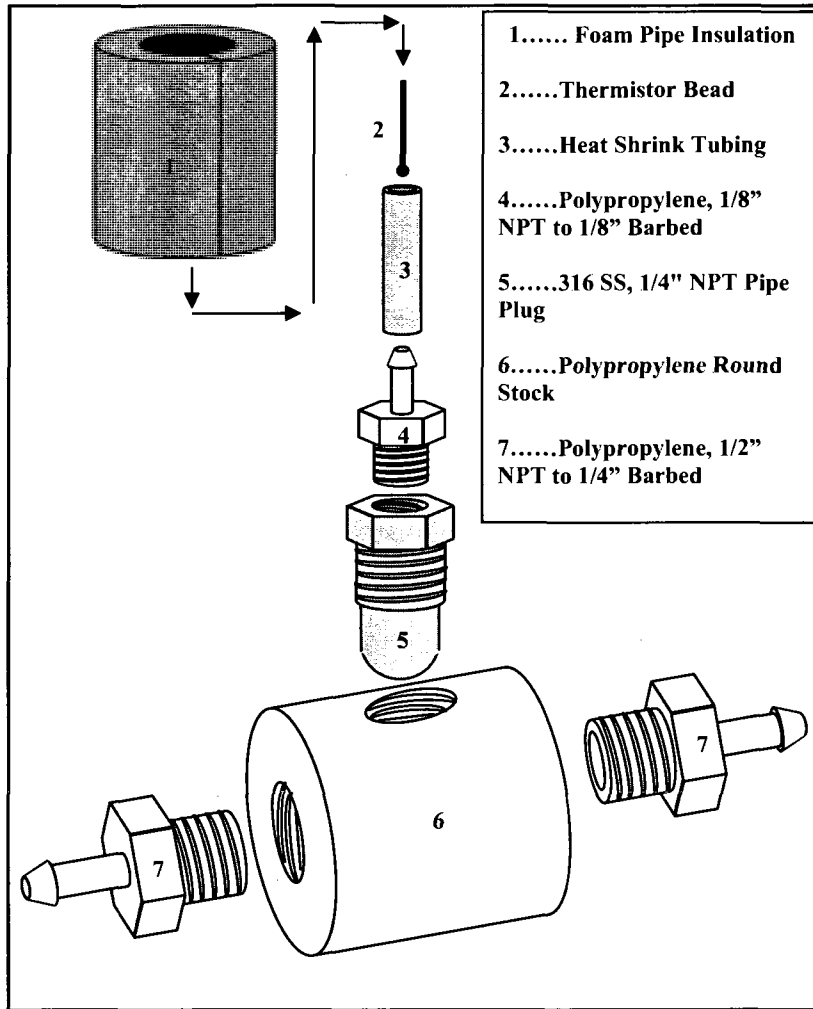


Figure 14. Thermistor housing assembly

The thermistors were wired to the Am16/32 multiplexer using a 3 wire half bridge configuration. This setup, shown in Figure 15, compensates for the lead resistance by assuming that the resistances of both current carrying wires are the same. Leads between the tracker and the shed are 22AWG, 4-wire, shielded cable.

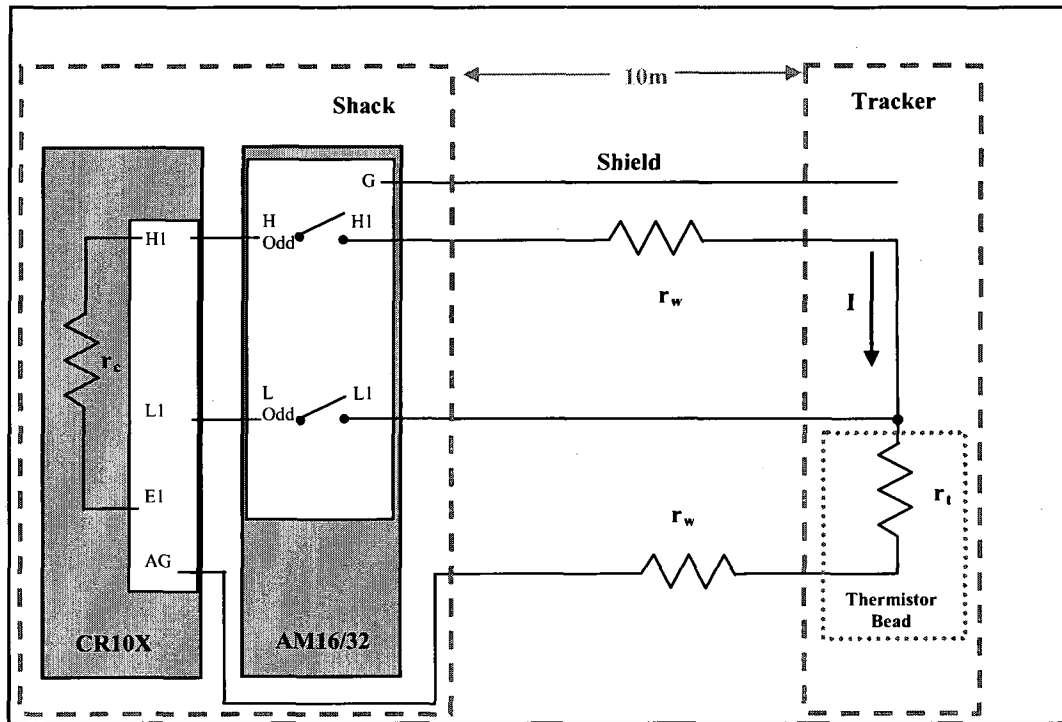


Figure 15. Three wire half bridge used for thermistor measurements

When the multiplexer is activated, the relays connecting terminals H1 and L1 to L and H odd close. After a delay of .2s an excitation voltage of 1850mV is applied to the system from terminal E1 on the datalogger. The excitation is kept on for .7 s to allow the system to achieve steady state. At the end of this period, a single ended voltage measurement is made at terminal H1. This sequence is repeated for terminal L1 After the both measurements are made, there is another delay of .2s before the first set of relays open and the second set closes. This process is then repeated for the other three thermistors. It is worthwhile to note here that Figure 15 shows the internal relays and connections between the multiplexer and the datalogger. These are shown to help clarify the sequence of events which occurs when a measurement is made using the multiplexer.

These details will be omitted from subsequent diagrams, as all measurements on the multiplexer will follow the same sequence of events listed below.

- (1) Close relay set
- (2) Delay for .2s
- (3) Measurement instructions
- (4) Open current relay set, close next set

From the two raw voltage measurements, the thermistor resistance r_t is calculated as follows:

The current through the circuit is given by Equation 5.

$$I = \frac{V_{E1} - V_{H1}}{r_c} \quad (5)$$

Where V_{E1} is the excitation voltage specified in the logger program, V_{H1} is the measured voltage at terminal H1 and r_c is 200k-ohm. The value of r_c was selected to allow the use of a high excitation voltage and a lower voltage range for the measurements. This ensures that the noise in the excitation does not have an effect on the signal noise. In addition to this, the relatively large resistance limits the current through the thermistor reducing the self heating error. YSI lists the self heating as being 8mW/°C for thermistors immersed in a well stirred oil bath. For the excitation voltage used, the maximum power which will be dissipated by the thermistor over the design temperature range will be 2μW. This results in a maximum self heating error of .0002 °C which is considered negligible.

The measured voltage drop between terminals H1 and L1 is given by Equation 6.

$$V_{H1} - V_{L1} = I r_w \quad (6)$$

Where r_w is the unknown lead resistance of one leg of the circuit. Similarly the voltage drop between terminal L1 and ground is given by Equation 7

$$V_{L1} = I(r_t + r_w) \quad (7)$$

This linear system can be solved for the unknown thermistor resistance as a function of the known values.

$$r_t = \left(\frac{V_{H1} - 2V_{L1}}{V_{H1} - V_{E1}} \right) r_c \quad (8)$$

The resistance values provided by YSI are 30000 ohm and 5359 ohm at 25 °C and 70 °C respectively. Because the wire resistance is small, the range for the voltage measurements V_{H1} and V_{L1} can be estimated using Equations 5-8, as 48-241mV using 60Hz noise rejection. In this range, the logger resolution is 66.6 μ V for a single ended voltage measurement. An uncertainty analysis was performed and is included in Appendix C. These calculations estimate the maximum total uncertainty for any absolute temperature measurement as $u_T = \pm 0.36$ °C.

For this experiment, the temperature data taken is used to define the thermodynamic state at the inlet and outlet of the individual cells. Because all calculations are based upon changes between the inlet and outlet, the absolute temperature accuracy of any individual thermistor is considered to be of secondary importance when compared to the accuracy of the temperature difference between two thermistors on the same cell. If the same

Steinhart coefficients are used for all sensors, the uncertainty of the ΔT measurement across either cell is given by Equation 9.

$$u_{\Delta T} = \sqrt{u_{T1}^2 + u_{T2}^2} = u_T \sqrt{2} = \pm .51^\circ C \quad (9)$$

At the time that the measurement system was being designed, the probable temperature change across the cell was estimated to be around 1-2 °C. Because the uncertainty would be a significant percentage of the measurement, a calibration method was devised to reduce it. To implement this, all four thermistor housings were moved to the same side of the tracker and heavily insulated as shown in Figure 16.

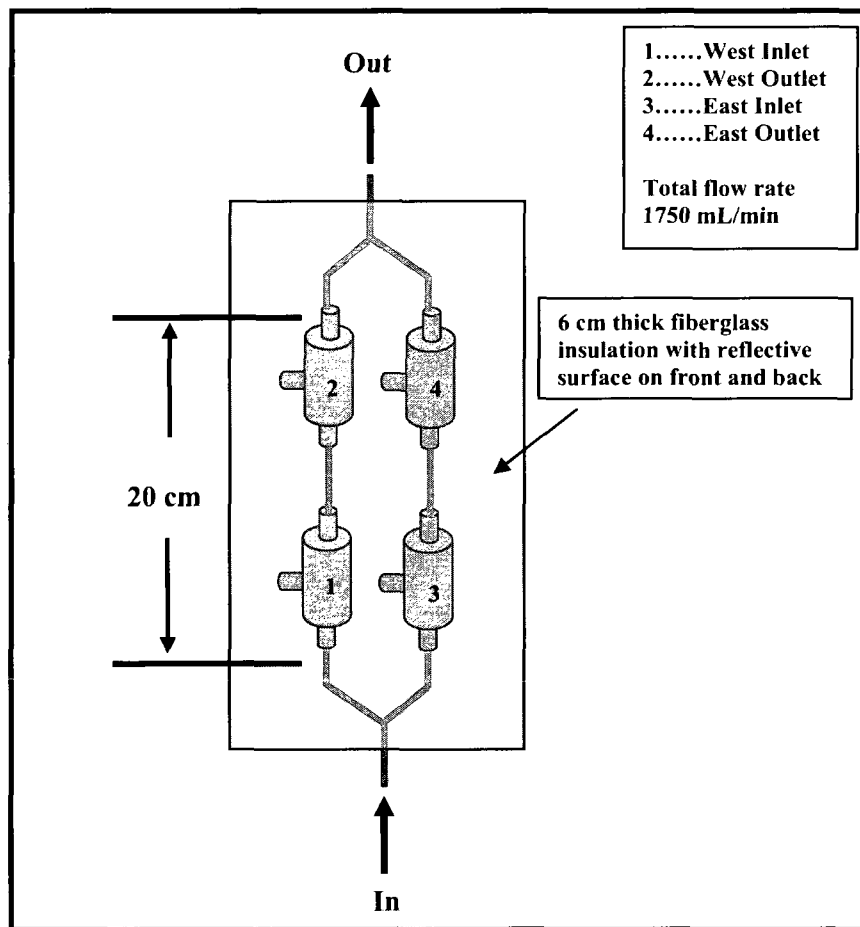


Figure 16. Configuration of thermistors during calibration

The test system was filled with 19 liters of high purity de-ionized water and the flowrate was set at 1650mL/min. The overall length of tubing was kept to a minimum and the thermistors were placed as close to one another as possible to keep temperature differences between sensors to a minimum. The system was taken through a heating/cooling cycle (from 25 °C to 70 °C) over the course of a day. Resistance data for the cycle was recorded at 1 minute intervals. As was alluded to previously, the temperature-resistance relationship for a thermistor can be expressed using the Steinhart-Hart equation.

$$T(r_i) = \left(\frac{1}{A + B \ln(r_i) + C \ln(r_i)^3} \right) - 273.15 \quad (10)$$

Where T is temperature in °C, r_i is the thermistor resistance in ohms, and A B and C are fitting coefficients specific to the type of thermistor compound being used and the range of temperatures being considered. The West outlet thermistor was arbitrarily selected to be used as the reference value. Its temperature resistance curve is calculated using equation 10 and the three coefficients provided by the manufacturer for the type 44032 thermistor between 25 and 70 °C. Using these coefficients, this measurement will be within .36 °C of the actual temperature. Steinhart coefficients will be selected for the other sensors to match them to this reference thermistor.

To facilitate the sensor calibration a multivariable optimization routine was written using MATLAB[®]. The two functions created for the algorithm are included in Appendix D. The routine takes as inputs the resistance data for the two sensors and the Steinhart-Hart coefficients for whichever sensor is being used as the reference. The algorithm then

determines the values of A B and C for the non-reference sensor which minimizes Equation 11 over the data set.

$$\theta = \sum_i |T_{ref_i} - T_{cal_i}| \quad (11)$$

Where T_{ref} is the temperature measured by the reference sensor, T_{cal} is the temperature measured by the sensor being calibrated, and θ is a measure of the overall disagreement over the data set between the two. The program was run several times as described by the following steps.

- (1) With the West outlet sensor used as the reference (using coefficients provided by manufacturer), match the East inlet sensor to this.
- (2) With the West outlet sensor used as the reference (using coefficients provided by manufacturer), match the West inlet sensor to this.
- (3) With the East inlet sensor used as the reference (using coefficients generated in step 1), match the East outlet sensor to this.

The resulting 3 sets of coefficients have been optimized to minimize differences between inlet and outlet sensors on a single cell as well as (although this is of secondary importance) differences between any sensor and the reference sensor (West outlet). Figures 17 and 18 show the calculated ΔT for the calibration resistance data set using

both the standard Steinhart coefficients as well as the optimized values for both sets of thermistors (East and West corresponding to their eventual position on the tracking unit).

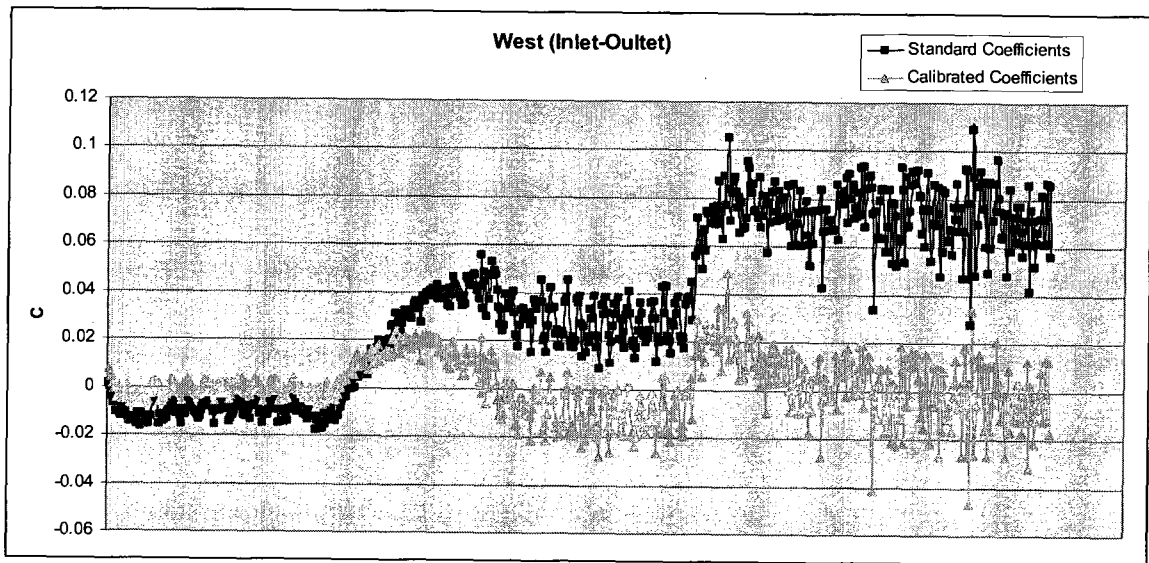


Figure 17. West side thermistor agreement before and after calibration

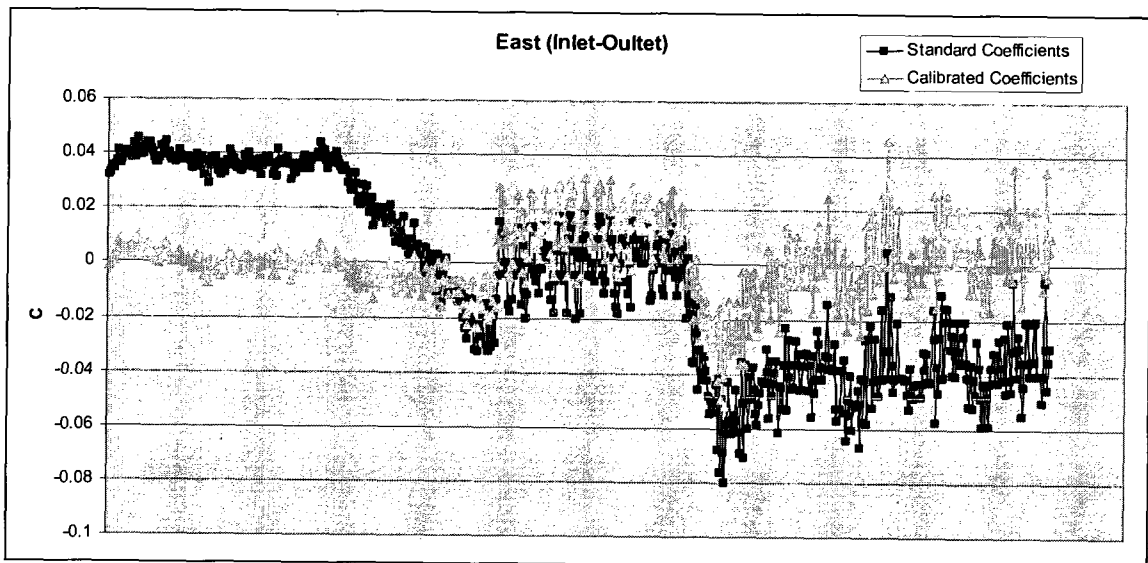


Figure 18. East side thermistor agreement before and after calibration

The figures demonstrate a substantial improvement in agreement using the calibrated coefficients compared to the standard values. The data also shows that the uncertainty for either ΔT measurement after the calibration can be estimated as $\pm .05$ °C.

Flowmeters

The flow rate of electrolyte through each cell as well as the bypass circuit is measured using an Omega[®] FT601B ultra low flow sensor shown in Figure 19.

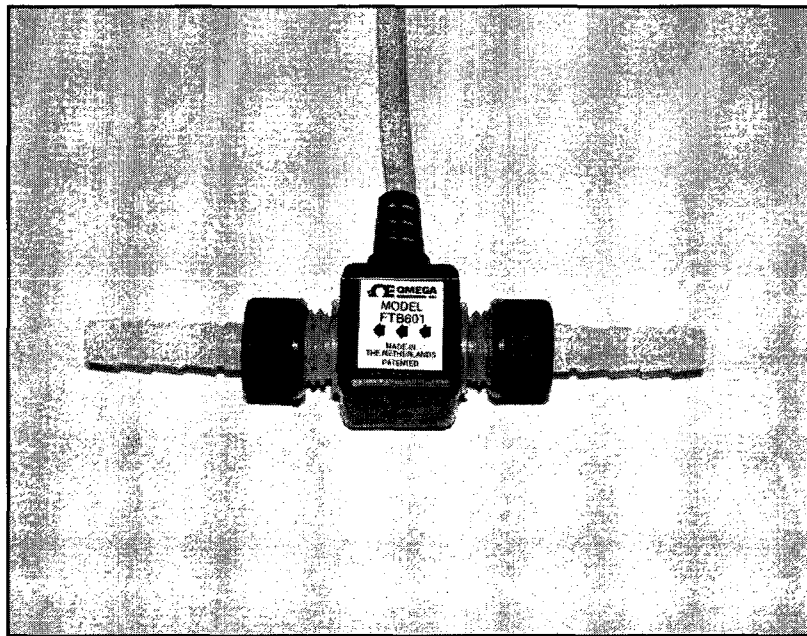


Figure 19. Omega FT601B ultra low flow sensor

These units are an axial paddlewheel turbine type and output a pulse signal at a frequency which is linearly proportional to the flow rate. The proportionality constant is 36000 pulses/L. The units selected for this project can measure from .1 to 2 Liters per minute with an accuracy of $\pm 3\%$ of the indicated value and as previously stated are compatible with many different types of electrolytes. Because the pulse counting error of the datalogger is much smaller than the uncertainty of the flowmeter, the total uncertainty

of the flow measurements can be estimated as being that of the flowmeters alone ($\pm 3\%$ of the reading). Detailed specifications for the flowmeters are included in Appendix B.

A barbed fitting at each end of the meter allows connection to the flexible tubing. When designing the flow path for the system, care was taken to ensure that at least 30 cm of straight tubing before the inlet and after the outlet of each meter would be maintained throughout the range of motion of the tracker. Due to the distance from the tracker to the shack, the leads of each meter were extended 8m, using 22AWG, 4-wire, shielded cable. All splices were soldered and wrapped with electrical tape to ensure a solid, watertight connection. The excitation voltage was taken from the power supply as shown in Figure 20. The 12V at the power supply is reduced to 7V using a 115 ohm resistor. Although the manufacture's specifications for the flowmeters claim that an excitation as low as 5V can be used, through trial and error it was found that using 7V greatly increased the reliability of the units. Due to the relatively high frequency of the output, the flowmeters could not be wired directly to the pulse channels on the datalogger. The SDM-IO16 expansion module is designed to work with the high frequency signal and the flowmeters are connected as shown in Figure 20.

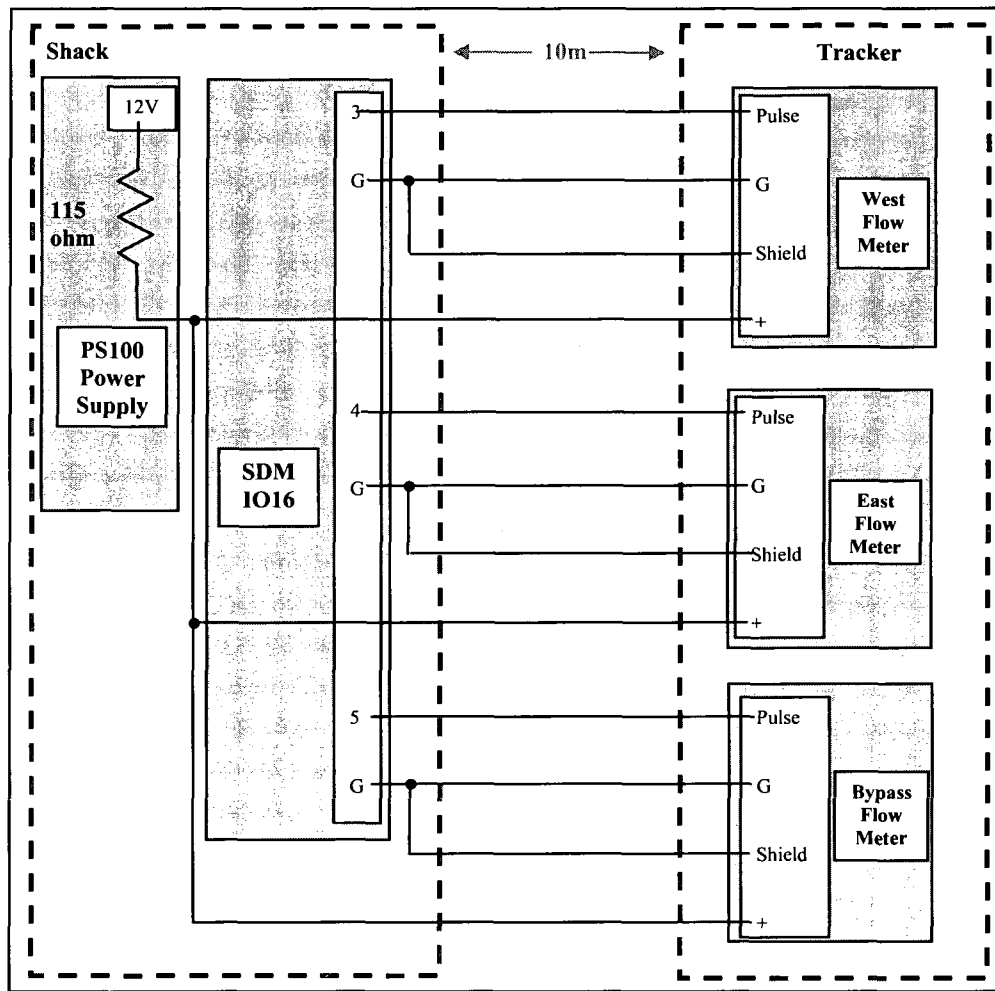


Figure 20. Flowmeter connection to SDMIO16 module

Resistivity Sensors

Electrolyte resistivity is measured using dual Foxboro® 873RS analyzers and 871cc contacting resistivity sensors. These are shown in Figures 21 and 22 respectively.

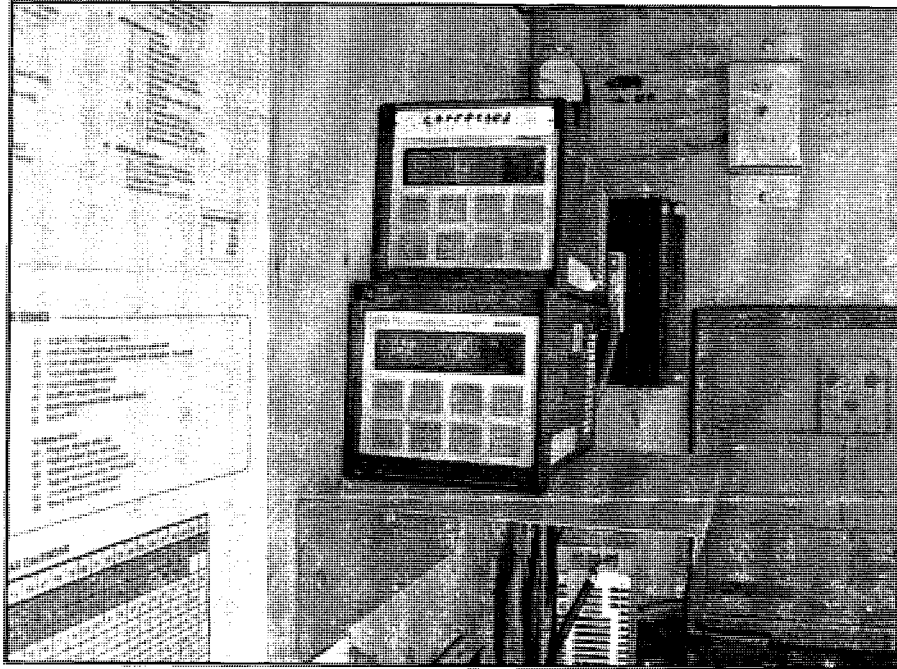


Figure 21. Dual Foxboro 873RS resistivity analyzers installed in shed

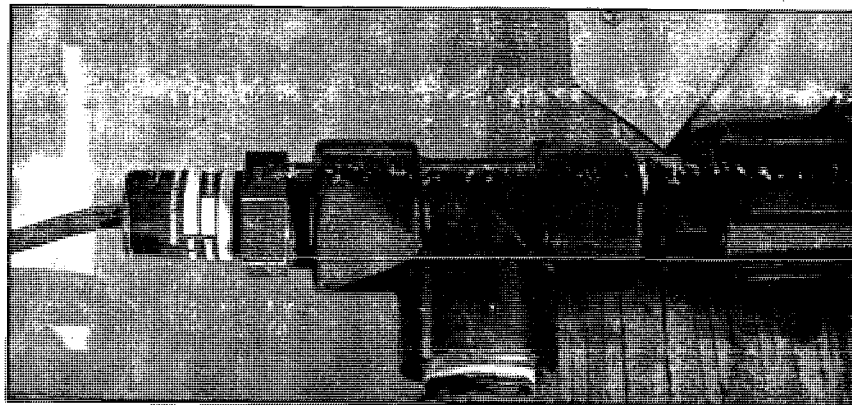


Figure 22. Foxboro 871CC contacting resistivity sensor installed in system

Two analyzers and sensors are used to allow both absolute as well as temperature compensated measurements to be recorded. The 871cc sensors are a contacting type with concentric titanium electrodes and are designed specifically for resistivity measurements in ultra-pure water. Each sensor has a built in 100k-ohm thermistor to be used for temperature compensation if desired. The units are individually calibrated at the factory and come with the correct cell factor and thermistor correction factor printed on the body of the sensor. The nominal cell factor for the sensors is .1. Detailed specs for both the analyzers and cells are included in Appendix B. The 873RS analyzers allow for measurement of either absolute or temperature corrected resistivity and output a scalable analog voltage proportional to the measurement. This output allows the analyzer output to be connected directly to the multiplexer as shown in Figure 23. To reach the shed, the sensor leads were extended 3m, using 22AWG, 4-wire, shielded cable.

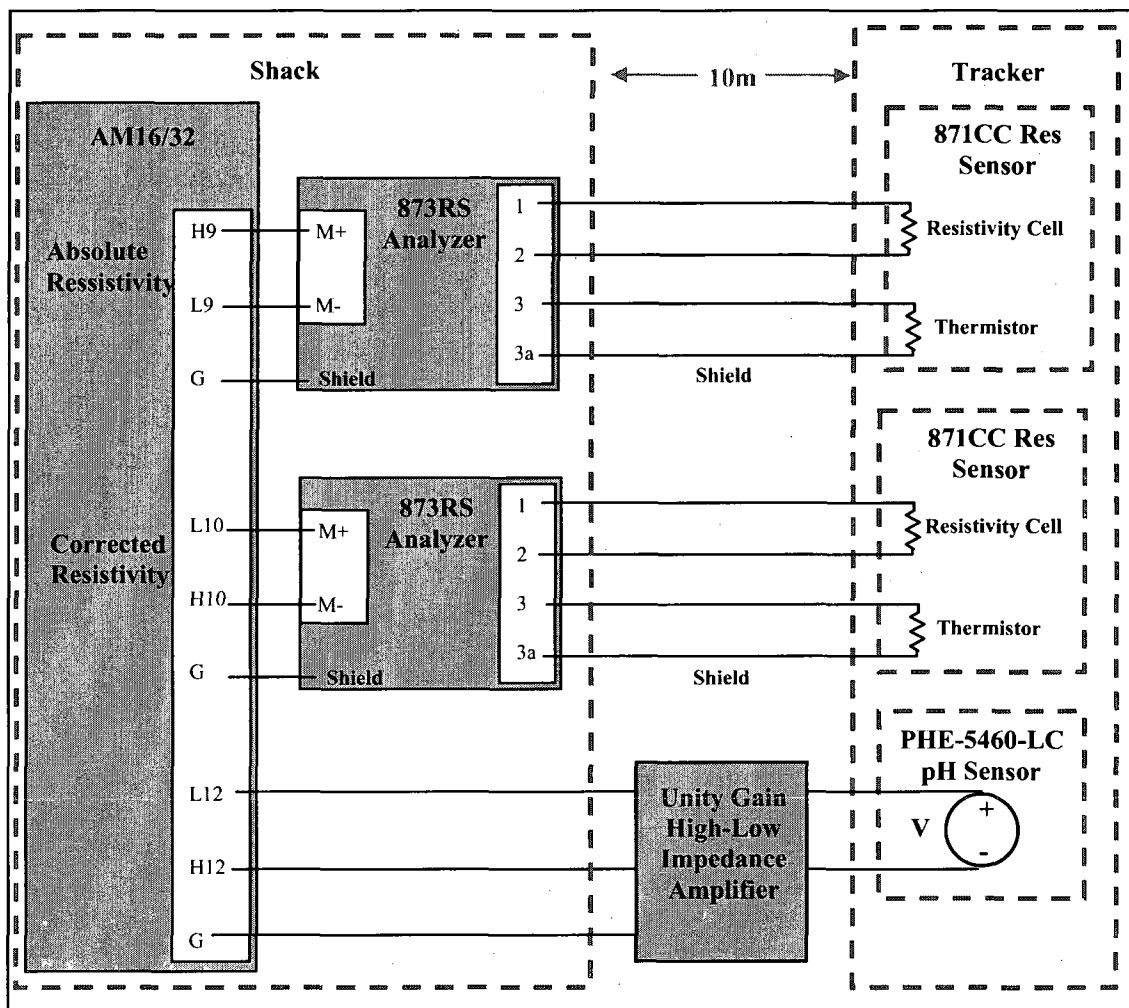


Figure 23. Resistivity analyzer and pH sensor connections to multiplexer

The signal is measured by the logger as an autorange differential voltage with 60 hz noise rejection. Both analyzers were bench calibrated as specified by the manufacturer and the cell factor and thermistor correction factor provided with each sensor were entered into each unit. The analog outputs were scaled such that a reading of 2.000 M-ohm cm produces a differential voltage of close to 2.5V which is the maximum that the logger can read. A reading of 0 M-ohm cm will result in an output of near 0V. To determine the best multiplier and offset to convert from voltage to resistivity in the

datalogger program, the analog outputs of both analyzers were held at 100%, 80%, 60%, 40%, 20%, 0% for a period of one hour for each setting. Differential voltage measurements were recorded at 1 minute intervals and an average voltage was calculated for each analyzer at each output level. These averaged values were then used to calculate the slope and intercept for the conversion to resistivity. The final relationship between voltage and resistivity used by the datalogger is demonstrated in Figures 24 and 25.

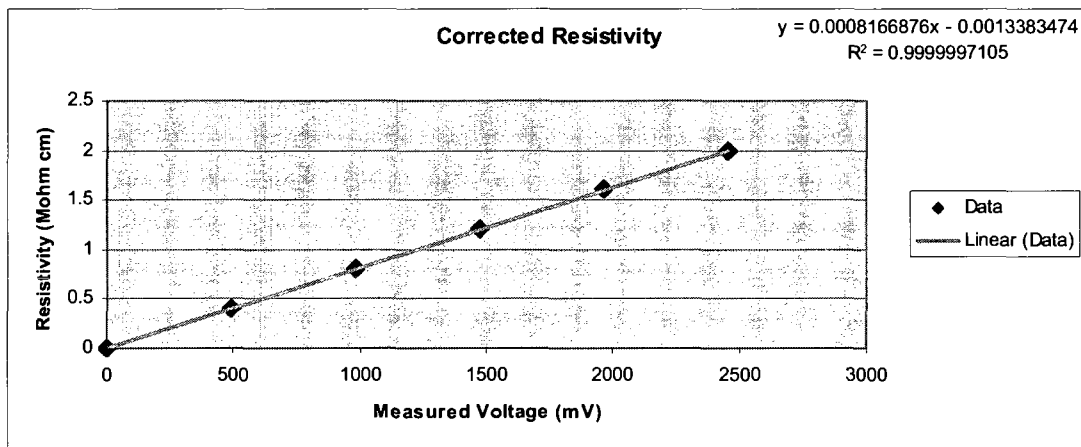


Figure 24. Corrected resistivity vs. voltage relation

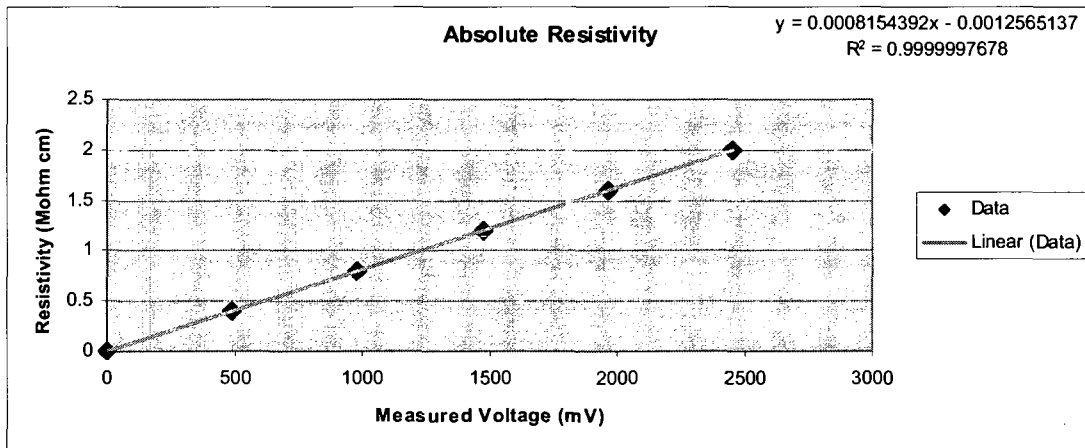


Figure 25. Absolute resistivity vs. voltage relation

The preceding figures show that the output signal of the analyzers is quite linear, so in retrospect it was not necessary to calibrate at so many points. This however was not known a priori. The reported accuracy for the 873RS analyzer paired with the 871cc sensor is $\pm 5\%$ of the full scale range. The total uncertainty for the measurement is estimated to be ± 0.01 M-ohm cm based upon the analysis included in Appendix C. The analysis shows the uncertainty contribution from the voltage measurement to be negligible but again this was not known until after the formal analysis was completed.

pH Sensor

Electrolyte pH is measured using an Omega PHE-5460-LC double junction, combination pH electrode. Complete specifications for the unit are included in Appendix B and the installed sensor is shown in Figure 26.

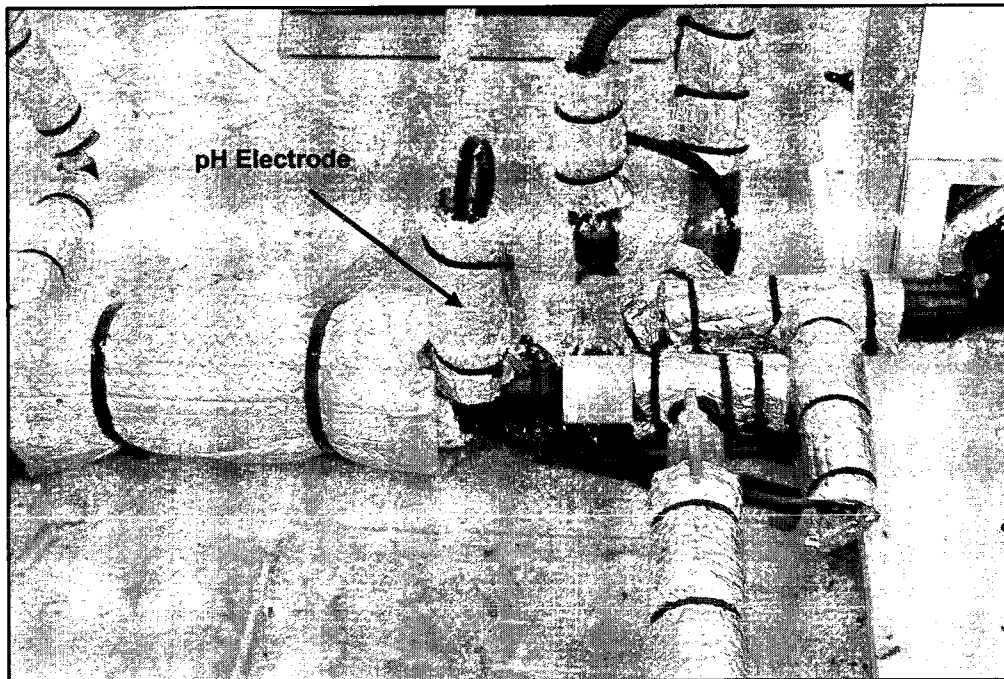


Figure 26. Omega PHE-5460-EC installed in system

The pH sensor is wired to the multiplexer as shown in Figure 23. As illustrated, the high impedance mV signal from the sensor is routed through a unity gain amplifier, converting it to a low impedance signal which can be measured as an auto range, 60Hz rejection, differential voltage by the logger. The sensor output is linear with pH so a two point calibration is used to determine the correct conversion multiplier. Sensor calibration is performed by immersing the electrode in two buffer solutions of known pH and measuring the mV output. Solutions of pH=4.01 and pH=7.0 are used for the calibration since this is the expected range of the system electrolyte. The buffers are maintained at 25 °C and 30 minutes of data is collected for each solution. An average value for each solution is then calculated from which the slope for the sensor @ 25 °C is determined.

The expected range of pH measurements is between 4.0 and 7.0 with electrolyte temperatures generally less than 50 °C. In this range, the change in the sensor slope due to temperature is considered negligible and no temperature compensation is implemented in the logger program. Changes in slope due to temperature are accounted for in the uncertainty analysis presented in Appendix C. Based upon this analysis the overall uncertainty for the pH measurement is estimated to be ± 0.22 pH.

Cell Potential

Figure 27 shows the connection of the cells to the two power supplies used to control the external potential applied to each electrode. It should be noted here that all connections for the voltage and current measurements are made using 16AWG, two conductor shielded cable with the shield grounded at the shed. To simplify the diagram, the shield wires are omitted from Figure 27.

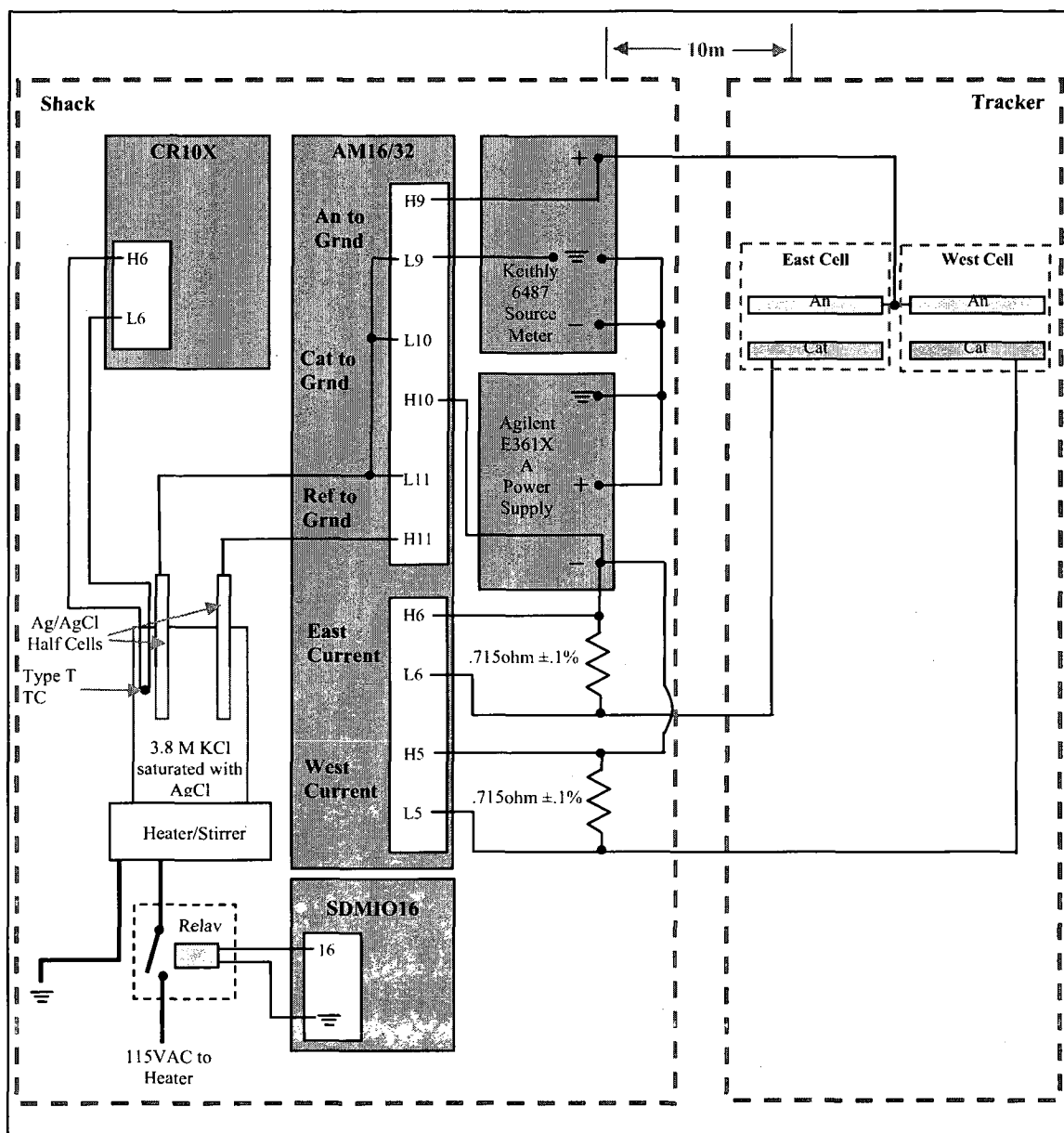


Figure 27. Wiring for cell potential and current measurements

The system is designed to allow adjustment of either anodic or cathodic potential relative to the standard hydrogen electrode at a known temperature. To accomplish this, the two power supplies are connected to one another as shown. The connection allows the positive terminal of the Keithly[®] supply to be adjusted to potentials positive of the

ground lug. Likewise, the negative terminal of the Agilent[®] unit can be set to potentials negative of the ground lug. Detailed specifications for both power supplies are included in Appendix B.

A reference cell was created using two Ag/AgCl reference half cells immersed in a 3.8M KCl solution which is saturated with AgCl, as an electrolyte. This electrolyte was selected because it is the same as the fill solution for the half cells themselves. This prevents any changes in the electrode fill solution due to diffusion of ions into the electrolyte caused by concentration gradients. As shown, the cell is placed on a heater/stirrer for temperature control and to keep the electrolyte well mixed. The heating element is wired to a relay which is switched using port 16 on the SDMIO16. In this manner, the reference cell temperature can be maintained at the same temperature as the working electrodes. Doing this ensures that all measured potentials are referenced properly in spite of the fact that the actual reference electrode is not physically located in the PEC cells.

The Ag/AgCl electrode is commonly used in place of the SHE because it is easier to re-create in the lab and its potential relative to the SHE at a given temperature is known and is relatively independent of current. Because both electrodes in the reference cell are identical, the potential across the reference cell by itself is zero at all temperatures. When one side of the cell is connected to the ground lug of the power supplies as shown, the potential between the ground state and the Ag/AgCl half cell can be measured. Because the applied anodic and cathodic potentials are measured relative to the ground lug they are now also known relative to the Ag/AgCl half cell and thus relative to the SHE. The temperature of the reference cell is measured using a special limits of error T-type

thermocouple encased in a thin silicone sheath, connected directly to the datalogger as shown. The relationship between temperature and the potential of the Ag/AgCl electrode relative to the SHE for the molarity being used was interpolated from data presented in [71] and is shown in Figure 28. The finished reference cell is shown in Figure 29.

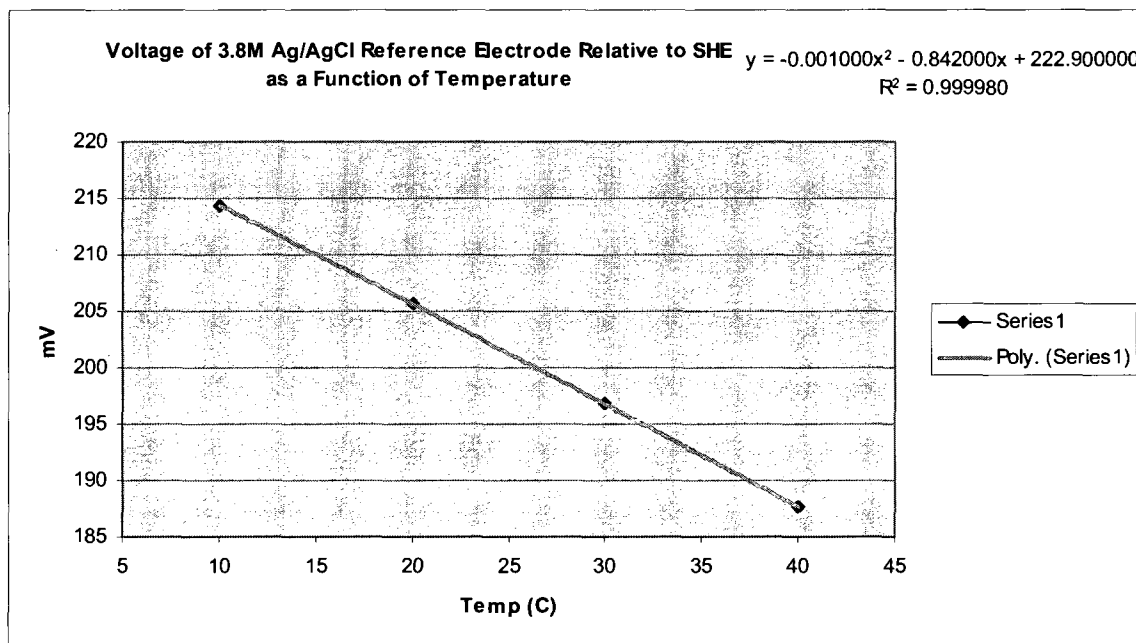


Figure 28. Potential of 3.8M Ag/AgCl reference electrode vs. temperature

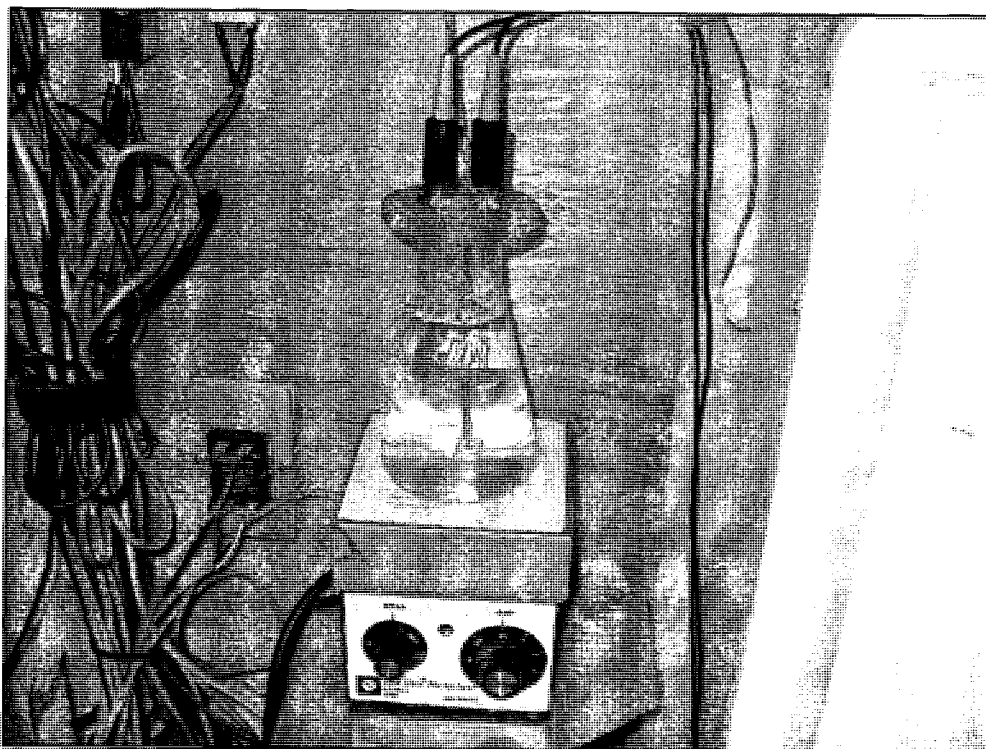


Figure 29. Finished reference cell

The total uncertainty for the electrode potential measurements relative to the SHE are estimated to be less than $\pm 3\text{mV}$ based upon the analysis included in Appendix C.

Cell Current

Cell currents are calculated by measuring the voltage drop across an inline precision resistor as shown in Figure 27. The resistors were selected such that their resistance (.715 ohm), is many orders of magnitude smaller than that of the cells. By doing this, the influence on the current caused by the measurement apparatus is made negligible. The maximum total uncertainty in the current measurement throughout the expected range of testing is $\pm .004\text{mA}$. This estimate is based upon the analysis included in Appendix C. It is worthwhile to note here that the uncertainty in the measurement is a function of the

magnitude of the current. The number presented here is for a cell current of 1mA, which is near the maximum value recorded during the final test series.

Integrated Solar Flux

Integrated solar flux is measured using a Licor[®] LI200X pyranometer mounted on the tracker as shown in Figure 30.

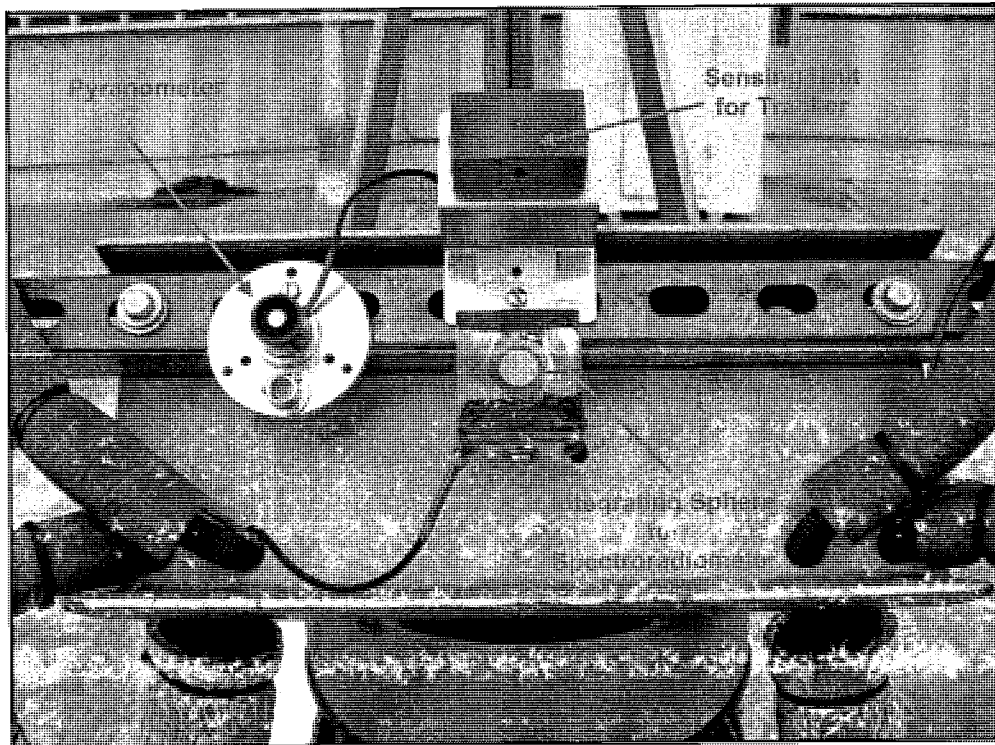


Figure 30. Pyranometer, spectroradiometer integrating sphere, and tracker sensor

This device uses a cosine corrected silicon photovoltaic detector [72] which outputs a current proportional to total hemispherical radiation per unit area. A variable resistor in parallel with the detector converts the signal to a differential voltage which can be read by the CR10X. The resistance value for each individual sensor is adjusted by the manufacturer such that the device outputs $.005\text{mV}$ per W/m^2 . Connection to the CR10X

is as shown in figure 31. It is worthwhile to note here that the sensors distributed by Campbell Scientific are essentially “plug and play” devices. This is to say that they are simply wired to the logger as shown in the instruction manual. The resistors and other electrical components shown in figure 31 are integral parts of the sensor as they arrive from Campbell Scientific. They are shown in the figure only to help illustrate how the actual measurement is made.

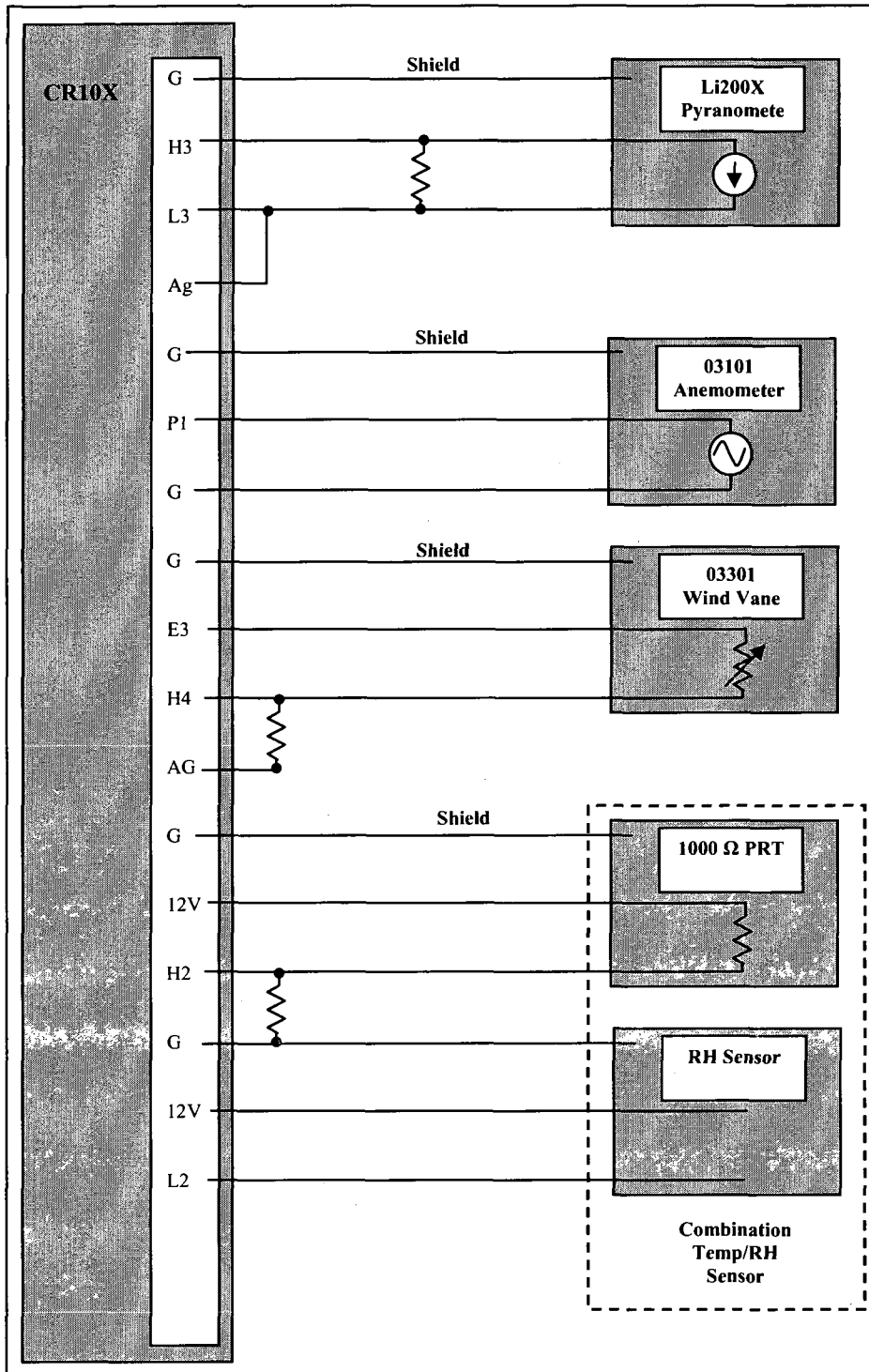


Figure 31. Connection of weather sensors to CR10X datalogger

Complete specifications for the pyranometer are included in Appendix B. Since this sensor is distributed by Campbell Scientific for use with the CR10X, the total uncertainty for the measurement can be estimated directly from the spec sheet as being $\pm 2\%$ of the measurement.

Wind Speed

Horizontal wind speed is measured using a R.M. Young[®] model 03101 anemometer. The device, shown in figure 32, consists of a three-cup anemometer and outputs an AC voltage at a frequency proportional to the horizontal wind speed.

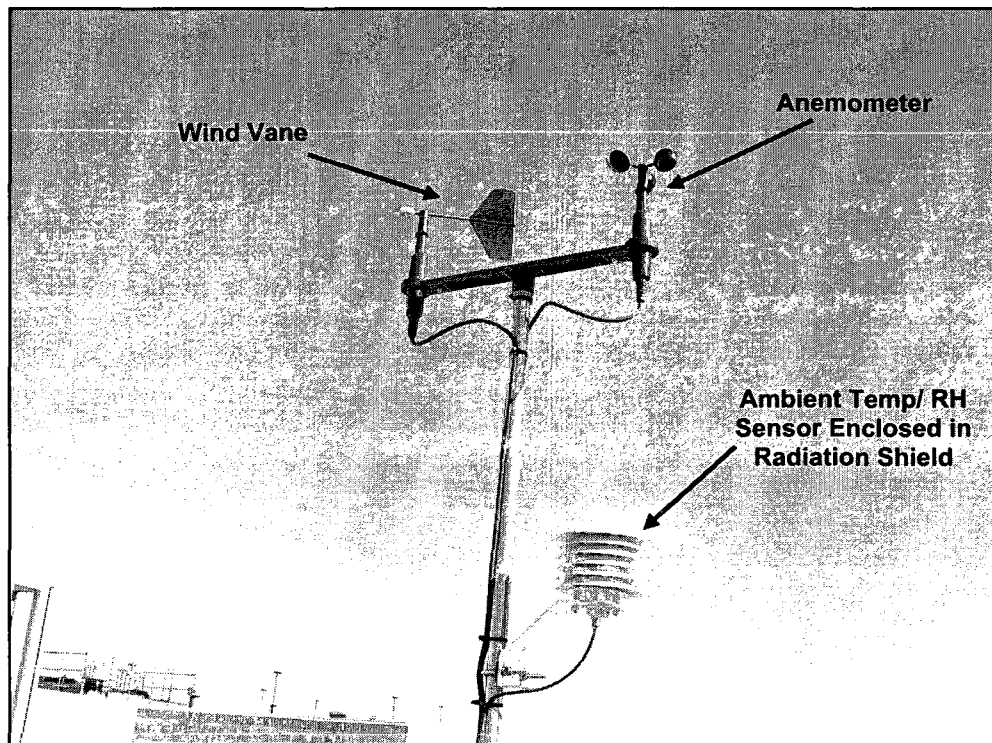


Figure 32. Various weather sensors installed on tracker

The anemometer is wired to the logger as shown in figure 31. As with the pyranometer, this device is distributed by the Campbell Scientific to be used with their dataloggers, so no formal uncertainty analysis is necessary. The value presented in the instrument manual is $\pm 5\text{m/s}$. Detailed specifications for the device are included in Appendix B.

Wind Direction

Wind direction is measured using a R.M. Young model # 03301 wind vane shown in figure 32. The sensor uses a variable resistor to sense direction and is wired to the datalogger as shown in figure 31. Again this sensor is distributed by the datalogger manufacturer, so no formal uncertainty analysis is performed. The uncertainty of the measurement presented in the spec sheet (Appendix B) is $\pm 5^\circ$.

Ambient Temperature and Relative Humidity

Ambient temperature and relative humidity are measured using a Campbell Scientific CS500 Temperature and relative humidity probe mounted in a model 41003 10-Plate radiation shield. The installed unit is shown in figure 32. The sensing device consists of a 1000Ω PRT (Platinum Resistance Thermometer) for temperature measurements and an INTERCAP[®] type sensor for relative humidity, mounted together in a single housing. The sensor is wired to the data logger as shown in figure 31. As with the previous 3 measurements, this device is distributed by the datalogger manufacturer, so no formal uncertainty analysis is performed. According to the specifications provided, the uncertainty of the temperature measurement is $\pm .08^\circ\text{C}$ over the range in which it is used. The accuracy of the relative humidity sensor is specified as $\pm 3\%$ at 20°C over the range in which it will be used. It should be noted that the accuracy of the relative humidity

sensor is temperature dependent. Complete specifications for this device are included in Appendix B.

Other CR10X Measurements

Two additional J-type thermocouples are used to monitor the heater temperature and the city water temperature on the shell side of the heat exchanger. The sensor mounted on the heater is used to control the safety shutoff for the heater when a set temperature is exceeded. The sensor on the heat exchanger is used as a gauge of available cooling capacity. These sensors are only used for ballpark measurements so the accuracy is not critical. The heat exchanger thermocouple is wired to differential voltage channel 5 on the logger. Due to the lack of any available differential analog channels, the thermocouple on the heater is tied to single ended channel 8 on the datalogger. The single ended measurement is not as accurate as a differential type but since the measurement is not used for the analysis its use can be justified in this case.

Spectroradiometer

Spectral solar intensity between 300nm and 900nm is measured using a Stellarnet[®] EPP200C spectroradiometer and IC2 integrating sphere. The sphere collects the solar flux through a 16mm mm diameter aperture, where any directionality is removed through multiple reflections within the device. The IC2 is mounted on the tracker as shown in figure 31, and like the pyranometer, remains normal to the sun at all times during testing. The integrator is connected to the spectroradiometer (housed in the shack) using a 10m length of 6 μ m fiber optic cable. The spectroradiometer is the only measurement device which, due to the large number of individual sensors within the instrument, cannot be logged directly using the Campbell Scientific system. Instead, this device connects

directly to the USB port on the laptop and is controlled using its own software. During the tests, the unit is configured to record a “snapshot” of the spectrum at 15s intervals which is the same interval used by the datalogger. Because the intervals are the same for both devices, correlation between the two data files is simplified.

Difficulties in measuring the solar spectrum were initially encountered when using the device with the factory calibration file. The unit was found to read much higher than it should have when taking actual solar measurements, often integrating to values higher than the extraterrestrial solar constant. In contrast, measurements made using calibrated lamps were shown to correlate well. Similar results were documented using calibration files from two independent sources. It was speculated that the problem could stem from the fact that the calibration files were generated using lamps, whereas the actual measurements were being made in a different range. To address this problem, an alternate calibration method was developed using the sun as the calibrated source. The NREL Solar Radiation Research Laboratory (SRRL) facility in Golden, Colorado collects spectral solar data which is posted to their website [73]. The SRRL uses a LiCor LI-1800 spectroradiometer with the receptor facing due South at an angle of 40 degrees from horizontal to take a snapshot of the solar spectrum at 5 minute intervals. The LI-1800 measures between 300 to 1100nm at 2nm resolution and is calibrated by NREL twice a year. The Stellarnet unit was taken to a location within 800m of the SRRL site. The receptor was mounted on a tripod and oriented due South using a Brunton® compass as shown in Figure 33.

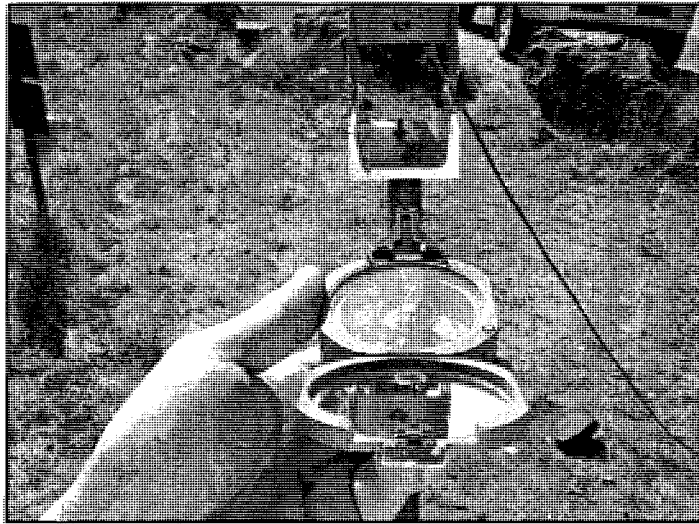


Figure 33. Facing the integrating sphere due South prior to calibration

The tripod was leveled in both directions and the receptor was inclined to the same 40 degree angle used by the SRRL unit as shown in Figure 34.

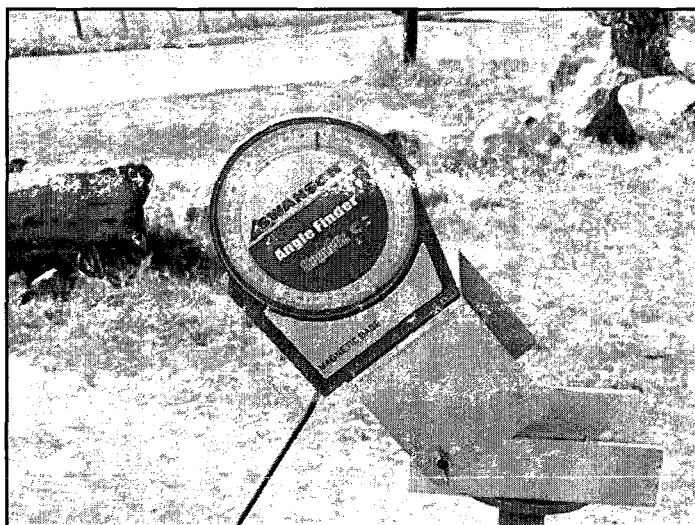


Figure 34. Setting the elevation angle of the integrating sphere

Snapshots of the spectrum were taken in 5 minute increments with the Stellarnet unit to correspond to the data collection times used by the SRRL instrument. The raw data generated by the uncalibrated Stellarnet spectroradiometer is in the form of a count for each wavelength between 300 and 900 nm in $\frac{1}{2}$ nm increments. This count is proportional to the flux of photons of a specific wavelength incident on the detector. To generate the calibration file, the 2nm resolution data generated by the SRRL was interpolated to the .5nm increments of the Stellarnet raw count data. The SRRL data is then divided by the Stellarnet raw count data for the corresponding time. The result is a calibration factor in units of $W/m^2 \text{ nm} / \text{count}$ for each $\frac{1}{2}$ nm increment measured by the Stellarnet. The final calibration file was created by taking the average values for 3 snapshots using a detector integration time of 15ms which is the same value which will be used during the tests. Uncertainty for the Stellarnet unit after the calibration is estimated to be that of the LI-1800 to which it was calibrated. This is reported as being $\pm 10\%$ of the reading. It is worthwhile to note that the figure reported here is the maximum uncertainty encountered at the smaller wavelengths. As the wavelength increases generally the uncertainty will decrease. The minimum value is presented as being $\pm 3\%$. Complete documentation for both instruments is included in Appendix B.

Measurement and Control Program

The Campbell Scientific datalogger and its peripherals are controlled by a master program which is uploaded to the CR10X from the USB port on the laptop. This program is used to specify the type order, and time sequence of the individual measurements as well as allocating temporary memory and controlling postprocessing of the measured parameters. In addition to this, the program is used to switch various control ports on and off based upon comparisons of measured parameters. In this manner, the logger can be used as both a control as well as a data recording device. The final version of the master program designed for this project is included in Appendix D. The purpose of this section is to outline the functions of the various parts of the final program.

Input Locations

The first few lines of the master program are used to designate and name the various temporary input locations used in the measurement and control sequence. These locations can be used to store constants, raw sensor data awaiting post processing, or control parameters which can be changed from the GUI such as temperature setpoint and deadband. The final program allocates a total of 120 temporary input locations. Many of these locations are only used for intermediate calculations and are not formally named. Of the 120 locations only 54 are utilized by the graphical user interface (GUI) and given formal names. As was alluded to previously, these names are listed in the first lines of the program.

Scan Rate

The scan rate is specified in the text following the "Mode 1" command. This number designates the frequency at which the main body of the program will be run. In this case,

the scan rate is 15s. This means that all of the measurements, calculations, and comparisons specified in the program will be repeated every 15s. It is important to note here that this value needs to be larger than the time that it takes to make the measurements and perform all of the manipulations specified. For this case, the program takes approximately 10s to run so there is a 5s latency between executions.

Measurement Instructions

The measurement instructions are implemented in lines 5-218. These lines include instructions for the sampling of sensors attached directly to the CR10X as well as activation, measurement and de-activation of the two peripheral devices (SDMIO16 and AM16/32). For simple measurements which require only that the raw data be multiplied or offset by a constant to convert to the appropriate units, this conversion is performed at the time that the measurement is made. For measurements requiring more complex calculations (thermistors, cell potential) the conversions are performed after all measurements have been completed.

Electrode Potential Calculations

Lines 232-237 are used to convert the raw differential voltage and temperature measurements into electrode potentials relative to the Ag/AgCl reference and then finally to the SHE at the reference cell temperature. As discussed in the previous section, the temperature dependence of the potential of the Ag/AgCl reference is modeled using a 2nd order polynomial.

Thermistor Calculations

Lines 275-320 are used to convert the thermistor raw voltage measurements into resistances. These resistances are then converted to temperatures using the Steinhart, Hart

equation and the calibrated coefficients discussed in the previous section. This conversion is performed in lines 325-445. It is worthwhile to note here that while all temperatures are presented in this writing in SI units, the actual program and GUI use the Fahrenheit scale as it is more intuitive to the author.

Temperature Control Constants

Lines 450-519 perform mathematical operations on the temperature control constants input from the GUI, as well as specifying how the average inlet temperature is calculated based upon which cells are considered active. These parameters are changed using two switches on the GUI and allow the system to function normally in the instance that either cell with its thermistors is removed from the system.

pH Calculations

Lines 520-521 are used to calculate the pH from the sensor mV signal based upon the relation determined from the calibration data.

Resistivity Control Constants

Lines 531 and 532 perform mathematical operations on the resistivity control constants, input from the GUI.

Resistivity Control Loop

Lines 533-564 define the logic used by the resistivity control loop. As shown in Figure 5, the system resistivity is increased by directing a portion of the flow through a resin bed de-ionizing filter using a solenoid valve. Since the resistivity will generally decrease naturally in the absence of other inputs, the system includes no means to actively reduce it. The loop takes 5 parameters input from the GUI, (Resistivity_Setpoint, Resistivity_Deadband_Hi, Resistivity_Deadband_Lo, Resistivity_Loop_Switch,

Resistivity_Selector_Switch,) and the two resistivity measurements (absolute and temperature corrected) to open or close the valve using a relay connected to control port 6 on the datalogger. The control logic for the resistivity loop is shown in Figure 35.

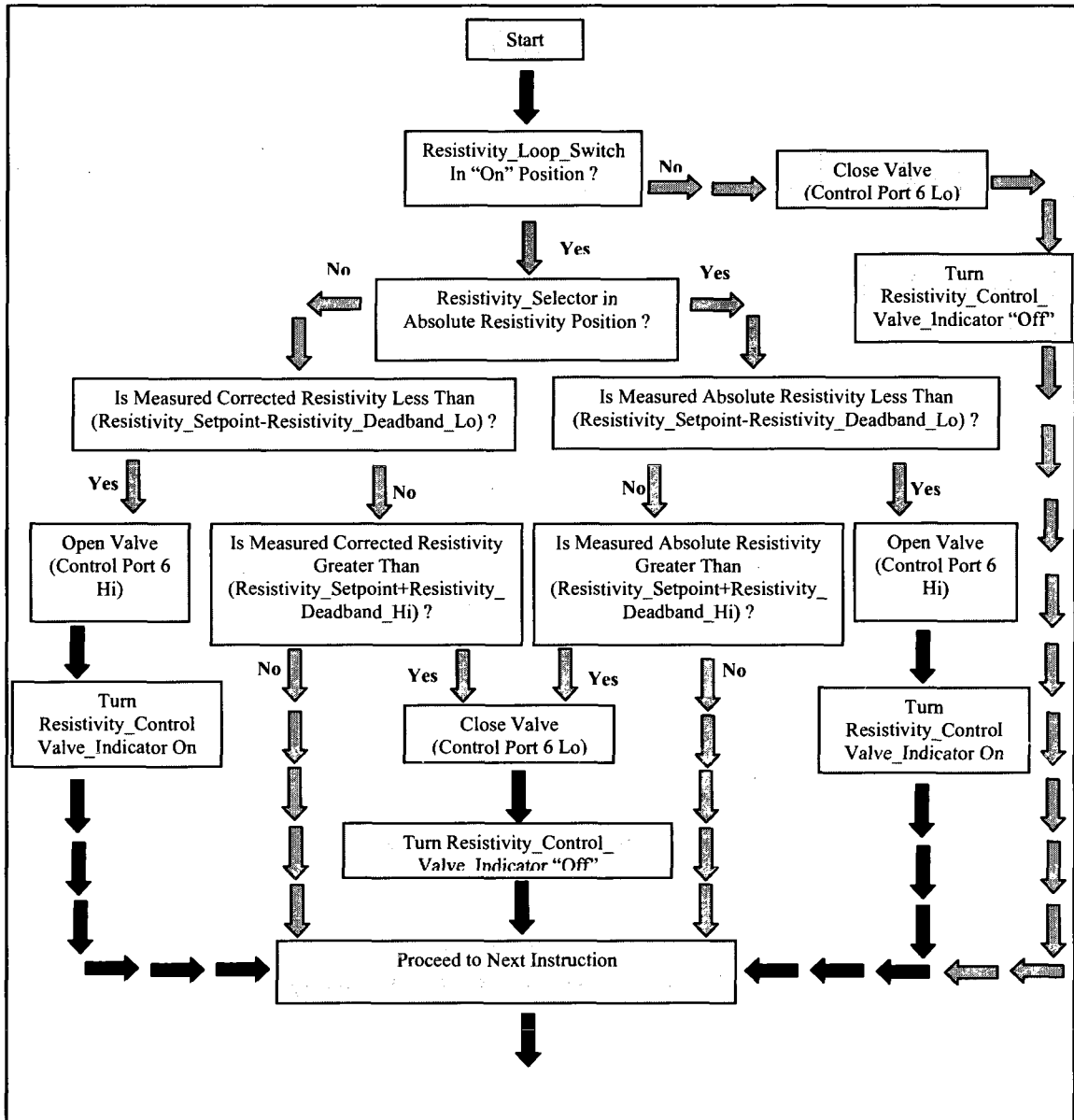


Figure 35. Logic for resistivity control loop

Temperature Control Loop

Lines 565-700 provide the logic for the temperature control loop. As shown in Figure 5, process temperature can be increased with an electric heater controlled using a solid state relay wired to control port 7. Temperature can be decreased by flowing city water through the shell side of the heat exchanger also shown in Figure 5. The flow of city water is started or stopped using a solenoid valve on a relay connected to control port 8. The temperature control loop takes 11 parameters input from the GUI, (Inlet_Setpoint, Temp_Deadband_Hi, Temp_Deadband_Lo, East_Cell_Active, West_Cell_Active, Low_Flow_Shutoff, Over_Temp_Shutoff, HAO_Mode_Switch, CAO_Mode_Switch, Heating_Loop_Switch, Cooling_Loop_Switch) as well as the inlet thermistor measurements to switch the two output ports on and off as required to maintain the setpoint. Additionally, the loop uses the two flow measurements and a temperature measurement from the thermocouple attached to the heating element as safety devices to shut the heater off in the event of either an over-temperature or zero-flow situation.

The temperature control can be operated in one of three modes depending on ambient conditions. In the normal operation mode, temperature is controlled by both the heater and cooler. In this mode, the heater will be switched on and the cooler switched off simultaneously when the temperature is low and vice versa when the temperature is high. On days when the ambient temperature is higher, the system can be run in CAO (Cooler Always On) mode. As the name implies, in this mode of operation the cooler is always running and temperature is controlled by cycling the heater. Similarly, on very cool days the system can be run in the HAO (Heater Always On) mode with temperature control being provided by cycling the cooler. Additionally, the heating and cooling loops can be

turned on or off independently of one another allowing for temperature control using one or the other devices under conducive ambient conditions. The logic for the temperature control loop is shown in Figure 36.

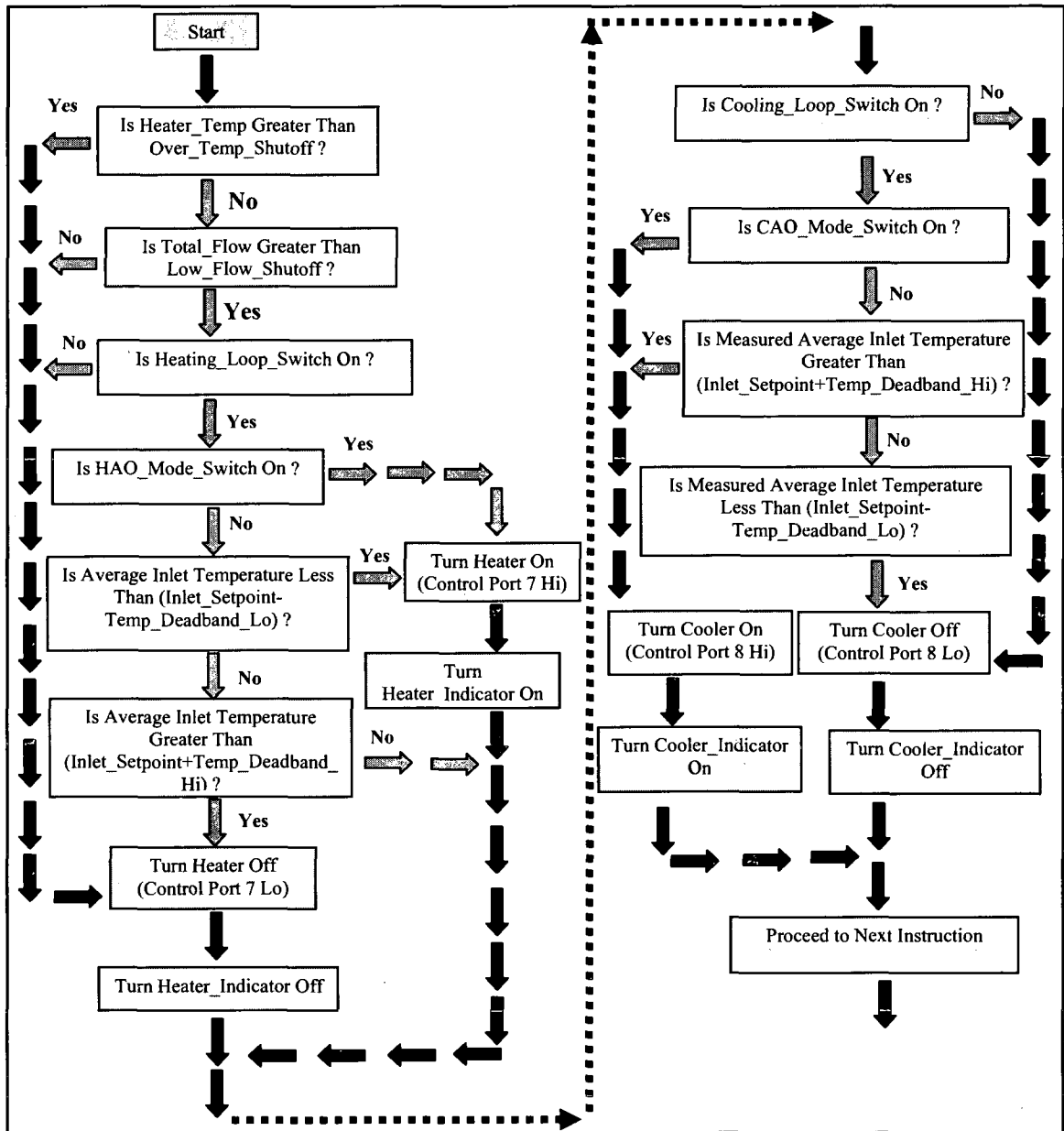


Figure 36. Logic for inlet temperature control loop

Reference Cell Temperature Control Constants

Lines 750 and 755 of the logger master program perform mathematical operations on the resistivity control constants, input from the GUI.

Reference Cell Temperature Control Loop

Lines 760-787 define the logic used by the reference cell temperature control loop. As discussed previously, all potentials are measured relative to an AG/AgCl reference electrode. These measurements can then be calculated relative to the standard hydrogen electrode for comparison to known values tabulated for the various reactions. This approach is only valid if the electrode being measured is at the same temperature as the reference. In order to maintain the reference cell at a specific temperature, the heating element of the heater/stirrer that the reference rests upon is controlled by a relay connected to port 16 of the SDM module. The logic shown in Figure 37 is used to switch the heater to maintain a specific setpoint.

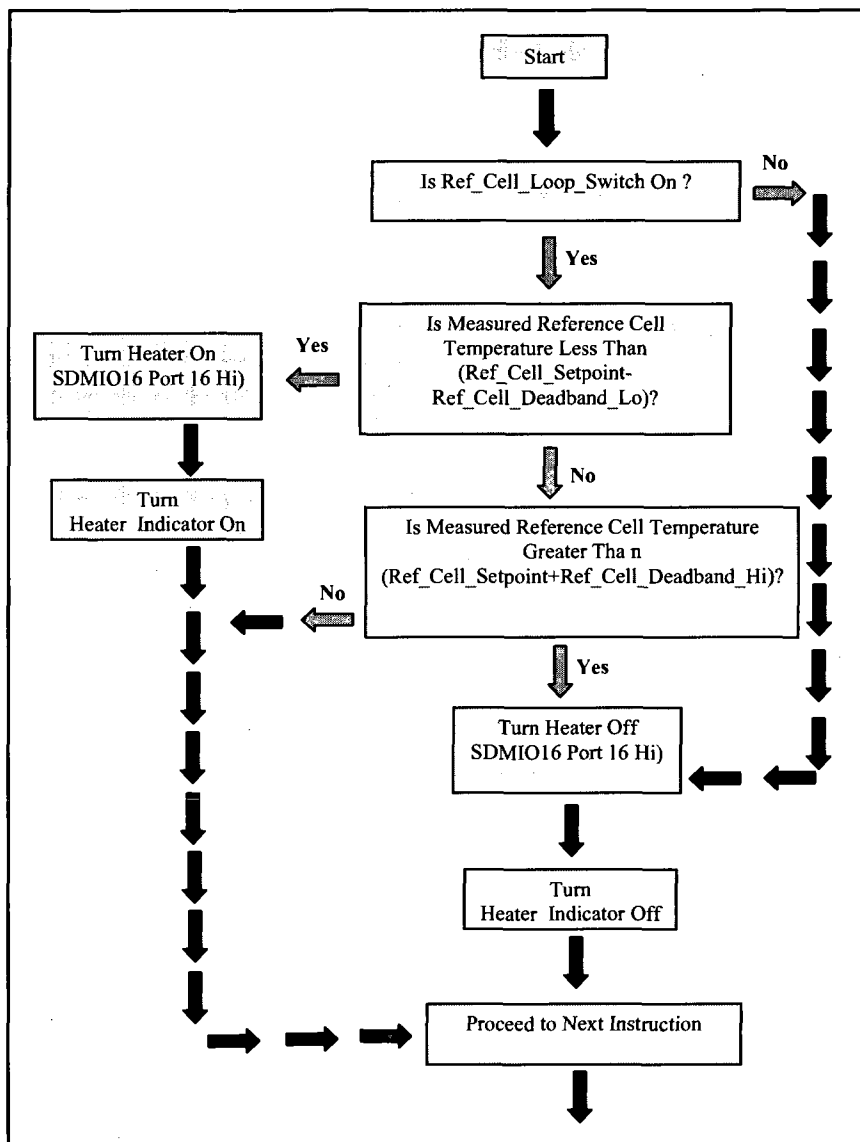


Figure 37. Logic for reference cell temperature control loop

Output File

Lines 797-856 of the program specify the parameters which are to be written to the final output file, as well as the resolution (the high resolution setting was used in this case) of the data. In addition to this, these lines are used to specify how often the final output file is updated and how many samples are to be averaged. In this case, the interval

for the final data file is the same as the scan rate (15s). This means that the data from the temporary input locations are written directly to the final output file during every execution of the program. The columns in the final data file are ordered as they are listed in the output section of the program.

Graphical User Interface (GUI)

The control functionality of the data acquisition system is further augmented by use of the Campbell Scientific software which facilitates the creation of a graphical user interface (GUI). This allows changes to be made to control program parameters, without disrupting the data acquisition process by having to formally upload a new version of the master program to the CR10X. In addition to this, the graphical user interface allows the various measurements to be monitored in real time. Figure 38 shows a screenshot of the GUI developed for this project in operation.

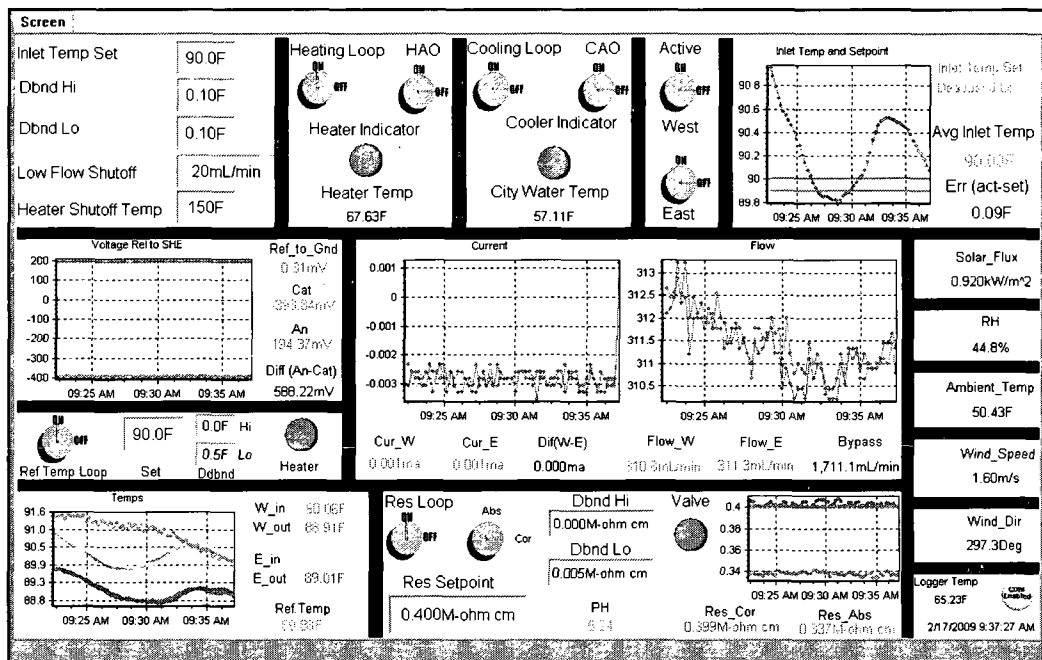


Figure 38. Graphical user interface used to monitor and control system

Design and Construction of Other System Components

In addition to the plumbing, and measurement control system documented in the previous sections, many of the other major components used in the experimental platform were also designed and custom built specifically for this work. The purpose of this section is to document the design and construction of these items.

Heat Exchanger (Cooler)

To remove heat from the system when required a shell and tube type heat exchanger was constructed as shown in Figure 39.

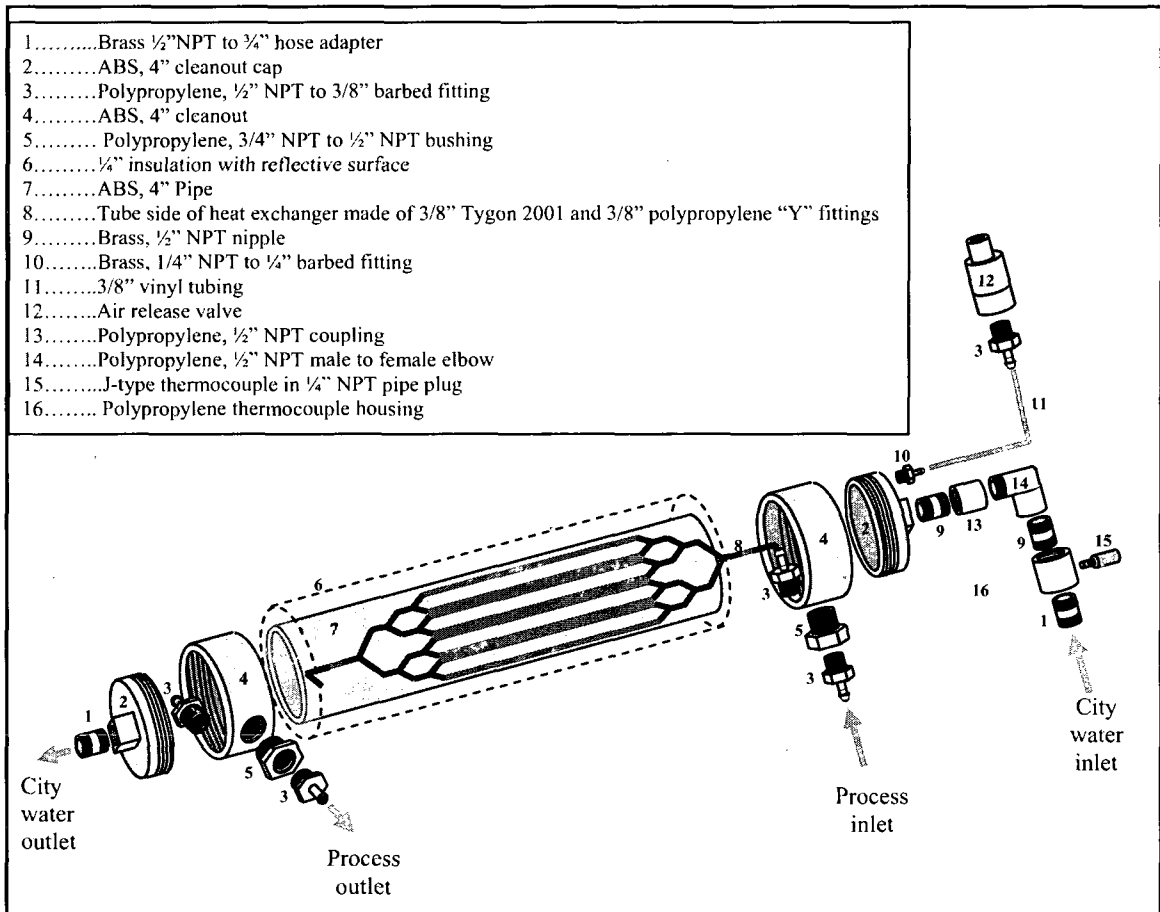


Figure 39. Construction details of shell and tube heat exchanger

As illustrated, the shell side of the unit is constructed from a 1.3 m length of 4" ABS pipe with cleanouts attached to both ends using ABS pipe cement. The tube side is made of 3/8" ID, Tygon formulation 2001 tubing with a 1.5mm wall thickness. The single inlet is branched into 8 parallel tubes and then back into a single outlet using polypropylene Y fittings. ABS cleanout caps are drilled for the appropriate fittings and after all internal connections have been made are screwed into the cleanout fittings at the ends of the heat exchanger. Pipe joint compound is applied to all threaded fittings on the shell side to prevent leakage. It is worthwhile to note that since the tube side of the unit uses the same tubing and fittings as the rest of the system, the heat exchanger does not expose the process to any materials not previously mentioned in section regarding wetted materials.

The finished heat exchanger is mounted at a 20 degree angle from the horizontal with the shell side outlet at the lower end. 6mm thick reflective insulation is wrapped around the outside of the heat exchanger. When the solenoid valve is closed the water will drain from the shell side due to its inclination. The stagnant air surrounding the tubes and the outer layer of insulation help to minimize heat loss when the cooling loop is off.

The barbed fitting at the upper end of the unit is connected to an air release valve. This valve uses a float mechanism to open the shell side to atmospheric pressure when the heat exchanger is filling or draining. When filling, the valve is open allowing the air at the top of the system to escape. When the water level reaches the valve, the float mechanism causes it to close and the shell side can be pressurized. When the solenoid valve closes the water drains slowly at first due to the vacuum created. As the water level recedes, the float drops and the valve is again open. This breaks the vacuum allowing the shell side to drain rapidly. It is worthwhile to note here that the valve, as received from

the manufacturer, leaked significantly when under pressure. To remedy this, the unit was cut open and the seal material was replaced with a softer compound. In addition to this, the air vent port was modified to prevent dust from entering the valve making it more suitable to outdoor use. The valve was then reassembled using a flanged connection to hold the two halves together. Figure 40 shows the modified valve mounted on the tracker and Figure 41 shows the finished heat exchanger installed on the system.

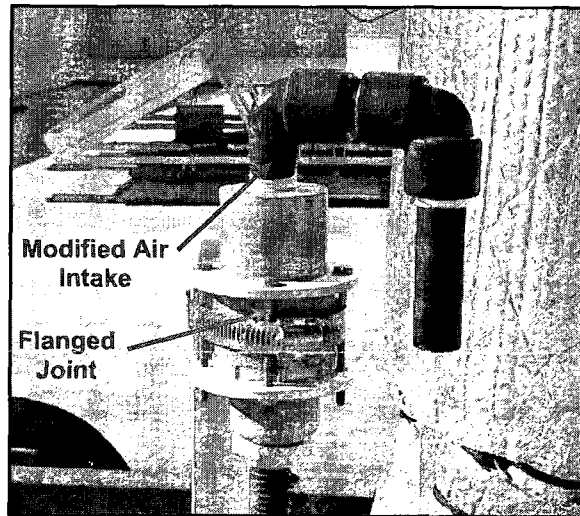


Figure 40. Modified air release valve used on heat exchanger

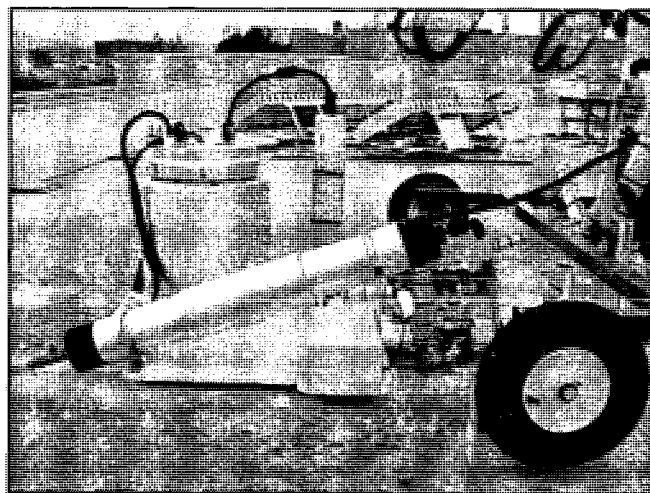


Figure 41. Finished heat exchanger installed on system

As shown, the bottom of the reservoir is drilled and tapped for a ½”NPT polypropylene nipple. This is connected to the other ½” polypropylene fittings which make up the pump inlet manifold. Placing the nipple at the bottom of the tank ensures that the suction side of the pump remains under a net positive pressure to prevent cavitation. The reservoir sits on a 5cm thick piece of Styrofoam insulation which is cut to allow clearance for the pump inlet piping. The sides of the reservoir are wrapped with 10 cm of plastic reflective barrier insulation to prevent heat loss from this area and the lid of the tank is drilled to accept the fittings for the main return line, the return line for the de-ionizer, and the nitrogen injection line.

To minimize CO₂ absorption by the electrolyte, a piston was machined from 19mm thick polypropylene stock. The piston floats on the surface of the electrolyte, minimizing the area which is exposed to the surrounding air. As shown, all return lines are run through holes in this piston to a point below the surface preventing the return streams from contacting the outside air. The center of the reservoir lid is drilled oversize to allow the heater to pass through without contacting the lid material. The heater selected is an immersion type rated at 405W and constructed of 316 stainless steel. The top of the unit is terminated with ½” NPT male threads. As shown, the depth of the heater in the tank is adjusted using a 316 stainless coupling and a 10 cm long 316 stainless steel pipe nipple to ensure that the element remains fully immersed at all times.

The heater is supported by a 6mm thick piece of solid fiberglass insulating material which has been drilled and tapped to accept the ½” NPT male threads of the pipe nipple. This assembly is mounted to the lid using 316 stainless steel machine screws. The interface between the fiberglass insulator and the polypropylene lid is coated with high

temperature silicone before assembly to prevent leaks into the system. In addition to this, all exposed portions of the fiberglass insulating material are coated with the silicone to prevent contact with the electrolyte. For this reason, the insulating material is not included in the list of wetted materials. A second 316 stainless coupling is screwed onto the portion of the heater above the lid to allow attachment of a J-type thermocouple using a hose clamp. As was described in the previous sections, this temperature is monitored as a safety shutoff for the heating element. The lid is then fitted with a 5cm thick Styrofoam insulation layer which has been cut to fit over the heater and return line fittings. The insulation layer is secured to the lid using high temperature silicone. The finished unit is shown in Figure 43.

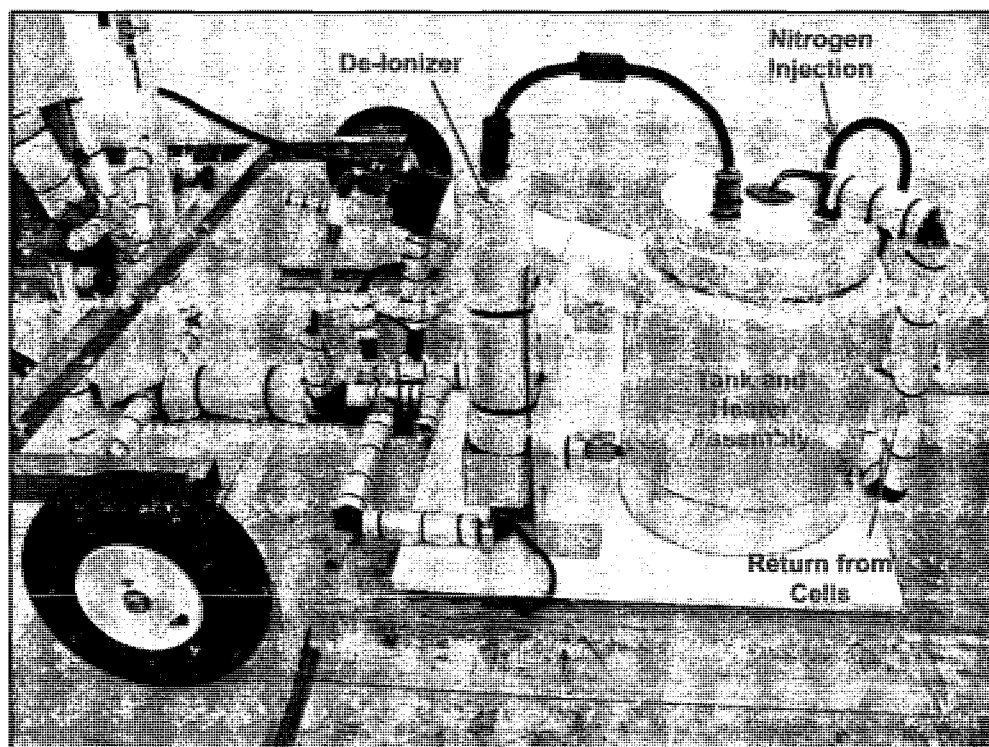


Figure 43. Finished heater and tank assembly installed on system

Finished System

The test facility described in this chapter was completed in the Summer of 2008. Preliminary testing has demonstrated that relatively good control of system parameters (flow, temperature, resistivity, cell potential) is possible under most situations which would occur during an actual experiment. All measurement devices were selected to provide the highest level of accuracy possible within the budgetary constraints of the project and the integrated logging/control/monitoring system allows the system to operate with minimal operator input. The finished system has proven robust enough to withstand summer ambient temperatures in excess of 48 °C as well as temperatures below freezing in the winter. Overall the system achieves the purpose for which it was designed, which is to provide an accurate, reliable, semi-autonomous, system for evaluating the performance of PEC type devices under actual solar illumination. Figure 44 shows the finished system in operation.

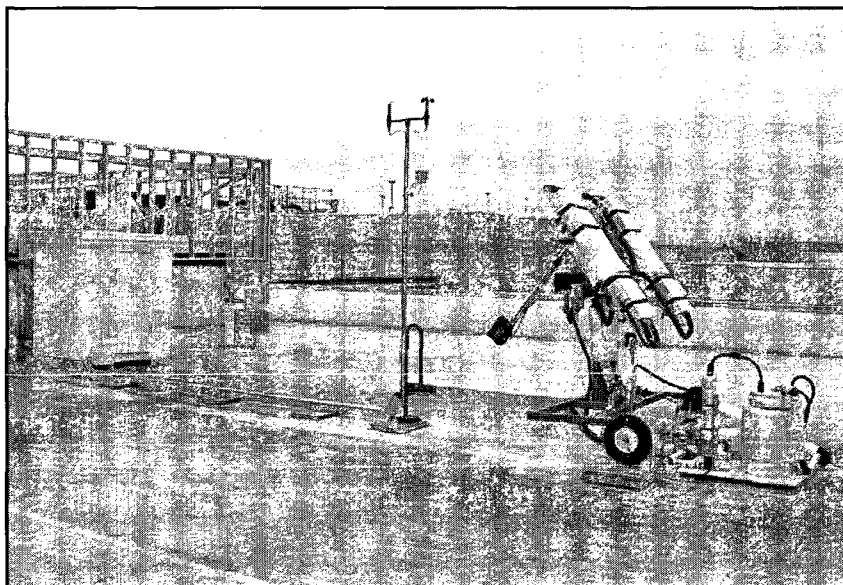


Figure 44. Completed test system in operation

CHAPTER 3

DESIGN AND CONSTRUCTION OF CELLS

Design Criteria

At the time at which this project was proposed, UNLV was working with the UK based firm “Hydrogen Solar” in the design and testing of WO_3 based photoanodes at the company’s Henderson, Nevada laboratory. The work conducted there was focused mainly upon shrinking the bandgap and tailoring the band edges of the anodes to more effectively utilize the energy contained in the solar spectrum. The cells being tested at the time used a variety of acidic electrolytes which tended to corrode the photoanode leading to premature failure of the device. Additionally, the cell bodies themselves tended to be crudely constructed resulting in a different electrode spacing each time the cells were assembled. Testing of the cells was performed using an artificial light source with the electrolyte essentially static. No attempt was made to control temperature or resistivity during these tests. For these reasons it was proposed that UNLV pursue a parallel research project focusing on a new cell design utilizing the current crop of “Hydrogen Solar” designed photoanodes. The design criteria for the new cells are listed below.

- (1) The cells would utilize the existing “Hydrogen Solar” anodes. UNLV would have no input in the design of these units with the exception of specifying the dimensions.
- (2) The cells would utilize the platinized titanium mesh currently being used by “Hydrogen Solar” as the cathode material.
- (3) A Nafion[®] membrane would be used to prevent gas recombination while allowing proton migration to the cathode.
- (4) The cells would be designed such that the electrolyte could be flowed uniformly across the anode and cathode surfaces. The rationale behind doing this is the idea that by moving the flow across the electrodes, any gas which is produced will be swept out with the electrolyte preventing it from building up on the electrodes and slowing the reaction.
- (5) The cells would be designed such that the anode to cathode spacing can be precisely adjusted and will not vary based upon assembly technique.
- (6) All cell parts should be interchangeable between units.
- (7) Cells should be dimensionally stable under temperature and pressure as well as resistant to the elements.

(8) Cells should be modifiable to allow for eventual gas separation although this was initially a secondary concern.

Photoanodes

As was mentioned previously, the photoanodes used in this work were manufactured entirely by UNLV's then industrial partner "Hydrogen Solar". Figure 45 shows the raw photoanode as received from the company.

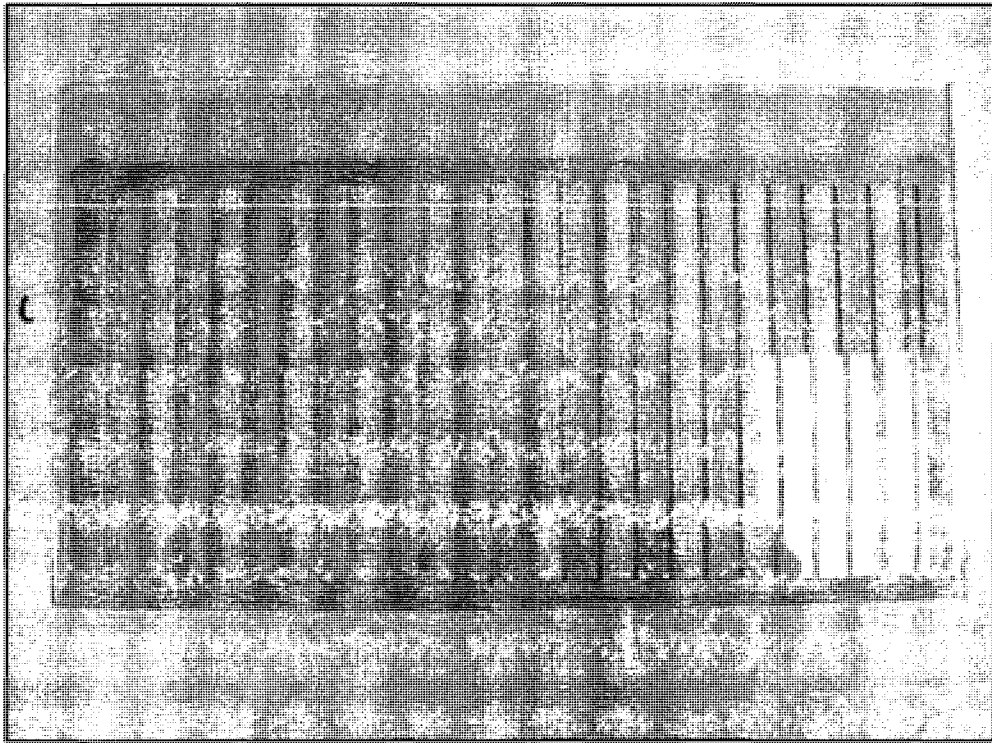


Figure 45. Photoanode as received from "Hydrogen Solar"

The anodes are constructed from 3mm thick electrically conductive glass. It is important to note here that while the glass is considered to be electrically conductive, it is nowhere near as conductive as a metal. Used alone, the resistance of the glass would

cause a significant ohmic loss over its length. For this reason, the glass is screen printed with a gold impregnated material to create the lined pattern shown in the figure. The photoactive material (WO_3) is then deposited onto the glass using a proprietary process. The anode size specified by UNLV is 152mm by 262mm. These dimensions were selected to minimize the cutting required on the glass blanks and also to ensure that the cell bodies would fit on the small milling machine used to make the parts.

Initial Conceptual Cell Design

At this project's inception, an initial conceptual cell design was created as a starting point upon which future designs could be built. As is documented later in this chapter, this initial design would go through two separate evolutions before actual testing was commenced. Figure 46 shows this preliminary cell design.

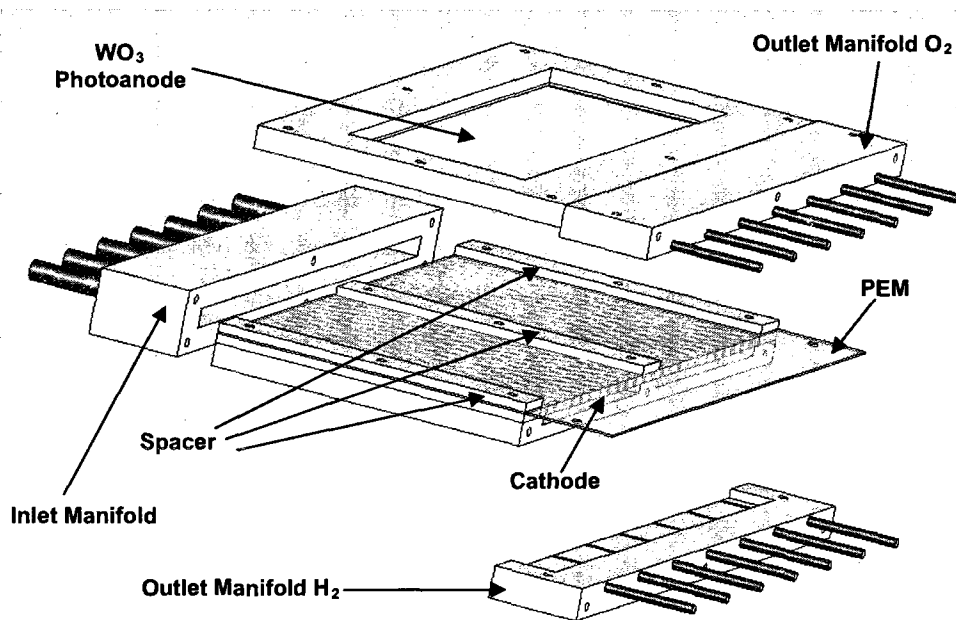


Figure 46. Initial conceptual design for test cells

As shown, the main cell body is made up two halves, which it was expected would be constructed of some type of high density plastic. The top half would have a rectangular section cut out to fit the anode, which would be set in place using silicone sealant. Variable thickness plastic spacers would be used to fix the spacing between the working surface of the anode and the PEM thus forming the upper flow channel. A second set of spacers of the same thickness as the cathode material would be placed underneath the PEM such that the membrane would be squeezed between the two sets of spacers to seal the cell while holding the cathode material in place. The lower half of the cell body would have three raised bosses of the same thickness as the upper spacers machined across it to form the lower flow channels. The two halves of the cell would be clamped together using machine screws through the eight holes shown in the upper and lower cell halves.

Uniform flow into the cell would be accomplished by branching a single inlet tube into the seven fittings shown on the one piece inlet manifold. The flow would then split with half moving through the upper channel and half through the lower with the PEM separating the two flows. At the outlet of the cell, the lower flow will consist of electrolyte as well as any hydrogen which was produced within the cell. Similarly the upper flow will consist of electrolyte plus any oxygen which was produced within the cell. To keep the gases separate, the PEM is extended beyond the cell body and is clamped between the two piece outlet manifold where the flows exit as separate streams.

It is worthwhile to emphasize at this point that the cell shown in the preceding figure is only a preliminary conceptual design. As is explained in the subsequent sections of this chapter, the final design required many changes due to practical issues.

Heat Bonded PEM/Cathode Attachment

One issue which would need to be addressed in any cell of the type described in the previous section, is maintaining physical contact between the PEM and the cathode material. These materials are shown in Figures 47 and 48 respectively.

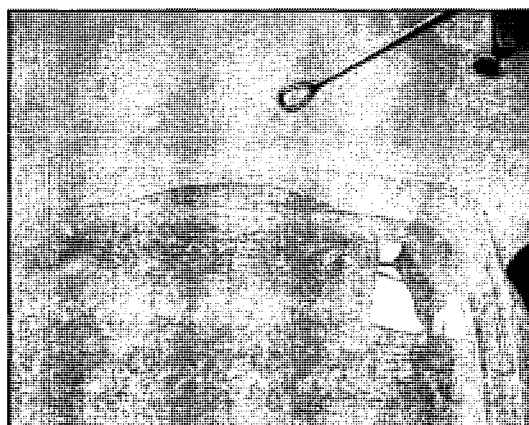


Figure 47. PEM (Nafion® 117) after hydration and cleaning process

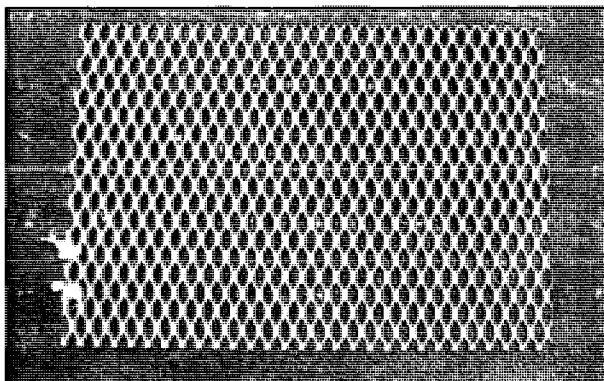


Figure 48. Platinized titanium mesh used for cathode

As shown in the figure, the PEM has no rigidity on its own and will tend to wrinkle or pull up from the cathode unless the two are physically attached to one another. One possible method of doing this which was explored during the course of this project was using heat and pressure to bond the two substrates together. It is worthwhile to note that this method as implemented here was not entirely successful and an alternative method was ultimately used in the final design. This section is included in this report to document the work performed and to provide a starting point for possible future research in this area.

The heat bond process is begun by pre-treating the PEM (in this case Nafion® 117) to hydrate the membrane as well as remove any organic deposits which may be present on the material. The cleaning process begins by soaking the new membranes in a .5M solution of sulphuric acid maintained at 80 °C for 1 hr. After this time, the material is moved to a 2% hydrogen peroxide solution (also at 80 °C) and allowed to soak for another hour. Finally the material is soaked in high purity de-ionized water maintained at the same temperature for an additional hour. The processed membranes are then stored in a sealed container containing high-purity de-ionized water until they are needed. It should be noted here that although this procedure is documented this section regarding the heat bonding process, the cleaning and hydration process described here is performed with all new membranes regardless of the method used to attach it to the cathode.

To minimize waste of both the membrane and cathode material, the size of the samples was limited to 3cm square. The cathode material first cleaned with isopropyl alcohol and allowed to air dry. The contact surface of the metal substrate is then coated with a 10% Nafion dispersion and allowed to dry for 30 min. The liquefied PEM is used

to fill the small recesses in the metal, providing good ionic contact between the two materials. Figure 49 shows the apparatus used to press the samples.

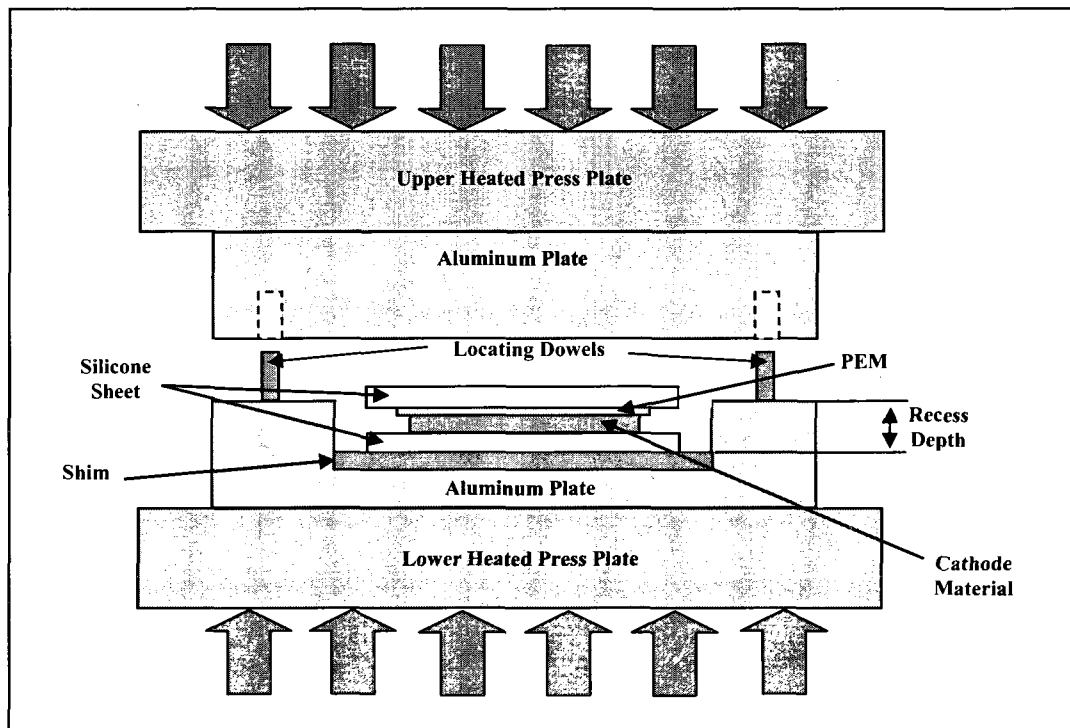


Figure 49. Setup used to heat bond PEM/cathode assembly

As shown, a piece of .8mm thick high temperature silicone sheet is placed in the machined recess of the lower aluminum plate. The cathode material is then set on top of the silicone layer with the liquid Nafion side facing up. The PEM sample is then placed over the cathode material and covered with another layer of the silicone. Pressure is then applied to the stack until there is no space visible between the two aluminum press plates. In this manner, the amount of pressure applied to the sample is controlled by varying the depth of the recess by adding or removing shims beneath the lower layer of silicone. Increasing the pressure was shown to improve the adhesion between the materials up to the point at which the PEM begins to rupture. Many samples were tested to determine the

maximum pressure which could be applied without damaging the sample. The optimal recess depth was found to be 2mm and this parameter was fixed at this value for the remainder of the tests. Other parameters which were varied were the press temperature and the time that the samples were pressed. Figure 50 shows one of the better test samples.

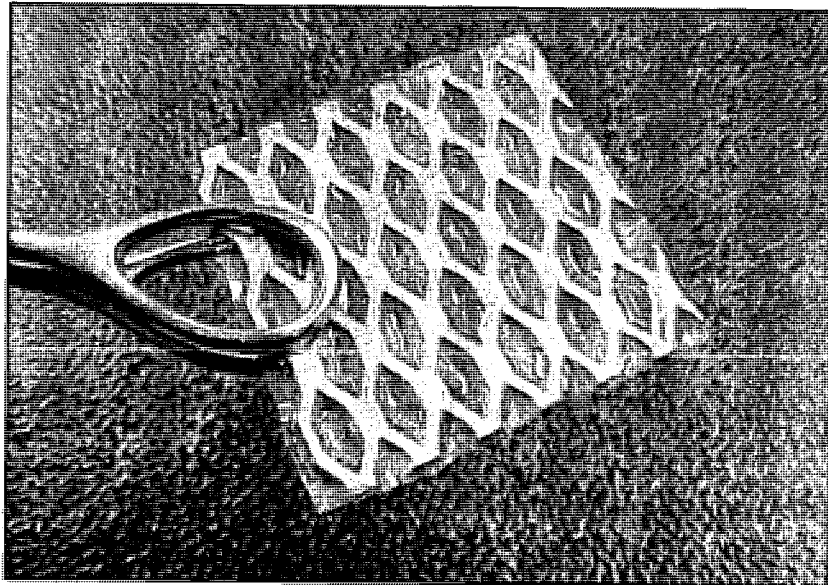


Figure 50. Sample heat bonded PEM cathode assembly

Several problems were encountered with this method of bonding. In general, the samples showed good adhesion and were relatively flat immediately after the test. Upon re-hydration at elevated temperatures, however, the bond became less reliable and the membranes developed a bubbled appearance due to the expansion of the material as it absorbed water. Additionally, the edge exposed to the incoming flow developed a wrinkled uneven appearance and tended to lift from the metal cathode. It should be noted here that the testing performed here was limited in its scope and many possible solutions

were not fully explored due to time constraints and a limited supply of the cathode material. For these reasons a complete study could not be performed for this project and due to the unreliability of the samples which were tested, this method of bonding was not implemented for the final cell design used in this project.

First Generation Cells

This section of the report is provided to document the first attempt at construction of a working cell designed for the “Hydrogen Solar” anode and the heat bonded PEM/cathode assembly. As will be discussed, this first generation of cells was not entirely successful but many aspects of the construction were eventually integrated into the final working design. Figure 51 shows the first generation cells and manifolds.

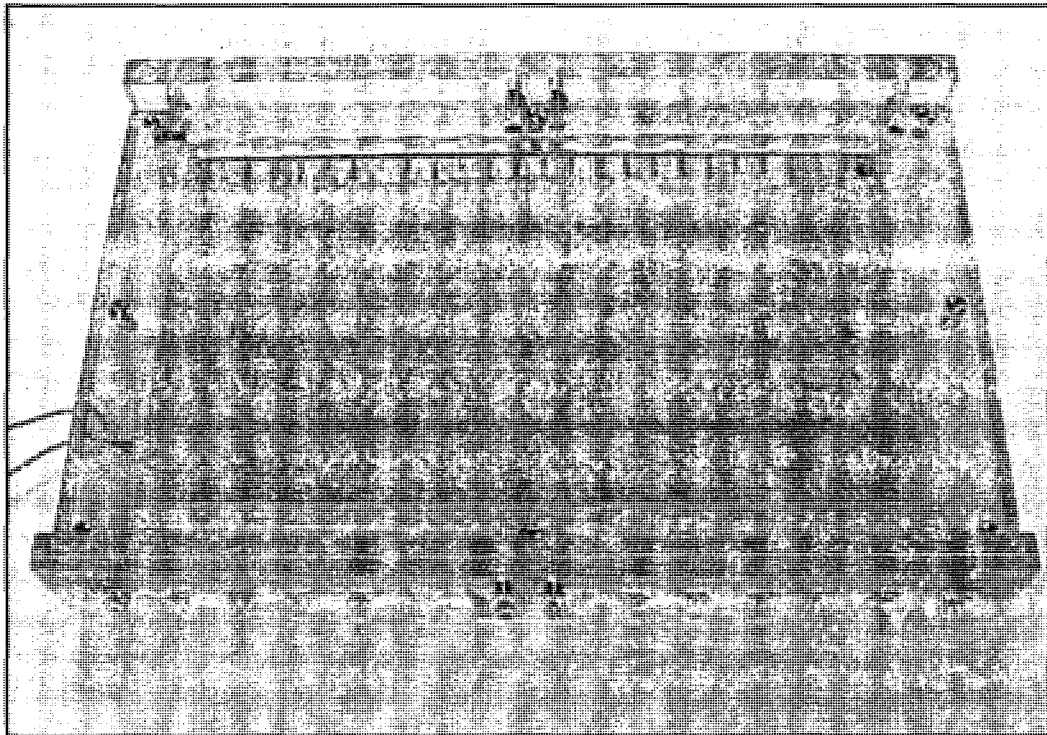


Figure 51. First generation cells and manifolds

The first cells were constructed of 13mm thick polycarbonate sheet and were designed to use the heat bonded cathode/PEM assembly described in the previous section. As shown, the two piece outlet manifold was not implemented at this time and the simpler one piece manifold is used at both the inlet and outlet. The decision to use the simpler manifold was based upon time constraints and the added complexity involved in manufacturing the two piece units. In future tests, if separation of the gases becomes necessary the two piece design could be implemented.

The cells and manifolds are held together using stainless steel machine screws threaded into self tapping inserts which are screwed into the plastic. The inserts were a beneficial addition which greatly simplified the assembly of the units and were eventually carried over to the final design. Problems were encountered however using them in the polycarbonate, as this material tended to develop stress cracks around the inserts as shown in figure 52.

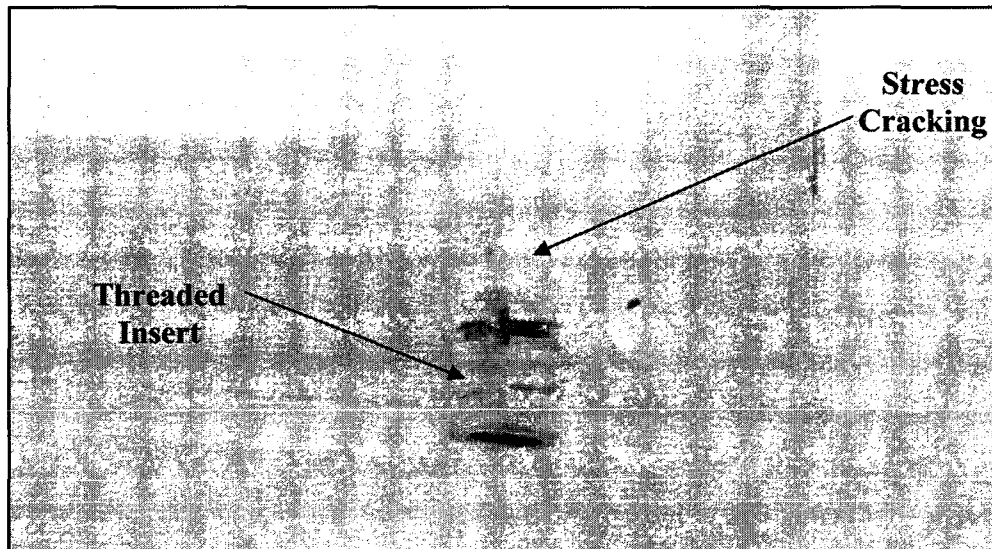


Figure 52. Stress cracking around threaded insert in polycarbonate cell body

The conceptual design shown in figure 46 was additionally modified such that the raised bosses machined into the back half of the cell body were replaced with removable spacers similar to those used for the top half. This was done to allow the channel depth to be adjusted without any additional machining on the cell body. Figure 53 shows a cross section of the flow channels for the first generation cells.

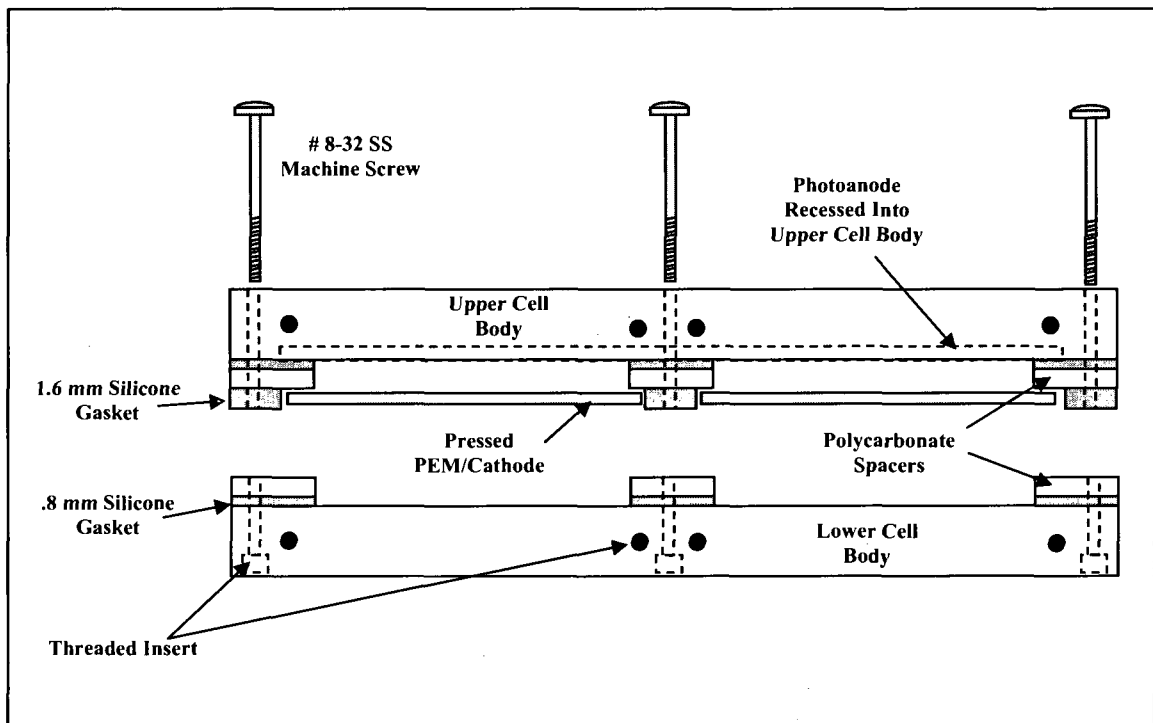


Figure 53. Cross section of flow channels for first generation cells

As shown, sealing between the cell bodies and the spacers is provided by .8mm thick silicone rubber gasket material. A 1.6mm thick piece of this material is also used to seal between the upper and lower sets of spacers. When the cell is assembled and the screws tightened, this gasket compresses until the upper and lower spacers clamp the cathode material firmly. It was believed that once this solid stop was encountered, additional

torque on the screws would not change the channel dimension. This is considered very important, as the electrode spacing should be the same every time the cells are assembled and not be influenced by slight differences in screw torque. In practice, this design was found to be flawed due to the fact that once the spacers contact the cathode/PEM assembly, any additional torque applied to the screw puts a bending moment on the upper cell body which is transferred to the glass photoanode. Several anodes were broken during assembly due to this. Additionally, the use of the .8mm silicone gasket material between the spacers and the cell body halves adds a considerable degree of uncertainty to the electrode spacing. This is due to variations in the distance it compresses depending again on the torque applied to the screws. Both of these issues would be addressed in the second generation cells.

Second Generation Cells

Design

Due to the problems encountered with the first generation cell design, it was decided that a complete rework of the units was required before testing could commence. This second generation of cells would build on the knowledge gained from the design and construction of the first set. Major changes to the design include, new material, new method of cathode/PEM attachment, new method of lead attachment, as well as various other improvements. Figures 54 and 55 show the final design of the second generation cells and manifolds.

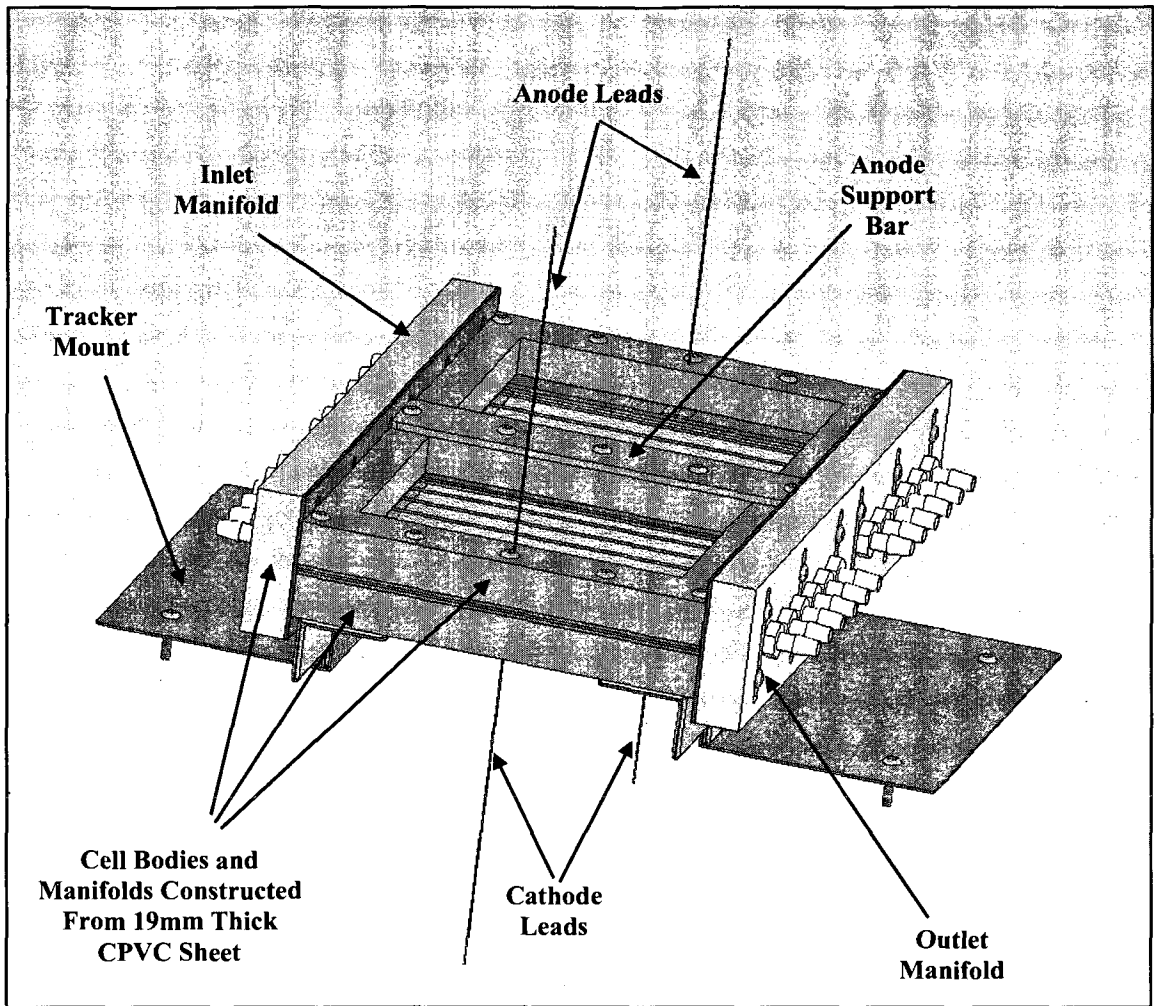


Figure 54. Second generation cells and manifolds

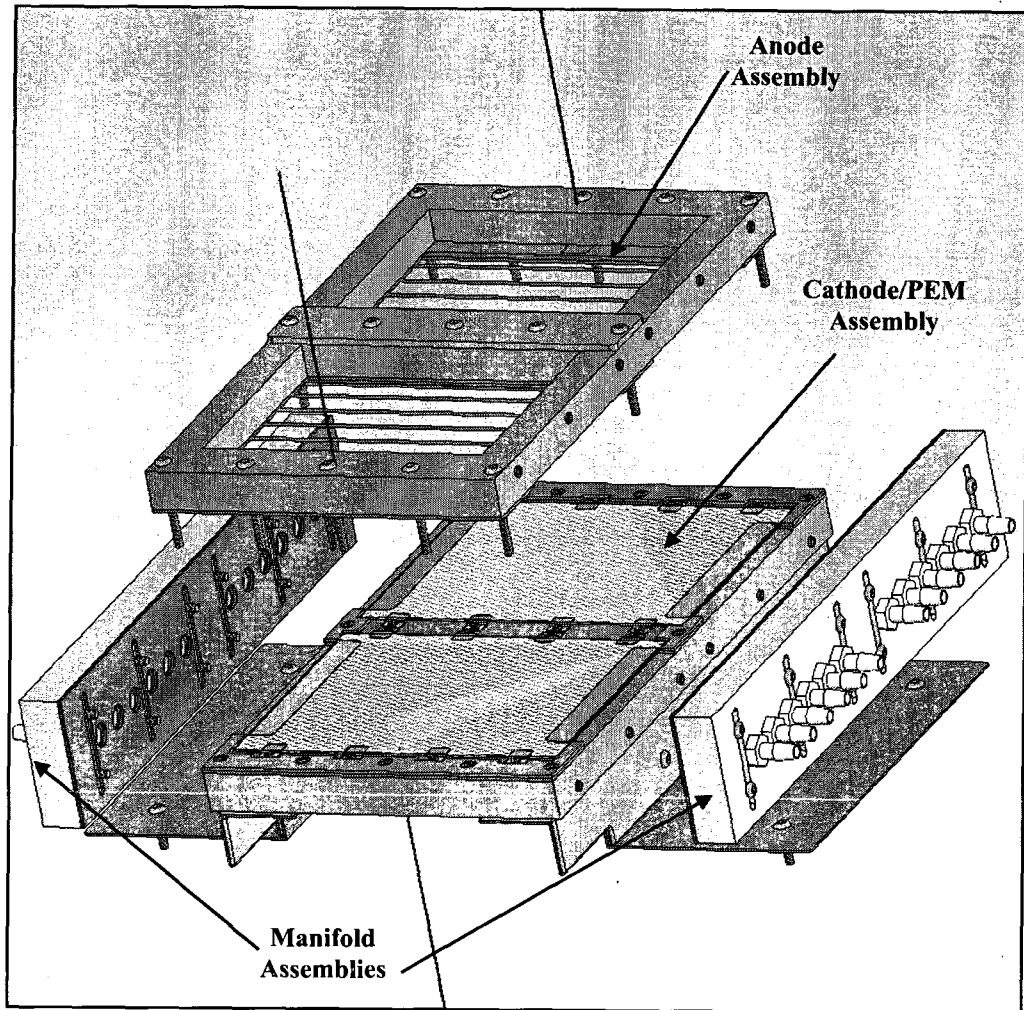


Figure 55. Exploded view of second generation cells

As shown, the new cells are constructed from CPVC instead of the polycarbonate used originally. This material exhibits excellent chemical and temperature resistance and is less susceptible to stress cracking than polycarbonate. As mentioned in the chapter 2 subsection regarding the wetted materials of the test setup, CPVC is already present in the system, so its use for the cell bodies has the additional advantage of not introducing any new materials into the experiment. With the exception of the PEM, this is true for all of the materials used in the new cells and so no new list of wetted materials need be presented here.

The strength of the new cells is enhanced by the use of 19 mm stock in place of the 13mm used for the first generation. To reduce the stress on the glass when the cells are pressurized, a support bar is run across the face of the anode as shown. It is worthwhile to note here that the anode area covered by support bar is already covered by the center spacer so its addition causes no reduction in the effective area of the cell. This support was added to the design after several anode ruptures occurred during the initial pressure testing of the new cells. In future designs, this support would be machined as an integral part of the upper cell body instead of being cut as a separate part as shown here.

To further augment the dimensional stability of the cells, the number of fasteners used was also increased and the manifold attachment method was modified to allow the manifolds themselves to take some of the bending load off of the anode frame and subsequently the anode itself. As shown in figure 56, a 1 mm thick polycarbonate washer is placed between the manifold and the cell body at each attachment point.

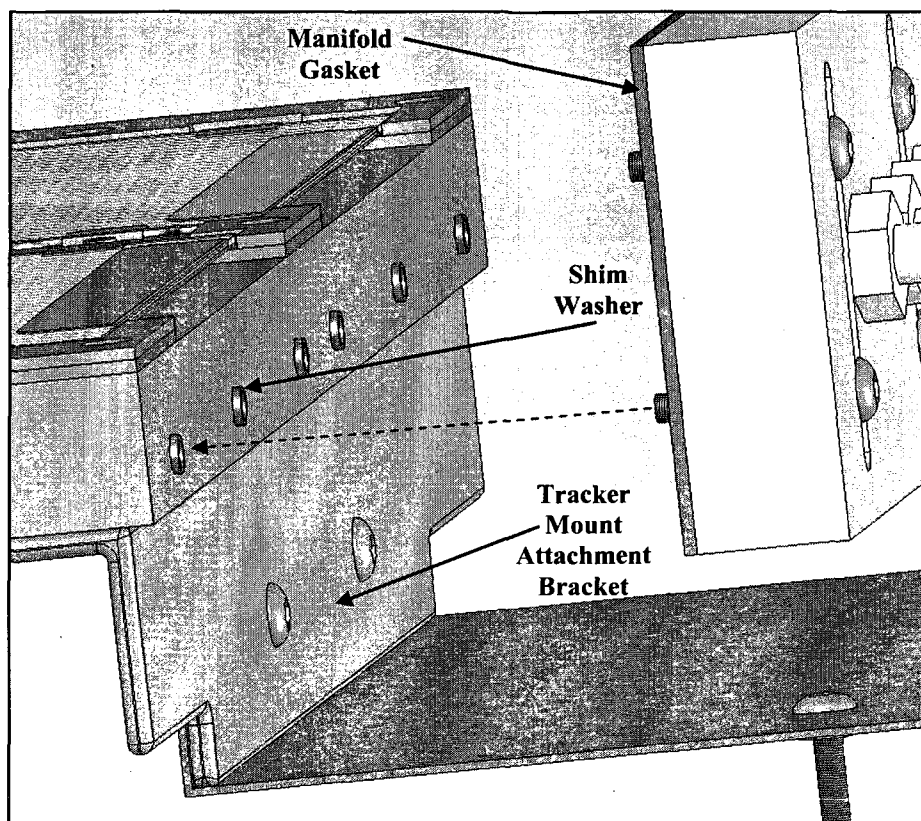


Figure 56. Details of manifold attachment and tracker mount

The washers provide a positive stop to prevent uneven compression of the gasket material while also creating a solid bearing surface between the parts. This prevents the unsupported sections of the cell body from creeping under pressure, putting stress on the glass. Additional rigidity is imparted to the cell body from the tracker mount attachment bracket also shown in figure 56. This piece is made from 38 by 38 by 3 mm steel angle which is secured to the lower cell body using machine screws and the previously mentioned threaded inserts.

Shim washers were also added at the fastening points between the two cell halves to prevent the anode breakage during assembly described in the previous section. The

washers are 1 mm thick and are made of 316 stainless steel. Figure 57 shows the gaskets and the shim washers prior to final cell assembly

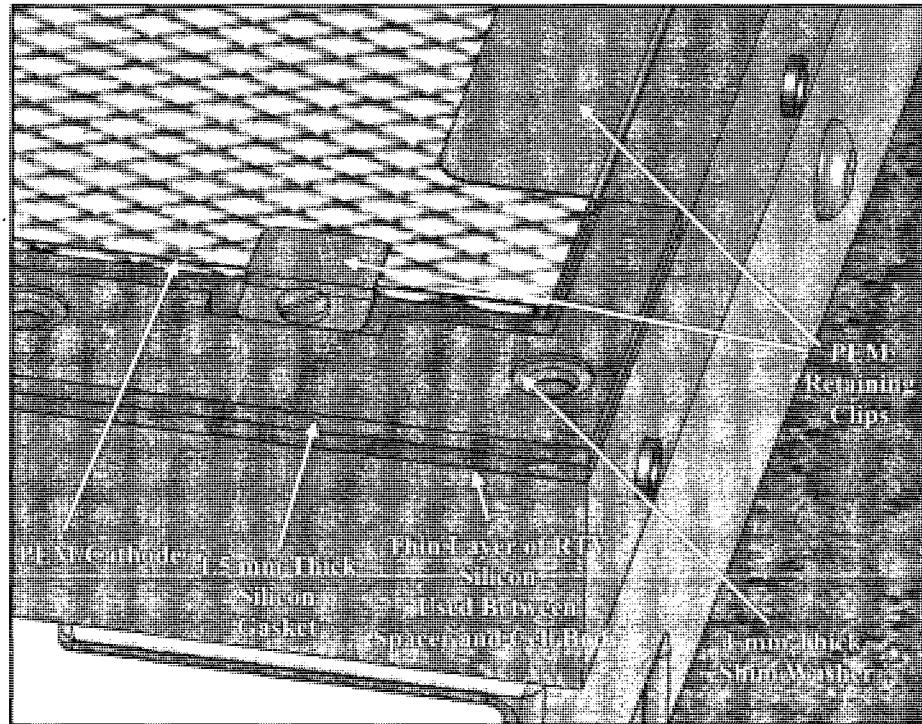


Figure 57. Details of PEM retaining clips and cell body gaskets

As shown, the washers are the same thickness as the cathode/PEM layer and .6 mm thinner than the gasket material. This limits the compression of the gasket while preventing the bending stress on the anode encountered in the original design. Figure 57 also demonstrates the replacement of the .8 mm thick silicone gasket between the cell body and the spacers with a very thin layer of RTV silicone sealant. Because this layer can be made extremely thin, the dimensional changes introduced by uneven compression of the solid gasket material are essentially eliminated.

Due to the difficulties encountered with the heat bond method of PEM to cathode attachment an alternative method was devised for use in the second generation of cells. As shown in figure 57 this method uses clips made of .25 mm thick 316 stainless steel shim stock to hold the PEM to the cathode material under tension in both directions. This is further demonstrated in figure 58.

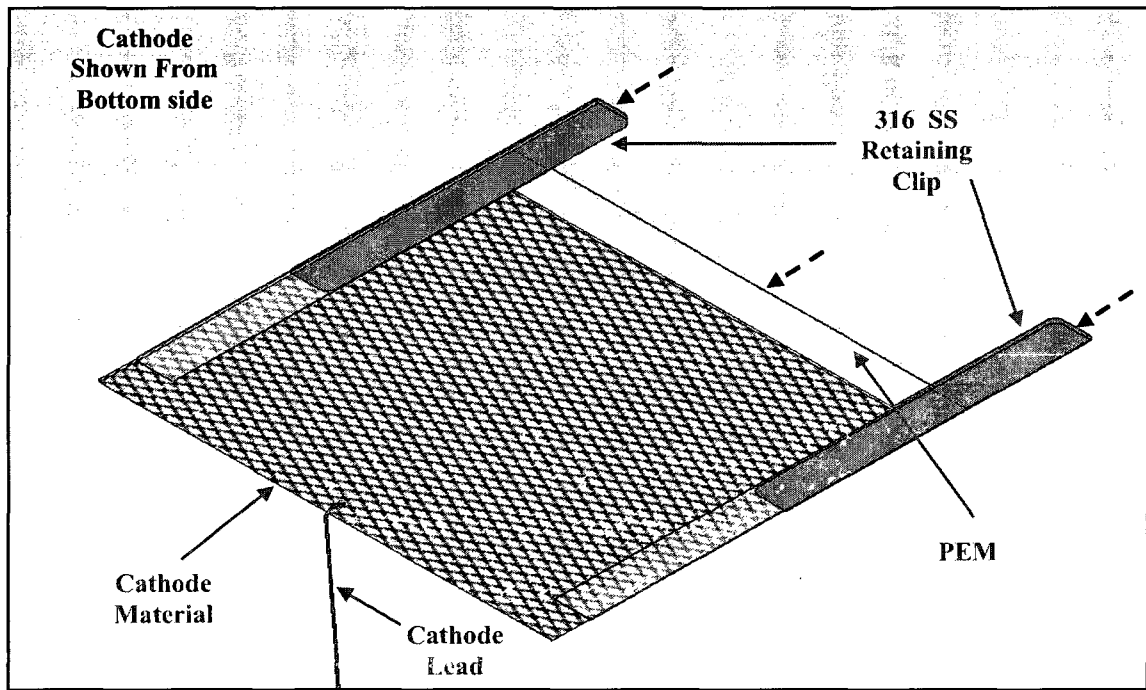


Figure 58. PEM/Cathode assembly

This method of attachment was found to work well, creating a smooth, well defined flow channel through the cells while maintaining positive contact between the PEM and cathode. Figure 59 shows the upper and lower flow channels formed when the two cell halves are brought together in the final assembly process. As shown, the clips present a clean edge to the incoming flow.

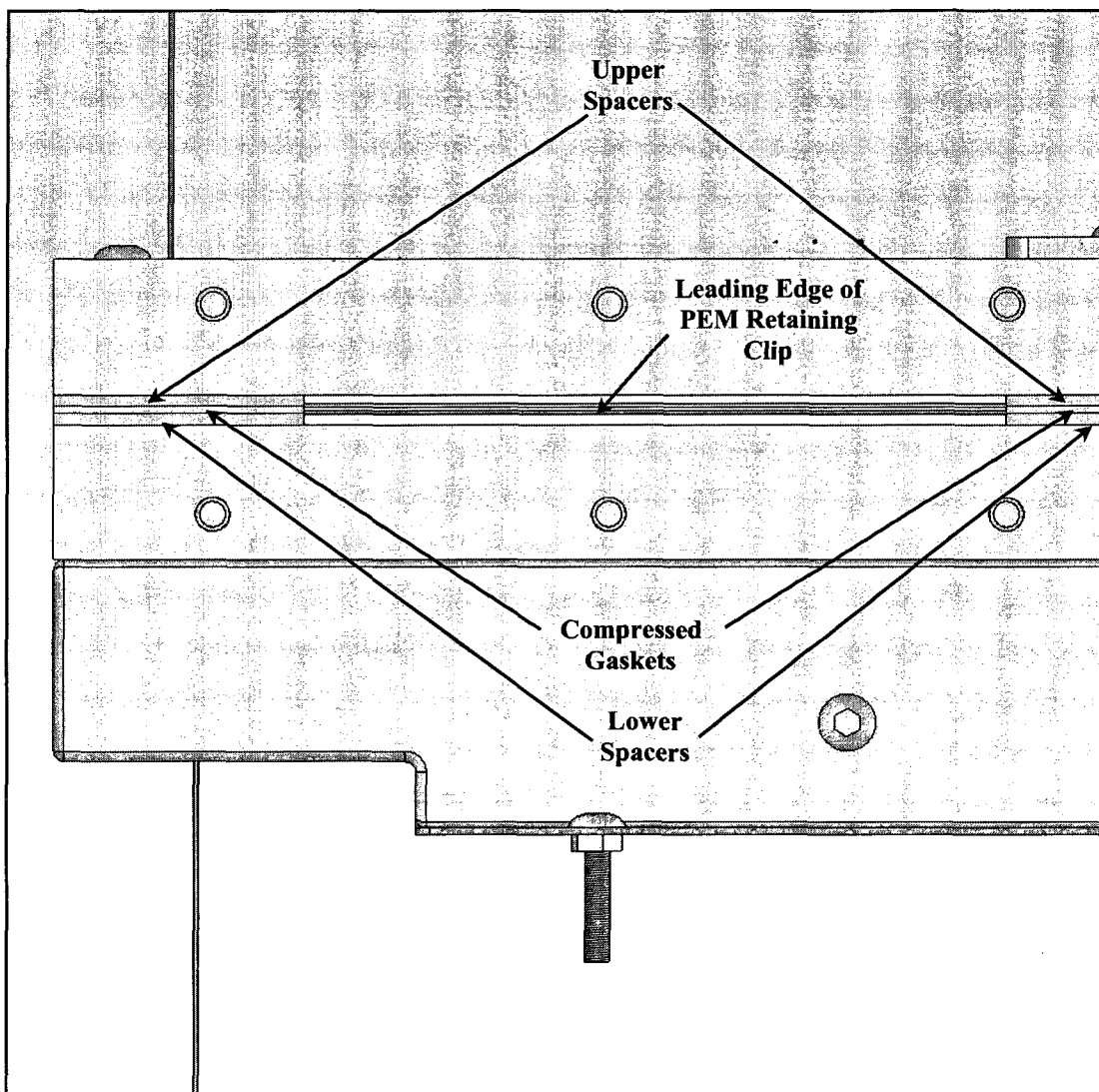


Figure 59. Details of upper and lower flow channels

In the first generation design, both the anode and cathode leads were attached using a silver filled conductive epoxy sealed with RTV silicone. This method was found to work well for the anode and was subsequently used for the final cell design. As shown in Figure 60, the wires are threaded through the lead holes after the anode is sealed in its frame using RTV silicone. After the silicone cures, the ends of the leads can be stripped and secured to the gold grid on the anode with the epoxy. After this sets, the joint is coated with RTV silicone and allowed to cure.

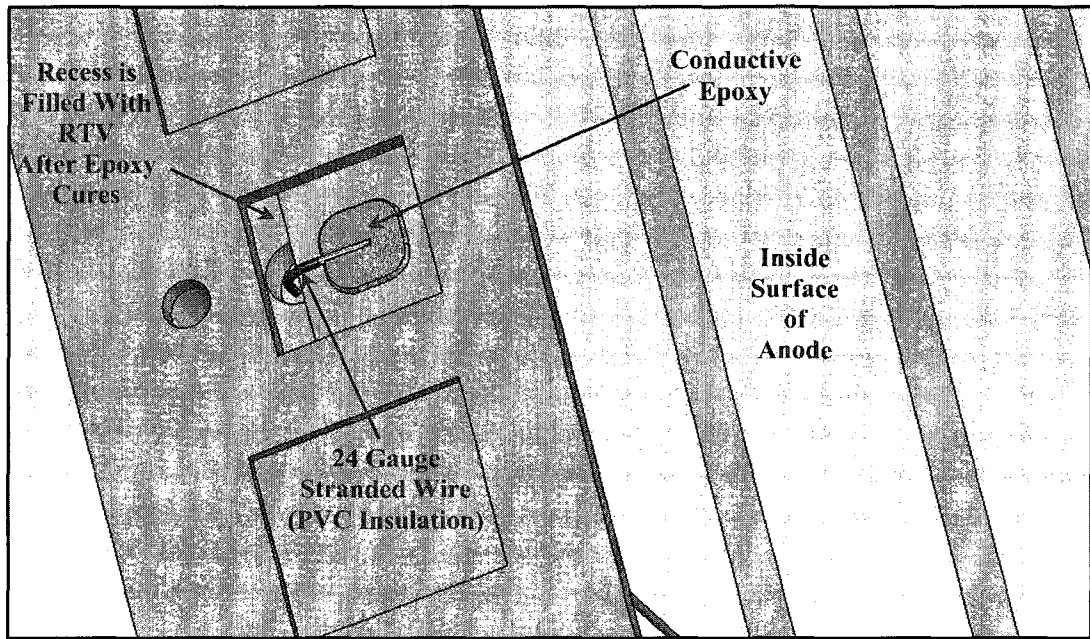


Figure 60. Details of anode lead attachment

It is worthwhile to note here that while only one lead is required to complete the anode circuit, this design uses one at each end for a total of two. The two leads are then joined outside of the cell and this junction is connected to the power supply terminal. This, in essence, connects the two sides of the anode in parallel with the voltage source. Doing this reduces by half the maximum length that electrons must travel through the anode which has relatively high ohmic losses compared to the metal wire. The result is that the potential is applied more evenly across the surface of the anode when compared to designs using a single lead.

Final assembly of the cell requires that the PEM/cathode assemblies be positioned while feeding the cathode leads through the hole in the lower cell body half. Because of this, the cathode lead joints are subjected to much greater stress than those of the anode. As was mentioned previously, the first generation cells used the same conductive epoxy used for the anode to make the cathode connections. This method was found to be

unreliable with many leads breaking off during the final cell assembly process. Because of this a new method was used in the final design. This is demonstrated in Figure 61.

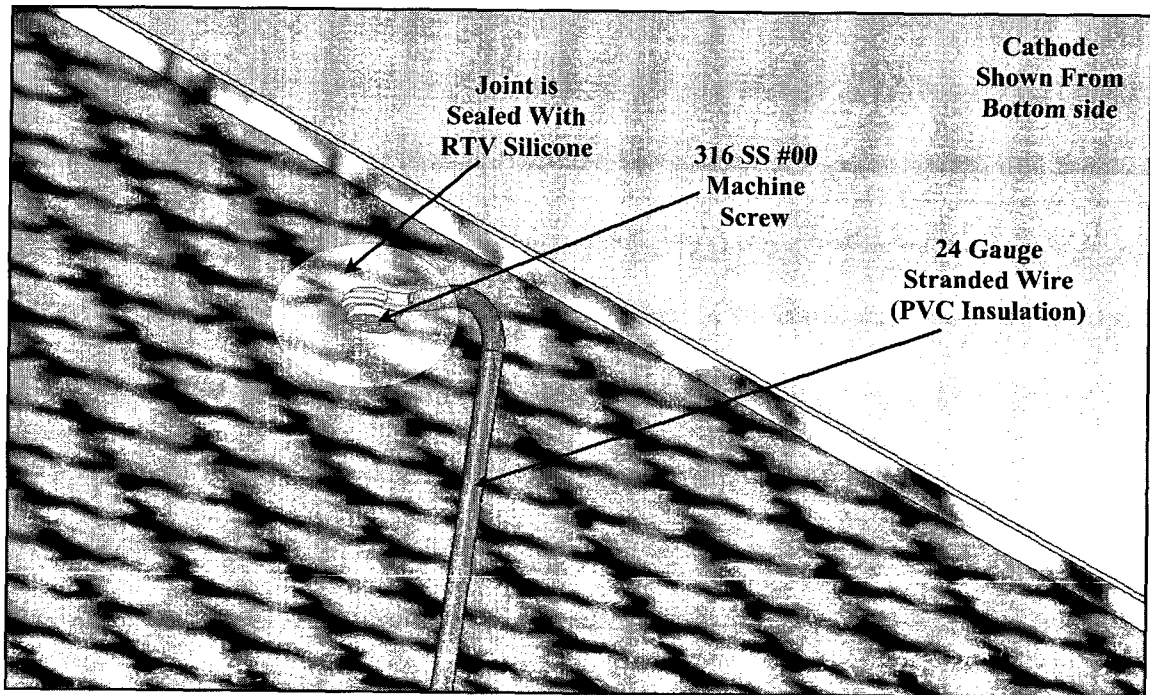


Figure 61. Details of cathode lead attachment

As shown, leads are attached to the cathodes using a #00 machine screw which is threaded into the metal cathode material. The end of the lead wire is stripped and then twisted around a mandrel to form a loop which is then soldered closed. The screw is then inserted through the loop and tightened to the cathode. The connection is then sealed using RTV silicone. It is important that this be done before the PEM is attached to prevent contamination of the membrane with the uncured sealant. The resulting joint is very robust and is able to withstand the bending and twisting loads placed on it when the cells are being assembled.

As with the anode, two leads are used for the cathode, although for different reasons. The cathode was made in two pieces only because there was not a large enough piece of material available to make them as a single unit. With the two piece design, there is no internal connection between the two halves so separate leads are necessary. In the event that additional cells were to be constructed, the cathode would be constructed using a single piece of the mesh material with a single lead. Because the electrical conductivity of the cathode material is so much higher than that of the anode, there is little benefit to adding a second lead to a one piece cathode.

Construction and Final Units

Construction of the final cells was begun in June of 2008 with a total of two cells being built to allow for simultaneous testing of cells using different spacer thicknesses. To ensure interchangeability between units, the plastic parts were manufactured using a Taig[®] CNC micro mill. High speed steel tooling was utilized and no coolant was used to prevent chemical contamination of the parts. Figure 62 shows the machining of one of the four manifolds.

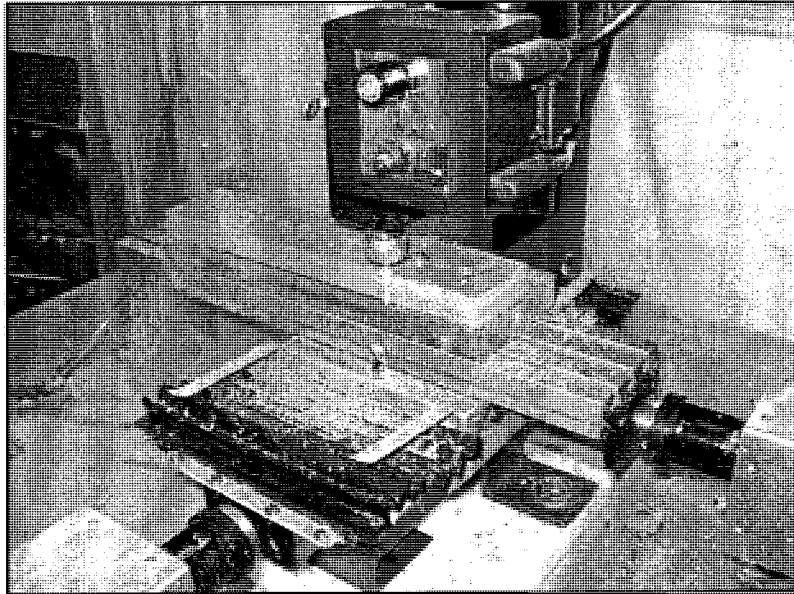


Figure 62. Machining the manifolds

Figure 63 shows the finished cathode assembly prior to final cell assembly. The sealing gaskets are initially cut oversize. These are then trimmed after the two cell halves are assembled.

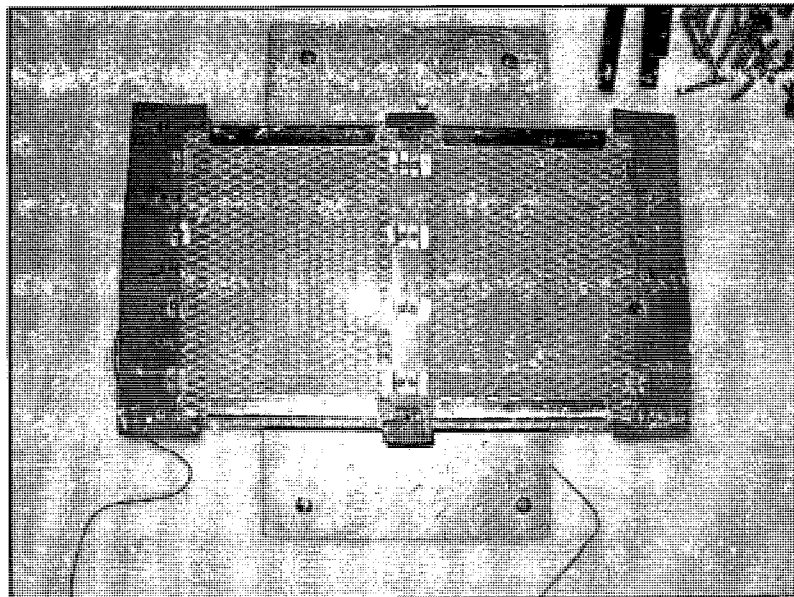


Figure 63. Cathode assembly prior to anode placement

As shown, the PEM is held tightly against the cathode material with no visible wrinkles.

Figure 64 shows a close up of the flow channels using the thicker (1.6mm) spacers prior to attaching the manifolds.

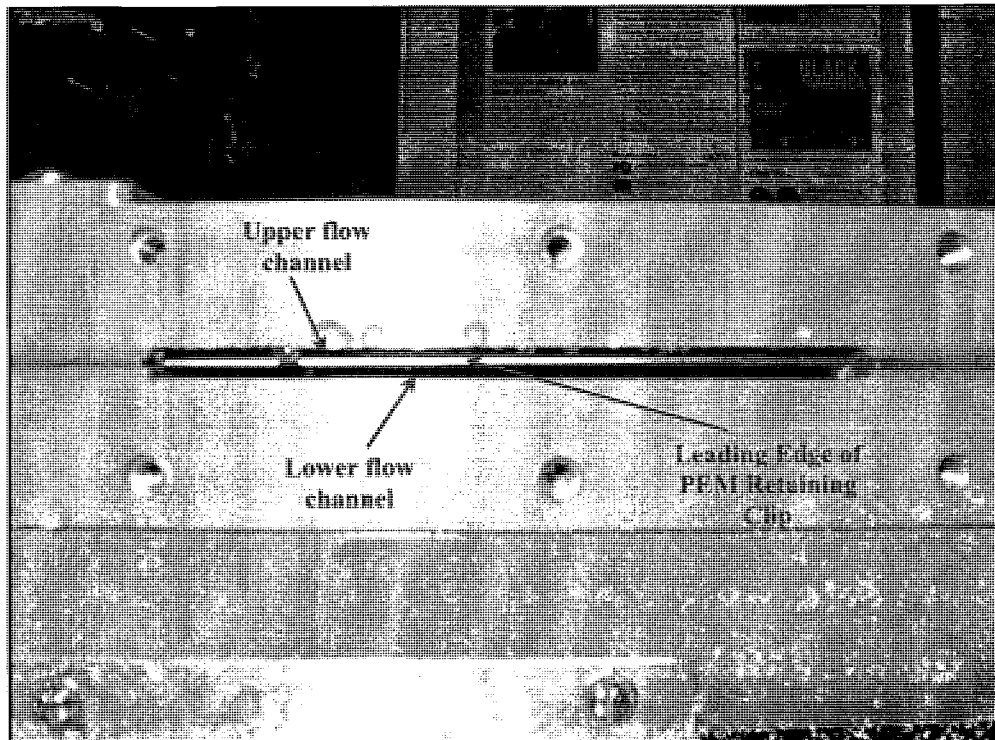


Figure 64. Flow channels on finished cells

The figure demonstrates the clean leading edge of the PEM/cathode assembly when the retaining clips are installed. The completed cells are shown in Figure 65

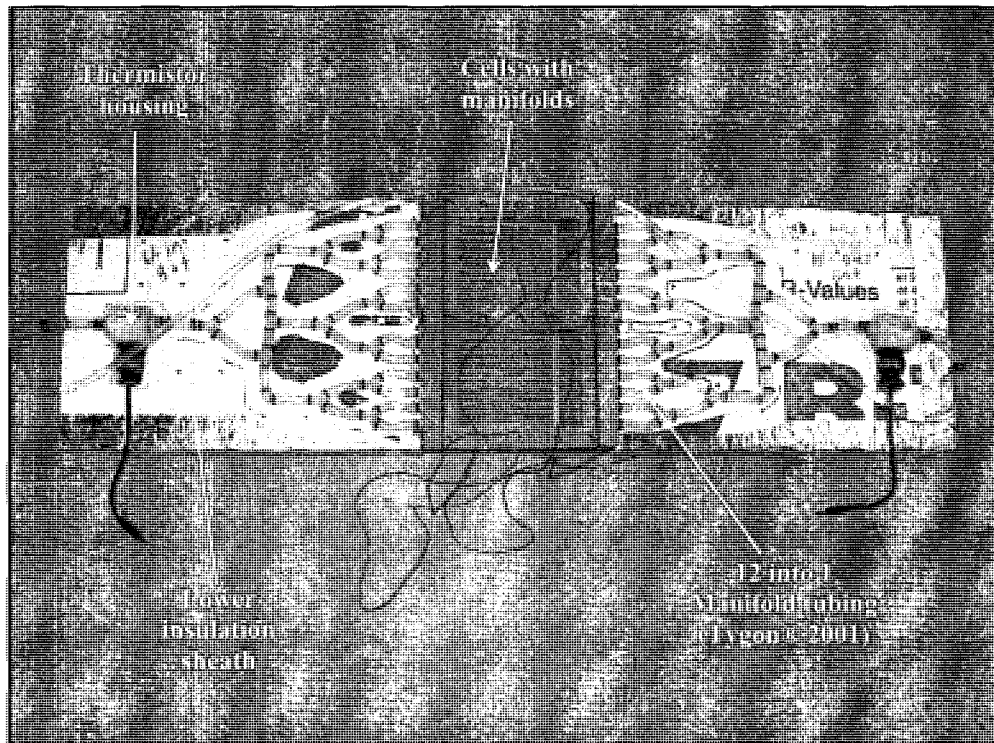


Figure 65. Fully assembled cells with manifolds

The figure shows the installed manifolds with the 12 into 1 tubing and thermistor housings installed. Also shown are the two lower halves of the tubing insulating sheaths. These were designed to minimize changes in the fluid temperature between the cell inlet and outlet and the point at which the measurements are made. To further facilitate this, the length of the 12 into 1 tubing is kept as small as possible without kinking the tubing. The sheaths are constructed of 50mm thick Styrofoam with recesses cut to fit the tubing and thermistor housings. The outside surfaces are covered with reflective aluminum tape to protect the Styrofoam and to minimize temperature changes due to incident solar radiation. Figure 66 shows the finished cells with the sheaths installed, mounted on the tracking unit during one of the initial test runs.

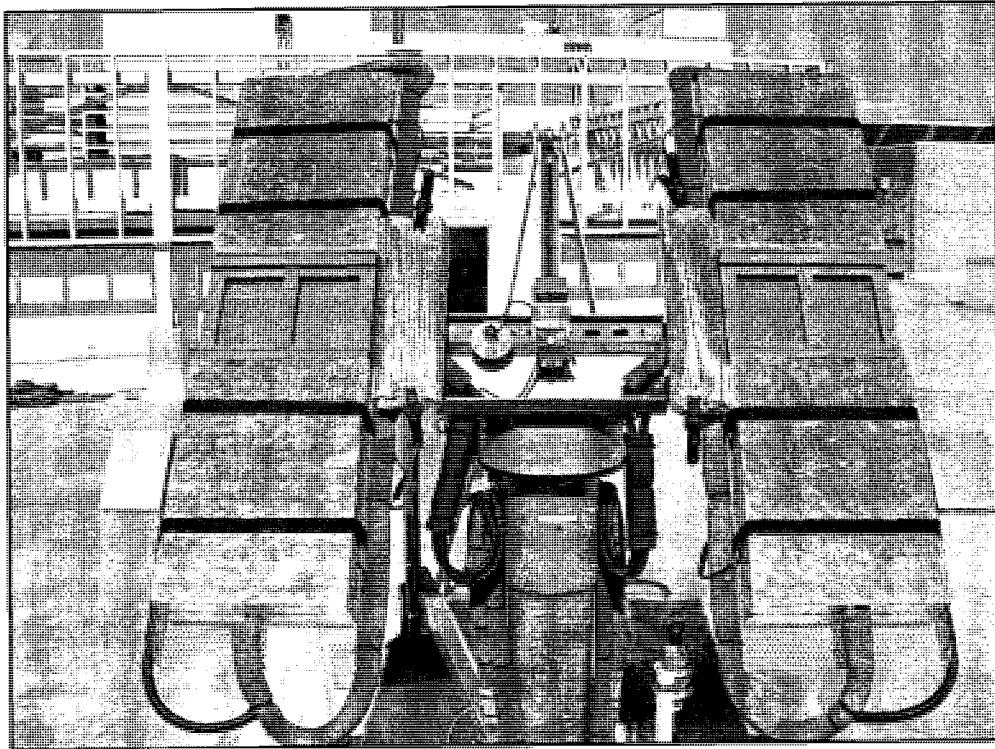


Figure 66. Finished cells with manifolds installed on tracker

The new cells were first run under pressure in the Fall of 2008. Throughout the preliminary testing phase, they performed as designed, with no leaks or ruptures observed. Since this time they have been running continuously for approximately 8 months with ambient temperatures ranging from 35° to 0° C. Electrolyte temperatures have been elevated to 60 ° C and the cells have been pressurized to 35 kPa over ambient for extended periods with no adverse effects. Internal lead connections are tested for continuity after each test and no problems have been encountered thus far. The cell channel dimensions appear consistent and there have been no observed instances of contact between the PEM and the glass anode even with the smaller (.8mm) spacers. Overall, the second generation design has proven to be a robust platform for on-sun testing of these types of PEC electrodes.

CHAPTER 4

EXPERIMENTAL PROCEDURE

Preliminary Tests

Upon completion of the experimental facility and cells, informal testing was commenced in the Fall of 2008. These first tests were designed primarily to get a general feel as to how the cells would respond to changes in the various inputs while at the same time exposing any deficiencies in the measurement and control system. Initially, it was not known what kind of performance to expect from the cells, as no literature was found documenting this type of testing. Issues such as determining instrument measuring ranges and meaningful parameter levels would all need to be addressed before the formal testing could commence. As a starting point, initial “educated guess” values were used and then refined based upon the observed results.

Very early on, it was determined that the cell response was more transient than had been anticipated. This fact led to the design of a much longer duration test than what had originally been planned for. Instead of multiple parametric changes being possible over the course of a given test day, tests were structured such that a single combination of parameters would be tested per day with minimal system disturbance. This approach is based upon the assumption that if the weather is clear and the tests are conducted at the same times each day within a few days of one another, then the solar insolation should be similar between tests. By this logic, cell current at 10:30 on day one under one set of

parametric inputs can be compared directly to cell current at 10:30 on day two under a different combination of input parameters. Because spectral data are being collected during each test, the validity of this assumption can be checked as will be demonstrated in the next section. The conclusions drawn from the early tests are listed below

- (1) The cells produce a small but measurable photocurrent.
- (2) The cells also produce a significant dark current.
- (3) The transient nature of the cells would require the individual tests to be longer than had been initially anticipated.
- (4) Variations of the input parameters were found to result in measurable changes in the cell current.
- (5) The input parameters can be controlled with reasonable accuracy over the course of an extended test.
- (6) The solar insolation is consistent enough on clear days to allow for direct comparison of data collected on different days. Additionally, if the test time is centered around solar noon, the solar insolation changes very little over the course of the experiment.

(7) The system pH was observed to fluctuate between 5.4 and 4.9 over the range of temperatures and resistivities tested.

(8) Anode degradation rate, while initially fast, levels off after the cells have been operating for a few months.

These basic conclusions created during this initial observational period form the basis for the formal test procedure presented in the subsequent sections of this writing.

Final Test Series

Test Structure

The final test series was designed based upon insights gained from the initial tests. This series involves a total of 4 parameters (corrected resistivity, flow, temperature, electrode spacing), with two levels apiece. To reduce the number of required tests, the effect of the electrode spacing is investigated by concurrently testing two cells with different spacer thicknesses on opposite sides of the tracker. This effectively reduces the number of parameters from 4 to 3 while providing the same data. The West cell uses a spacing of $d=0.8\text{mm}$ whereas the spacing for the East cell is set as $d=1.6\text{mm}$. A full factorial set of experiments for this situation consists of a total of 8 tests and would explore every possible combination of parameter settings. The anodic potential will be swept through a range of values for each test while the cathodic potential remains fixed. Additionally, each combination of parameter settings will be run once with the cells covered (dark) and once with the cells uncovered (light), for a total of 16 days of testing.

This method allows direct comparison of the total current and dark current for any combination of input parameters and allows for calculation of the photocurrent by taking the difference between the light and dark tests. The test matrix is shown in Table 1.

Test #	Flow (mL/min)	Temp (C)	Corrected Res (M-ohm cm)
1 Light 1 Dark	300	35.0	1.000
2 Light 2 Dark	300	51.7	1.000
3 Light 3 Dark	150	51.7	1.000
4 Light 4 Dark	150	35.0	1.000
5 Light 5 Dark	150	35.0	.500
6 Light 6 Dark	150	51.7	.500
7 Light 7 Dark	300	51.7	.500
8 Light 8 Dark	300	35.0	.500

Table 1. Test matrix for final series

The values for high and low parameter levels shown in the preceding table were selected based upon observations made during the initial testing phase. The low flow value was selected to be as near as possible to the static case while still providing reliable temperature control. For simplicity, the high value was selected to be twice this. The high/low values for temperature were selected based upon the observed limits of the temperature control system. On warmer days, the cooler was able to maintain the inlet at a minimum of 35.0 °C with the cells uncovered. For this reason, the low setting was set at this value. The high setting was limited by the system materials. Although the system had

been tested up to temperatures of 60 °C, for issues of reliability a lower value of 51.7 °C was used instead for this setting. The low level for the corrected resistivity was selected such that it is the same as that for commercially available distilled water which is around .5 M-ohm cm. Again, for simplicity, the high value is selected to be twice this number. It is worthwhile to mention here that although two resistivity values (absolute and temperature corrected) are measured and the system allows for control of either, the temperature corrected value is a better measure of impurities in the system and thus is the value which is controlled for these tests.

The cathode potential will be fixed at -500mV relative to the SHE for all tests. Due to the fact that the metal cathode is not the photoactive side of the cell, it is considered of secondary importance compared to the anode. For this reason it was felt that fixing this potential at a value sufficient to cause the reduction reaction under all test conditions would allow for a better analysis of the anode. The cathodic potential is set based upon the pH values observed during the initial test phase. pH data is collected during the final test series to validate this assumption. The minimum potential for the hydrogen evolution reaction can be expressed as a function of pH and Kelvin temperature T_K using the Nernst equation.

$$E_{H^+ / H_2} = E_{H^+ / H_2}^0 - \frac{2.303RT_K}{F} pH \quad (11)$$

Where E^0 is the standard potential (defined as zero at all temperatures for this reaction), R is the gas constant, and F is Faraday's constant.

Figure 68 shows equation 12 as a function of pH for the high and low temperatures used in this experiment.

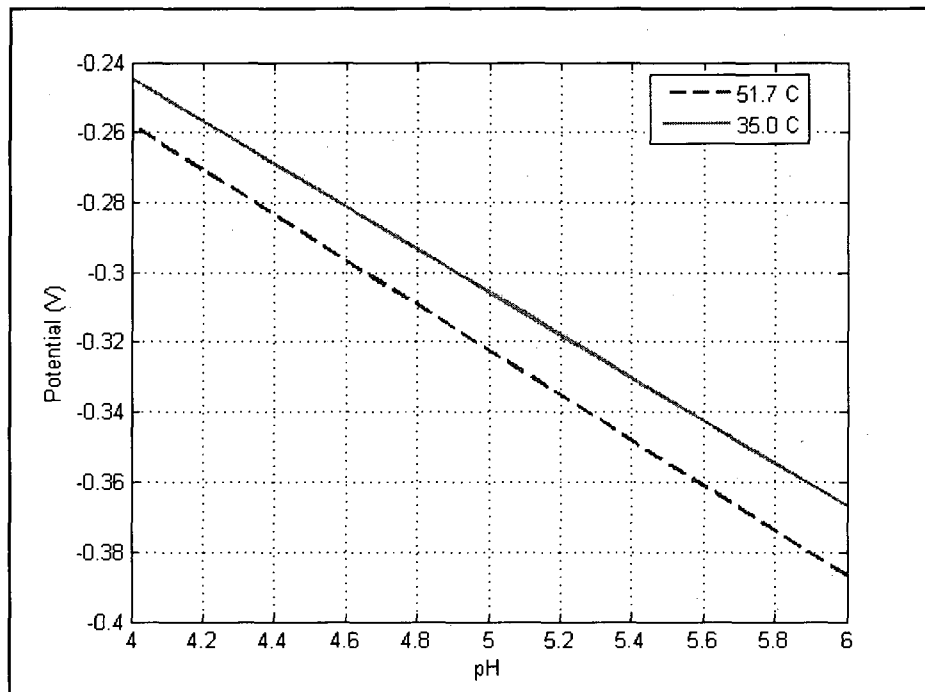


Figure 67. Variation of Nernst potential with pH for test high and low temperatures

The figure demonstrates that for the range of pH expected, a potential of -500mV will be thermodynamically sufficient for the cathodic reaction to occur at both the high and low temperatures. This value is actually in excess of the theoretical minimum to allow for any overpotentials present in the system.

Unlike the cathode potential which is fixed, the potential at the anode will be swept through a range of values during each experiment. Initially, it was thought that this input would be treated as a two level high/low parameter. For this case, the number of tests for a full factorial series doubles from 8 to 16. This makes for a total of 32 tests including the dark runs. While it is not unthinkable to have 16 clear days in a row during summertime

in the southwestern United States, the actual testing was conducted in February and March when the likelihood of this is small. Sweeping the potential for each combination of parametric settings provides more information from each individual test as well as reducing the number of test days required for a complete series.

The anodic voltage is initially set at the same potential as the cathode (-500mV) such that the initial ΔV across the cell is near zero. Over the course of the test, this potential is made more positive in 100mV increments 15 minutes apart. These values were selected such that the test could be completed in a reasonable amount of time (3.5 hrs) and that the final ΔV across the cell would be near the 1.23V standard potential for the anode reaction.

Formal Test Procedure

Due to the time dependent nature of the testing, in order to directly compare results from different days, it is critical that test events occur at the same time for each experiment. For this reason, a standard form was created which is filled out during each test to ensure the uniformity of the test series. The formal procedure dictated by the form is as follows.

Evening Before Test:

- (1) The electrolyte flowrate is set at the value which will be used for the experiment.
- (2) The inlet temperature is set at the test value.
- (3) The reference cell temperature is set at the same value as the inlet.

- (4) The temperature corrected resistivity is set at .1 M-ohm cm below the test value.
The parameter is set below the test value the evening before because it tends to increase sharply then leveling off about .08 M-ohm cm higher than the start value when the nitrogen injection is commenced on the morning of the test.
- (5) The cathode voltage is set to -500mV relative to SHE with the cell cathode leads connected.
- (6) The anode sweep parameters are entered into the Keithly sourcemeter and the trigger set. At this point the anode leads are still disconnected.

Day of Test 8:00 AM:

- (1) The laptop computer is rebooted.
- (2) A resistance measurement is made across the anode with a digital multimeter.
This is done as a measure of the deterioration of the anode surface. It had been observed early on that a drastic change in this resistance would often precede failure of the anode. The values were found to be relatively constant over the course of the tests with the West cell reading near 1.0 ohm and the East cell reading near 1.2 ohm.
- (3) The nitrogen injection is started.
- (4) Any required final adjustments to the flow, voltage, or temperature are made.
- (5) The spectroradiometer software is started and a reading is taken with the sensor aperture covered to check the dark response. The instrument is zeroed if necessary.
- (6) The spectroradiometer sensor is uncovered

(7) The old datalogger file is deleted automatically creating a new one with a start time of 8:00AM

Day of Test 9:00AM:

(1) The temperature corrected resistivity is set at its final test value.

Day of Test 9:45 AM:

(1) All parameters are checked for stability at their respective setpoints at this time. If the system is not stable the test must be aborted at this time.

(2) The spectrometer data collection is started. The unit is set to record a snapshot of the spectrum every 15 s throughout the remainder of the test.

(3) The cells are uncovered if the test is to be light.

Day of Test 10:00 AM:

(1) The anodic voltage sweep is started.

(2) The anode leads are connected

Day of Test 10:30AM-1:30PM:

(1) The system is allowed to run, with checks made every $\frac{1}{2}$ hour. Notes are made regarding weather conditions and system operation at each checkpoint.

Day of Test 1:30PM (end of test):

- (1) Spectroradiometer collection is stopped.
- (2) The logger data file is moved to the new folder, ending the test.

Post Test Procedure:

- (1) The cathode leads are checked for continuity. This cannot be measured directly with a multimeter as there is no internal electrical connection between the two cathode halves. Instead, the cells are uncovered and the current is observed with both cathode leads attached and then with only one. If the current decreases by approximately half between the two cases, both cathode connections are assumed to be good.
- (2) The anode resistance is checked and recorded as it was at the start of the test.

Solar Spectrum Measurements

The final test series was conducted from late February to mid March in 2009. Illuminated tests were run only on exceptionally clear days to provide good consistency between experiments. Figures 68-75 show the measured solar intensity as a function of time and wavelength for the 8 illuminated tests. The MATLAB code used to generate the surface plots as well as all other algorithms used in the analysis are included in Appendix C.

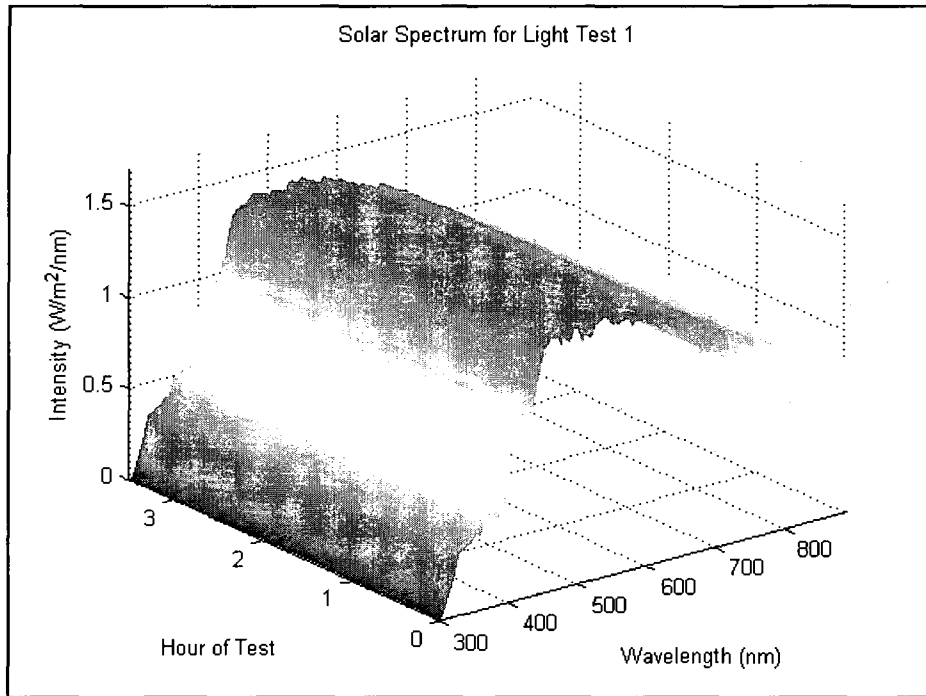


Figure 68. Solar intensity vs. time and wavelength for Test 1

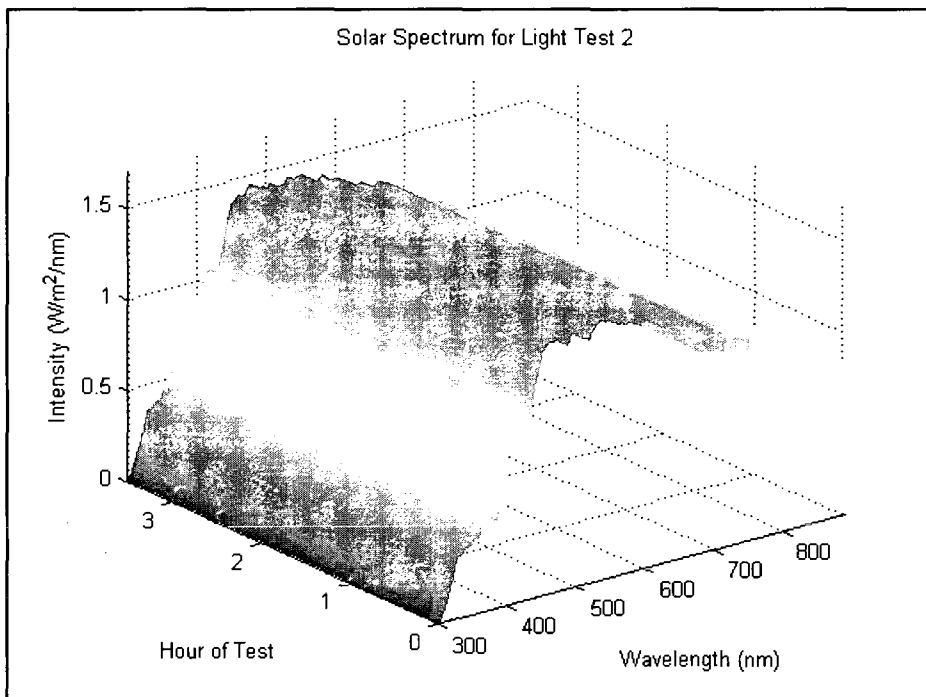


Figure 69. Solar intensity vs. time and wavelength for Test 2

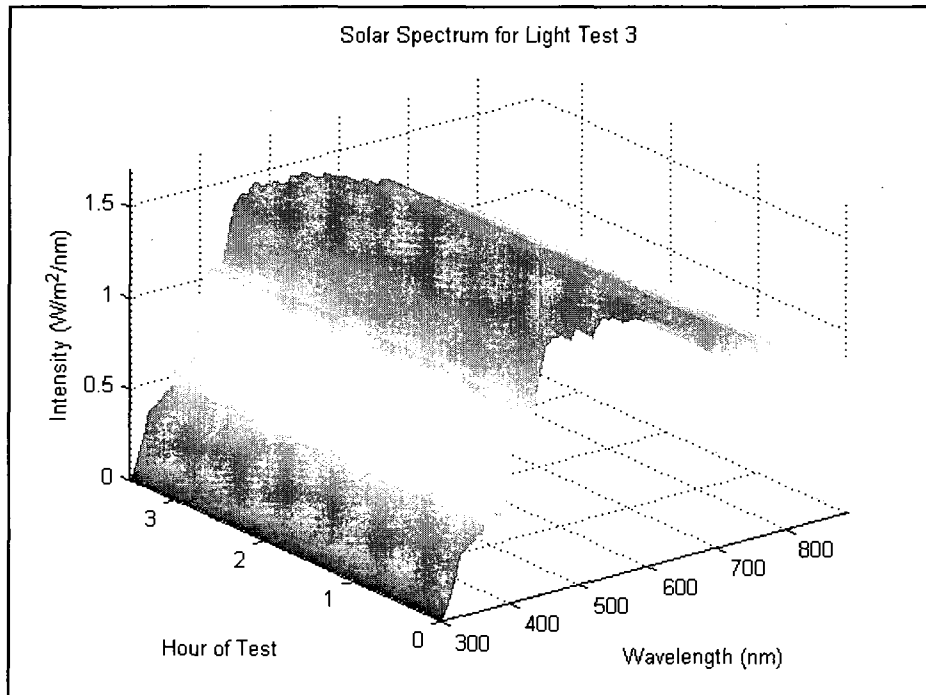


Figure 70. Solar intensity vs. time and wavelength for Test 3

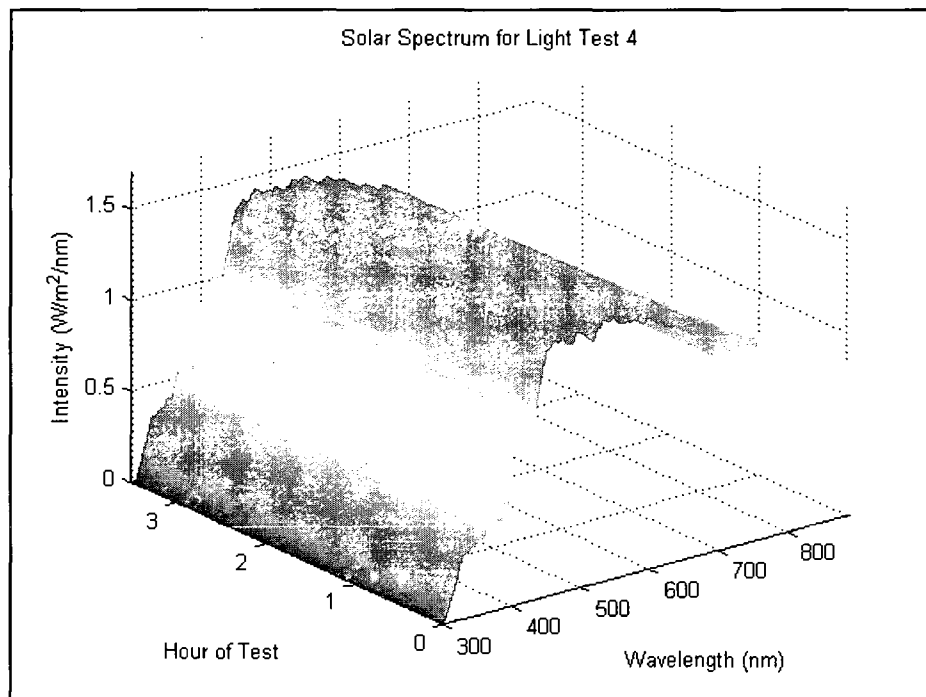


Figure 71. Solar intensity vs. time and wavelength for Test 4

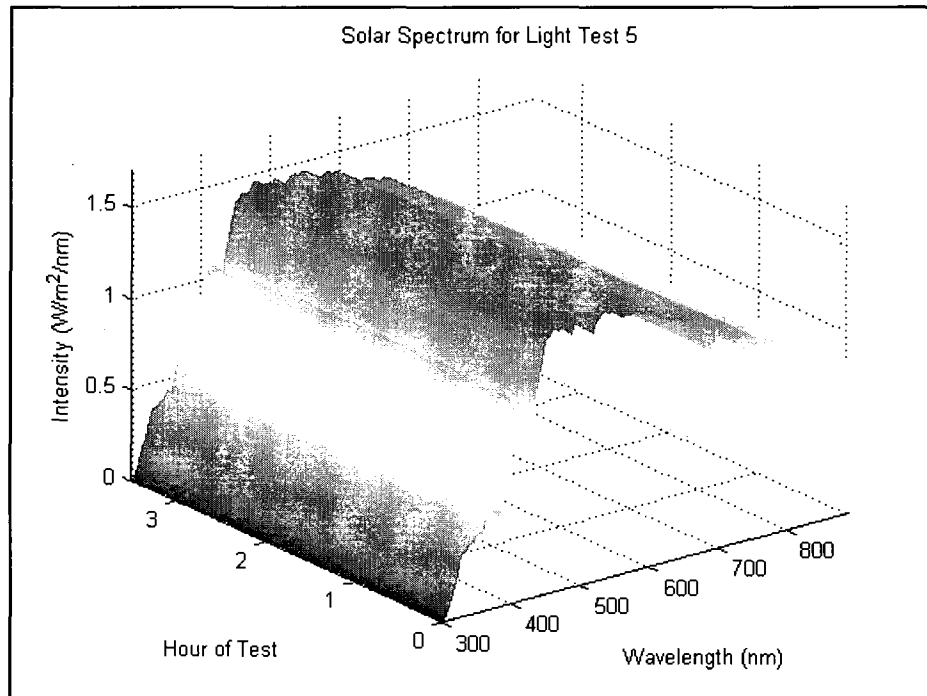


Figure 72. Solar intensity vs. time and wavelength for Test 5

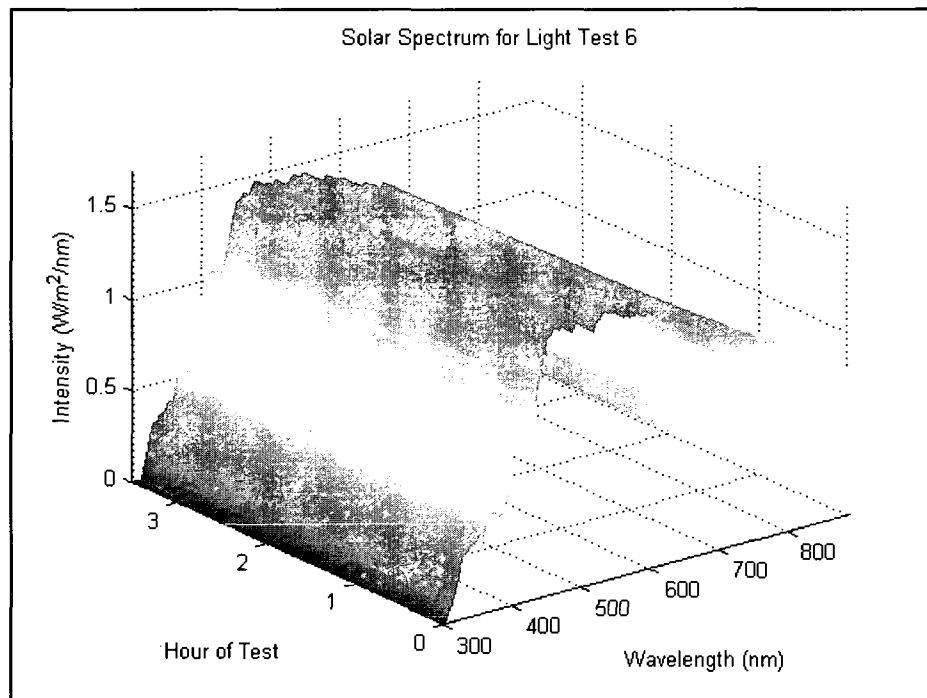


Figure 73. Solar intensity vs. time and wavelength for Test 6

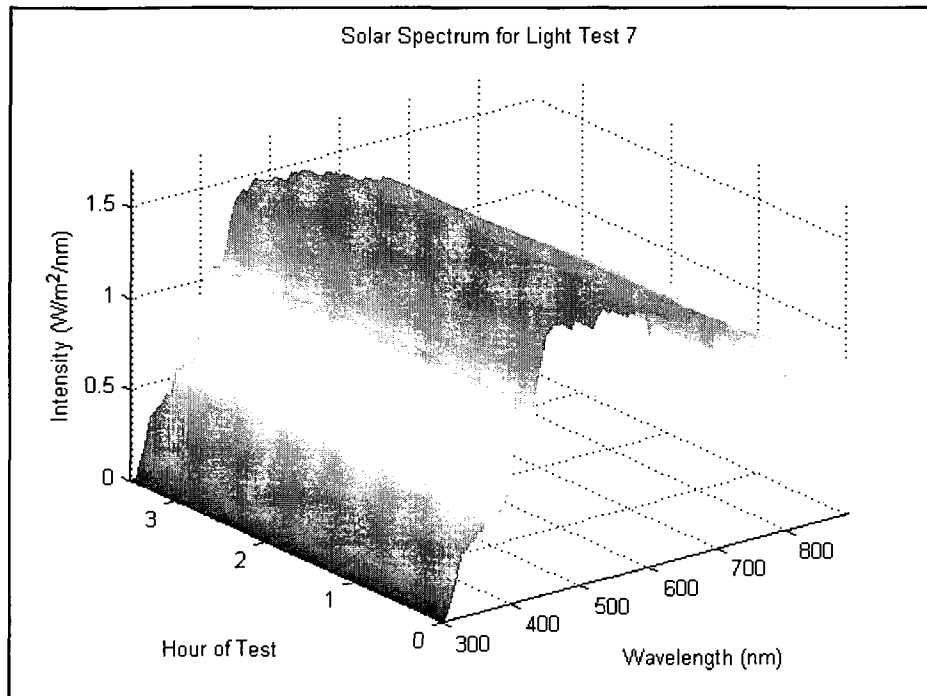


Figure 74. Solar intensity vs. time and wavelength for Test 7

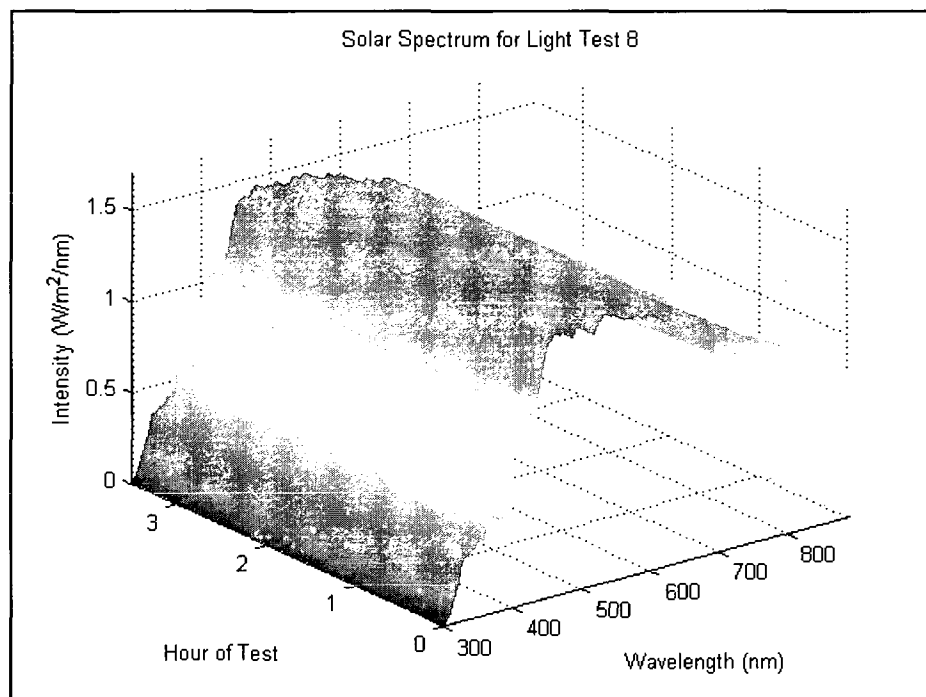


Figure 75. Solar intensity vs. time and wavelength for Test 8

The figures demonstrate that the intensity is relatively constant over the course of the individual tests as well as being consistent between tests run on different days. This consistency supports the notion that direct comparison of results from tests on different days can be a valid approach. The 3d surface plots of the spectral data shown in figures 68-75 are useful for qualitatively comparing the general shapes of the curves for the various tests but due to the large amount of data they represent, direct quantitative comparison between tests in a given series is difficult. To circumvent this problem, an algorithm was created using MATLAB which compares the raw spectral intensity data J for a single test at timestep i , to data at timestep j . The mismatch of the two spectra for any combination of i and j can be quantified using equation 13.

$$\delta_{i,j} = \sum_{k=1} |J_{i,k} - J_{j,k}| \quad (13)$$

Where k is a counter related to wavelength and the maximum value of δ corresponds to the worst case mismatch for a given test. The algorithm tests every possible combination of i and j and finds the two times which maximize δ for any single test day. Figures 76-83 show the worst case spectra for each individual test and the times at which each was measured.

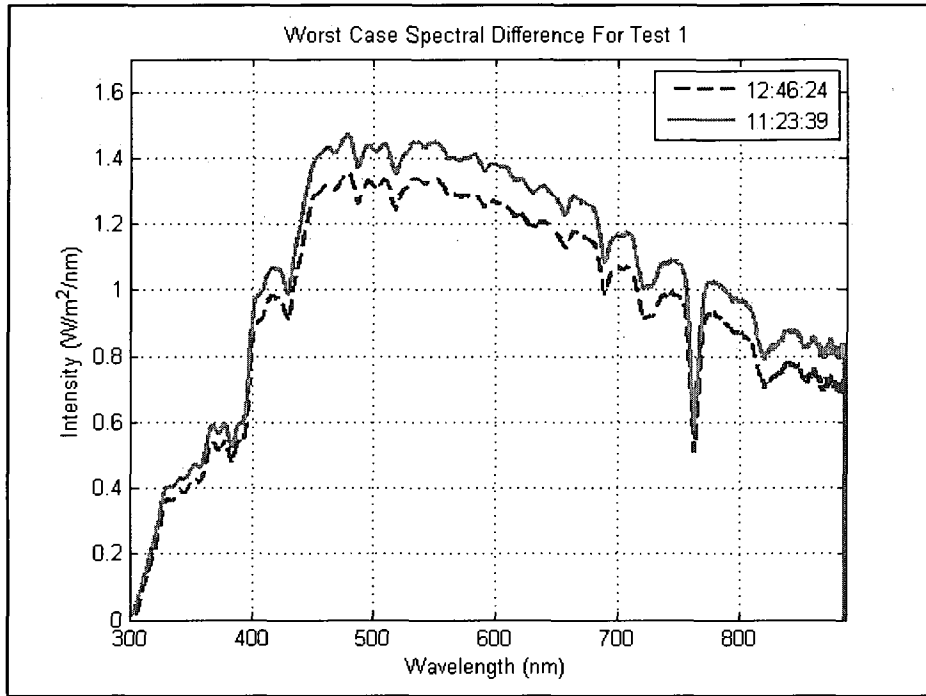


Figure 76. Maximum spectral mismatch for Test 1

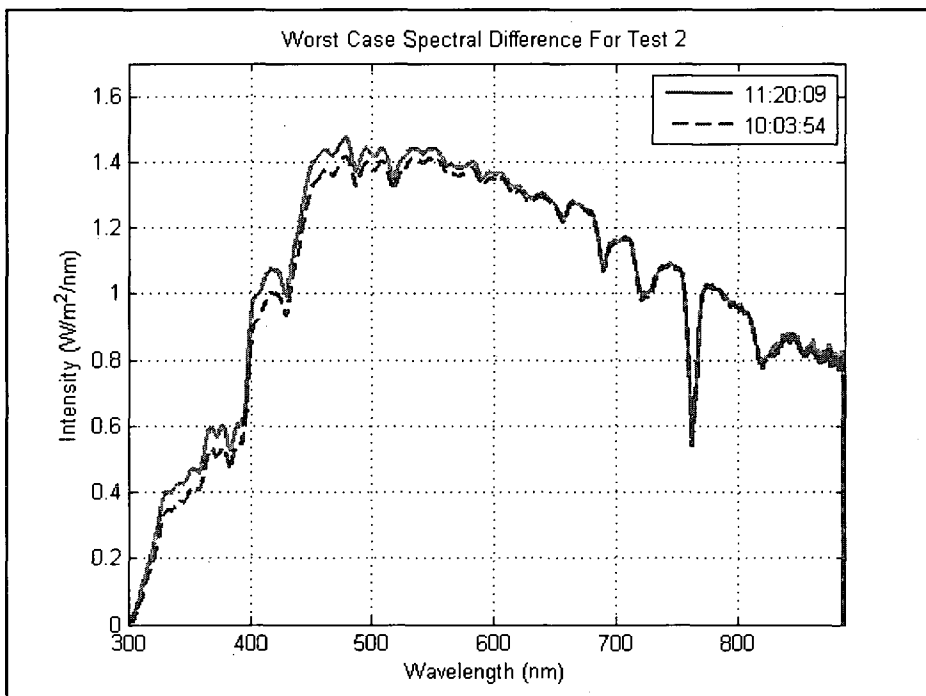


Figure 77. Maximum spectral mismatch for Test 2

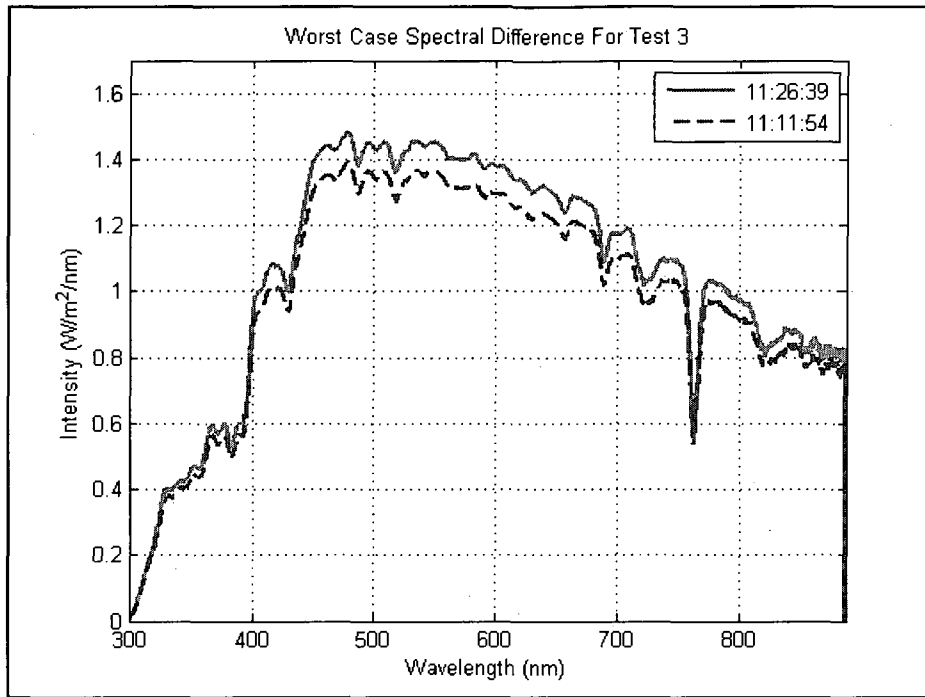


Figure 78. Maximum spectral mismatch for Test 3

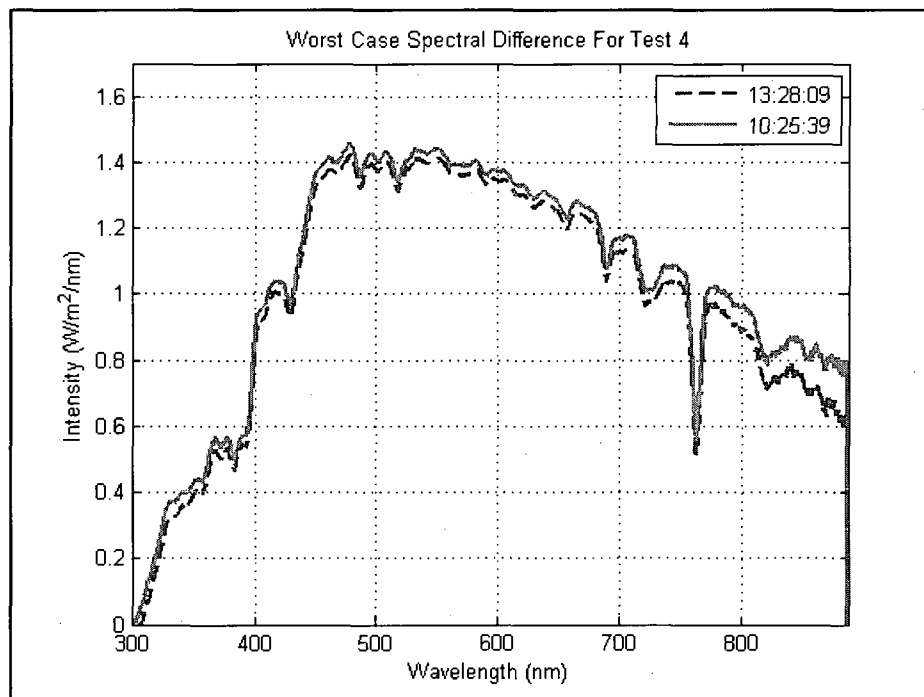


Figure 79. Maximum spectral mismatch for Test 4

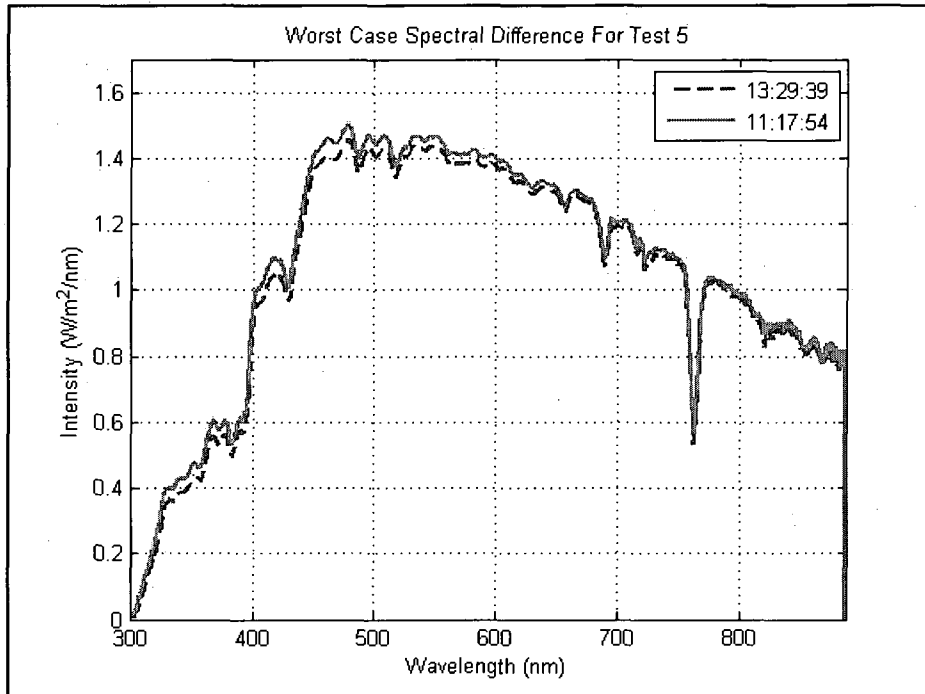


Figure 80. Maximum spectral mismatch for Test 5

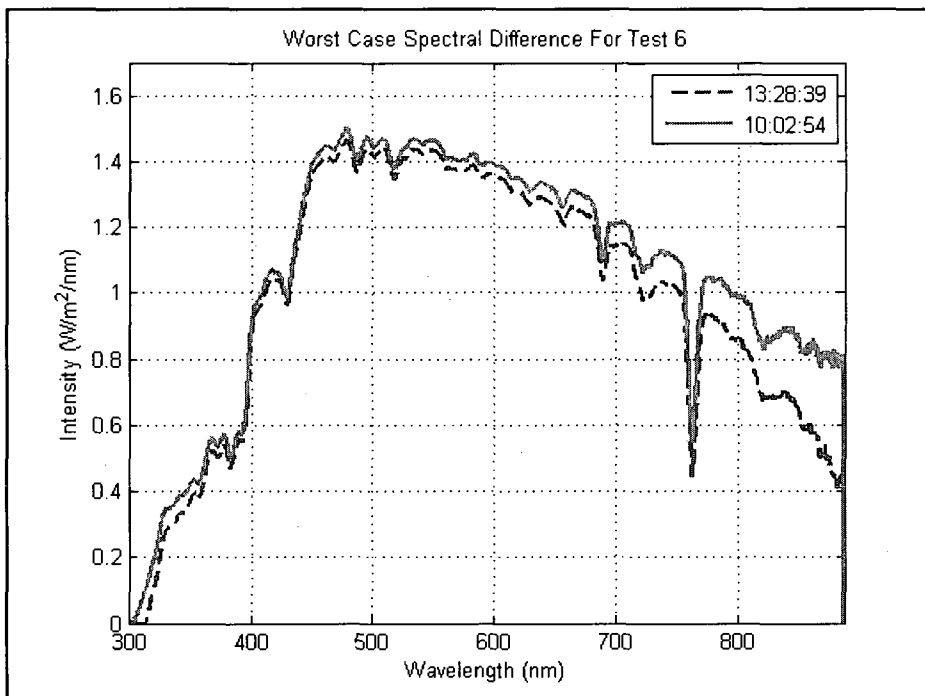


Figure 81. Maximum spectral mismatch for Test 6

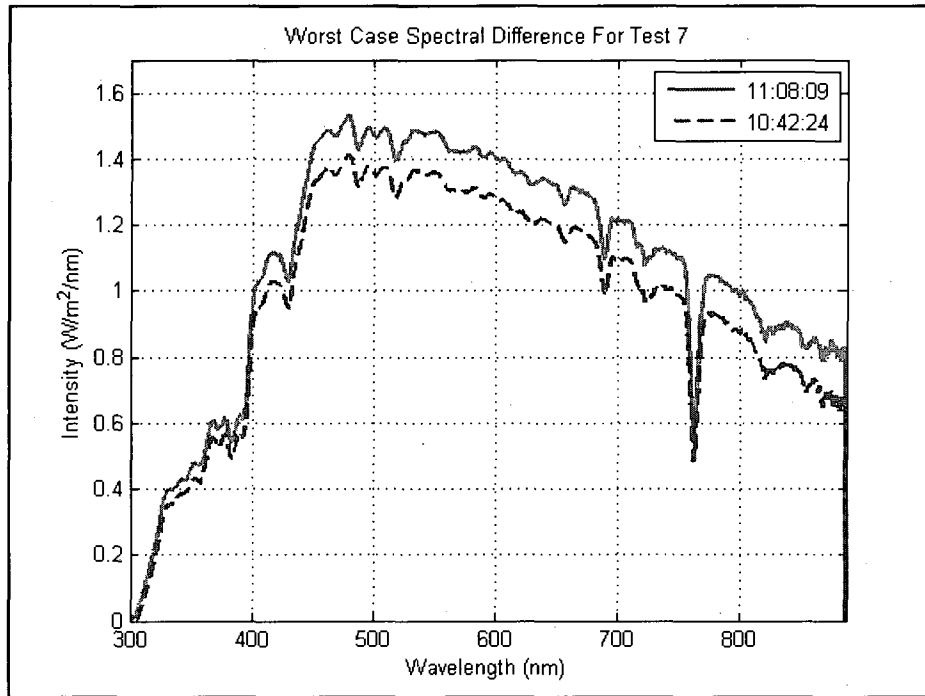


Figure 82. Maximum spectral mismatch for Test 7

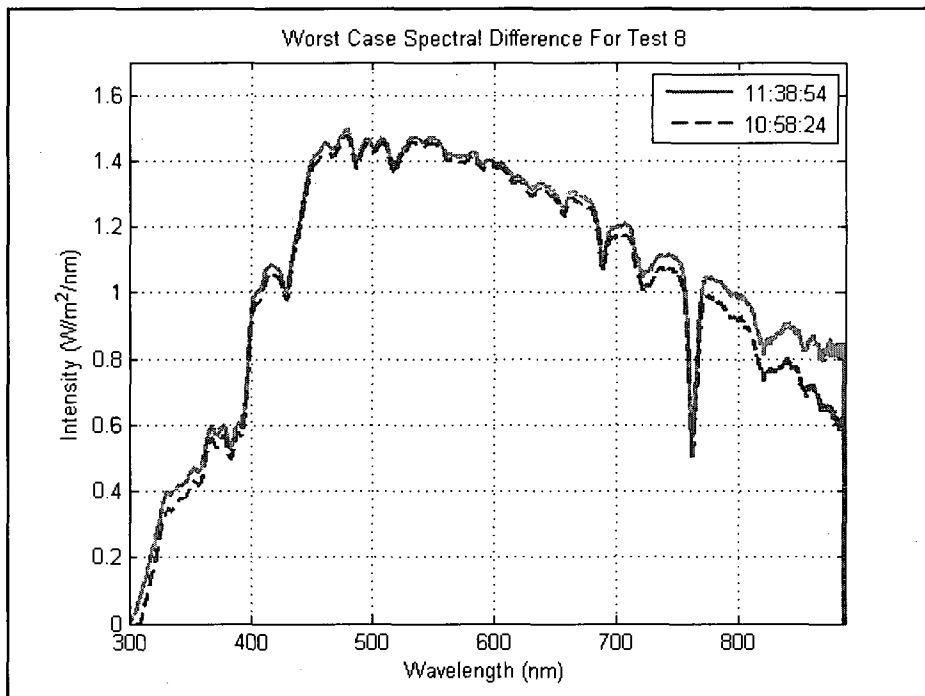


Figure 83. Maximum spectral mismatch for Test 8

Table 2 summarizes the integrated values for the worst case spectral mismatch for each of the 8 individual illuminated tests.

Test	Times for Worst Case Mismatch	Integrated Difference (W/m ²)	Integrated % Difference
1	12:46:24 11:23:39	53	9
2	11:20:09 10:03:54	17	3
3	11:26:39 11:11:54	37	6
4	13:28:09 10:25:39	27	4
5	13:29:39 11:17:54	16	3
6	13:28:39 10:02:54	45	7
7	11:08:09 10:42:24	60	10
8	11:38:54 10:58:24	26	4

Table 2. Integrated values for worst case spectral differences

The data indicates that the flux over the course of any test was relatively constant with the worst mismatch of 10% occurring during test 7. Additionally, figures 78-84 demonstrate that much of the mismatch occurs above 600nm beyond which the photons are considered to be of insufficient energy for photo-absorption by the anode in any event.

In addition to the comparison of spectra collected during a single test day, another measure of solar consistency for the series is a comparison of spectra measured at a given time on two different test days. As before, a MATLAB algorithm was implemented to compare spectra from test m and n at time i using equation 14.

$$\delta_{m,n,i} = \sum_{k=1} |J_{m,i,k} - J_{n,i,k}| \quad (14)$$

The result, $\delta_{m,n,i}$, is a measure of the dissimilarity of the spectrum between tests m and n at time i . The maximum value of α corresponds to the worst case spectral mismatch between tests for any time in the test series. The algorithm compares every possible combination of m and n for all times to find this maximum. The routine then outputs the two test numbers which produced the maximum and the time at which they occurred. For the series presented here, the worst correlation occurred between tests 1 and 5 at 12:46:24. The integrated difference between the two spectra was 57 W/m^2 for an approximate mismatch of 9%. As was the case with the single test comparisons, much of the mismatch occurs above 600 nm where there is no absorption. The two worst case spectra are shown in Figure 84.

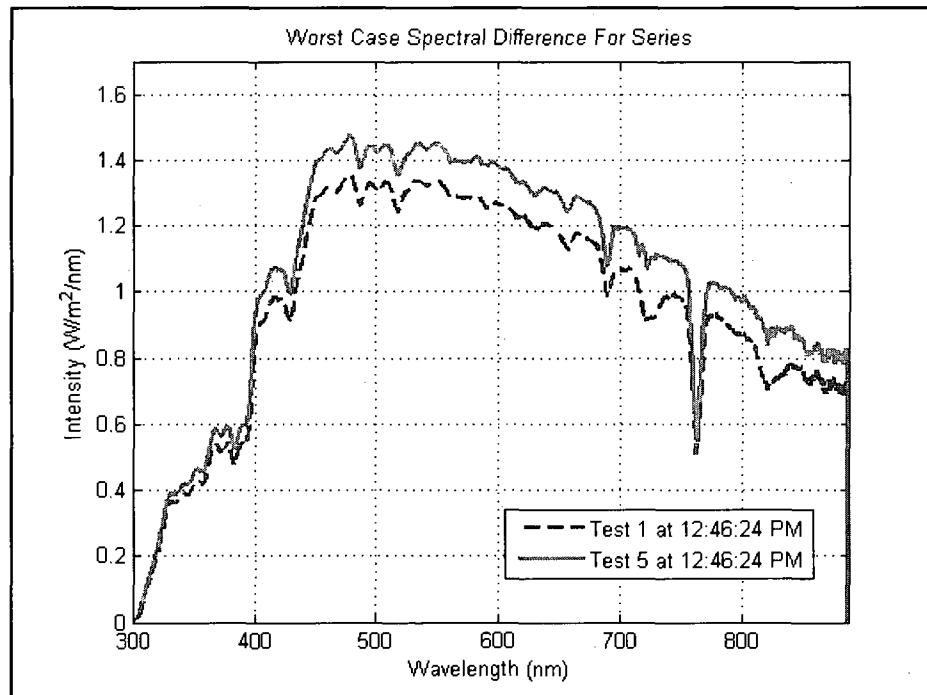


Figure 84. Maximum spectral mismatch between tests conducted on different days

Based upon the preceding analysis it is concluded that it is not an unreasonable assumption that the solar input may be treated as a constant for the series. From this, it can be surmised that any observed variations in the cell currents are not due to changes in this input. To quantify the solar input for the series, the results for the 8 lighted tests in the series were averaged at each wavelength to produce an average series spectrum. Figures 85 and 86 show the average spectrum compared to the two standards discussed in chapter 1.

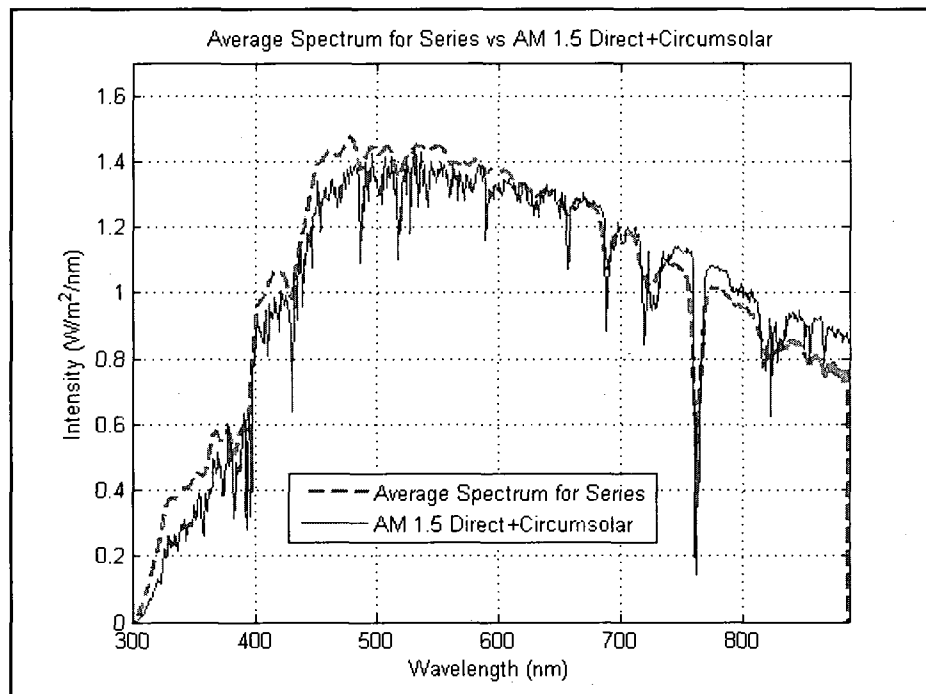


Figure 85. Average series spectrum compared to AM 1.5 Dir+Circ

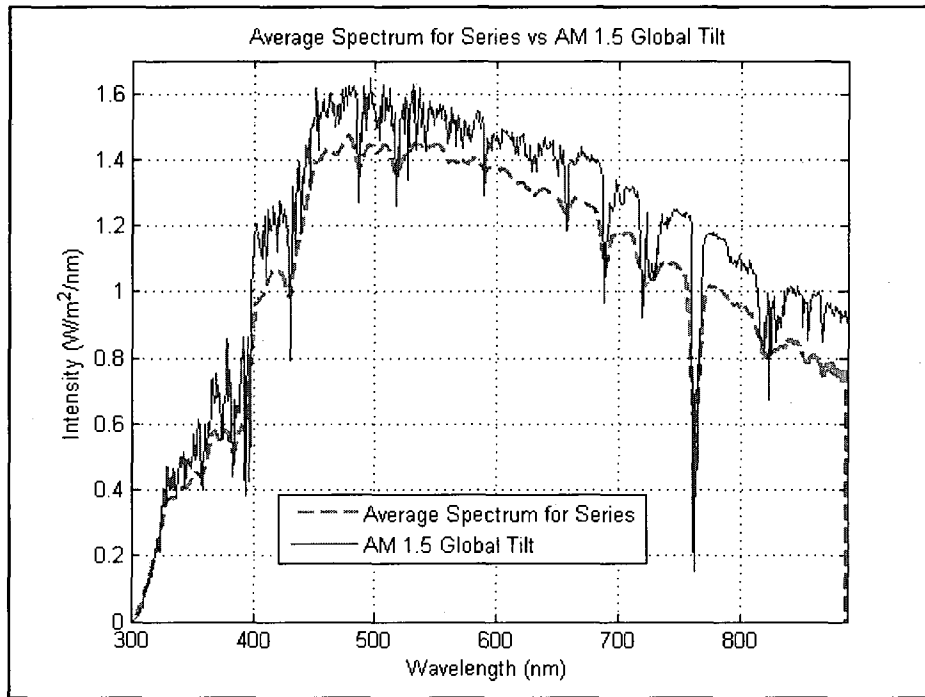


Figure 86. Average series spectrum compared to AM 1.5 Global Tilt

The preceding figures demonstrate a relatively good correlation between the average series spectrum and the two standards. The integrated results are summarized in table 3.

Spectra	Integration (300-886nm) (W/m ²)	Integrated % Difference for Series Average
Series Average	605	-
AM 1.5 Direct+Circumsolar	586	3
AM 1.5 Global Tilt	677	10

Table 3. Integrated values for series average and reference spectra

Controlled Input Parameters

As was discussed in chapter 2 the experimental setup is designed to control several system parameters. As with any control system there will always be some deviation from the parameter setpoint due to external disturbances. The purpose of this section is to

quantify these deviations for the various input parameters being controlled for this experiment.

Due to the large amount of parametric data collected over the 16 tests in the series direct presentation of all of the measurements is not practical. To condense the results to a more manageable form, an average series setpoint deviation for a specific controlled input parameter is defined using equation 15.

$$\sigma_i = \frac{\sum_{g=1}^G (|X_{g,i} - \gamma_g|)}{G} \quad (15)$$

Where $X_{g,i}$ is the measured parameter value for test g at time i , γ_g is the setpoint for test g , and G is the number of tests in the series (in this case 16). Figures 87-92 show the average series setpoint deviation for the controlled parameters.

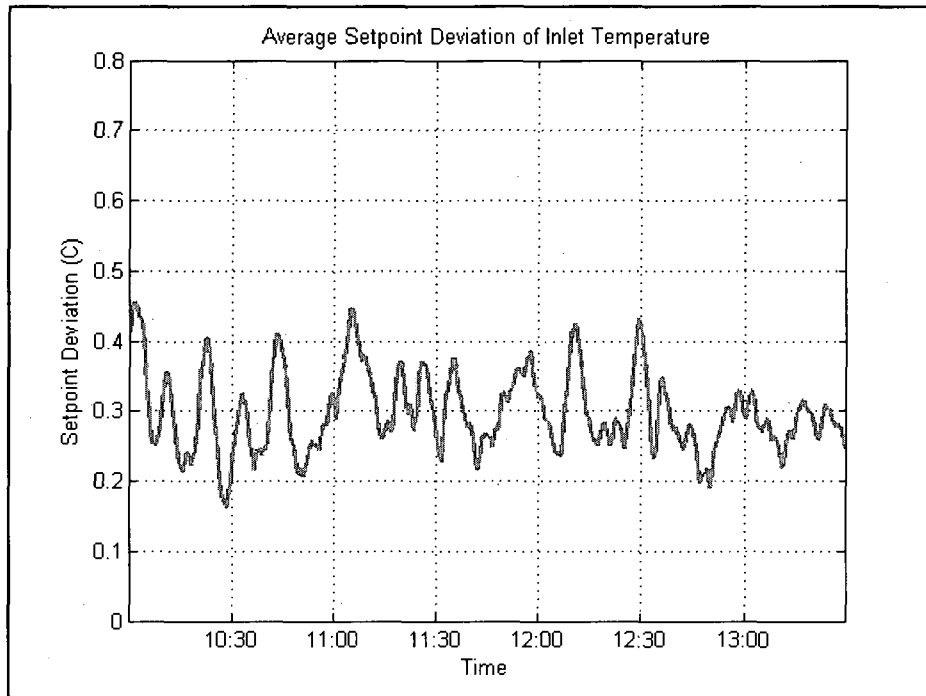


Figure 87. Series average setpoint deviation for inlet temperature

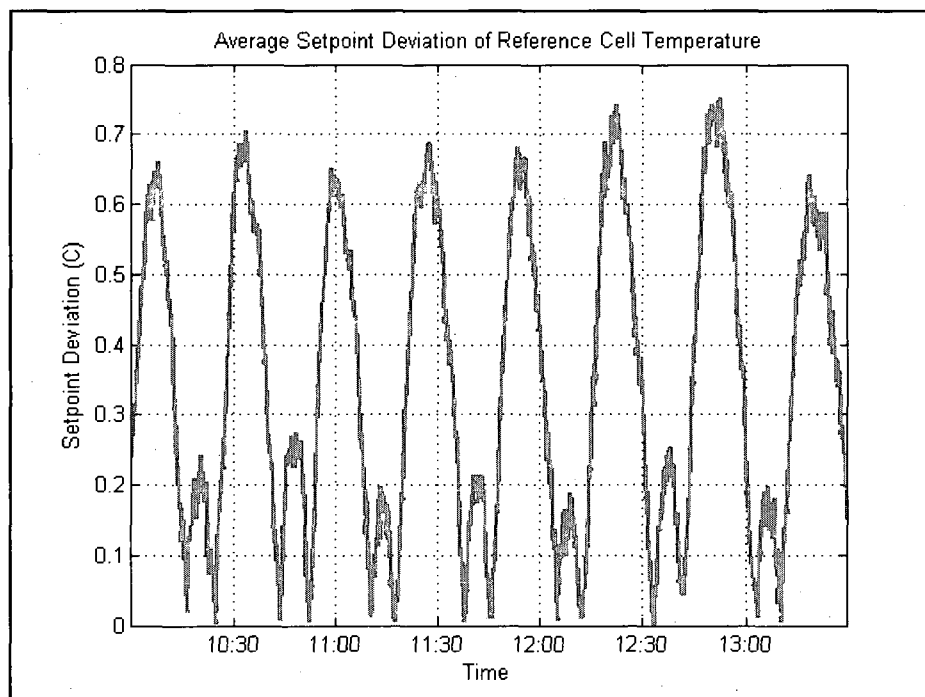


Figure 88. Series average setpoint deviation for ref cell temperature

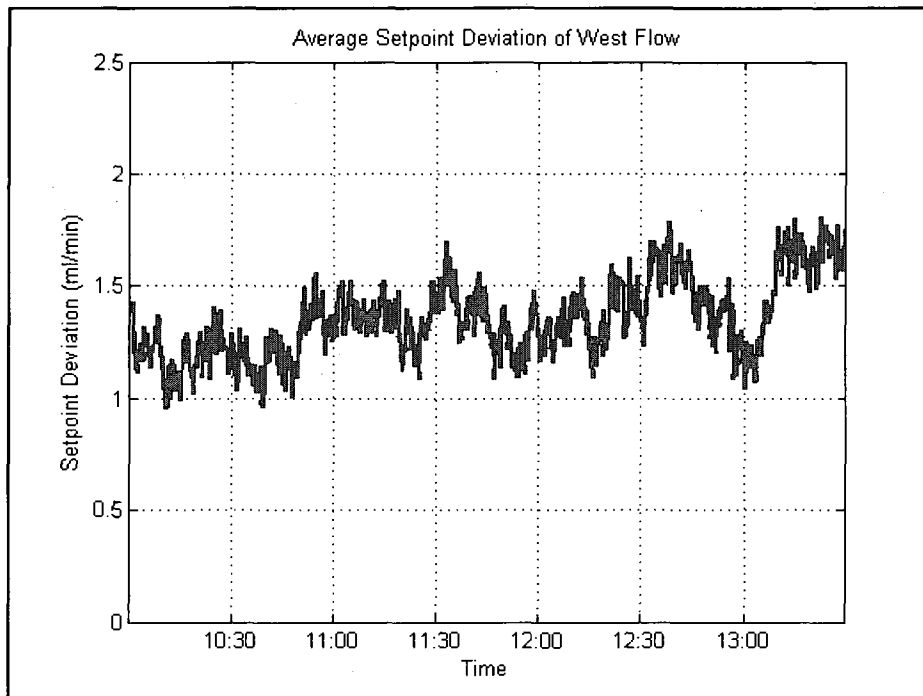


Figure 89. Series average setpoint deviation for West flow

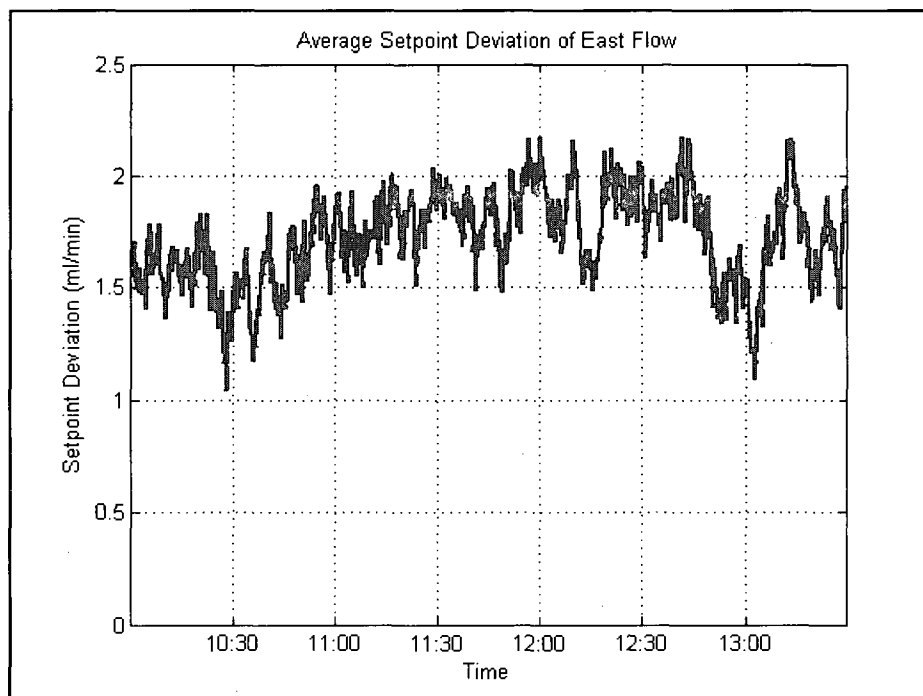


Figure 90. Series average setpoint deviation for East flow

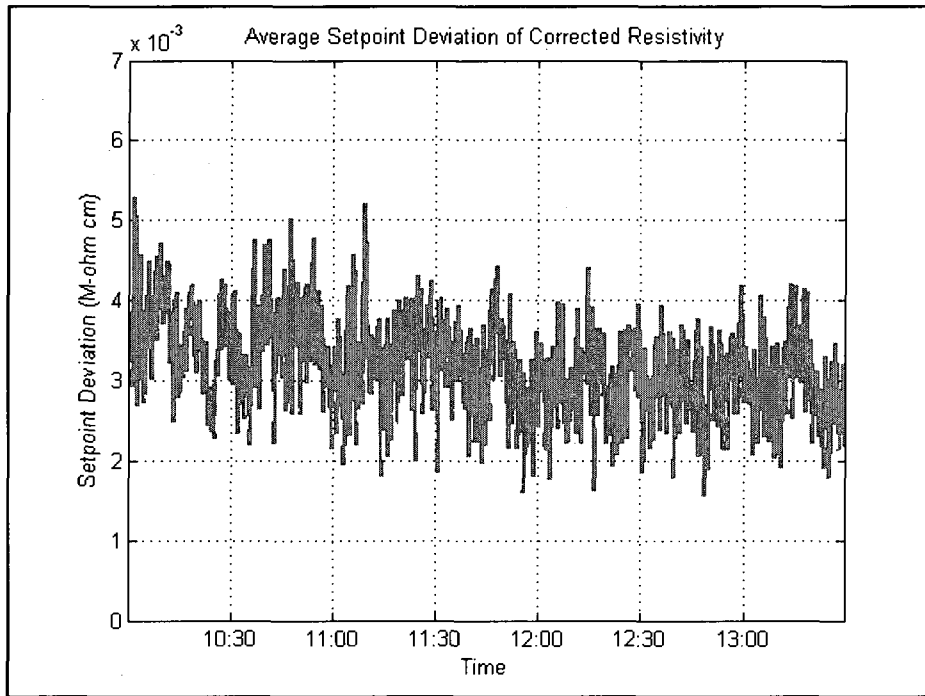


Figure 91. Series average setpoint deviation for temp corrected resistivity

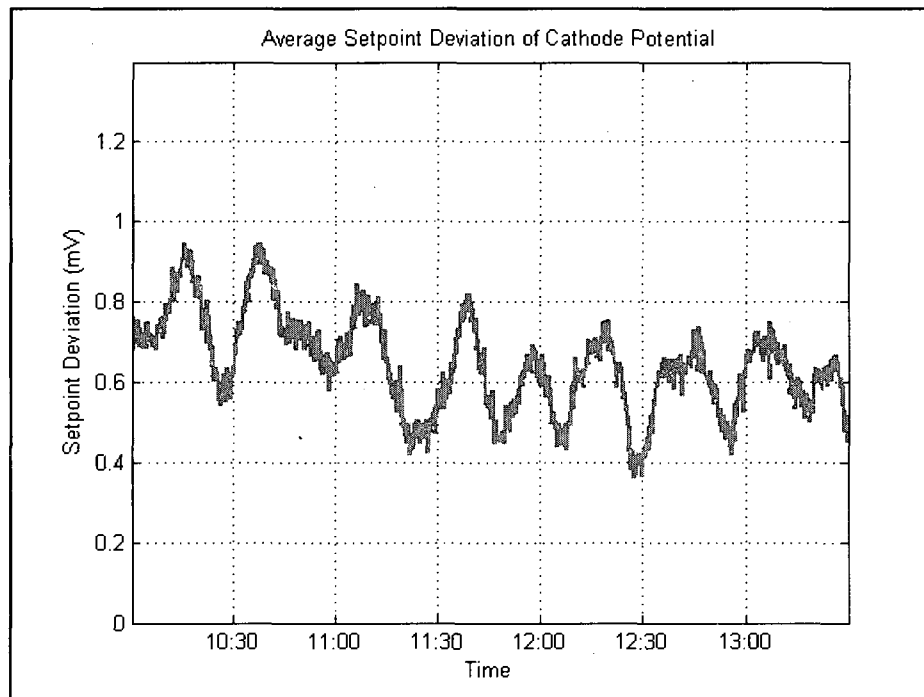


Figure 92. Series average setpoint deviation for cathode potential

Table 4 summarizes the maximum and time averaged series setpoint deviations for the various controlled parameters.

Parameter	Maximum of Series Average Setpoint Deviation	Time Averaged Mean of Series Average Setpoint Deviation
Inlet Temp	.5 C	.3 C
Ref Cell Temp	.8 C	.3 C
West Flow	1.8 ml/min	1.3 ml/min
East Flow	2.2 ml/min	1.7 ml/min
Cor Resistivity	.005 MΩ cm	.003 MΩ cm
Cat Potential	.9 mV	.6 mV

Table 4. Maximum and time averaged mean values of avg series setpoint deviation

The preceding figures demonstrate relatively good parametric control for the test series. Based upon this analysis it is considered a reasonable assumption that any observed variations in the cell currents are not due to unwanted deviations of the various input parameters from their respective setpoints.

Other Input Parameters

In addition to the directly controlled parameters discussed in the previous section, measurements are also made of other parameters which influence cell performance but are not actively controlled. These inputs, (pH and absolute resistivity) are assumed to vary predictably with changes in other inputs (temperature and temperature corrected resistivity) and are therefore not treated as formal input parameters themselves. The purpose of this section is to demonstrate the validity of these assumptions beginning with the absolute resistivity.

As was mentioned previously, the testing system allows for control of either absolute resistivity or a temperature corrected value. The two measurements are required due to the fact that the absolute resistivity can vary by either of two mechanisms. First, a change in the concentration of the dissolved ionic species will cause changes in absolute resistivity. Second, changes in the mobility of the dissolved ionic species (as with temperature variation) will cause variations as well. The temperature corrected measurement is designed to compensate for changes in ion mobility due to temperature variations and is thus a measurement of system impurities alone. Because of this, the absolute resistivity of the system should be fully described by the corrected resistivity value and the temperature, both of which are actively controlled. This being the case, the measurement should be relatively constant for each of the four possible combinations of corrected resistivity and temperature tested for this series. Figure 97 shows the time varying series average values of the absolute resistivity for each of these four combinations.

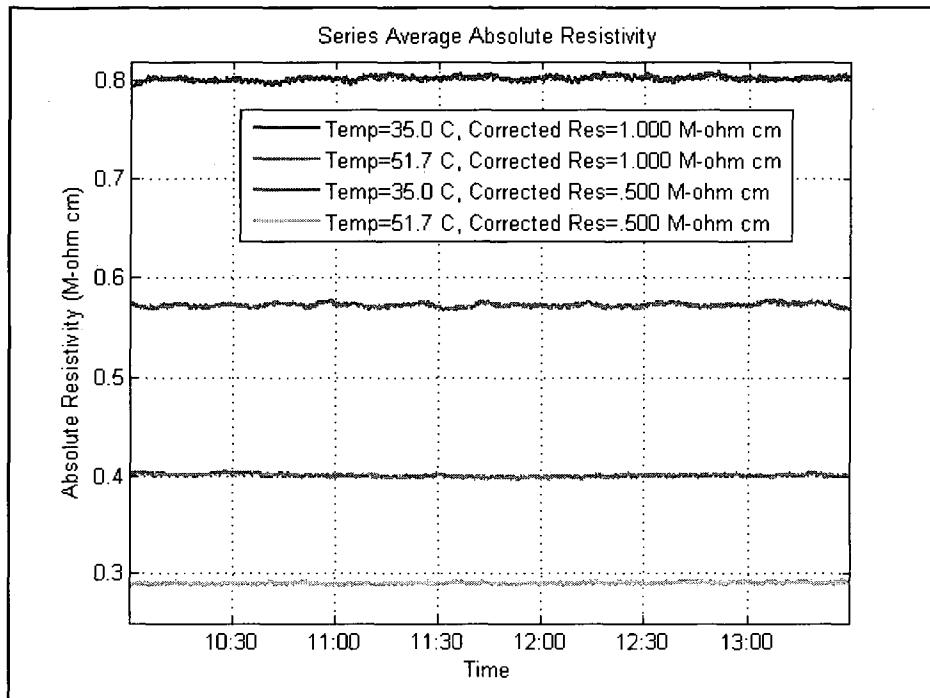


Figure 93. Series average absolute resistivity for the four cases

Figures 94-97 show the time varying standard deviation for each the four cases presented in figure 93.

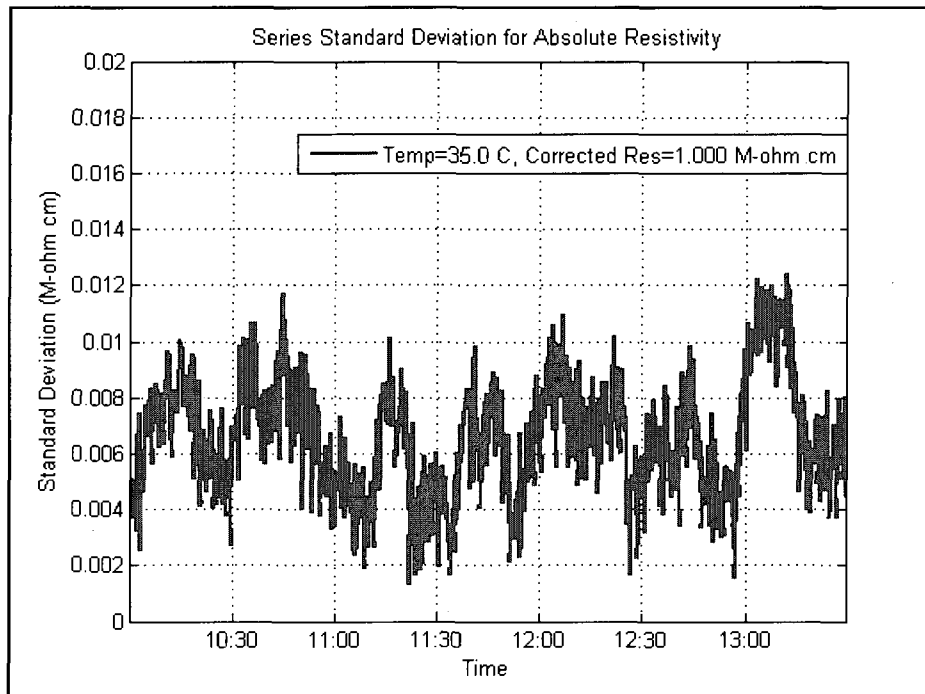


Figure 94. Time varying series standard deviation of absolute resistivity

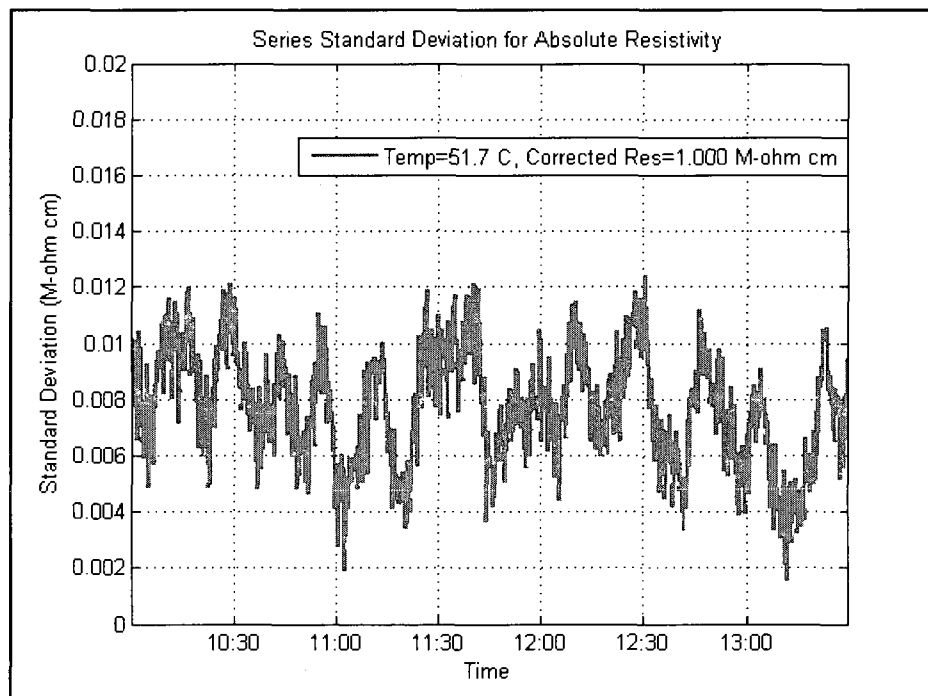


Figure 95. Time varying series standard deviation of absolute resistivity

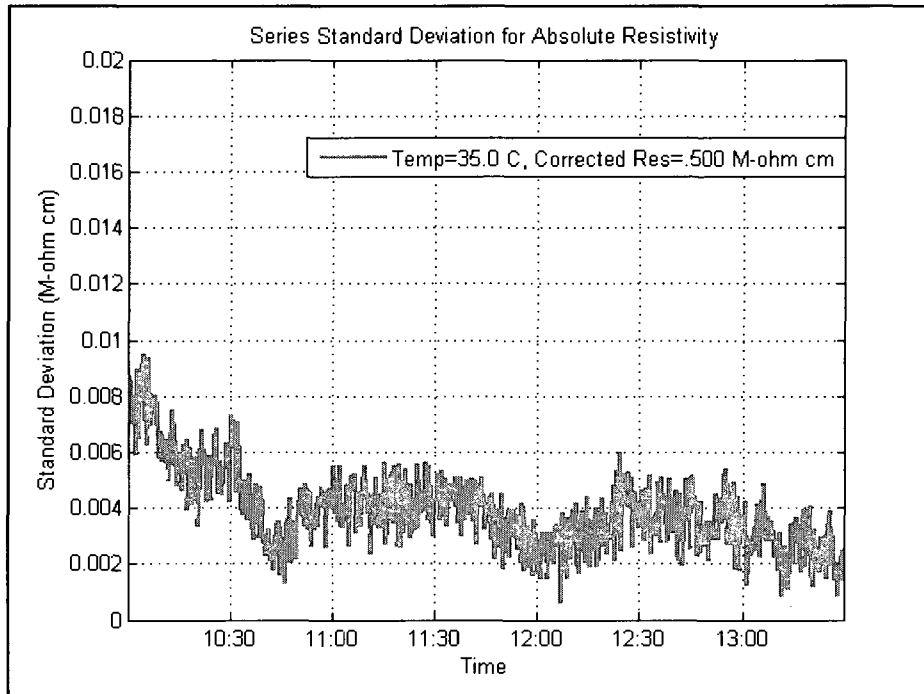


Figure 96. Time varying series standard deviation of absolute resistivity

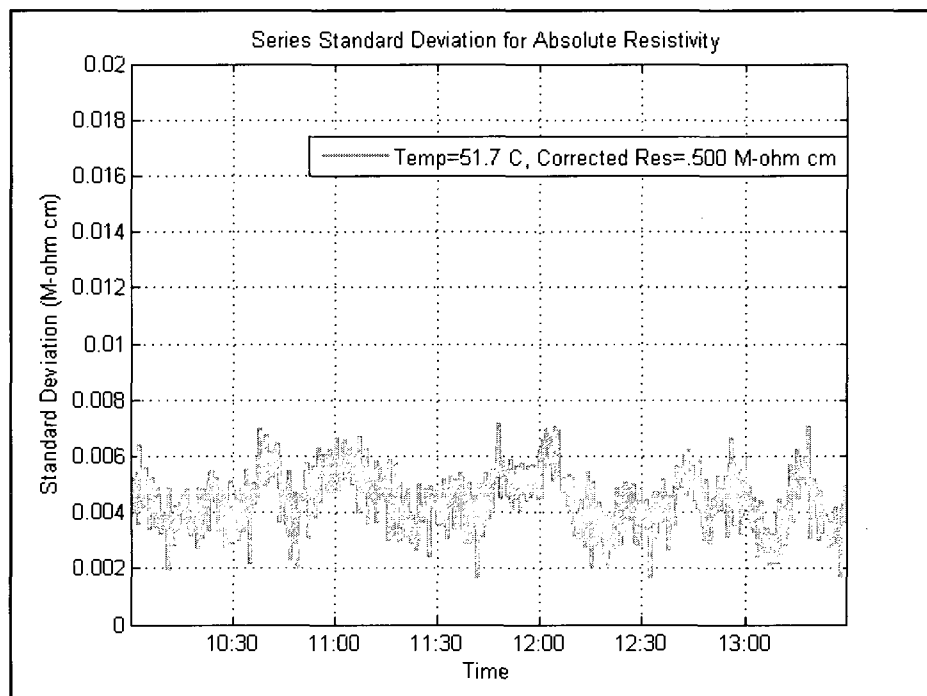


Figure 97. Time varying series standard deviation of absolute resistivity

Table 5 summarizes the maximum series standard deviation and time averaged mean for each of the four cases presented in the preceding figures.

Temp and Corrected Resistivity Setting	Maximum of Series Standard Deviation	Time Averaged Mean of Series Average Absolute Resistivity
Temp=35.0 C Cor Res=1.000 (M-ohm cm)	.012 (M-ohm cm)	.803 (M-ohm cm)
Temp=51.7 C Cor Res=1.000 (M-ohm cm)	.012 (M-ohm cm)	.573 (M-ohm cm)
Temp=35.0 C Cor Res=.500 (M-ohm cm)	.010 (M-ohm cm)	.400 (M-ohm cm)
Temp=51.7C Cor Res=.500 (M-ohm cm)	.007 (M-ohm cm)	.291 (M-ohm cm)

Table 5. Maximum std deviation and time averaged mean values for abs resistivity

The data suggests that, while level of consistency for the absolute resistivity is acceptable, there would appear to be some source of deviation between tests of similar temperature and corrected resistivity setpoints. Given that the control of these parameters was shown to be quite good (Figures 87 and 91) it is improbable that these discrepancies were caused by deviation from the setpoints during the individual tests. Further analysis of the data has shown that in general, for four tests at a given inlet temperature and corrected resistivity setting, tests conducted at like flowrates will agree better than those run at different settings. This seeming flow dependency can be explained based upon the locations in the system at which the measurements are made. The system is constructed

such that there is a considerable distance between the tank and the point where the inlet temperature is measured. As a consequence of this, at the lower flowrates, there is greater time for heat transfer to the ambient between the tank and the point at which the inlet temperature measurement is made. For this reason, the temperature in the tank (and subsequently at the resistivity sensor) will generally be higher for a lower flowrate at a given inlet temperature setpoint. This means that there will be a difference that increases inversely with flowrate between the measured inlet temperature which is used for control and the temperature measured at the resistivity sensor which is used for temperature compensation. By definition, this difference should have no effect on the temperature corrected resistivity, which is solely a measure of ion concentrations in the system. The data shows this to be the case. The absolute resistivity however, will be effected by differences in temperature at the measurement point. This effect is also consistent with the measured data. In essence, the observed discrepancies are caused by the assumption that the temperature measured at the resistivity sensor is the same as the cell inlets. By this logic, if the discrepancies are in fact caused by flowrate induced temperature differences, then regardless of the absolute resistivity measured at the sensor, the absolute resistivity at the cell inlet will be the same for any tests of like corrected resistivity and inlet temperature setpoints. This assumption holds as long as the inlet temperatures are consistent between the four tests, which was shown to be the case.

Based upon this analysis it is expected that the deviations shown in Figures 94-97 are actually much smaller at the cell inlets, which is the point in the system at which consistency is critical. It is important to recognize at this point that while it is the temperature corrected resistivity which is actively controlled for these tests, the absolute

resistivity will determine the internal cell resistance. For this reason, meaningful comparison of tests at different flowrates requires that this parameter be fully described by the other two controlled inputs. From the arguments presented in this section, this is assumed to be the case.

As with the absolute resistivity, the pH of the system is a parameter which is not actively controlled during the experiment but is instead assumed to be fully described by the corrected resistivity and inlet temperature. Figure 98 shows the time varying series average values of pH for each of the four possible combinations of these variables.

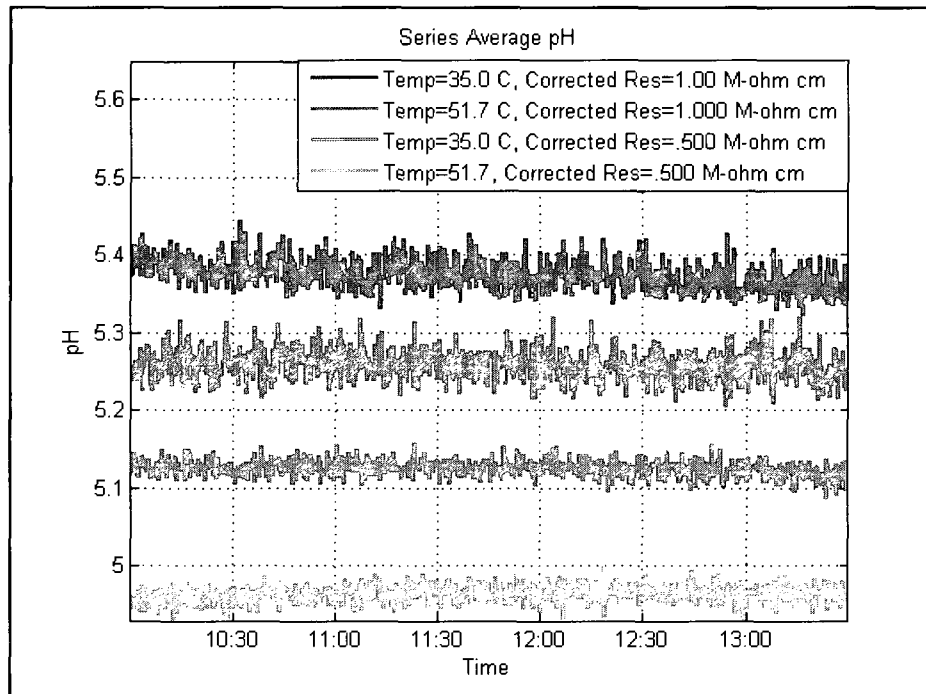


Figure 98. Series average pH for the four cases

Figures 99-102 show the time varying standard deviation for each the four cases presented in figure 98.

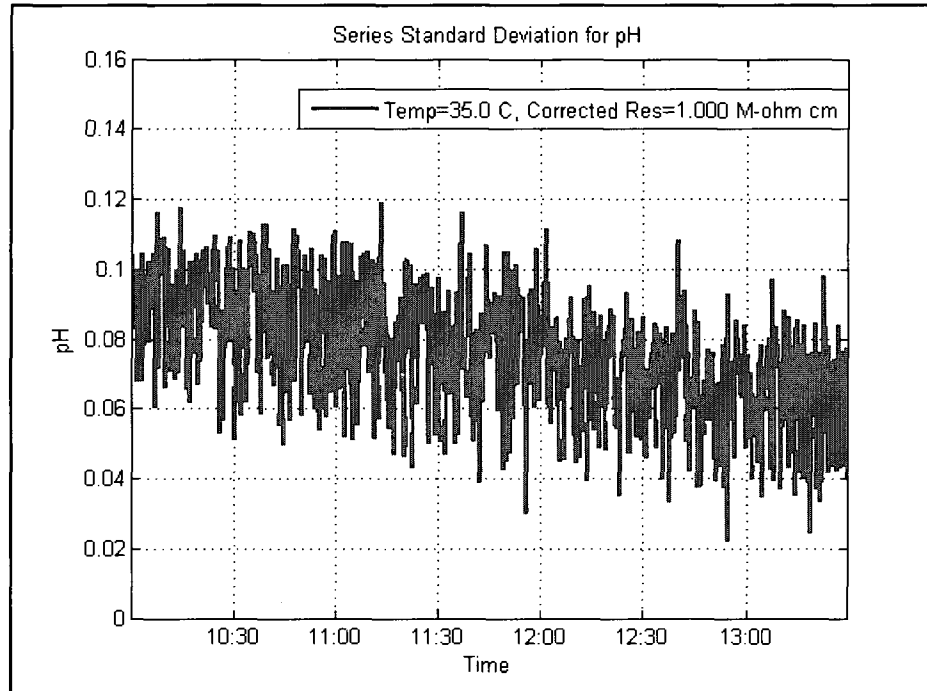


Figure 99. Time varying series standard deviation of pH

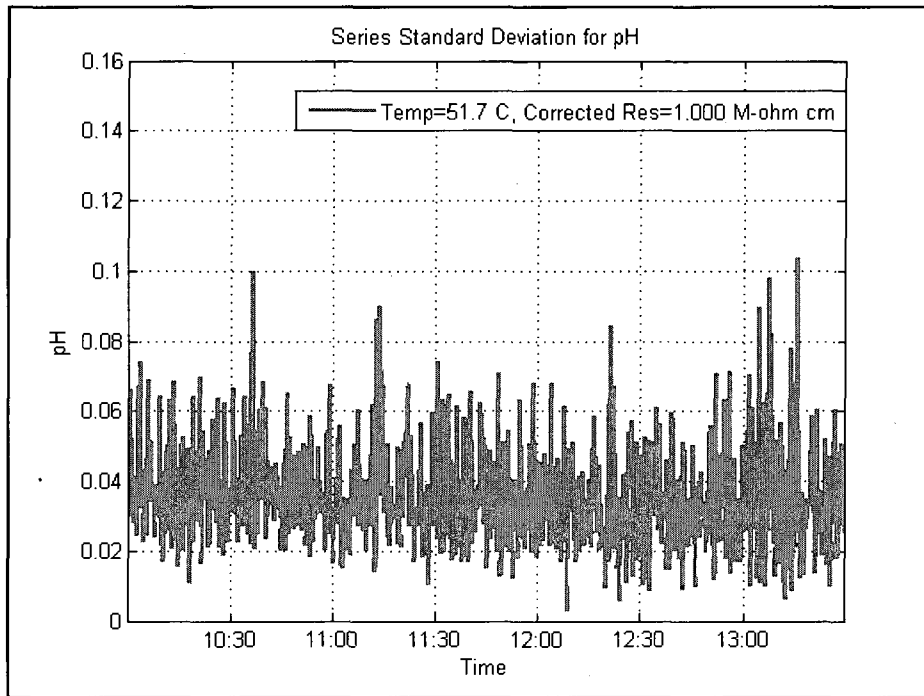


Figure 100. Time varying series standard deviation of pH

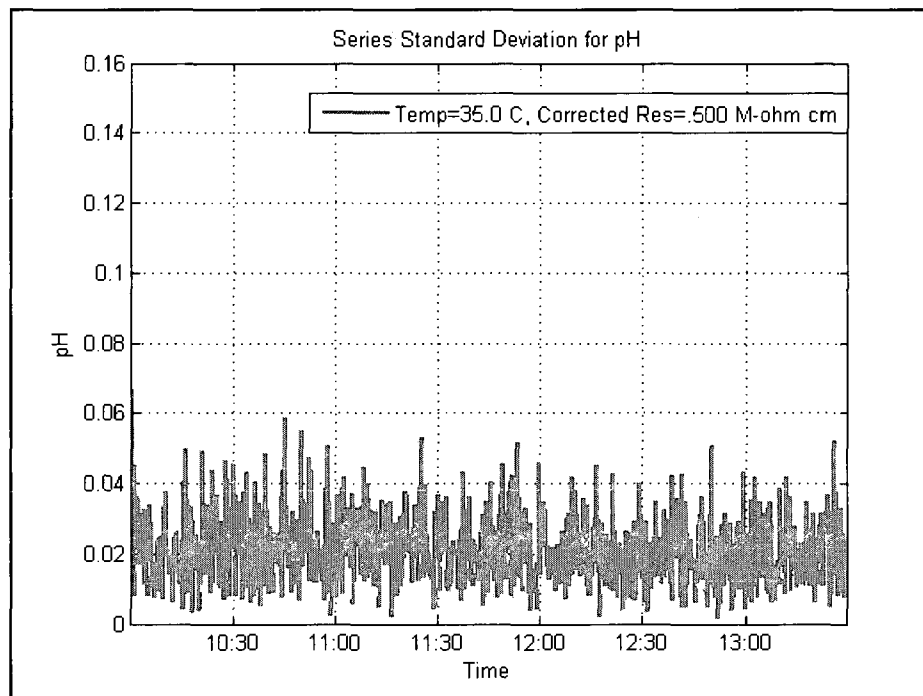


Figure 101. Time varying series standard deviation of pH

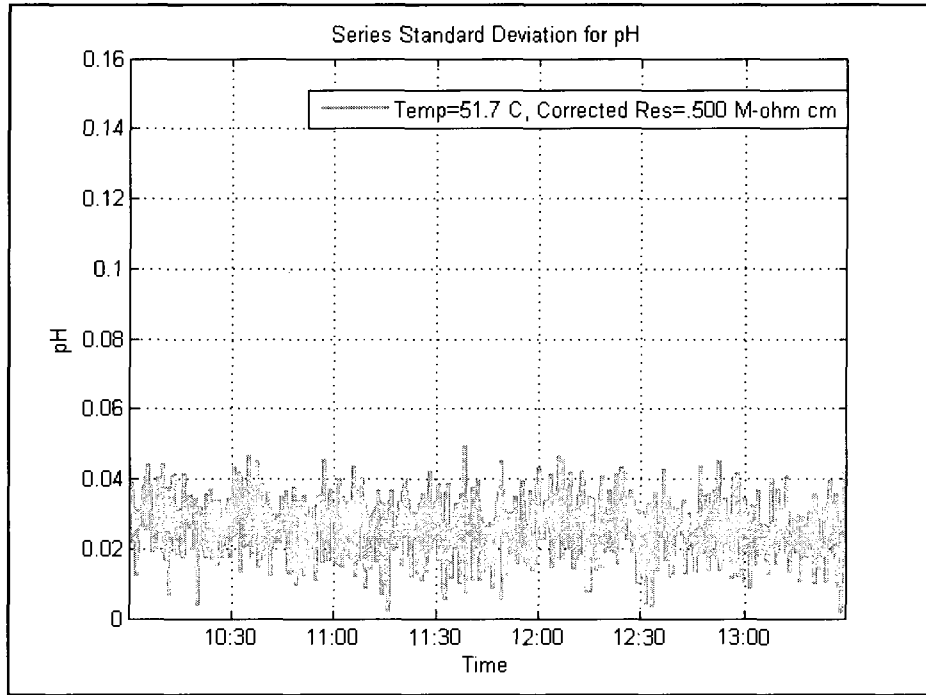


Figure 102. Time varying series standard deviation of pH

The data presented in the preceding four figures is summarized in Table 6

Temp and Corrected Resistivity Setting	Maximum of Series Standard Deviation	Time Averaged Mean of Series Average Absolute Resistivity
Temp=35.0 C Cor Res=1.000 (M-ohm cm)	.12	5.37
Temp=51.7 C Cor Res=1.000 (M-ohm cm)	.10	5.26
Temp=35.0 C Cor Res=.500 (M-ohm cm)	.07	5.13
Temp=51.7C Cor Res=.500 (M-ohm cm)	.05	4.96

Table 6. Maximum std deviation and time averaged mean values for pH

The data shown in Table 6 demonstrates an acceptable level of correlation between pH and the two controlled parameters, temperature and corrected resistivity. As was the case with the absolute resistivity, the pH is assumed to be fully described by fixing these inputs. Based upon this argument, any observed changes in current between tests of like temperature and corrected resistivity settings are assumed not to be caused by differences in pH. Similarly, for comparisons between tests of dissimilar setpoints, differences in pH are considered to be the result of differences in either (or both) of these controlled inputs and their effect on cell performance is not analyzed separately.

In addition to the preceding conclusions, the pH data collected for the test series demonstrate that the level selected for the cathodic potential setpoint is in fact valid. Comparison of the mean values listed in Table 6 to the plot of the Nernst potentials shown in Figure 67, demonstrate that the -500mV used for the cathode potential setpoint is more than thermodynamically sufficient for the cathodic reaction to proceed at either temperature setting.

CHAPTER 5

TEST RESULTS AND ANALYSIS

Test Results

The raw data for the test series described in the previous chapter are presented in the following figures. For clarity, data for each set of input parameters is expressed using three separate plots. The first figure shows the time varying anodic potential for the light and dark test days. The next figure shows the time varying currents (light and dark) for the West cell ($d=0.8\text{mm}$) for a specific set of input parameter setpoints. The final plot shows the same data for the East cell ($d=1.6\text{mm}$).

Test 1 was run with a flowrate of 300 ml/min, an inlet temperature of 35.0 °C, and a corrected resistivity of 1.000 M-ohm cm. The light and dark tests were conducted on 03-18-09 and 02-25-09 respectively. Figures 103-105 show the results for Test 1.

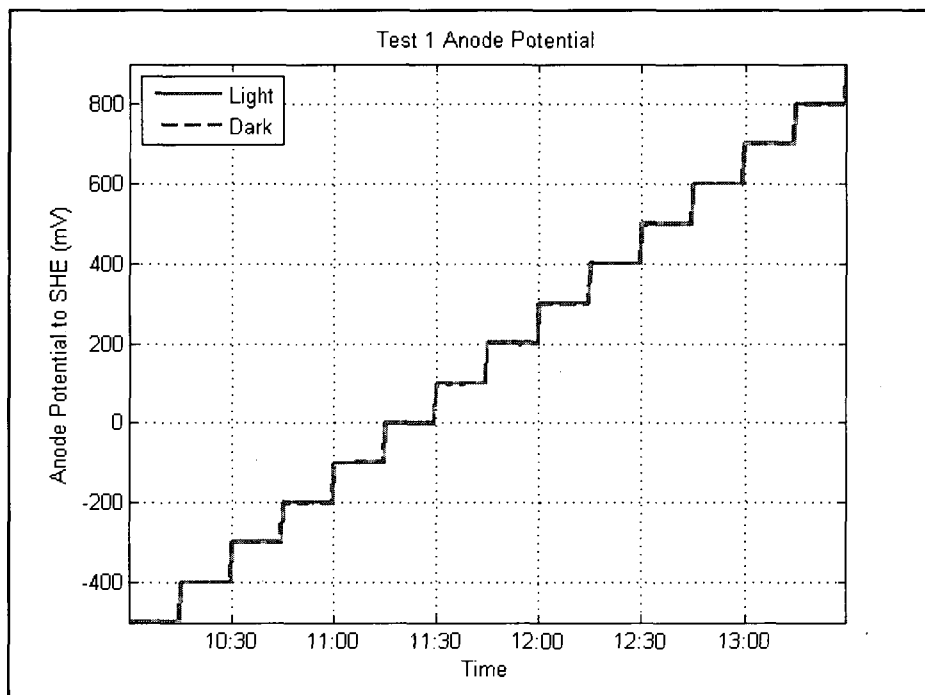


Figure 103. Test 1 anode potential

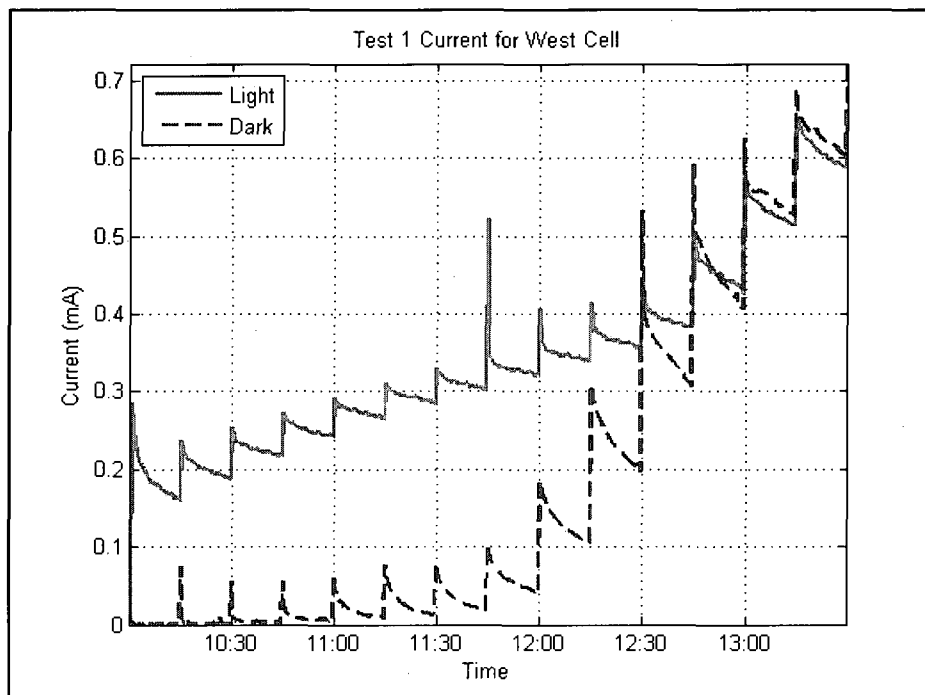


Figure 104. Test 1 currents for West cell (d=.8mm)

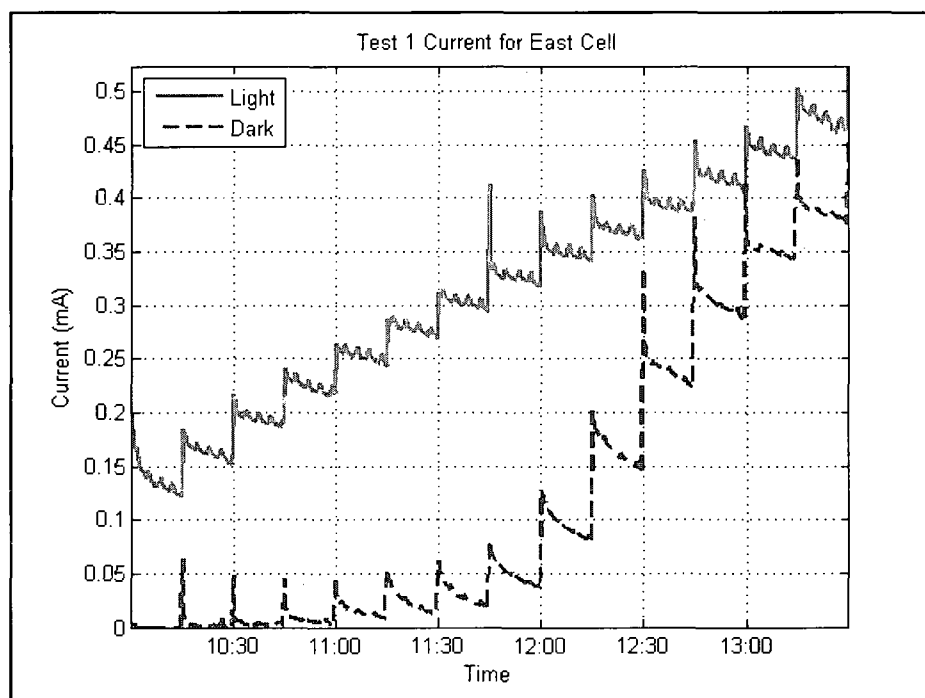


Figure 105. Test 1 currents for East cell (d=1.6mm)

Test 2 was run with a flowrate of 300 ml/min, an inlet temperature of 51.7 °C, and a corrected resistivity of 1.000 M-ohm cm. The light and dark tests were conducted on 03-16-09 and 02-26-09 respectively. Figures 106-108 show the results for Test 2.

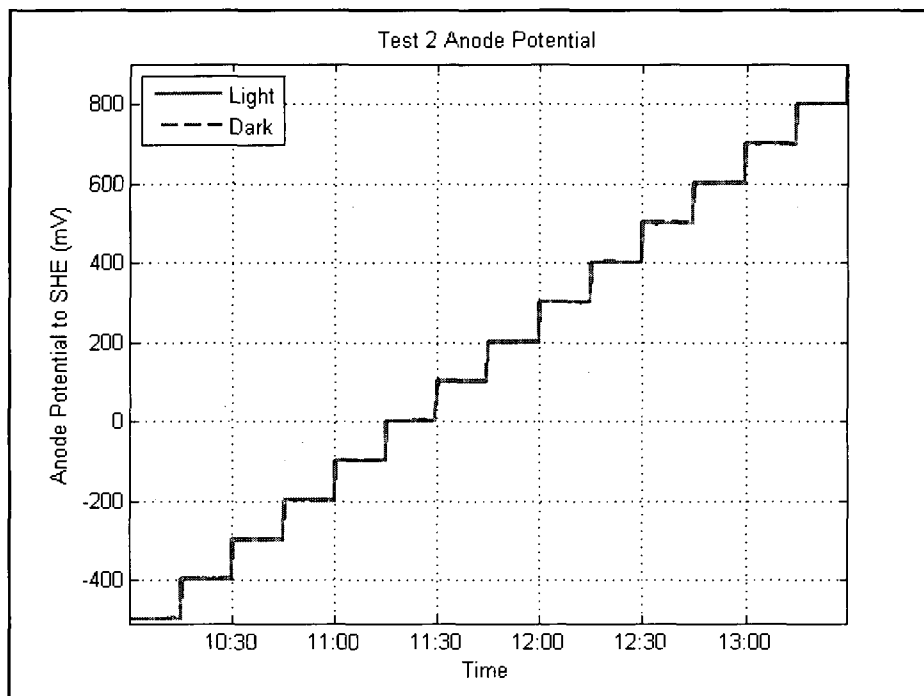


Figure 106. Test 2 anode potential

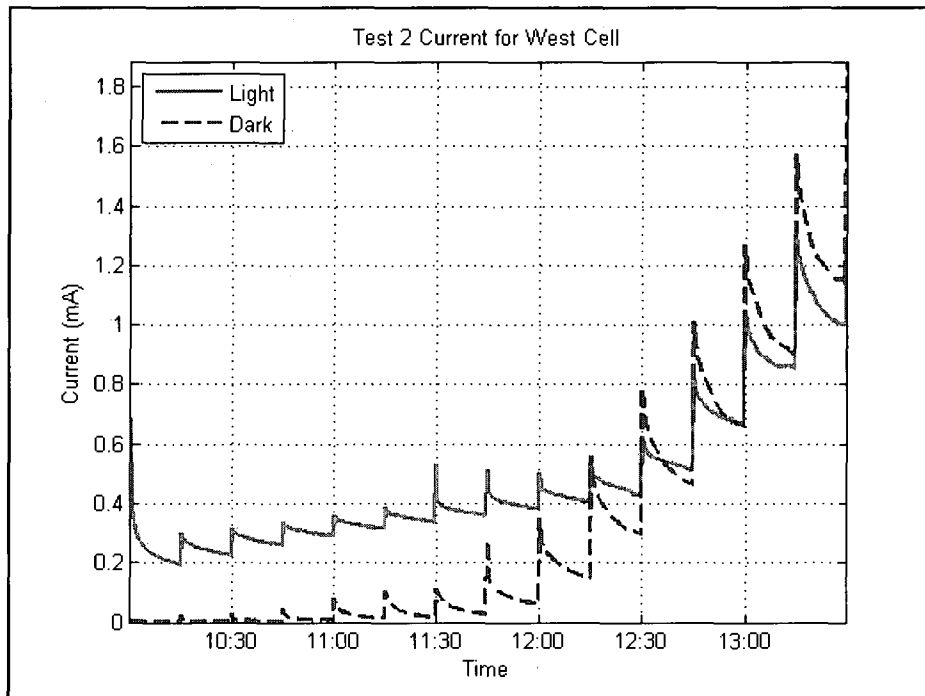


Figure 107. Test 2 currents for West cell (d=.8mm)

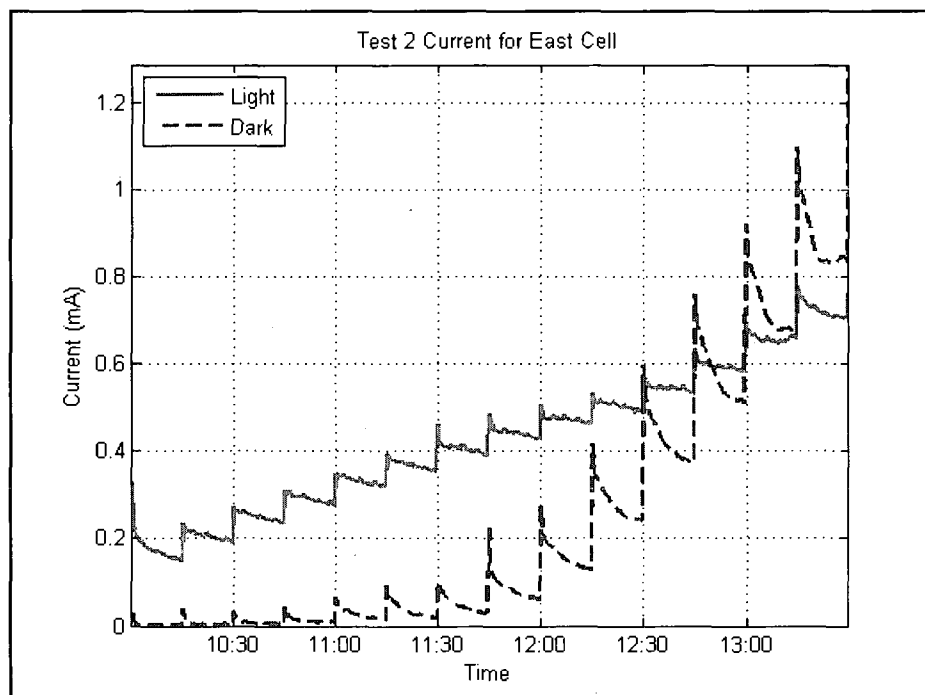


Figure 108. Test 2 currents for East cell (d=1.6mm)

Test 3 was run with a flowrate of 150 ml/min, an inlet temperature of 51.7 °C, and a corrected resistivity of 1.000 M-ohm cm. The light and dark tests were conducted on 03-15-09 and 02-27-09 respectively. Figures 109-111 show the results for Test 3.

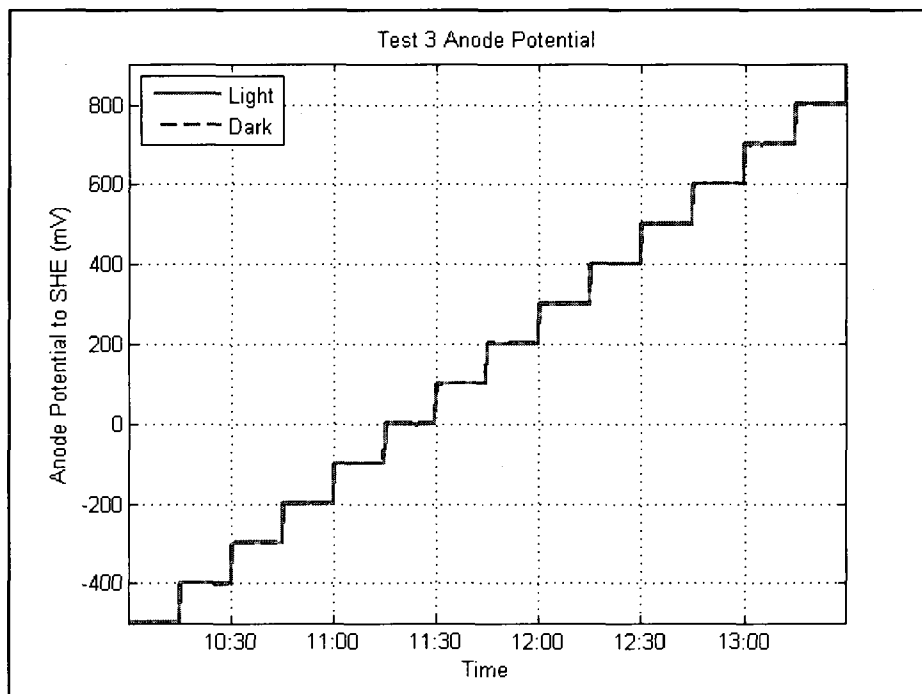


Figure 109. Test 3 anode potential

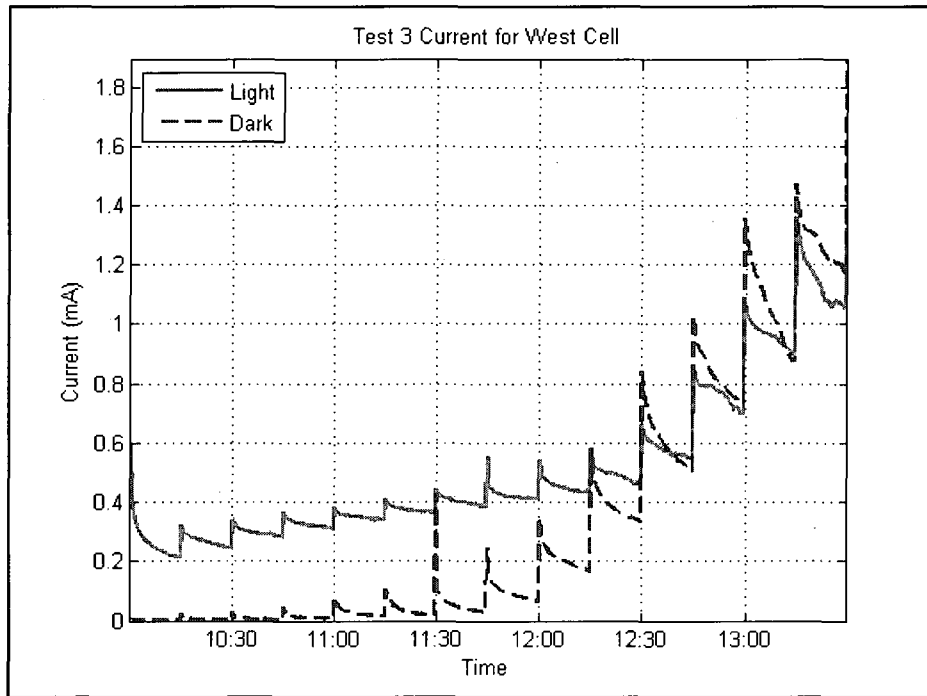


Figure 110. Test 3 currents for West cell ($d=0.8\text{mm}$)

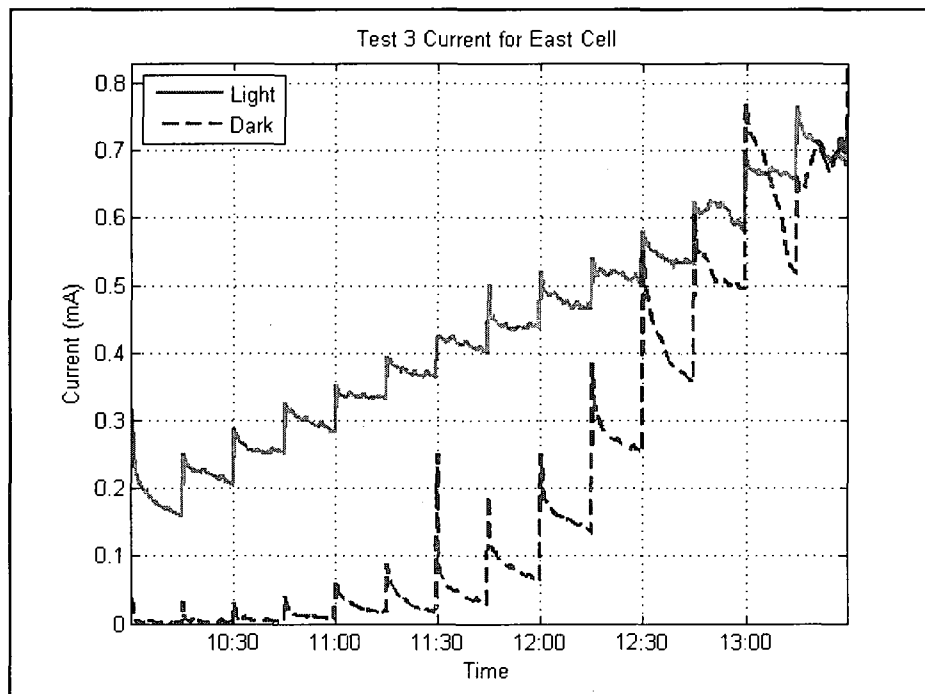


Figure 111. Test 3 currents for East cell ($d=1.6\text{mm}$)

Test 4 was run with a flowrate of 150 ml/min, an inlet temperature of 35.0 °C, and a corrected resistivity of 1.000 M-ohm cm. The light and dark tests were conducted on 03-20-09 and 02-28-09 respectively. Figures 112-114 show the results for Test 4.

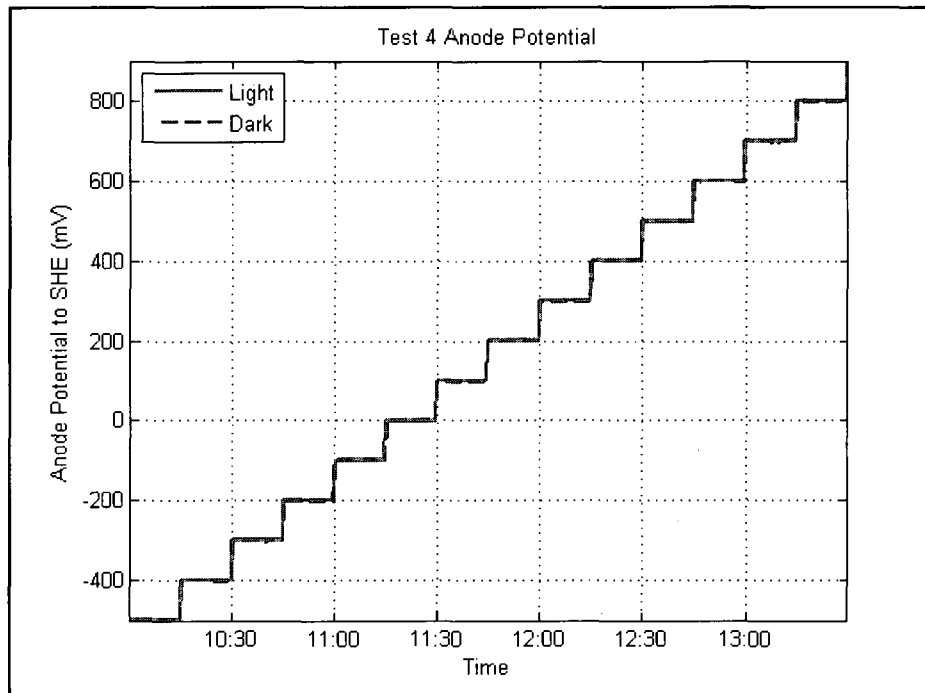


Figure 112. Test 4 anode potential

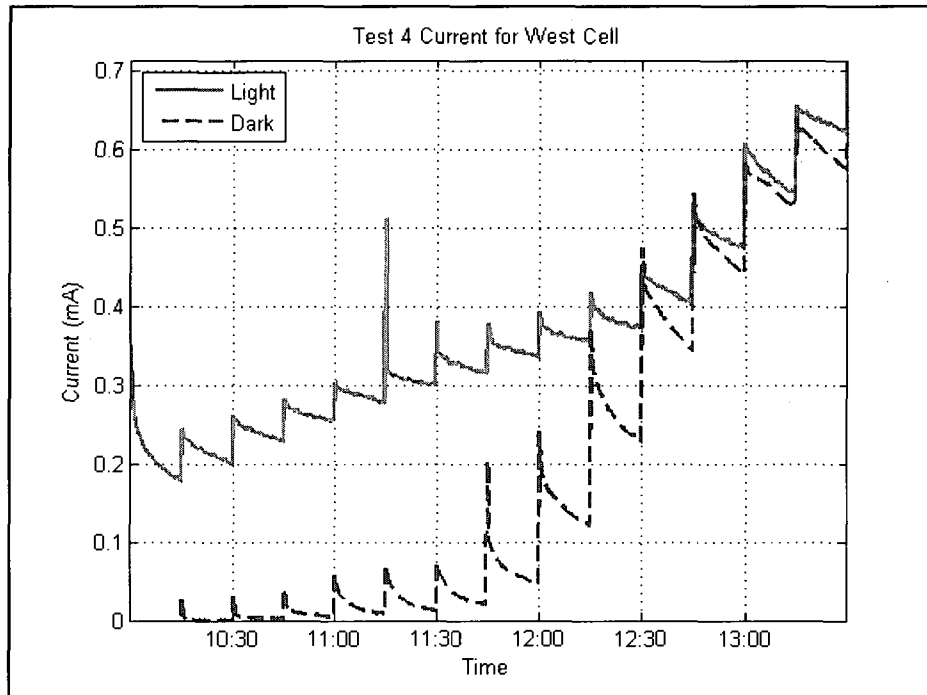


Figure 113. Test 4 currents for West cell ($d=0.8\text{mm}$)

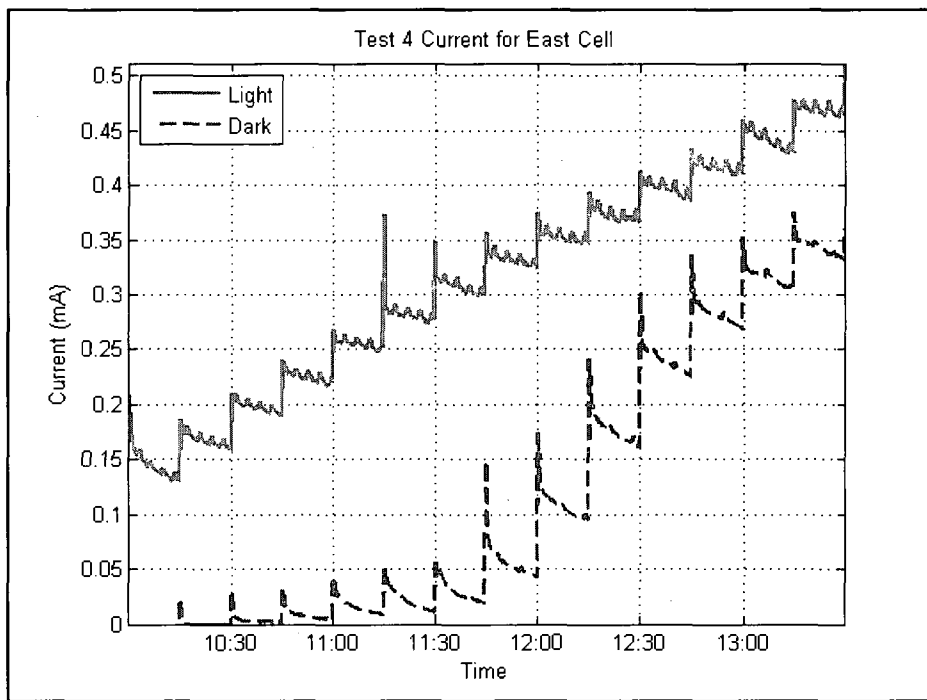


Figure 114. Test 4 currents for East cell ($d=1.6\text{mm}$)

Test 5 was run with a flowrate of 150 ml/min, an inlet temperature of 35.0 °C, and a corrected resistivity of .500 M-ohm cm. The light and dark tests were conducted on 03-10-09 and 03-02-09 respectively. Figures 115-117 show the results for Test 5.

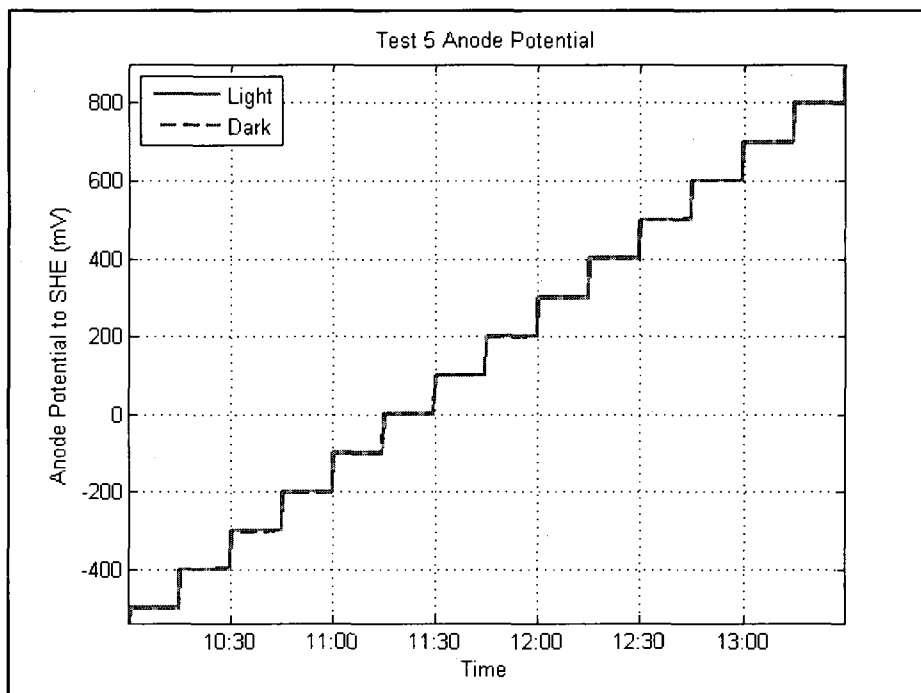


Figure 115. Test 5 anode potential

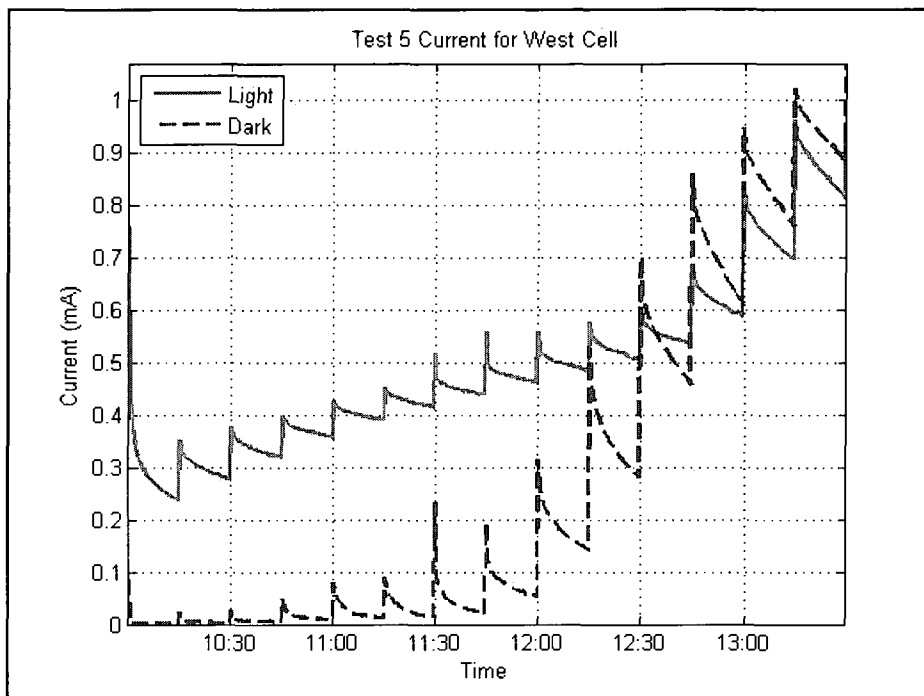


Figure 116. Test 5 currents for West cell (d=.8mm)

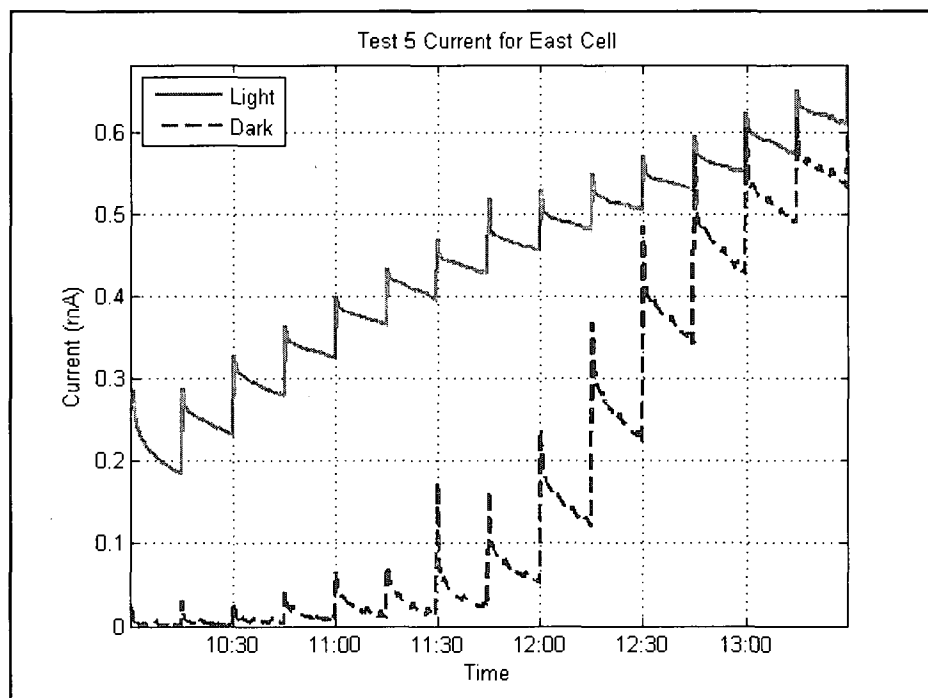


Figure 117. Test 5 currents for East cell (d=1.6mm)

Test 6 was run with a flowrate of 150 ml/min, an inlet temperature of 51.7 °C, and a corrected resistivity of .500 M-ohm cm. The light and dark tests were conducted on 03-08-09 and 03-03-09 respectively. Figures 118-120 show the results for Test 6.

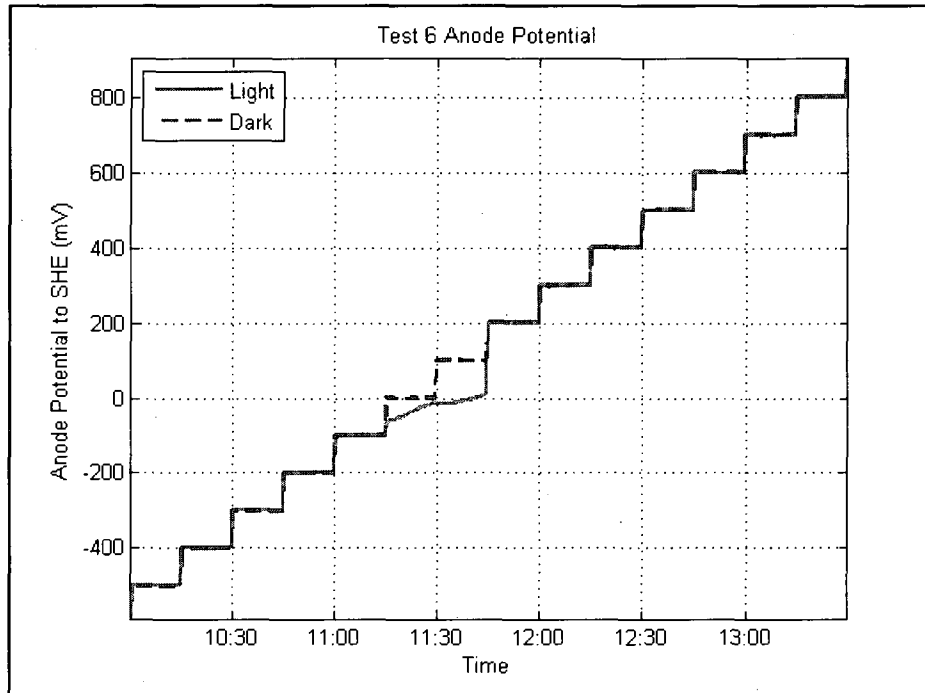


Figure 118. Test 6 anode potential

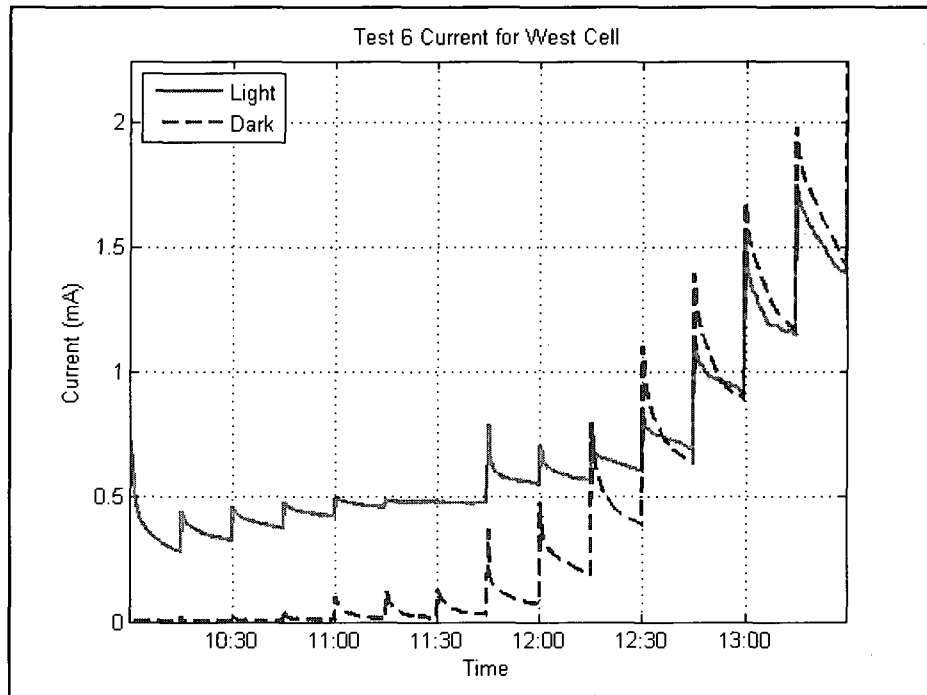


Figure 119. Test 6 currents for West cell (d=.8mm)

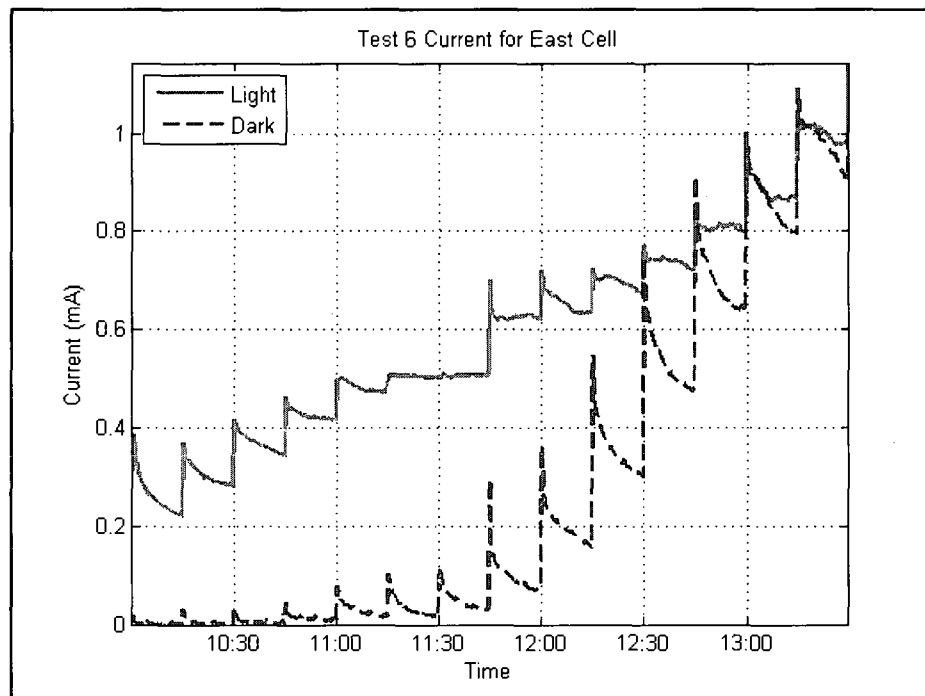


Figure 120. Test 6 currents for East cell (d=1.6mm)

Test 7 was run with a flowrate of 300 ml/min, an inlet temperature of 51.7 °C, and a corrected resistivity of .500 M-ohm cm. The light and dark tests were conducted on 03-07-09 and 03-04-09 respectively. Figures 121-123 show the results for Test 7.

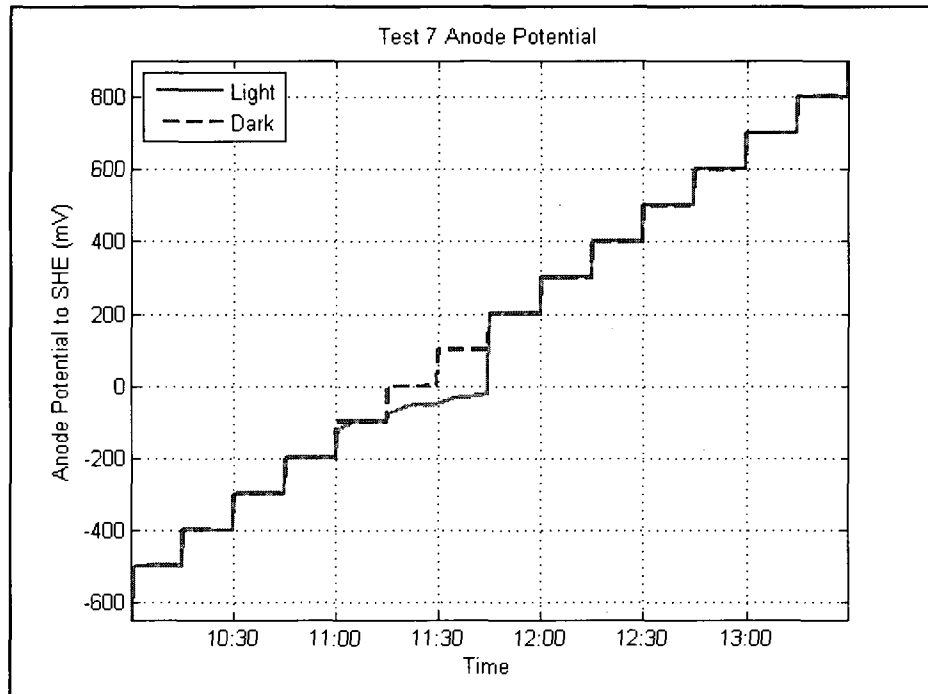


Figure 121. Test 7 anode potential

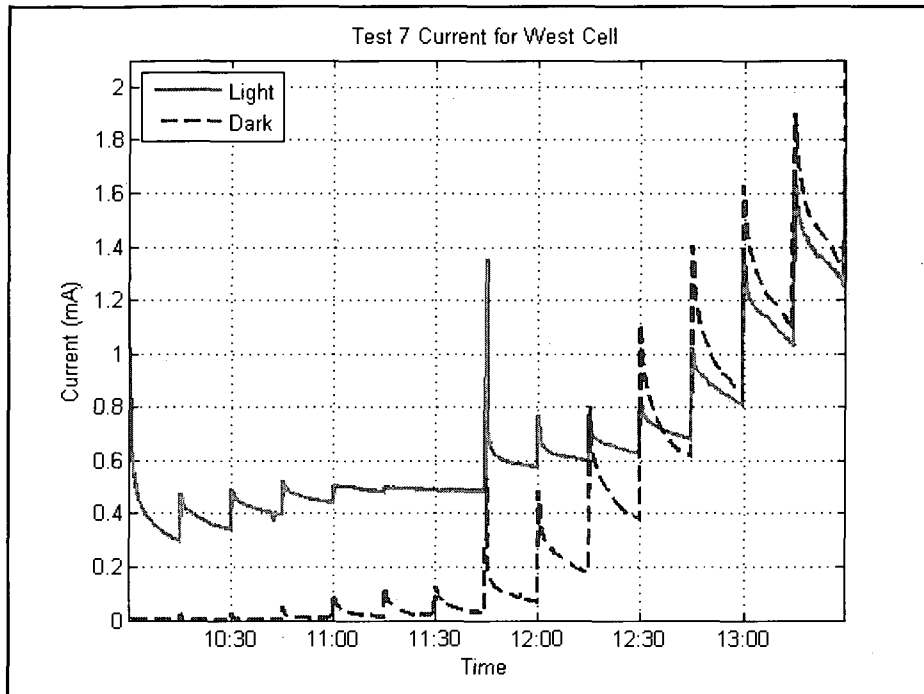


Figure 122. Test 7 currents for West cell (d=.8mm)

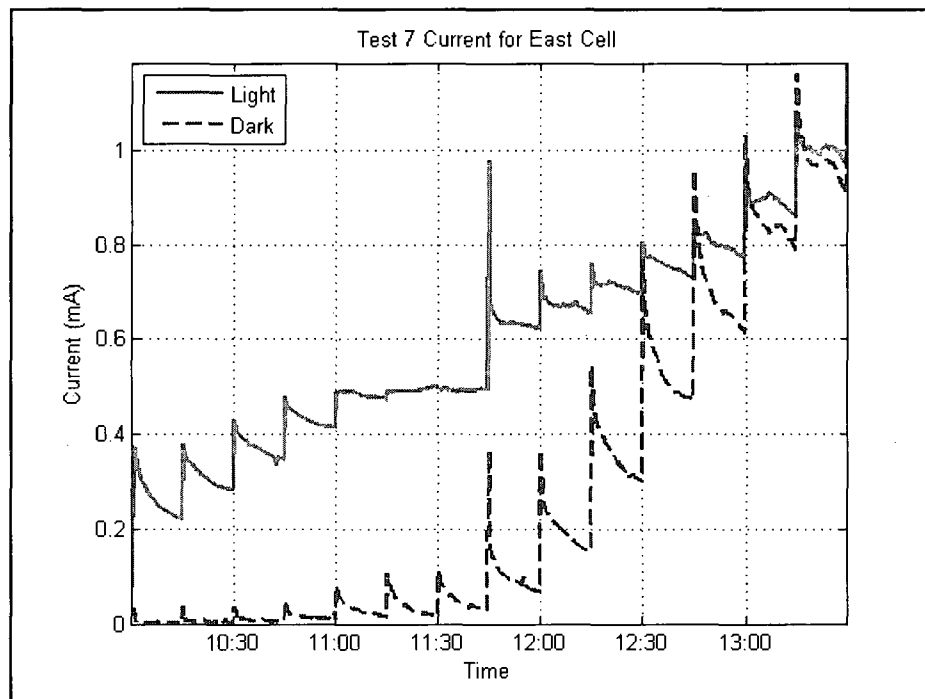


Figure 123. Test 7 currents for East cell (d=1.6mm)

Test 8 was run with a flowrate of 300 ml/min, an inlet temperature of 35.0 °C, and a corrected resistivity of .500 M-ohm cm. The light and dark tests were conducted on 03-05-09 and 03-06-09 respectively. Figures 124-126 show the results for Test 8.

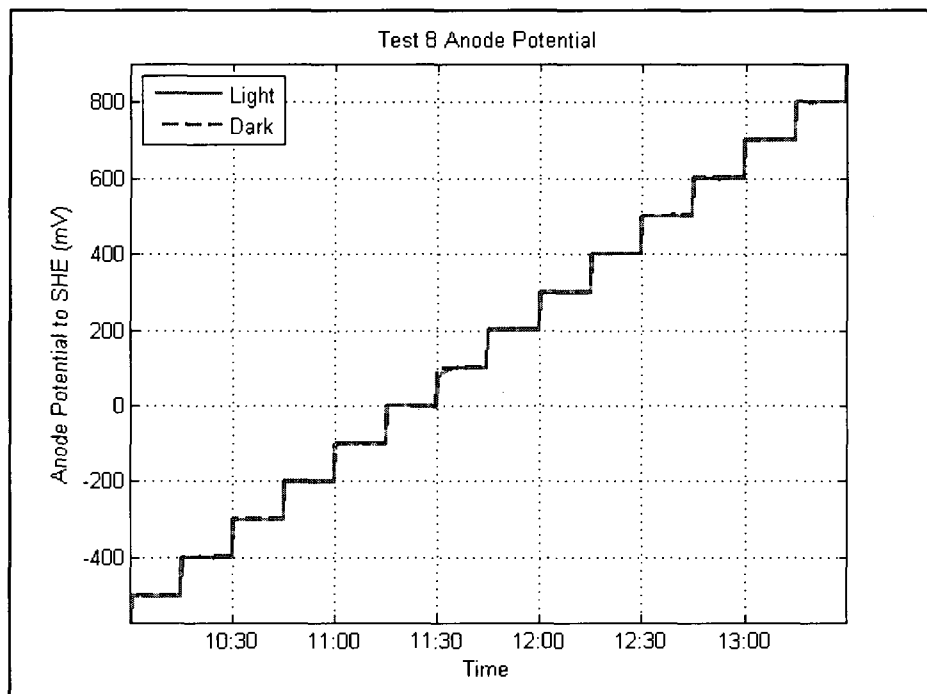


Figure 124. Test 8 anode potential

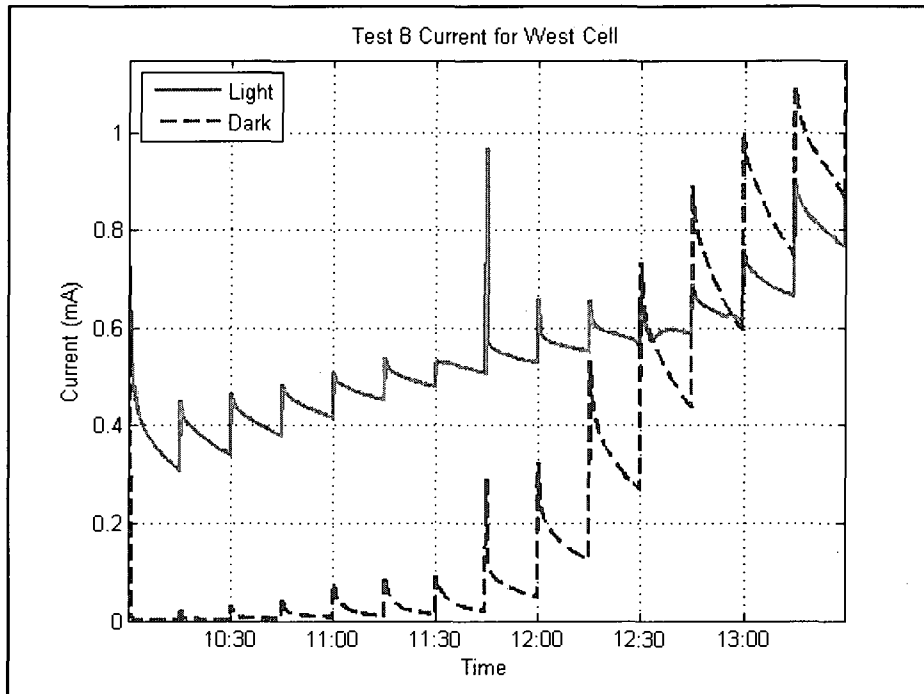


Figure 125. Test 8 currents for West cell (d=.8mm)

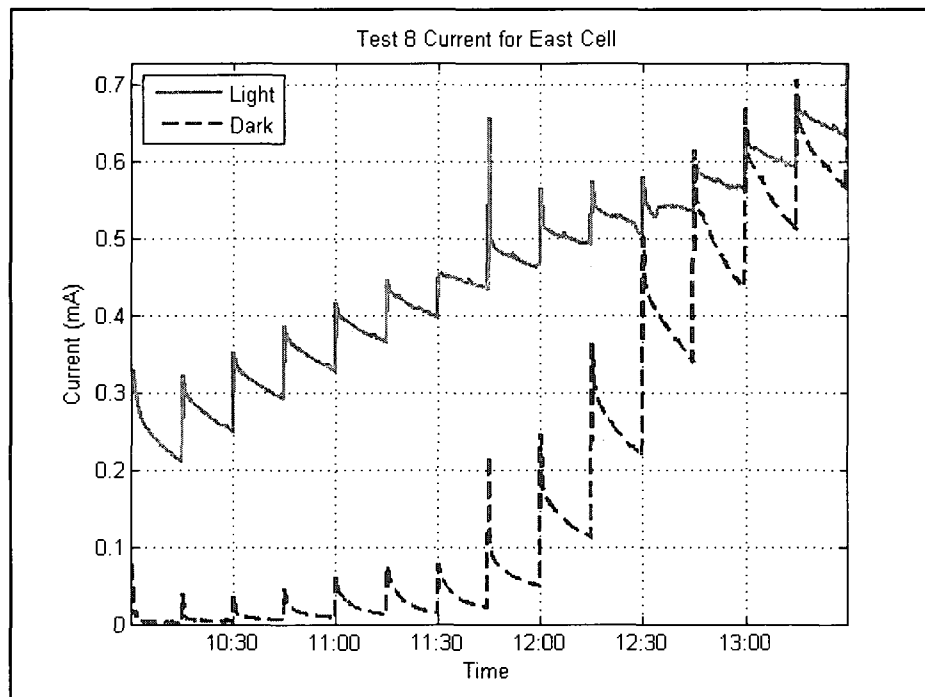


Figure 126. Test 8 currents for East cell (d=1.6mm)

The data for the series shows that both cells produce a small but measurable photocurrent at all of the parametric setpoint combinations tested. Additionally, the plots of the anode potential demonstrate that the light and dark sweeps were essentially identical with the exception of illuminated tests 6 and 7. The data for these two experiments demonstrate an anomaly which was encountered on illuminated tests using this combination of temperature and resistivity. Instead of the well defined steps shown for the other tests, the potential seems to hang between 11:15 and 11:45, rising to its correct value at the 11:45 sweep increment. These experiments were run twice on non-consecutive test days with the same effect occurring at the same sweep increments. Additionally, the measurements were checked against a separate voltmeter with these measurements agreeing well with the values being recorded with the datalogger. Based upon this, it is believed that the measurement itself is correct and that the deviation from the programmed sweep increments is caused by the anode creating its own potential at these parameter settings. This potential is superimposed on top of the potential of the power supply causing the observed effect. The causes of this additional anodic potential at these settings are beyond the scope of this report and since the anomaly is in fact a real effect inherent to these parametric settings, its effect on the measured current (which based upon the trends for other tests is expected to be small) is included in the analysis.

Analysis

Quantifying Test Results

The photocurrent produced for each set of input parameters is calculated by taking the difference of the light and dark currents for each cell. To remove the transient spikes occurring at the voltage sweep increment points, the data was processed with a filtering algorithm after the difference was calculated from the raw data presented in the previous section. Figures 127-134 show the time varying photocurrent for each of the 8 tests.

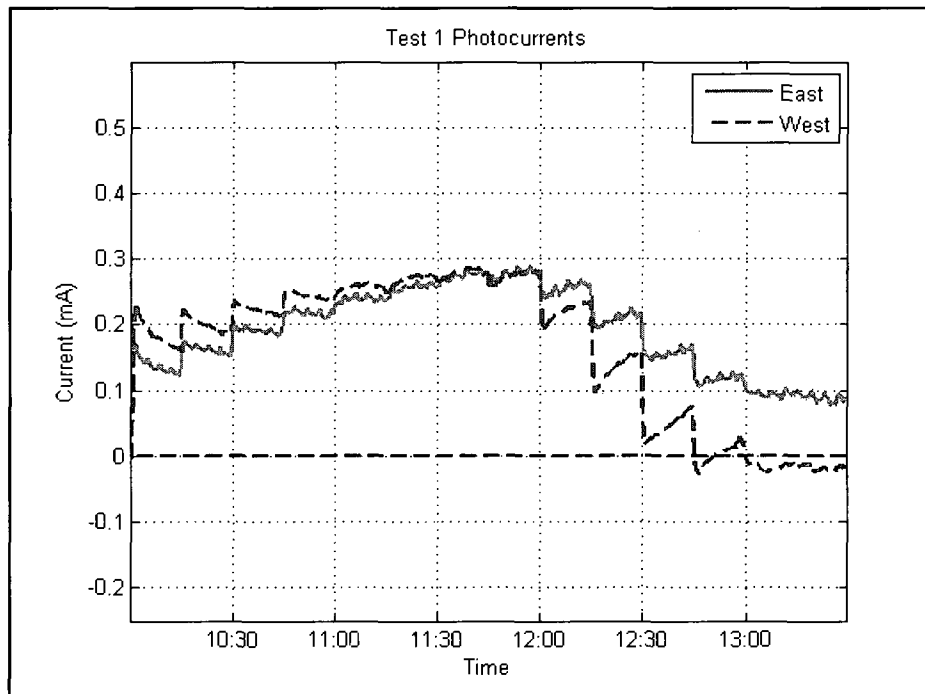


Figure 127. Photocurrent for Test 1

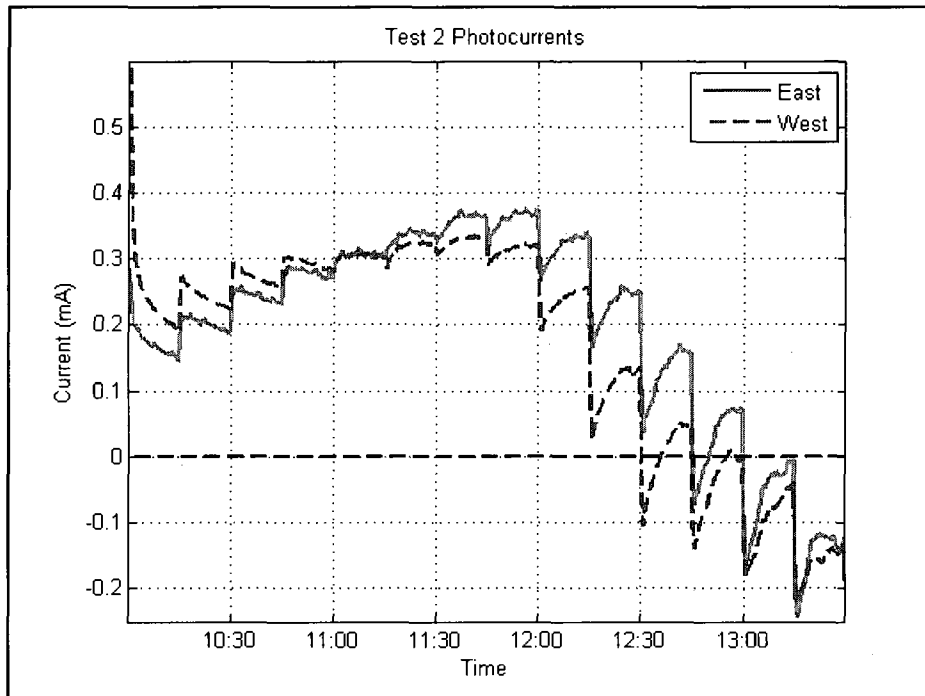


Figure 128. Photocurrent for Test 2

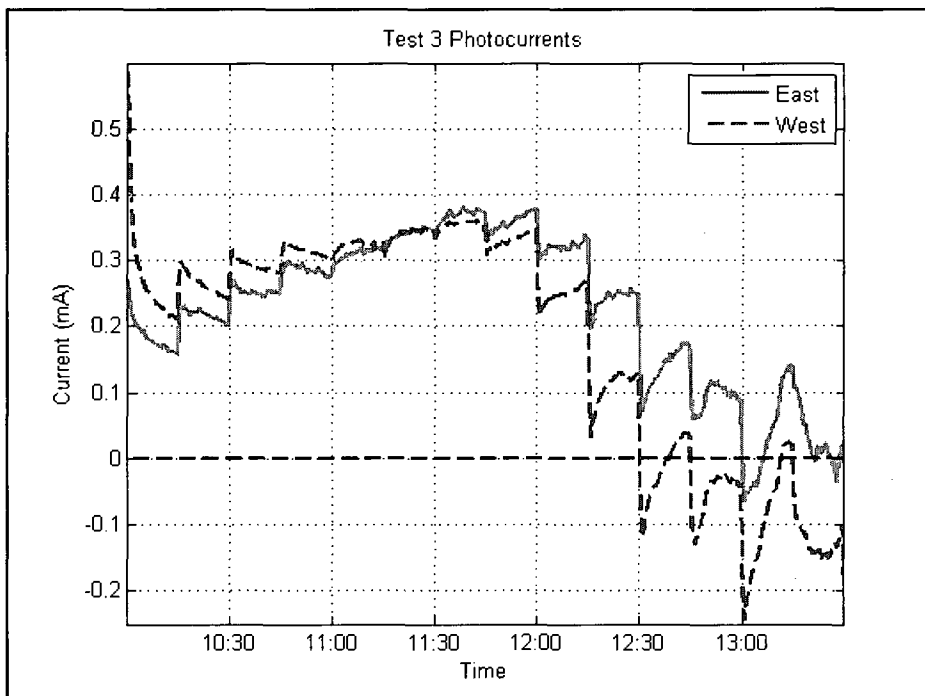


Figure 129. Photocurrent for Test 3

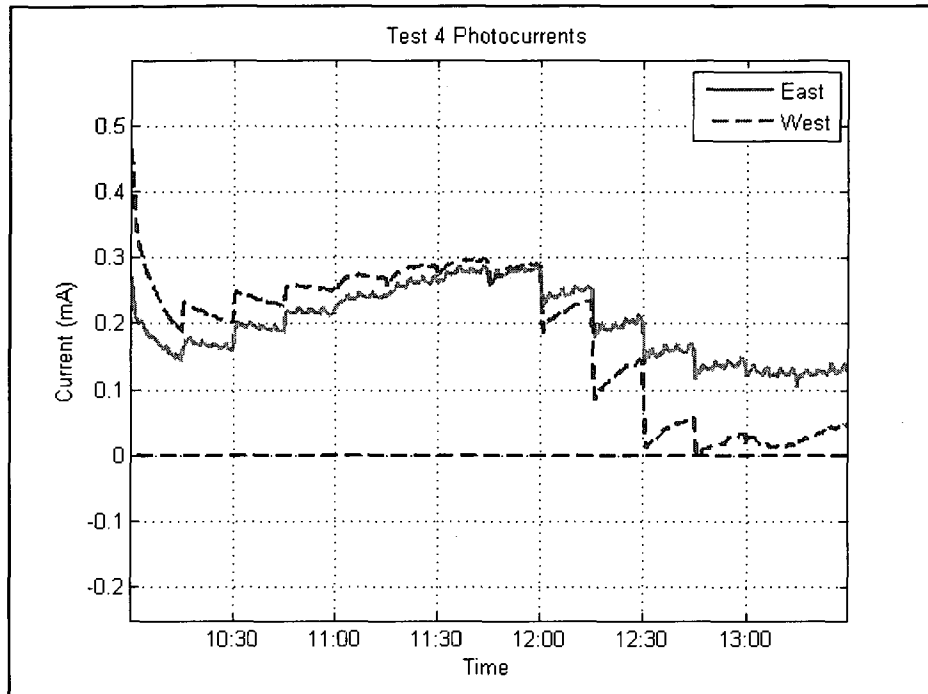


Figure 130. Photocurrent for Test 4

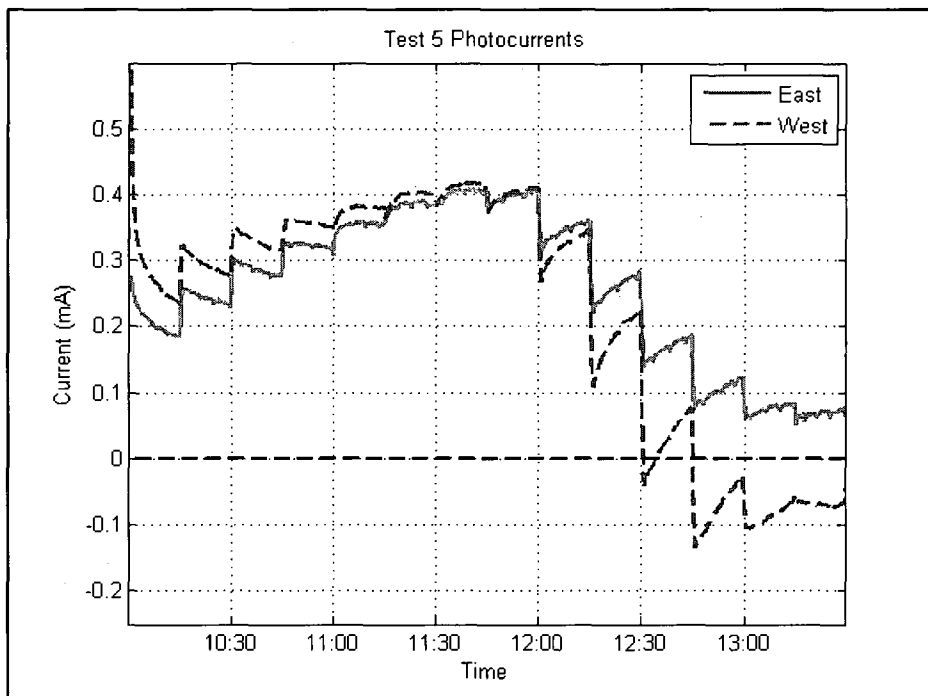


Figure 131. Photocurrent for Test 5

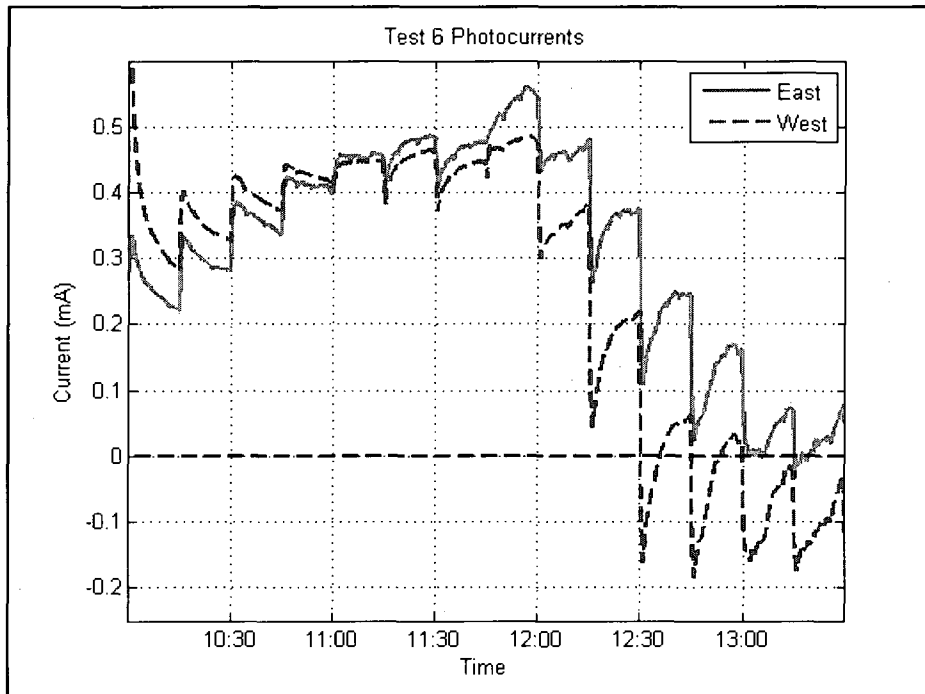


Figure 132. Photocurrent for Test 6

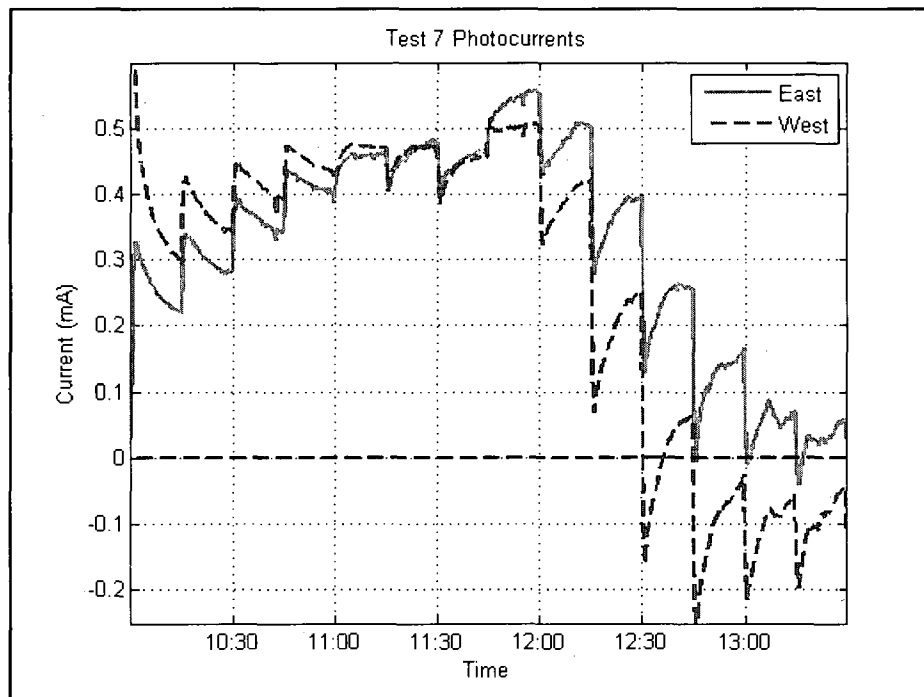


Figure 133. Photocurrent for Test 7

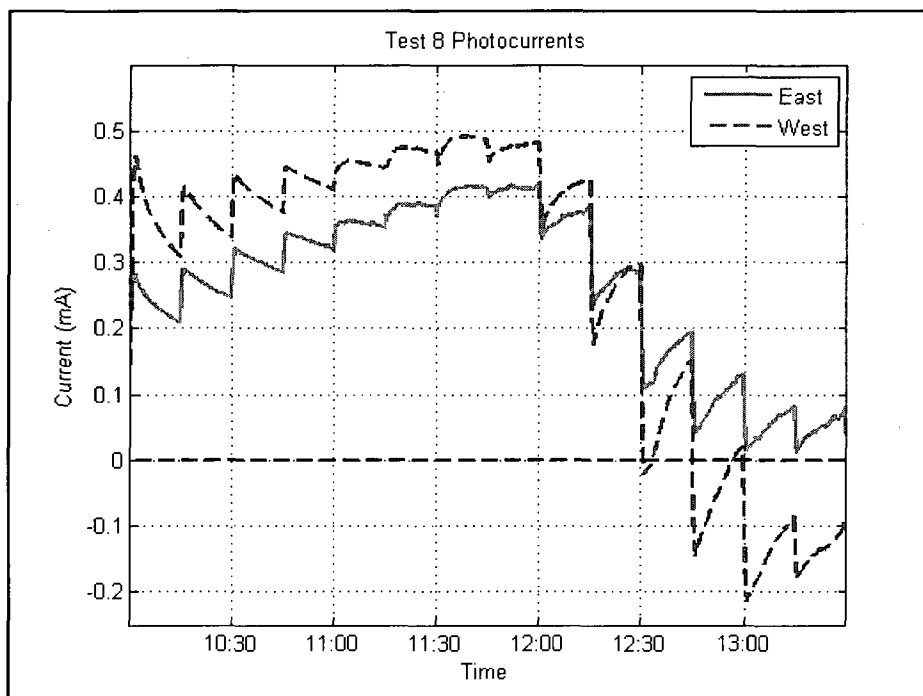


Figure 134. Photocurrent for Test 8

As an overall measure of the effectiveness of a given set of parametric inputs, the positive values of the photocurrents presented in figures 127-134 are integrated over the duration of the experiment (10:00AM-1:30PM). Negative values or instances where the dark current was larger than the illuminated value are not considered. This integration gives the total positive photo induced charge moved through the cell during the test in millicoulombs and is directly proportional to the total amount of hydrogen produced for a given set of inputs. It is this integrated value which will be used to gauge the impact of parametric changes on cell performance. Table 7 summarizes the values calculated for the positive photo charge transfer (PPCT) as well as the total light and dark values for each test.

Test #	Light (millicoulomb)	Dark (millicoulomb)	PPCT (millicoulomb)
1	West=4305 East=3903	West=2270 East=1517	West=2084 East=2386
2	West=5991 East=5381	West=3909 East=2951	West=2393 East=2650
3	West=6405 East=5445	West=4146 East=2622	West=2547 East=2842
4	West=4561 East=3931	West=2287 East=1417	West=2275 East=2514
5	West=6175 East=5485	West=3372 East=2260	West=3025 East=3225
6	West=8364 East=7437	West=5158 East=3478	West=3475 East=3964
7	West=8231 East=7495	West=4893 East=3479	West=3671 East=4026
8	West=6780 East=5656	West=3356 East=2357	West=3742 East=3300

Table 7. Total charge transfer for light and dark tests and PPCT

The uncertainty for the integrated values shown in the preceding figure can be estimated based upon the uncertainty in the two current measurement used calculate them. For the range being measured, this is estimated to be .004 mA for both the light and dark tests based upon the analysis presented in Appendix C. Based upon this, the uncertainty in the integrated values is calculated to be ± 3 millicoulombs.

Effects of Single Parameter Variations

To quantify the effects of changes to each input parameter, the change in the positive photo charge transfer between tests with 3 of the 4 inputs at the same level are plotted as a function of the fourth input. As an example, a comparison of the West cell for tests 1 and 4 gives the effect of flowrate on a cell with constant electrode spacing, temperature and resistivity. Similarly, comparison of the East and West cells for test 1 gives the effect

of electrode spacing on a cell with constant temperature, flowrate, and resistivity. Figure 135 shows the variation of the PPCT between tests where only the flow is changed.

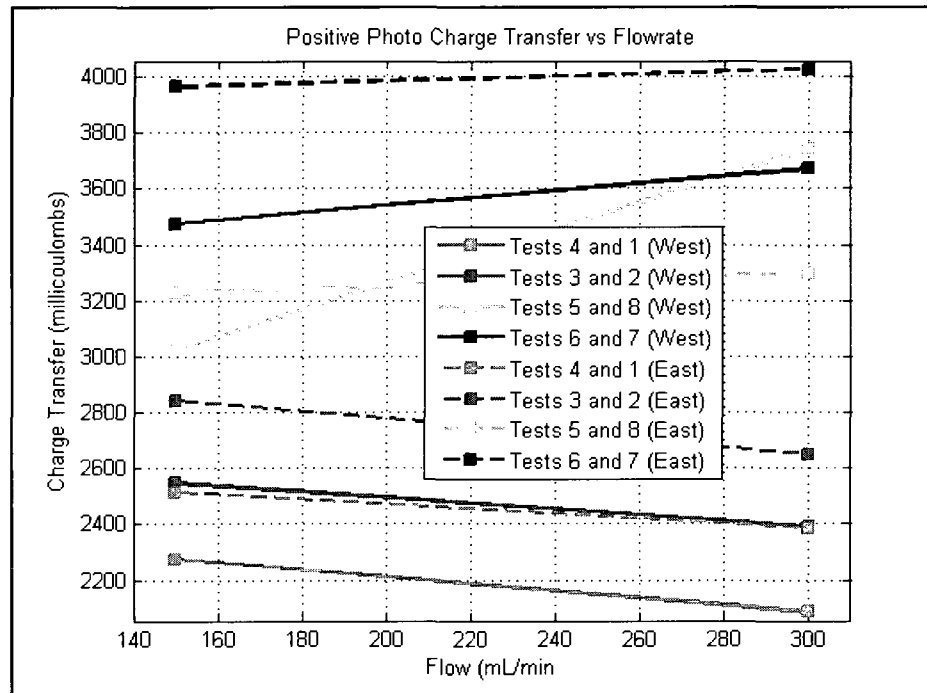


Figure 135. Variation of PPCT between tests where only flow is changed

The figure shows that with the exception of the West cell between tests 5 and 8, there is very little change in the PPCT with flow rate. Additionally, the data demonstrates a slightly positive slope for all tests conducted at the higher resistivity setting and a slightly negative slope for those conducted at the lower setpoint. This grouping of the data suggests a combined effect (albeit a relatively weak one) between these two input parameters. The comparison between tests 5 and 8 for the West cell follows the same general trend as the rest of the data taken at the lower resistivity setpoint but the slope is much more pronounced. The fact that the charge transfer for the west cell during Test 8 is so much higher than the trend of the other curves suggest that it should be implies that

this configuration should most likely be retested to double check this result. The results shown in figure 141 are summarized in Table 8.

Tests	Change in PPCT (millicoulombs)	Change in PPCT %
4-1 West	-191	-8
3-2 West	-154	-6
5-8 West	717	24
6-7 West	196	6
4-1 East	-128	-5
3-2 East	-193	-7
5-8 East	75	2
6-7 East	63	2
Average	48	1

Table 8. Changes in PPCT due to flow

As was done with the flow rate, a similar comparison is performed for the cell inlet temperature. Figure 136 shows the variation of the positive photo charge transfer between tests where only the temperature is varied.

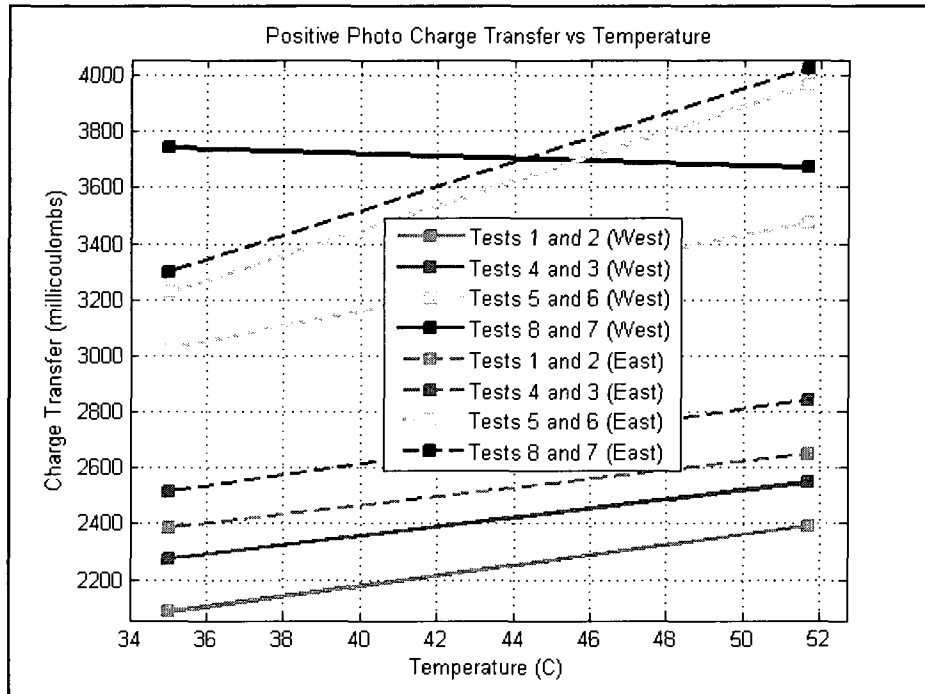


Figure 136. Variation of PPCT between tests where only temp is changed

Again, with the exception of Test 8 for the West cell, the data trends are quite consistent. With the aforementioned exception, all of the curves show decidedly positive slope for this parameter change. It is worthwhile to emphasize here that, while it is intuitive that both of the cell currents (light and dark) should increase with temperature due to the lower absolute resistivity and the reduction of the Gibbs energy, the results presented here are based upon a difference between the light and dark tests. This being the case, the results presented in Figure 136 indicate that the impact of the increase in temperature is different for the light and dark runs. The reasons for this are less intuitive and beyond the scope of this report, but the data suggests this to be the case. The results shown in figure 136 are summarized in Table 9.

Tests	Change in PPCT (millicoulombs)	Change in PPCT %
1-2 West	309	15
4-3 West	273	12
5-6 West	450	15
8-7 West	-72	-2
1-2 East	264	11
4-3 East	328	13
5-6 East	739	23
8-7 East	727	22
Average	377	14

Table 9. Changes in PPCT due to temperature

As with the previous two inputs, a similar analysis can be performed with respect to the temperature corrected resistivity. Figure 143 shows the variation of the PPCT between tests where only this parameter is varied.

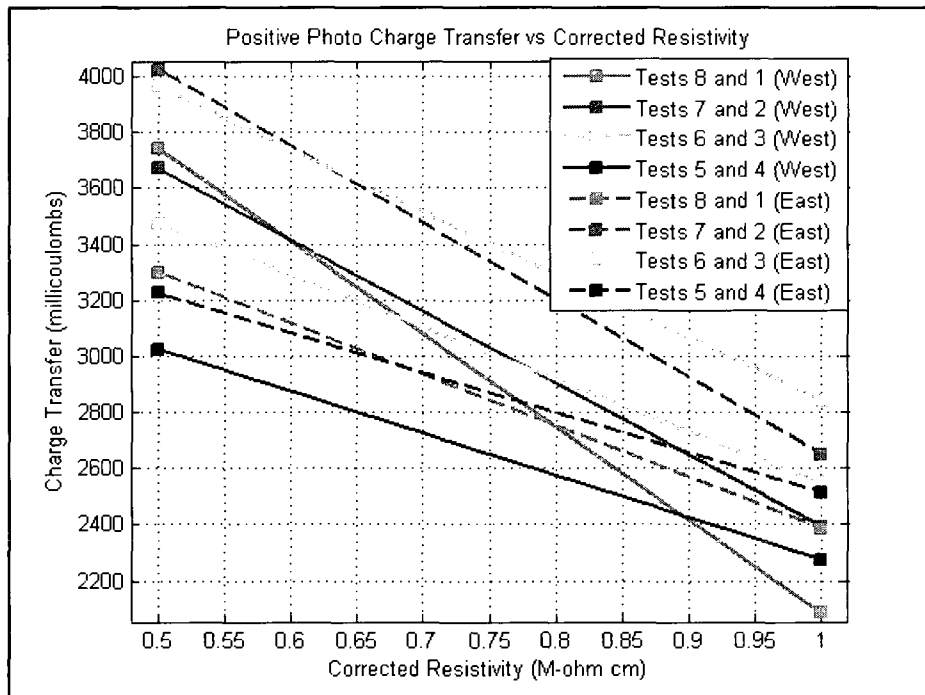


Figure 137. Variation of PPCT between tests where only corrected res is changed

The data demonstrate a strong negative trend to changes in this parameter for all test combinations. Again, it is expected that both light and dark currents will vary inversely with the resistivity, but as was the case with temperature, the data shows that the effect is not the same for both. The results shown in Figure 143 are summarized in Table 10.

Tests	Change in PPCT (millicoulombs)	Change in PPCT %
8-1 West	-1659	-44
7-2 West	-1278	-35
6-3 West	-927	-27
5-4 West	-750	-25
8-1 East	-914	-28
7-2 East	-1377	-34
6-3 East	-1121	-28
5-4 East	-711	-22
Average	-1092	-30

Table 10. Changes in PPCT due to corrected resistivity

The same type of analysis as in the previous 3 cases can be applied to the fourth and final input, electrode spacing. It is worthwhile to mention at this point that this comparison is slightly different in nature than the other three previously mentioned cases. Instead of being a comparison of the same cell for tests on different days this is a comparison between different cells of different electrode spacing for tests conducted on the same day. The end result is the same but the process is slightly different. Figure 144 shows the variation of the PPCT between tests where only the electrode spacing is varied.

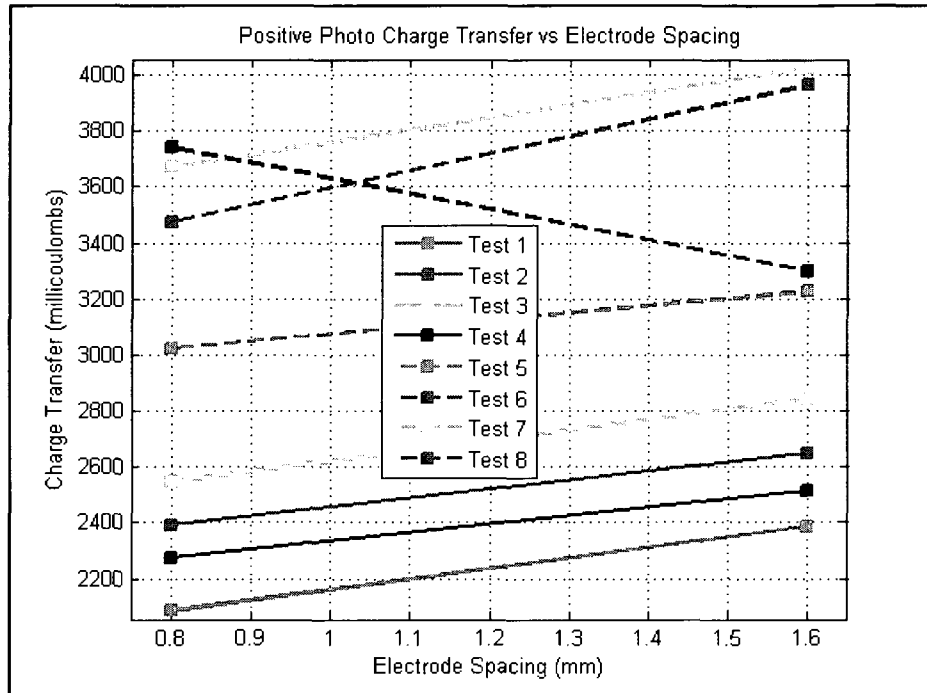


Figure 138. Variation of PPCT between tests where only spacing is changed

Again, with the exception of the one suspect test, the data is quite uniform, showing a consistent positive slope for all combinations. An important point which should be considered when comparing tests between cells of dissimilar electrode spacing is that for this series, the effect of changes to this variable is twofold. First, reducing the electrode spacing will reduce the overall ohmic resistance of the cell which is the main reason that this parameter is being studied. In addition to this main effect, however, a reduction of this spacing will also result in a higher average electrolyte velocity through the cell for a given flowrate. This higher average velocity results in a lower residence time for the ions involved in the reaction and will tend to reduce the current. It is speculated that this effect is dominant over the reduction in cell resistances caused by the reduced spacing, and is believed to be the cause of the preference for the large electrode spacing ($d=1.6\text{mm}$)

shown in Figure 138. Table 11 provides estimates of the residence times for each of the four combinations of flowrate and spacing tested.

Flow (mL/min)	d=1.6mm	d=.8mm
300	19.2	9.6s
150	38.4s	19.2s

Table 11. Estimated residence times for four cases tested

Future tests could be conducted such that the volumetric flowrates are scaled in such a way that the average velocities through the cells (and thus the residence times) would not vary with the electrode spacing. Implementation of this was considered for this test series but since this is one of the first series and knowledge of the actual velocity profiles within the cells are yet unknown, it was deemed too complicated an endeavor at this stage. For this study, the aforementioned effects of changes to the electrode spacing are taken as a whole and no effort is made to distinguish between the two. The results shown in Figure 144 are summarized in Table 12.

Tests	Change in PPCT (millicoulombs)	Change in PPCT %
1 West-East	302	15
2 West-East	257	11
3 West-East	295	12
4 West-East	239	11
5 West-East	200	7
6 West-East	489	14
7 West-East	356	10
8 West-East	-442	-12
Average	212	8

Table 12. Changes in PPCT due to electrode spacing

To quantify the effects of the single parameter changes shown in Figures 135-138, the average change in the PPCT is calculated for the 8 comparisons shown in each figure. This average is used as the final measure of the effectiveness of variations to the individual inputs.

To verify that the final results were not skewed by the possible bad data point caused by Test 8 for the West cell, these average values were calculated once for the complete data set and then again with the comparisons to the suspect test omitted. Very little difference was observed in the results and all subsequent results presented here are based upon the complete test series. Figures 139 and 140 show the average change in the PPCT for the four inputs tested.

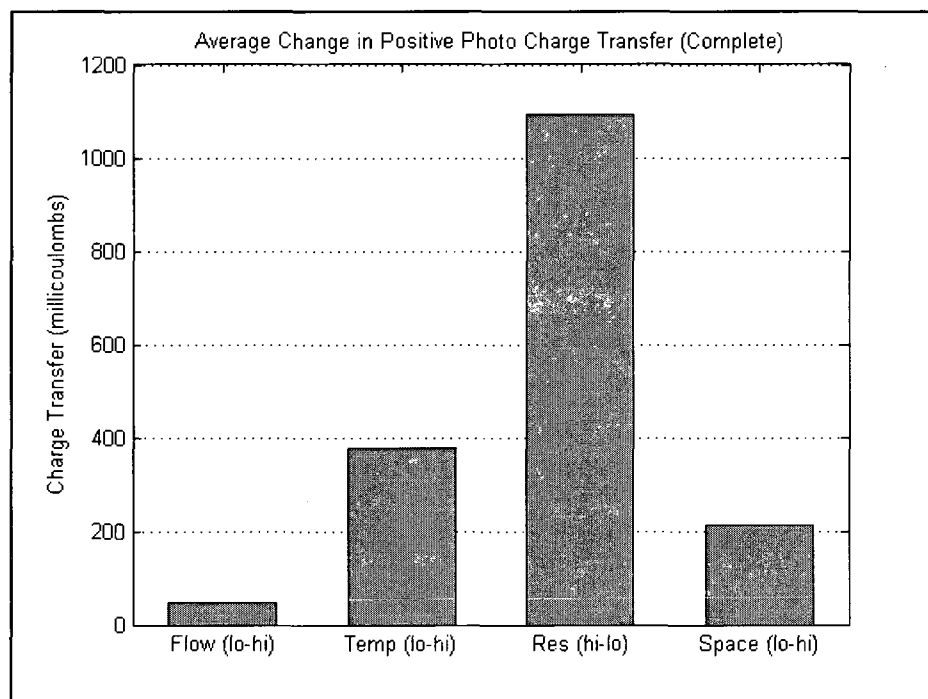


Figure 139. Average change in PPCT (mC) due to variations of the four inputs

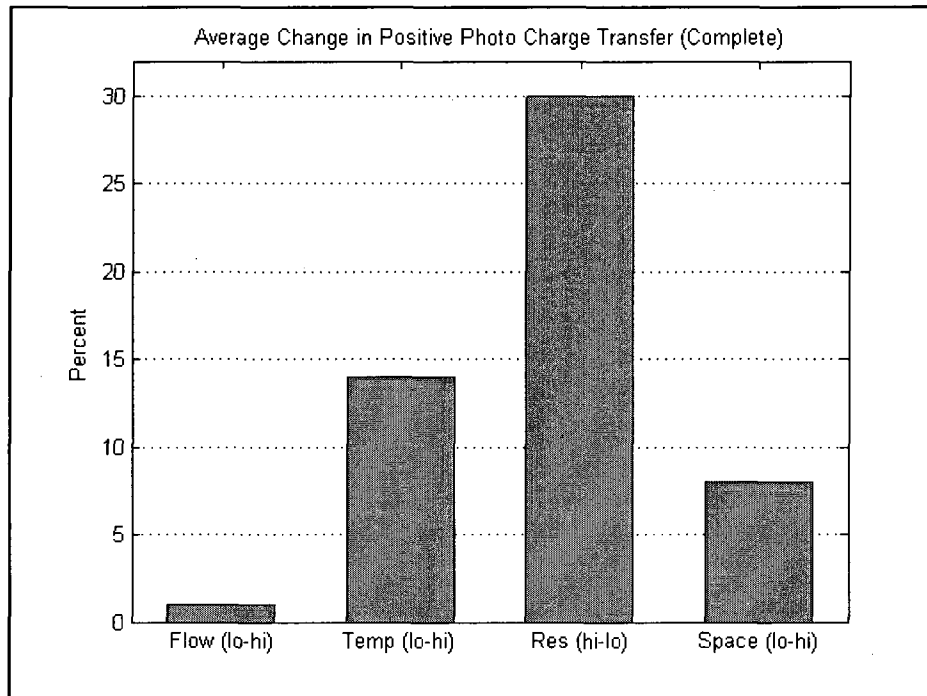


Figure 140. Average change in PPCT (percent) due to variations of the four inputs

The results expressed in the preceding two figures demonstrate that within the ranges of parameter settings tested, reducing corrected resistivity has by far the greatest impact on the cell performance with an average increase in PPCT of 30%. Increases in temperature as well as electrode spacing were also found to increase this value although to a lesser extent. The change in PPCT due to variations in these two parameters was shown to be 14 and 8 percent respectively. The increase in flowrate was found to have a net positive effect on charge transfer. This being the case, the average 1% increase calculated is considered to be within the range of error of the experiment and overall there was shown to be no strong preference for one level or the other.

CHAPTER 6

CONCLUSIONS AND FUTURE WORK

The project described in this work was begun with very specific goals in mind. The original idea was the construction an outdoor test facility where various photoanodes produced by UNLV's industrial partner "Hydrogen Solar" could be tested under realistic operating conditions. The work conducted at the university was expected to be conducted in parallel with the laboratory tests being performed at the company's Henderson, NV facility. Since the time of the project's inception, the focus of the research being conducted by Hydrogen Solar has shifted direction and the Henderson laboratory has since been closed. Because of this, much of the work presented here has been conducted with minimal interaction with the company. This being the case, every effort was made to remain true to the original project goals without the technical assistance and manufacturing capabilities of the company. It is the purpose of this chapter to reiterate these objectives and draw some basic conclusions with regards to the level to which they were met. Additionally, some ideas for improvements to the various aspects of the project as well as some thoughts regarding possible future work are presented here.

Test Facility

The experimental facility documented in Chapter Two of this writing serves as the framework for the project as a whole. From an academic standpoint, there is little which is especially profound about its design and construction, and ideally the system would have existed at the start of the project. This would have allowed more time for the testing and analysis phase which would be of greater interest to the academic community. This unfortunately was not the case and without its construction, these other aspects of the project could not commence. Additionally, as documented in Chapter Two, the design and construction of such a system, while not academically profound, was far from a trivial task. For this reason, the documentation regarding this part of the project is considered as integral to this work as a whole as any other section.

The experimental system was designed to serve as a platform from which long term data could be collected with a reasonable level of control over the various inputs. As was documented in Chapter 4, the system in its final incarnation achieves this relatively well. The various measurement devices were selected to provide the highest level of accuracy possible within the budgetary constraints of the project and estimates of the uncertainty associated with these measurements are documented. System components were selected to be compatible with a wide range of acidic or basic electrolytes with minimal process contamination. The location selected for the system provides an unobstructed view of the sky throughout the year, and the system itself has proven to be quite robust in this relatively harsh environment. While the experimental system described here is considered to have met the criteria for which it was originally constructed, as with any design, there

is always room for improvement. Possible future modifications include but are not limited to the following:

Use of more rigid pipe in place of flexible tubing:

The rigid polypropylene pipe was found to be far more durable for outdoor applications such as this as well as being more resistant to deformation due to temperature and pressure. The flexible tubing would be used only where absolutely necessary, such as the connections at the rotating tracker azimuth drive.

Use of precision needle valves for flow control:

The plastic gate valves used to control the flow were selected mainly because they were relatively inexpensive and as documented in the previous chapter, once set, these units were found to provide adequate flow control. Fine adjustments of the flow, however, were difficult with these and much setup time could have been saved if a precision needle valve had been used instead.

Incorporation of the reference cell into the electrolyte tank:

The separate control loop used to maintain the reference cell (located in the instrumentation shed) at the cell inlet temperature was found to work serviceably well during this test series. This additional control loop could be eliminated and the system simplified however, if the reference could be located inside the electrolyte tank where the temperature is already being controlled. Implementation of this would eliminate the

necessity to monitor the cell temperature separately, thus simplifying the testing procedure.

Cells

As was the case with the testing system, ideally a workable cell design would have already existed at the time that this project was begun. Again this was not the case, and testing could not commence until these units were constructed. As was documented in Chapter 3, the cells used for this experiment were designed to allow for testing of various types of glass photoanodes and cathode/PEM configurations under dynamic flow conditions in a harsh outdoor environment. Additionally, the original design criteria specified that the cells should allow for a variable flow channel width and that they be dimensionally stable and relatively easy to reconfigure in this respect. The cells in their final manifestation are considered to have achieved these goals. The final units have been pressurized and have been tracking on the system now for over 8 months. They have withstood sustained pressures of up to 35 kPa at temperatures in excess of 60 °C without deformation, ruptures or leakage. A complete reconfiguration of the cells including anode replacement and changing the spacer thickness can be accomplished in one day with time allowed for the curing of the liquid silicone used during assembly. The method of lead attachment has been much improved and the breakages encountered during assembly of the cells have been virtually eliminated. In addition to this, various methods of securing the PEM to the cathode have been explored and as documented, a workable method has been devised. As was previously stated the cells have been active

for a considerable length of time and no separation or major wrinkles in the membranes have been observed. Possible improvements with regard to cell design are listed below:

Elimination of the liquid silicone sealant used in cell construction:

As was mentioned previously, much of the time involved in reconfiguring the cells is spent waiting for the liquid silicone sealant to properly cure. Future cell designs would seek to replace this material with reusable solid gaskets. Implementation of this is expected to cut the cell reconfiguration time considerably.

Use of a different gasketing material:

The solid gaskets used in the test cells were made of a silicone rubber material. The compound used is extremely soft and seals well without an excessive amount of clamping force. Once the cells are together the material performs quite well with no leaks being detected during the 8 months that the cells have been in operation. The problem with this material is that upon disassembly of the cells, the gaskets are permanently deformed and are generally not reusable. The construction of new gaskets adds a great deal to the time required to reconfigure the cells. The use of a slightly harder compound in future cells could help address this issue.

Use of a single piece cathode:

The two piece cathode used in the cells tested during this experiment was used primarily due to cost issues. The platinized titanium mesh used in the cells had already been purchased at the time that this project was begun and the pre cut pieces were not large

enough for the cathode to be constructed as a single piece. The high cost of this material prevented new larger pieces from being purchased. Cost issues aside, if in fact the cathode could be constructed as a single piece, this would greatly simplify the design and eliminate the need for many of the parts required due to the two piece construction.

Test Procedure and Final Results

The test procedure documented in chapter 4 of this report was developed based upon observations of cell performance during the preliminary test phase. It was designed to provide a rigid set of guidelines which would ensure that valid comparisons between tests would be possible. The time schedule dictated by the procedure was found to work relatively well and will remain the standard used at this facility for future testing of this type.

The final testing was performed as a full factorial series and was designed to test every possible combination of input parameters under both light and dark conditions. The analysis of the parametric data shows that the control of these inputs for the series was sufficient enough to assume that the values are constant over the course of an individual test in the series. Additionally, it was demonstrated that the two parameters (absolute resistivity and pH) which are measured but not actively controlled are well defined by the other inputs, and thus the effects of their variation need not be considered separately.

The format of the test series described here relies heavily on the assumption that the solar input can be treated as being relatively constant both over the duration of an individual test as well as between tests conducted on different days. To quantify the validity of this assumption, algorithms were developed to determine the maximum

spectral mismatch both over the course of an individual test, as well as for the series. The spectral data collected for the final test series was shown to support this assumption with the maximum integrated values for the two types of mismatch being shown to be 10% or less. Additionally, the average spectrum calculated for the series was found to be in good agreement with the two standards defined by NREL. The mismatch based upon integrated values was calculated to be 10% and 3% between the series average and the global tilt and direct + circumsolar standards respectively. Future studies could be conducted to check the validity of this test method during other times of the year, as well as to determine the sensitivity of the devices to varying levels of solar insolation.

The data presented in Chapter 4 shows that the current densities produced by the cells are measurable but are, in general, significantly smaller than those being presented in other studies. These low numbers recorded are mainly attributed to the combined effect of two factors. The first of these is the relatively high resistivity of the electrolyte (water) being used. The decision to run the cells with pure water was made mainly to extend the life of the limited supply of photoanodes remaining after the closure of “Hydrogen Solar’s” Henderson, NV facility. In addition to the high resistivity of the electrolyte, a second factor believed to contribute to the relatively low currents measured during this series is related to the quality of the photoanodes themselves. When the cells were first put on sun for the preliminary testing it was observed that the currents were initially significantly higher than the ones presented here. The magnitude of this current found to decline quickly over the first few weeks of these initial experiments, leveling off near the present values after a couple of months of operation. For this reason, it is felt that the anodes used for this project, while stable for the experiments being presented here, were

not of the same level of quality of those being produced at the beginning of the project. This questionable anode quality as well as the very limited supply after the closure of the Henderson facility has limited the options available as far increasing the magnitude of the currents. Again, it is important to emphasize that the test series presented here was intended as the first of many such tests involving a variety of anodes and electrolyte combinations. The limited involvement of UNLV's industrial partner at the time testing had commenced has limited the extent to which this could be carried out. Be this as it may, the photocurrents measured for this test series, while small, are sufficient in magnitude to allow for a meaningful analysis and the establishment of some general trends.

The analysis presented in Chapter 5 seeks to quantify the results of the large amount of data collected during each individual test. The photocurrents for each test were calculated and an additional parameter (positive photo charge transfer) was defined as a gauge of the effectiveness of a given combination of input parameters. The change in this quantity was shown as a function of variations in each of the four input parameters and with the exception of the one suspect test point the trends suggested by the data were quite consistent. The average change in the positive photo charge transfer was calculated for each input variation and is used as the final measure of the effectiveness of changes to the individual parameters. The results obtained through this analysis were found to be independent of whether the suspect test point was included in the calculations or not. Based upon this analysis it was shown that for the cells tested here, a reduction of the corrected resistivity is by far the most effective means of increasing the photo induced charge transfer over the duration of the experiment, for the range of parametric variation

tested. The average increase was shown to be 30 % for a change from 1.000 M-ohm cm to .500 M-ohm cm. Changes in the PPCT due to variations of the other parameters was shown to be 14, 8 and 1 percent for changes in temperature (35.0 °C to 51.7 °C), electrode spacing (.6mm to 1.8mm), and flow (150 mL/min to 300 mL/min) respectively.

Summary

The project presented in the preceding chapters of this writing is presented as a work in progress. Since its inception, many aspects have changed due to events beyond the author's control. As was previously stated, however, every effort was made to remain true to the original goals of this endeavor and in most respects this has been achieved. The test system, cells, and test methodology developed over the course of this work have been demonstrated to provide a valid method of analyzing these types of PEC devices which has many advantages over other methods being used. This being the case, the manufacture of the photoanodes is currently beyond the capabilities of UNLV's Center for Energy Research and collaboration with other entities is required for additional studies to proceed. It is hoped that future alliances with other outside companies or collaboration with other departments within the university would allow this work to be continued.

APPENDIX A

NOMENCLATURE

A=Generic Steinhart coefficient
B=Generic Steinhart coefficient
C=Generic Steinhart coefficient
d=Electrode spacing (mm)
 E_{gap} =Bandgap Energy (eV)
 $E_{\text{H}^+/\text{H}_2}$ =Nernst potential for hydrogen evolution reaction (V)
 $E^0_{\text{H}^+/\text{H}_2}$ =Standard potential for hydrogen evolution reaction (V)
F=Faraday's constant (coulomb/mol)
g= Summation counter corresponding to specific input parameter
G=Number of tests
h=Planck's Constant (eV s)
i=Summation counter corresponding to specific time
I=Current (mA)
j=Summation counter corresponding to specific time
J=Solar intensity ($\text{W}/\text{m}^2/\text{nm}$)
k=Summation counter corresponding to specific wavelength
m=Summation counter corresponding to specific test number
n= Summation counter corresponding to specific test number
pH=Electrolyte pH
PPCT=Positive photo charge transfer (millicoulombs)
r= Resistance (ohm)
R=Gas constant ($\text{J}/\text{mol}/\text{K}$)
T=Temperature ($^{\circ}\text{C}$ or K depending on context)
u=Measurement uncertainty (units depend on context)
V=Voltage (mV)
X=Measured parametric data (units depend on context)

v=Frequency (Hz)
 σ =Average setpoint deviation (units depend on context)
 δ =Measure of spectral dissimilarity ($\text{W}/\text{m}^2/\text{nm}$)
 γ =Parameter setpoint (units depend on context)

APPENDIX B

EQUIPMENT SPECIFICATIONS

Campbell Scientific CR10X Datalogger

CR10X Specifications

Electrical specifications are valid over a -25° to $+50^{\circ}\text{C}$ range unless otherwise specified; non-condensing environment required. To maintain electrical specifications, Campbell Scientific recommends recalibrating dataloggers every two years.

PROGRAM EXECUTION RATE

Program is synchronized with real-time up to 64 Hz. One channel can be measured at this rate with uninterrupted data transfer. Burst measurements up to 750 Hz are possible over short intervals.

ANALOG INPUTS

NUMBER OF CHANNELS: 6 differential or 12 single-ended, individually configured. Channel expansion provided by AM16/32 or AM16 Relay Multiplexers and AM25T Thermocouple Multiplexers.

ACCURACY: $\pm 0.1\%$ of FSR (-25° to 50°C); $\pm 0.05\%$ of FSR (0° to 40°C); e.g., $\pm 0.1\%$ FSR = $\pm 5.0\text{ mV}$ for $\pm 2500\text{ mV}$ range

RANGE AND RESOLUTION:

Full Scale Input Range (mV)	Resolution (mV)	Differential	Single-Ended
± 2500	33.3	66.6	66.6
± 250	3.33	6.66	6.66
± 25	0.333	0.666	0.666
± 2.5	0.033	0.066	0.066

INPUT SAMPLE RATES: Includes the measurement time and conversion to engineering units. The fast and slow measurements integrate the signal for 0.25 and 1.72 ms, respectively. Differential measurements incorporate two integrations with reversed input polarities to reduce thermal offset and common mode errors.

Fast single-ended voltage:	2.6 ms
Fast differential voltage:	4.2 ms
Slow single-ended voltage:	5.1 ms
Slow differential voltage:	5.1 ms
Differential with 60 Hz rejection:	23.9 ms
Fast differential thermocouple:	8.6 ms

INPUT NOISE VOLTAGE (for $\pm 2.5\text{ mV}$ range)

Fast differential:	0.82 $\mu\text{V rms}$
Slow differential:	0.25 $\mu\text{V rms}$
Differential with 60 Hz rejection:	0.18 $\mu\text{V rms}$

COMMON MODE RANGE:

$\pm 2.5\text{ V}$

DC COMMON MODE REJECTION:

$>140\text{ dB}$

NORMAL MODE REJECTION:

70 dB (60 Hz with slow differential measurement)

INPUT CURRENT:

$\pm 9\text{ nA}$ maximum

INPUT RESISTANCE:

20 Gohms typical

ANALOG OUTPUTS

DESCRIPTION: 3 switched, active only during measurement, one at a time.

RANGE:

$\pm 2.5\text{ V}$

RESOLUTION:

0.5 mV

ACCURACY:

$\pm 5\text{ mV}$; $\pm 2.5\text{ mV}$ (0° to 40°C)

CURRENT SOURCING:

25 mA

CURRENT SINKING:

25 mA

FREQUENCY SWEEP FUNCTION:

The switched outputs provide a programmable swept frequency, 0 to 2.5 V square wave for exciting vibrating wire transducers.

RESISTANCE MEASUREMENTS

MEASUREMENT TYPES: The CR10X provides ratiometric bridge measurements of 4- and 6-wire full bridge, and 2-, 3-, and 4-wire half bridges.

Excite dual polarity excitation using any of the switched outputs eliminates dc errors.

Conductivity measurements use a dual polarity 0.75 ms excitation to minimize polarization errors.

ACCURACY: $\pm 0.32\%$ of FSR plus bridge resistor error.

PERIOD AVERAGING MEASUREMENTS

The average period for a single cycle is determined by measuring the duration of a specified number of cycles. Any of the 12 single-ended analog input channels can be used. Signal attenuation and ac coupling are typically required.

INPUT FREQUENCY RANGE:

Signal peak-to-peak ¹ Min.	Max.	Min. Pulse w.	Max Freq. ²
500 mV	5.0 V	2.5 μs	200 kHz
10 mV	2.0 V	10 μs	50 kHz
5 mV	2.0 V	50 μs	5 kHz
2 mV	2.0 V	100 μs	5 kHz

¹Signals centered around datalogger ground

²Assuming 50% duty cycle

RESOLUTION: 35 ns divided by the number of cycles measured

ACCURACY: $\pm 0.01\%$ of reading (number of cycles >100); $\pm 0.03\%$ of reading (number of cycles <100)

TIME REQUIRED FOR MEASUREMENT: Signal period times the number of cycles measured plus 1.5 cycles + 2 ms

PULSE COUNTERS

NUMBER OF PULSE COUNTER CHANNELS: 2

Eight-bit or 16 sixteen-bit; software selectable as switch closure, high frequency pulse, and low level ac.

MAXIMUM COUNT RATE: 16 kHz, eight-bit counter; 400 kHz, sixteen-bit counter. Channels are scanned at 8 or 64 Hz (software selectable).

SWITCH CLOSURE MODE

Minimum Switch Closed Time: 5 ms

Minimum Switch Open Time: 6 ms

Maximum Bounce Time: 1 ms open without being counted

HIGH FREQUENCY PULSE MODE

Minimum Pulse Width: 1.2 μs

Maximum Input Frequency: 400 kHz

Voltage Thresholds: Count upon transition from below 1.5 V to above 3.5 V at slow frequencies.

Larger input transitions are required at high frequencies because of input filter with 1.2 μs time constant. Signals up to 400 kHz will be counted if centered around $+2.5\text{ V}$ with deviations $>\pm 0.5\text{ V}$ for $\pm 1.2\text{ V}$.

Maximum Input Voltage: $\pm 20\text{ V}$

LOW LEVEL AC MODE

Typical of magnetic pulse flow transducers or other low voltage, sine wave outputs.

Input Hysteresis: 14 mV

Maximum ac Input Voltage: $\pm 20\text{ V}$

Minimum ac Input Voltage:

(Sine wave mV RMS)

Range (Hz)

20 1.0 to 1000

200 0.5 to 10,000

1000 0.3 to 15,000

DIGITAL I/O PORTS

8 ports, software selectable as binary inputs or control outputs. 3 ports can be configured to count switch closures up to 40 Hz.

OUTPUT VOLTAGES (no load): High 5.0 V $\pm 0.1\text{ V}$; low $< 0.1\text{ V}$

OUTPUT RESISTANCE: 500 ohms

INPUT STATE: High 3.0 to 5.5 V; low -0.5 to 0.6 V

INPUT RESISTANCE: 100 kohms

SDI-12 INTERFACE STANDARD

Digital I/O Ports C1-C8 support SDI-12 asynchronous communication; up to ten SDI-12 sensors can be connected to each port. Meets SDI-12 Standard Version 1.2 for datalogger and sensor modes.

CR10XTCR THERMOCOUPLE REFERENCE

POLYNOMIAL LINEARIZATION ERROR: Typically $\pm 0.5^{\circ}\text{C}$ (-35° to $+50^{\circ}\text{C}$); $\pm 0.1^{\circ}\text{C}$ (-24° to $+45^{\circ}\text{C}$).

INTERCHANGEABILITY ERROR: Typically $\pm 0.2^{\circ}\text{C}$ (0° to $+60^{\circ}\text{C}$) increasing to $\pm 0.4^{\circ}\text{C}$ (-35°C).

CE COMPLIANCE (as of 09/01)

STANDARD(S) TO WHICH CONFORMITY IS DECLARED:

EN50202: 1995 and EN61326: 1998

EMI and ESD PROTECTION

IMMUNITY: Meets or exceeds following standards:

ESD: per IEC 1000-4-2; $\pm 8\text{ kV}$ air, $\pm 4\text{ kV}$ contact discharge

RF: per IEC 1000-4-3; 3 V/m, 80-1000 MHz

EFT: per IEC 1000-4-4; 1 kV power, 500 V D/C

Surge: per IEC 1000-4-5; 1 kV power and 1 V/O

Conducted per IEC 1000-4-6; 3 V 150 kHz-80 MHz

Emissions and immunity performance criteria available on request.

CPU AND INTERFACE

PROCESSOR: Hitachi 6303

PROGRAM STORAGE: Up to 15 kbytes for active program; additional 16 kbytes for alternate programs. Operating system stored in 128 kbytes Flash memory.

DATA STORAGE: 128 kbytes SRAM standard (approximately 50,000 data values). Additional 2 Mbytes Flash available as an option.

OPTIONAL KEYBOARD DISPLAY: 8-digit LCD (0.5" digits)

PERIPHERAL INTERFACE: 9 pin D-type connector for keyboard display, storage module, modem, printer, card storage module, and RS-232 adapter.

BAUD RATES: Selectable at 300, 1200, 3600 and 76,800 bps for synchronous devices. ASCII communication protocol is one start bit, one stop bit, eight data bits (no parity).

CLOCK ACCURACY: ± 1 minute per month

SYSTEM POWER REQUIREMENTS

VOLTAGE: 9.6 to 16 Vdc

TYPICAL CURRENT DRAIN: 1.2 mA quiescent, 13 mA during processing, and 46 mA during analog measurement.

BATTERIES: Any 12 V battery can be connected as a primary power source. Several power supply options are available from Campbell Scientific.

The Model CR2430 lithium battery for clock and SRAM backup has a capacity of 270 mAh.

PHYSICAL SPECIFICATIONS

SIZE: 7.8" x 3.5" x 1.5" - Measurement & Control Module; 9" x 3.5" x 2.5" - with CR10XWP Wiring Panel. Additional clearance required for serial cable and sensor leads.

WEIGHT: 2 lbs

WARRANTY

Three years against defects in materials and workmanship.

We recommend that you confirm system configuration and critical specifications with Campbell Scientific before purchase.

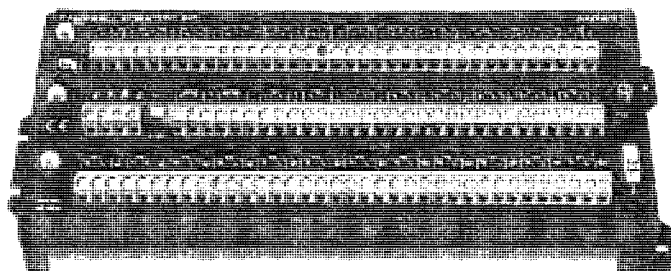
 **CAMPBELL SCIENTIFIC, INC.**
2115 M. 4000 N. • Logan, Utah 84321-7794 • (435) 753-2042 • FAX (435) 753-6940
Offices also located in: Australia • Brazil • Canada • England • France • South Africa • Spain

Copyright © 1998, 2004
Campbell Scientific, Inc.
Printed March 2004

Relay Multiplexer

Model AM16/32

The AM16/32 Multiplexer increases the number of sensors that can be measured by a CR800, CR850, CR10X, CR1000, CR3000, CR5000, or CR7 datalogger. The AM16/32 sequentially multiplexes 16 groups of four lines (a total of 64 lines) through four common (COM) terminals. A manual switch setting allows it to multiplex 32 groups of two lines (also a total of 64 lines) through two COM terminals. Compatible sensors include thermistors, potentiometers, load cells, strain gages, vibrating wires, water content reflectometers, and gypsum soil moisture blocks. The AM16/32 not only increases system channel capacity, it also reduces the cost of cabling individual sensors on long wire runs. The maximum distance between the datalogger and the AM16/32 is determined by the sensors used, the datalogger's scan rate, and the cable used in the application.



The AM16/32 can be manually configured to multiplex channels in 16 groups (four lines at a time) or 32 groups (two lines at a time).

Maximum Number of Sensor Connections

The maximum number of sensors multiplexed through one AM16/32 depends on the type(s) of sensors measured. For example, assuming identical sensors, the AM16/32 can multiplex:

- Up to 32 single-ended or differential sensors that require two wires (e.g., thermistors, half bridges)
- Up to 16 single-ended or differential sensors that require four wires (e.g., full bridges, four-wire half bridges)
- Up to 48 half-bridge measurements (assumes common excitation and completion resistors at the datalogger)
- Up to 32 vibrating wire sensors (16 with temperature) in conjunction with a CR800, CR850, CR10X, CR1000, or CR3000 and AVW1, AVW4, or AVW100 Vibrating Wire Sensor Interface
- Up to 32 gypsum soil moisture blocks (model 223 or 253). The AM16/32 eliminates the requirement for dc blocking capacitors, significantly reducing sensor cost
- Up to 48 CS616 Water Content Reflectometers (assumes common excitation)

Datalogger programs written for the AM416 or AM32 multiplexers will work with the AM16/32. Short Cut version 1.1 or higher (available free of charge from our Web site) supports simple programs and generates wiring diagrams for AM16/32 applications. Mixing sensor types may require special considerations. Contact Campbell Scientific for assistance.

Datalogger Connections

When used in 4 x 16 mode, a four-conductor cable (with shield) connects the measurement/excitation channels of the datalogger with the COM terminals of the multiplexer. When used in 2 x 32 mode, a two-conductor cable (with shield) is required. Campbell Scientific offers the MUXSIGNAL-L cable that supports use in either mode.

A four-conductor cable (with shield) supplies power and control signals from the datalogger to the AM16/32. The AM16/32 requires one datalogger control port for enable (reset terminal), and a second control port to advance through the channels (clock terminal). Either the datalogger's power supply or a separate 12 V supply is used to power the multiplexer. Campbell Scientific offers the MUXPOWER-L cable to connect the AM16/32 to the datalogger's power terminals and control ports.



Scanning Multiple AM16/32s

Several AM16/32s may be connected to the same datalogger depending on the number of control ports and analog inputs available. For example, some customers have connected six multiplexers to one datalogger. This assumes adequate analog inputs, plus eight control ports, two for clock lines and six for enable lines, are available.

Environmental Enclosures

The AM16/32 operates in most field conditions but requires a non-condensing environment. A weather-resistant enclosure equipped with desiccant is required for field use. The ENC10/12 is the enclosure of choice for multiplexers housed at a distance from the datalogger.

If the AM16/32 is to be housed in the datalogger's enclosure, a CR800/PS100, CR3000, CR1000/PS100, or CR10X/PS400, and one AM16/32 will fit in an ENC12/14. For convenience in wiring, a larger enclosure (e.g., ENC16/18) is recommended.

Specifications

Electrical

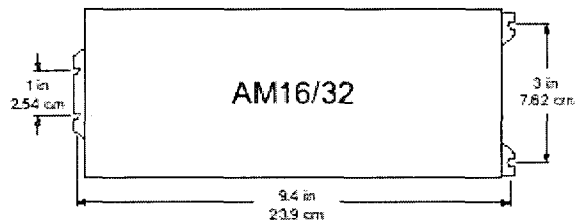
- Power: 9.6 to 16 Vdc (under load), unregulated
- Current drain: <210 μ A quiescent; 6 mA active (typical)
- Reset levels: <0.9 V inactive; 3.5 to 16 V active
- Clock levels: Scan advance occurs on the leading edge of the clock pulse transition (from below 1.5 V to above 3.5 V)
- Minimum clock pulse width: 1 ms
- Maximum actuation time for relay: 20 ms
- Relay operation: break before make
- Initial relay resistance, closed: 0.1 Ohm
- Maximum switching current: 500 mA. Switching currents greater than 30 mA (occasional 50 mA) acceptably degrade the suitability of that channel for switching low-voltage signals.
- Minimum contact life: 10^7 closures
- CE Compliance:
EN 61326: 1998
EN 55022: 1998 Class B

Physical

- Operating temperature: -25° to +50°C (standard); -55° to +85°C (extended)
- Operating humidity: 0 to 95%, non-condensing
- Size: 4.0"W x 9.4"L x 1.8"D (10.2 x 23.9 x 4.6 cm)
Weight/shipping: 1.5 lbs/6.0 lbs (0.7 kg/2.7 kg)

Mounting

- AM16/32 in enclosure: compatible with 1" on center hole grid (see foot print below)
- Enclosure to pipe: 1.25" IPS pipe (1.660" OD)
3.175 cm (4.22 cm OD)



If you have questions concerning the use of the AM16/32 in your application, please call Campbell Scientific at (435) 753-2342.



815 W. 1800 N. | Logan, Utah 84301-1784 | USA | phone (435) 753-2342 | www.campbellsci.com
Australia | Brazil | Canada | England | France | Germany | South Africa | South Korea | USA (headquarters)

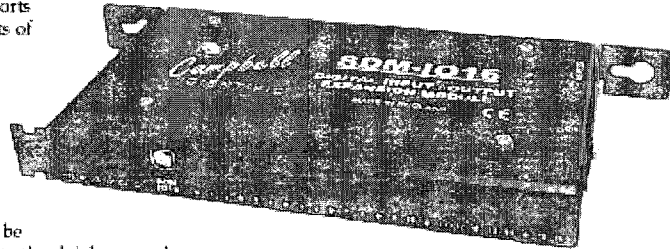
Copyright © 2001, 2008
Campbell Scientific, Inc.
P.O. Box 480000, Reno, NV 89500-0000

Campbell Scientific SDMIO16 Input Output Expansion Module

16-Channel I/O Expansion Module

Model SDM-IO16

The SDM-IO16 provides 16 digital I/O ports that function similarly to the control ports of the majority of Campbell Scientific dataloggers. When configured as an input, each port can monitor logic state, count pulses, measure signal frequency, and determine duty cycle. An option in the pulse counting mode enables switch debounce filtering allowing the SDM-IO16 to accurately count switch closures. The SDM-IO16 can also be programmed to send an interrupt signal to the datalogger when one or more input signals change state. When configured as an output, each port can be set to 0 or 5 V by the datalogger. A 'boost' circuit allows an output that is set HI to source a current of up to 100 mA for controlling external devices such as low voltage valves or relays.



SDM Operation

The SDM-IO16 is a synchronously addressed datalogger peripheral. Three ports on the datalogger are used to address the SDM-IO16. Advanced error checking techniques ensure correct data transmission to and from the SDM-IO16. Up to sixteen SDM-IO16 modules can be addressed allowing up to 256 ports to be controlled by the datalogger.

Power Considerations

The datalogger's rechargeable power supply can power the SDM-IO16 for most pulse counting or status input applications. However, when driving loads, the SDM-IO16 power requirements may be large compared to most Campbell Scientific products. For these applications, an external power supply is recommended.

Mounting

Mounting brackets are provided for attaching the SDM-IO16 to the backplate of an ENC12/14 or larger enclosure.

Specifications

Compatible dataloggers:	CR800, CR850, CR1000, CR3000, and CR5000 dataloggers support all of the functions; our CR7 supports the output mode only. Referred dataloggers that support all of the functions include the CR10X (OS 1.17 or later) and CR20X (OS 1.14 or later).
Software requirements:	Support for all the functions requires CRBasic's SDMIO16 instruction or Edlog's Instruction 188. Instruction 188 is available in Edlog templates that post date March 2002 (LoggerNet version 2.1 contains this template). A PC208W patch is available at www.campbellsci.com/downloads for users with PC208W 3.0 or later. Edlog templates that predate March 2002 can support only the output mode using Instruction 104. Instruction SDMCD16AC supports only the output mode in CRBasic.
SDM and I/O port:	0/5 V logic level ports for connecting to the datalogger's control/SDM ports
Operating range:	-25° to +50°C
EMC status:	Complies with EN 61326:1997



CAMPBELL SCIENTIFIC, INC.
WHEN MEASUREMENTS MATTER

Specifications (continued)

Power

Operating voltage:	12 Vdc (nominal 9 to 18 V)
Current drain @ 12 Vdc:	600 μ A typical standby (all ports high, no load, excludes pulse counting) 3 mA maximum (active with all 16 ports counting pulses at 2 kHz and no output load) Current consumption is roughly proportional to input signal frequency and number of ports used. Current drawn from any output must be added to the quiescent level to obtain the total current drain.

Output

Voltage (no load):	ON/HI—nominal 5 V, minimum 4.5 V OFF/LO—nominal 0 V, maximum 0.1 V
Sink current:	Output will sink 8.6 mA from a 5 V source
Source current:	Output will source 42 mA @ 3 V; 133 mA short-circuited to ground
Maximum current (total all outputs):	Limited by 12 V supply

Input

Voltage:	High—4.0 V minimum threshold Low—1.0 V maximum threshold
Protection:	Input clamped at -0.6 V and ± 5.6 V relative to ground via a 33 ohm resistor to withstand a continuous current flow of 200 mA
Impedance:	Biased to +5 V relative to ground by a 100 kohm resistor

Pulse Counting

Maximum frequency:	2.0 kHz on all channels simultaneously with switch debounce-mode turned off with a 50/50 duty cycle. 150 Hz on all channels with default switch debounce mode enabled and a 50/50 duty cycle.
Minimum frequency:	0 Hz is reported if there are less than two high-to-low signal transitions in the measurement interval.
Minimum pulse width:	244 μ s
Default switch debounce timing:	Input and ground must remain closed for 3.17 ms then remain open for 3.17 ms to be counted as a closure
Internal clock accuracy (-25° to 50°C):	$\pm 0.01\%$, worst case
Maximum measurement interval:	15.9375 s

Physical

Dimensions:	9" x 4" x 1" (23.0 x 10.0 x 2.4 cm)
Weight:	12 oz (350 g)
Maximum cable length:	20 ft (6 m)



818 W. 1800 N. | Logan, Utah 84321-1784 | USA | phone | 480 | 788-2542 | www.com.physical.com
Australia | Brazil | Canada | England | France | Germany | South Africa | Spain | USA (headquarters)

Copyright © 2010, 2011
Pulsed Systems, Inc.
Printed August 2010

Campbell Scientific PS100 Power Supply

1. General Description

The PS100 is a 12-volt power supply that includes a charging regulator and a 7 amp hour battery. The CH100 is a charging regulator that is used with a Campbell Scientific battery pack such as the BP12 or BP24 or with a user-supplied battery. Charging power is typically supplied by an AC transformer or an unregulated solar panel.

The PS100 and CH100 each have one adapter connector that will allow connecting one of the following adapters.

The A100 Null Modem Adapter has two 9-pin connectors that provide a null modem for use in a site, without a datalogger. The A100 connects and powers two Campbell Scientific peripherals that would normally be connected to a datalogger. These peripherals are typically modems linking different communications technologies; e.g., telephone to radio.

The A105 Additional 12 V Terminals Adapter may be used to provide additional 12 V and ground terminals where the power supply is used to power several devices.

2. Specifications

Input Voltage (CHG terminals)	15 to 28 VDC or 18 VAC RMS
Battery Connections	
Charging Output Voltage:	Temperature compensated float charge for 12 V Battery
Temperature Compensation Range:	-40 to +60°C
Charging Current Limit:	1.2 Amps typical
Power Out (+12 terminals)	
Voltage:	Unregulated 12 V from Battery
Current Limited w / 3 A Thermal Fuse:	> 3 A @ < 20°C 3 A @ 20°C 2.1A @ 50°C 1.8 A @ 60°C

Battery Packs

Operating Temperature Range: -40 to +60°C
Capacity:
PS100 7 Amp hours
BP12 12 Amp hours
BP24 24 Amp hours

WARNING

These batteries are designed to be float charged. Permanent damage occurs and battery life is shortened if the battery is allowed to discharge below 10.5 volts.

AC Transformer: CSI Model No. 9591

Input Voltage: 120 VAC
Output Voltage: 18 VAC RMS
Output Current (max): 1.2 Amps RMS
Protection (automatic reset): 85°C thermal reset breaker
UL Approval: UL-1950

AC Transformer: CSI Model No. 14014

Input Voltage: 90 - 264 VAC; 47 - 63 Hz
Output Voltage: 18 VDC
Output Current (max): 1.3 Amps
UL Approved, File No.: E137895

PS100

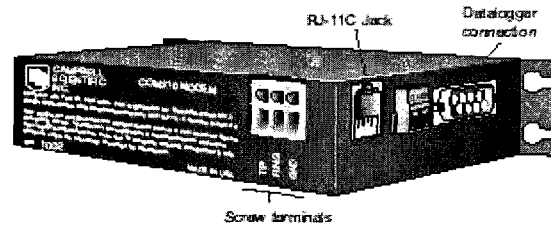
Physical Specifications: 10.5 cm tall, 19 cm long,
7 cm wide

Campbell Scientific COM210 Modem

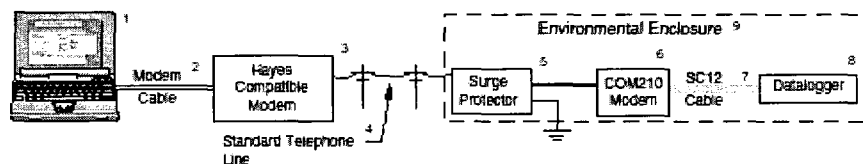
Telephone Modem

Model COM210

The COM210 modem enables communications between a computer and a Campbell Scientific datalogger over a public switched telephone network. A Hayes-compatible modem is required at the computer base station. The COM210 connects to the datalogger at the field site. The COM210's wide operating temperature range and low power requirements make it ideal for use at remote sites.



The RJ-11C jack connects the COM210 to a surge-protected phone line. Alternatively, the screw terminals connect the COM210 to a phone line via a surge protector.



Hardware Requirements

At Computer Base Station

- 1) User-supplied PC running PC400 or LoggerNet Datalogger Support Software
- 2) Serial cable (7026 for 9-pin serial ports, SC25PS for 25-pin serial ports, or equivalent)
- 3) Customer-supplied, Hayes-compatible modem
- 4) Switched telephone network that connects the computer base station with each datalogger field site

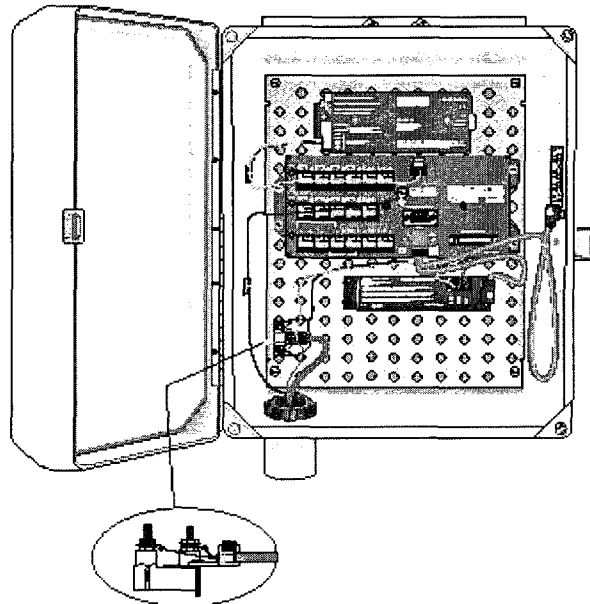
At Field Site

- 5) Telephone surge protector if the telephone company has not installed surge protection
- 6) COM210 modem
- 7) SC12 cable (included with COM210); the longer SC12R-6 cable is available as an option
- 8) CR510, CR800, CR10X, CR1000, CR3000, CR7, or CR5000 datalogger
- 9) Typically an ENC12/14, ENC14/16, or ENC16/18 environmental enclosure
- 10) Power supply, usually the datalogger's sealed rechargeable battery recharged with ac power or solar panel



CAMPBELL SCIENTIFIC, INC.

750 N. 2000 St. - Logan, Utah 84301-1705 • (801) 750-2200 • FAX (801) 750-2202 • www.campbellsci.com



COM210 in ENC12/14 enclosure with CR1000 datalogger, PS100 power supply, and enclosure-mounted surge protector (Model 6362).

COM210 Specifications

- Standards
Bell 212A, CCITT V.22, V.32bis
- FCC Registration
B9QUSA-31402-MM-T
- Operating voltage:
12 volts
- Current drain
120 μ A quiescent
160 mA active
- Bits per second (bps)
1200, 4800, 9600
- Speaker
- Operation
Full-duplex over standard analog phone lines
- Operating temperature
-25° to +50°C std, -55° to +85°C optional
- Size
5.2" x 1.7" x 3.6" (13.1 x 4.3 x 9.2 cm)
- Weight
0.75 lbs (.34 kg)
- COM210 shipped with SC12 cable, ground cable, and telephone patch cord



CAMPBELL SCIENTIFIC, INC.

315 West 1900 North • Logan, Utah 84301 • (801) 732-8200 • Fax (801) 732-8200
 Offices also located in Australia • Brazil • Canada • England • France • Germany • South Africa • Spain

Copyright © 2007, 2008
 Campbell Scientific, Inc.
 Printed June 2008

Campbell Scientific SC32B Optically Isolated Datalogger to RS-232 Interface

SC32B

Optically Isolated Datalogger to RS-232 Interface



The SC32B Optically Isolated Interface is used to connect a datalogger's CS I/O port with a PC's RS-232 port. This interface converts the computer's RS-232 voltage levels to the CMOS levels of the datalogger. It also isolates the computer's electrical system from the datalogger, thereby protecting against ground loop, normal static discharge, and noise.

An interface such as the SC32B is required for direct communications between a PC and a CR510, CR10X, or CR7 datalogger. For our CR800, CR850, and CR1000 dataloggers, the SC32B is often used to provide optical isolation between the datalogger and PC. Although the on-board RS-232 port of the CR3000, CR5000, or CR9000X dataloggers is isolated, the SC32B can be interfaced with their CS I/O port when a second RS-232 port is required in the application.

The SC32B is shipped with an SC12 cable for attachment to the datalogger and a 10873 cable for attachment to the PC. Alternatively, an SC12R-6 cable (purchased separately) can be used instead of the standard SC12 when a longer cable is needed.



Specifications

Baud rates supported: up to 115 kbps

Power: Drawn from the serial ports of the PC and datalogger

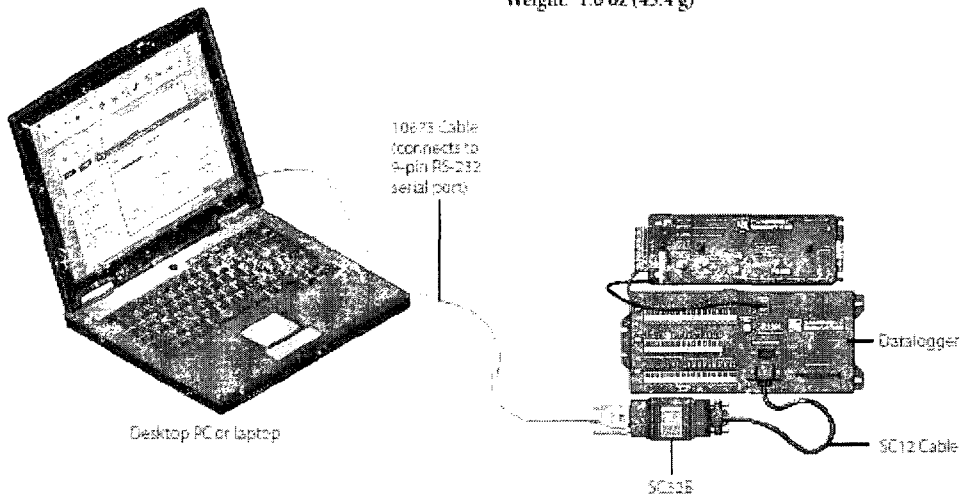
Current (supplied by datalogger):
<200 μ A quiescent; ~15 mA active

Connections:
9-pin RS-232 female port configured as DCE
9-pin male port

Operating temperature range: -25° to +50°C

Size: 1.6" x 0.9" x 3.0" (4.1 x 2.3 x 7.6 cm)

Weight: 1.6 oz (45.4 g)



815 W. 1860 N. Logan, Utah 84321-1784 USA (435) 753-2342 www.campbellsci.com
Australia Brazil Canada England France Germany South Africa Spain USA (headquarters)

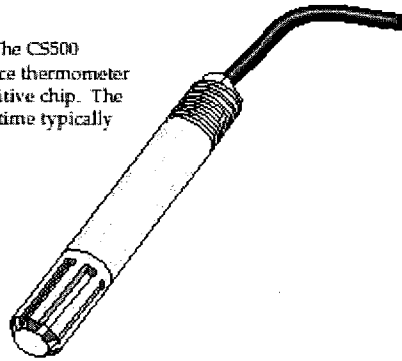
Copyright © 2002, 2006
Campbell Scientific, Inc.
Printed October 2006

Temperature and Relative Humidity Probe Model CS500

The CS500 is a modified version of Vaisala's 50Y Humitter. The CS500 measures air temperature with a 1000 ohm platinum resistance thermometer (PRT); RH is measured by a laser-trimmed INTERCAP capacitive chip. The chip is field-replaceable, as needed, and eliminates the downtime typically required for the recalibration process.

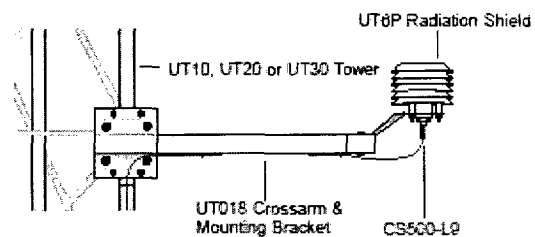
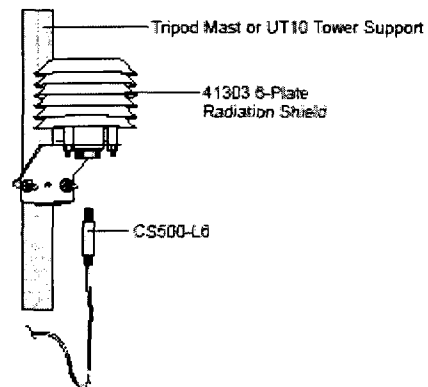
Sensor Mounts

When exposed to sunlight, the CS500 must be housed in a radiation shield. If the CS500 is mounted to a CM6/CM10 tripod or a UT10 tower, a model 41303 6-plate radiation shield is used. If the CS500 is mounted on a UT20 or UT30 tower, a UT018 Crossarm and Mounting Bracket and a UT6P 6-plate radiation shield are used.



Ordering Information

- CS500-L6 6 ft lead length for use with CM6/CM10 tripods or a UT10 tower.
- CS500-L9 9 ft lead length for use with a UT10, UT20 or UT30 tower and a UT018
- 9598 Replacement chip for the CS500.
- UT018 Crossarm and Mounting Bracket; required for mounting the CS500 to a UT20 or UT30 tower



CAMPBELL SCIENTIFIC, INC.

7701E 1/99/11 • Logan, Utah 84301-1704 • (435) 752-8540 • FAX (435) 752-8549 • www.campbellsci.com

Specifications

Relative Humidity

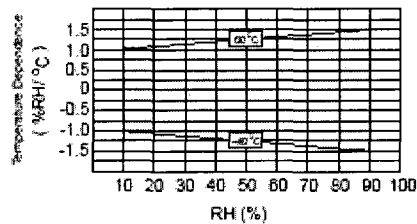
Operating Range: 0 to 100% RH

Accuracy: 0-10% range: unspecified

10-90% range: $\pm 3.0\%$

90-100% range: $\pm 6.0\%$

Temperature Dependence of Relative Humidity Measurement:

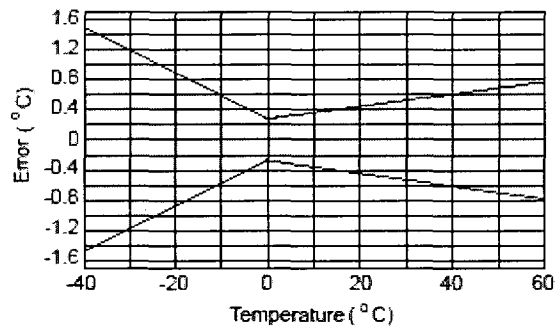


Typical Long-Term Stability: Better than $\pm 1\%$ RH per year

Temperature

Measurement Range: -40° to $+60^{\circ}\text{C}$

Temperature Accuracy:



General

Supply Voltage: 7-28 Vdc (typically powered by datalogger's 12 V supply)

Current Consumption: < 2 mA typical

Diameter: 0.47" (12 mm)

Length: 2.66" (67.5 mm)

Housing Material: ABS plastic



CAMPBELL SCIENTIFIC, INC.

915 W. 1900 N. • Logan, Utah 84321-1704 • (801) 783-3342 • FAX (801) 768-0540
Offices located in: Australia • Brazil • Canada • England • France • South Africa • Spain

Copyright © 1998, 2003
Campbell Scientific, Inc.
Printed February 2003

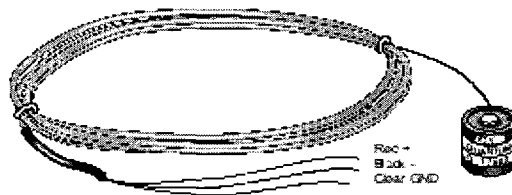
Solar Radiation Sensors

LI-COR's LI190SB Quantum Sensor & LI200X Silicon Pyranometer

LI190SB and LI200X measure solar radiation with a silicon photovoltaic detector mounted in a cosine-corrected head. A shunt resistor in the sensor's cable converts the signal from microAmps to millivolts, allowing the LI190SB and LI200X to be measured directly by a Campbell Scientific datalogger. Please note that the LI190SB and LI200X are not compatible with our CR200-series dataloggers.

LI190SB Quantum Sensor

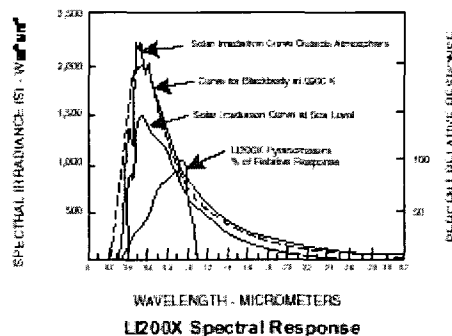
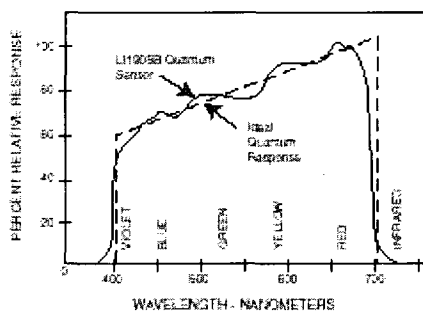
LI190SB accurately measures Photosynthetic Photon Flux Density (PPFD) in both natural and artificial light. PPFD is the number of photons in the 400 to 700 nm waveband incident per unit time on a unit surface. Because PPFD describes photosynthetic activity, the LI190SB is ideal for growth chambers and greenhouses.



LI190SB Quantum Sensor. The LI200X has a similar appearance and identical wiring.

LI200X Silicon Pyranometer

The LI200X Silicon Pyranometer is calibrated against an Eppley Precision Spectral Pyranometer (PSP) to accurately measure sun plus sky radiation. The LI200X is used extensively in solar, agricultural, meteorological, and hydrological applications. The LI200X should not be used under vegetation or artificial lights because it is calibrated for the daylight spectrum (400 to 1300 nm).

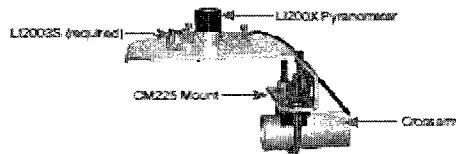


CAMPBELL SCIENTIFIC, INC.

410 W. 1000 N. • Logan, Utah 84301-1704 • (435) 789-0000 • FAX (435) 789-0000 • www.campbellsci.com

Sensor Mounts

To ensure accurate measurements, the sensor should be leveled using a LI2003S leveling fixture which incorporates a bubble level and three adjusting screws. The LI2003S leveling fixture mounts to a tripod or tower using the CM225 mount. For most applications, Campbell Scientific recommends attaching the CM225 to a CM202, CM204, or CM206 crossarm. The CM225 can also be attached to a tripod or tower mast.



To attach the CM225 to a CM202, CM204, or CM206 crossarm, place the u-bolt in the holes on the bottom of the bracket (shown). If the CM225 is attached to a mast, place the u-bolt in the holes in the side of the bracket.

Ordering Information

- LI190SB-L Quantum Sensor with user specified lead length. Enter the lead length after the L. For example, LI190SB-L11, orders an 11' lead length.
- LI200X-L Silicon Pyranometer with user specified lead length. Enter the lead length after the L. For example, LI200X-L11, orders an 11' lead length.
- LI2003S Base and leveling fixture required to level the sensor.
- CM225 Mount for attaching to the LI2003S and sensor to a tripod, tower, or vertical pipe.

Common Specifications

- Stability: $< \pm 2\%$ change over a 1 year period
- Response Time: 10 μ s
- Temperature Dependence: 0.15% per $^{\circ}$ C maximum
- Cosine Correction: Cosine corrected up to 80 $^{\circ}$ angle of incidence
- Operating Temperature: -40 $^{\circ}$ to +65 $^{\circ}$ C
- Relative Humidity: 0 to 100%
- Detector: High stability silicon photovoltaic detector (blue enhanced)
- Sensor Housing: Weatherproof anodized aluminum case with acrylic diffuser and stainless steel hardware
- Size: 0.94" dia x 1.00" H (2.38 x 2.54 cm)
- Weight: 1 oz. (28 g)

LI190SB Specifications

- Calibration: $\pm 5\%$ traceable to the U.S. National Institute of Standards Technology (NIST)
- Sensitivity: Typically 5 μ A per 1000 μ moles $s^{-1} m^{-2}$
- Linearity: Maximum deviation of 1% up to 10,000 μ moles $s^{-1} m^{-2}$
- Shunt Resistor: 600 Ω
- Light Spectrum Waveband: 400 to 700 nm

LI200X Specifications

- Accuracy: Absolute error in natural daylight is $\pm 5\%$ maximum; $\pm 3\%$ typical
- Sensitivity: 0.2 $kW m^{-2} mV^{-1}$
- Linearity: Maximum deviation of 1% up to 3000 $W m^{-2}$
- Shunt Resistor: Adjustable, 40.2 to 90.2 Ω , factory set to give the above sensitivity
- Light Spectrum Waveband: 400 to 1100 nm



CAMPBELL SCIENTIFIC, INC.
315 West 1900 North • Logan, Utah 84301 • (801) 752-8800 • Fax (801) 752-8800
Offices also located in: Australia • Brazil • Canada • England • France • Germany • South Africa • Spain

Copyright © 1992-2008
Campbell Scientific, Inc.
Printed May 2004

Wind Speed and Direction Sensors

03001 Wind Sentry Anemometer/Vane & 03101 Wind Sentry Anemometer

R. M. Young's Wind Sentry Anemometer and Vane accurately measure wind speed and direction. These sensors interface directly with Campbell dataloggers; no signal conditioning is required. The Wind Sentry is compatible with all of our contemporary dataloggers and many of our retired dataloggers (e.g., 21X, CR25X).

The cup anemometer measures wind speed. Rotation of its cup wheel produces an ac sine wave that is directly proportional to wind speed. The frequency of the ac signal is measured by a datalogger pulse count channel, then converted to engineering units (mph, m/s, knots). The Campbell Scientific version uses shielded bearings which lowers the anemometer's threshold.

Wind direction is sensed by a potentiometer. With the precision excitation voltage from the datalogger applied to the potentiometer element, the output signal is an analog voltage that is directly proportional to azimuth of the wind direction.

An ideal application for the Wind Sentry is Wind Profile Studies. For this application, the LLAC4 4-channel Low Level AC Conversion Module can be used to increase the number of Wind Sentrys measured by one datalogger. The LLAC4 allows datalogger control ports to read the anemometer's ac signals instead of using pulse channels. Dataloggers compatible with the LLAC4 are the CR200-series (ac signal \leq kHz only), CR500, CR850, CR1000, CR3000, and CR5000.

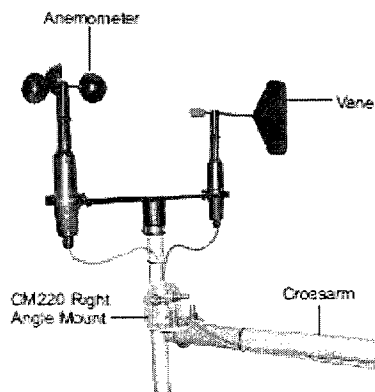
Ordering Information

Wind Sentry Options

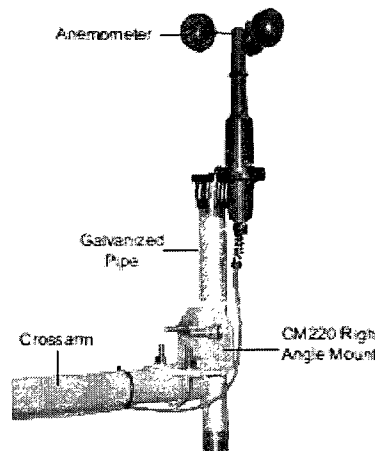
- 03001-L Wind Sentry Set; enter wind speed lead length, in feet, after the L, then enter wind direction lead length
- 03101-L Wind Sentry Anemometer; enter lead length, in feet, after the L.

Mounts

- 1049 $\frac{3}{4}$ " x 1" NU-RAIL Fitting for attaching the Wind Sentry to a crossarm, such as a CM202, CM204, or CM206.
- CM220 Right Angle Mounting Bracket for attaching the Wind Sentry to a crossarm, such as a CM202, CM204, or CM206.
- CM216 Sensor Mounting Kit for attaching the Wind Sentry to the top of a CM110, CM115, or CM120 stainless-steel tripod.



The 03001 is secured to one end of the CM206 cross-arm with the CM220 Right Angle Bracket.



When purchased separately, the Wind Sentry Anemometer is supplied with a galvanized 10" x 3/4" diameter threaded pipe, which mounts to a crossarm via a CM220 Mount or NU-RAIL fitting. A female, it can mount to an stainless-steel tripod via the CM216.

Recommended Lead Lengths

These lead lengths assume the sensor is mounted atop the tripod/tower via a CM202 crossarm.

CM6	CM10	CM110	CM115	CM120	UT10	UT20	UT30
10'	13'	13'	19'	24'	13'	24'	34'

Specifications

Wind Speed (Anemometer)

Range:	0 to 50 m s ⁻¹ (112 mph), gust survival 60 m s ⁻¹ (134 mph)
Sensor:	12 cm diameter cup wheel assembly, 40 mm diameter hemispherical cups
Accuracy:	±0.5 m s ⁻¹ (1.1 mph)
Turning Factor:	75 cm (2.5 ft)
Distance Constant (63% recovery):	2.3 m (7.5 ft)
Threshold:	0.5 m s ⁻¹ (1.1 mph)
Transducer:	Stationary coil, 1350 ohm nominal resistance
Transducer Output:	AC sine wave signal induced by rotating magnet on cup wheel shaft 100 mV peak-to-peak at 60 rpm; 6 V peak-to-peak at 3600 rpm
Output Frequency:	1 cycle per cup wheel revolution; 0.75 m s ⁻¹ per Hz
Cup Wheel Diameter:	12 cm (4.7 in)
Weight:	113 g (4 oz)

Wind Direction (Vane)

Range:	360° mechanical, 355° electrical (5° open)
Sensor:	Balanced vane, 16 cm turning radius
Accuracy:	±5°
Damping Ratio:	0.2
Delay Distance (50% recovery):	0.5 m (1.6 ft)
Threshold	0.8 m s ⁻¹ (1.8 mph) at 10° displacement; 1.8 m s ⁻¹ (4 mph) at 5° displacement
Transducer:	Precision conductive plastic potentiometer; 10 kohm resistance; 0.5% linearity; life expectancy 20 million revolutions. Rated 1 watt at 40°C, 0 watts at 125°C.
Transducer Output:	Analog dc voltage proportional to wind direction angle with regulated excitation voltage supplied by the datalogger
Vane Length:	22 cm (8.7 in)
Vane Weight:	170 g (6 oz)

Wind Sentry Assembly

Operating Temperature:	-50° to +50°C assuming non-icing conditions
Overall Height:	32 cm (12.6 in)
Crossarm Length:	40 cm (15.7 in) between instruments (center-to-center)
Mounting Diameter:	26.7 mm (1.05 in), mounts on standard 3/4 in. pipe

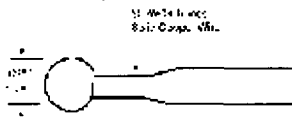


815 W. 1800 N. | Logan, Utah 84321-1784 | USA | phone (435) 753-2342 | www.campbellsci.com
Australia | Brazil | Canada | England | France | Germany | South Africa | Spain | USA (headquarters)

Copyright © 1994, 2007
Campbell Scientific, Inc.
Printed March 2007

Thermistors

YSI 44000 Series



Precision Interchangeable Thermistors

YSI thermistors provide highly accurate and stable temperature sensing for applications of temperature measurement, control, indication and compensation. Typical uses include precise measurements without the necessity of individual circuit calibration and with the advantage of precision interchangeability of sensors. Precise cold junction compensation of thermocouples may be designed directly without "bread boarding" after mathematically deriving the circuit because of the superior interchangeability of YSI precision thermistors.

Two interchangeability tolerances and two thermistor configurations are offered. Teflon encased thermistors allow exposure to hostile environment such as conductive or corrosive liquids and particulate suspensions. A stiff wire placed in the tube also allows the thermistor leads to be formed to various shapes with slight finger pressure.

Time Constant

The time required for a thermistor to indicate 63% of a newly impressed temperature is the time constant. For a thermistor suspended by its leads in a well-stirred oil bath it is 1 sec. max. for standard thermistor and 2.5 sec. max. for teflon encased thermistors. In still air it is 10 sec. max. for standard thermistors and 25 sec. max. for Teflon encased thermistors.

Dissipation Constant

The power in mW required to raise a thermistor 1°C above surrounding temperature is the dissipation constant. For all thermistors suspended by their leads in a well-stirred oil bath it is 8mW/°C min. or 1mW/°C in still air.

Stability

YSI thermistors are chemically stable and not significantly affected by aging or exposure to strong nuclear radiation.

Ordering Part #	Teflon Encased	Power Resistance Ohms @25°C	Resistance Ratio 25-125°C	Max Working Temp °C	Stor. & Work. Temp for best Stability °C	Price Standard
±0.2°C Interchangeability Tolerance 0 to 70°						
44001A		100	11.49	100°C	-80 - +50C	\$8.00
44002A		300	15.15	100°C	-80 - +50°C	8.00
44003A		1000	17.33	100°C	-80 - +50°C	8.00
44035		1000	17.33	100°C	-80 - +120°C	9.00
44004	44104	2252	29.26	150°C	-80 - +120°C	8.00
44005	44105	3000	29.26	150°C	-80 - +120°C	8.00
44007	44107	5000	29.26	150°C	-80 - +120°C	8.00
44017		6000	29.26	150°C	-80 - +120°C	8.00
44018		10K	29.26	150°C	-80 - +120°C	8.00
44008	44108	10K	23.51	150°C	-80 - +120°C	8.00
44008	44108	30K	29.15	150°C	-80 - +120°C	8.00
44011	44111	100K	34.82	150°C	-80 - +120°C	8.00
44014	44114	300K	48.02	150°C	-80 - +120°C	8.00
44015	44115	1Meg	61.96	150°C	-80 - +120°C	8.00
±0.1°C Interchangeability Tolerance 0 to 70°						
44033		2252	29.26	75°C	-80 - +75°C	\$9.00
44030		3000	29.26	75°C	-80 - +75°C	9.00
44034		5000	29.26	75°C	-80 - +75°C	9.00
44036		10K	29.26	75°C	-80 - +75°C	9.00
44037		8K	29.26	75°C	-80 - +75°C	9.00
44031		10K	23.51	75°C	-80 - +75°C	9.00
44032		30K	29.15	75°C	-80 - +75°C	9.00

1-925-706-7433

iProcesSmart.com

Omega FTB601B Ultra Low Flow Sensors

FTB600B Series Installation



IMPORTANT: READ INSTRUCTIONS THOROUGHLY BEFORE INSTALLING FLOW METER

Section 1 - Introduction

A. General Description

The FTB600B Series is an axial paddle wheel turbine type flow meter based on the pelton wheel principle. This unique patented design makes the FTB600B Series a very accurate, repeatable, linear device. Not only is the FTB600B Series precise, but it is also a rugged, trouble-free flow meter, which can be used in a wide variety of industries including: medical, pharmaceutical, chemical processing, pulp & paper, semiconductor, biotech, agriculture etc.

B. Principle of Operation

Fluid flows through the meter, first passing through a helical nozzle, which causes flow to spiral, rotating in a helical pattern. The spiraling fluid then impacts on the flat blade rotor causing the rotor to spin. The rotor is designed to immediately develop a rotation-induced friction free fluid bearing, thus eliminating any potential bearing wear. An infrared electro-optical transmitter and receiver is molded into the body of the meter along with a pair of miniature circuit boards, providing voltage stabilizers.* This design inherently bleeds off entrained gas, improving the accuracy of the meter.

* Clear, transparent & translucent fluids: must transmit infrared light.

1



FTB600B Series Installation

C. Material Characteristics of PVDF

(Polyvinylidene Fluoride)

1. Material of construction

Trade name - Kynar

All wetted parts of the FTB600B Series are PVDF, excluding the O-ring. Wetted parts include any part of the meter that will or could come in contact with the fluid.

List of wetted parts:

- | | |
|---------------------------------------|-------------|
| 1. Barbed fittings | 5. End caps |
| 2. Flow meter body | 6. Strainer |
| 3. Rotor | 7. Bearings |
| 4. Helical nozzle (Viton O-ring seal) | |

2. Chemical Composition

Polyvinylidene Fluoride is a fluoropolymer consisting of three basic materials (carbon, hydrogen and fluorine)

3. Effects of Various Fluids

- Weak acids - no effects
- Strong acids - attacked by fuming sulfuric & nitric acids at high temperature.
- Weak alkalis - no effects
- Strong alkalis - no effects
- Organic solvents - Resistant to most. Slight attack by some. Imbrittled by some amines, keystone and esters.

2

Section 2. - Operating Parameters

A. Temperature

Since the FTB600B Series has printed circuit boards molded into the body of the meter it is strongly recommended that 180°F not be exceeded. Exceeding 180°F can cause irreparable damage to the circuit boards.

B. Flow Ranges

The FTB600B Series is available in six different sizes, which cover a flow range from 0.1 to 120 lpm.

Specific flow ranges

FTB601B	0.1 to 2 lpm	(0.03 to 0.53 gpm)
FTB602B	0.3 to 9 lpm	(0.08 to 2.38 gpm)
FTB603B	0.5 to 15 lpm	(0.13 to 3.96 gpm)
FTB604B	1.0 to 30 lpm	(0.26 to 7.93 gpm)
FTB605B	2.5 to 75 lpm	(0.66 to 19.8 gpm)
FTB606B	4.0 to 120 lpm	(1.52 to 32 gpm)

WARNING

Over range may permanently damage the flow meter.

C. Recommended Viscosity

Range 1-5 cSt (w/o correction)

The effects of changing viscosity on the FTB600B Series are the same as any other turbine flow meter. It is important to remember that a turbine meter is a viscosity dependent device, where as the viscosity increases the linearity of the flow meter will decrease. (Water-like viscosities are ideally suited for use with the FTB600B Series) The FTB600B Series is factory calibrated with water.

Correction procedure for higher viscosity

For viscosities greater than 5 cSt consult the factory. The FTB600B Series can be used on fluids greater than 5 cSt, however, the K-factor (linearity) will change. This requires a recalibration of the FTB600B Series at the known viscosity to determine the new K-factor.

D. Filter Recommendations

Meter	Micron	Mesh
FTB601B	35	400
FTB602B	50	300
FTB603B	100	80
FTB604B	100	80
FTB605B	100	80
FTB606B	100	80

Section 4 - Infrared Sensor

A. Supply Voltage

24 Vdc. Do not exceed 24 Vdc. Doing so can cause overheating and eventual failure of all PC boards. Printed circuit boards are non-repairable.

B. Frequency Output

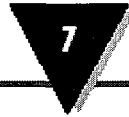
1. Square wave pulse, unscaled (See Figure 4-1)
2. Output impedance 75 ohms
3. Directly proportional to flow rate
4. Output - dc frequency
5. Offset 0.64 volts
6. Peak voltage = Supply voltage - 1.2 volts
7. Peak to peak voltage Supply voltage - 1.2 volts - 0.64 volts
8. Output signal cycle 66.7% (i.e. at 100 Hz there is a 6 millisecond "on" time and a 4 millisecond "off" time)
9. TTL/CMOS circuit compatibility. The FTB600B Series has an operational amplifier output, which has a high input impedance and a low output impedance.

7

Section 6 - Specifications

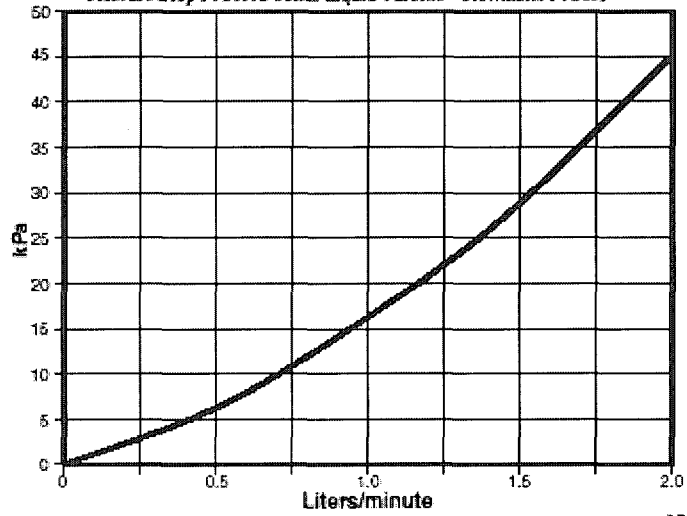
Accuracy:	±3% of reading
Repeatability:	±0.1% of reading
Linearity:	±1% of reading
Viscosity Range:	1 to 15 centistokes
Working Pressure:	150 PSIG at 175°F
Wetted Materials:	PVDF
Power Supply:	5 to 18 Vdc, 6 to 33 mA
Output Signal:	Unscaled square wave
Pressure Drop:	See Section 7

14



Section 7 - Pressure Drop Curves

Pressure Drop FTB600B Series Liquid Turbine - Flowmeter FTB601



15

Foxboro 873RS-ATPFGZ Resistivity Analyzer

1. Introduction

M1617-168 - July 2001

Standard Specifications

Table 1. Standard Specifications

Supply Voltages	-A 120 V ac -B 220 V ac -C 240 V ac -E 24 V ac -J 100 V ac
Supply Frequency	50 or 60 Hz, ± 3 Hz
Output Signal	I 4-20 mA isolated T 0-10 V dc isolated E 0-20 mA isolated
Ambient Temperature Limits	-25 to +55°C (-13 to +131°F)
Measurement Ranges	0 to 2.000 M Ω -cm (minimum) 0 to 5.000 M Ω -cm 0 to 10.00 M Ω -cm 0 to 15.00 M Ω -cm 0 to 20.00 M Ω -cm (maximum)
Temperature Measurement Range	-17 to +150°C (0 to 302°F)
Temperature Compensation Range	0 to 120°C (32 to 248°F)
Relative Humidity Limits	5 to 95%, noncondensing
Accuracy of Analyzer	$\pm 0.5\%$ of FSC range utilized at 25°C
Analyzer Identification	Refer to Figure 4.
Dimensions	Plastic Enclosure 92(H) x 92(W) x 183(L) mm, 3.6" x 3.6" x 7.6" Metal Enclosure 92(H) x 92(W) x 259(L) mm, 3.6" x 3.6" x 10.1"
Enclosure/Mounting Options	-P General Purpose (Noryl Plastic) Panel Mount -W Field Mount (Metal) Panel Mount -X Field Mount (Metal) Surface Mount -Y Field Mount (Metal) Pipe Mount -Z Field Mount (Metal) Movable Surface Mount
Approximate Mass	General Purpose Enclosure 0.68 kg (1.5 lb) Metal Field (NEMA 4X) Enclosure (with Brackets) Panel Mounting 1.54 kg (3.4 lb) Pipe Mounting 2.31 kg (5.1 lb) Fixed Surface Mounting 2.22 kg (4.9 lb) Movable Surface Mounting 3.13 kg (6.9 lb)
Instrument Response	Three second response for 90% change when used for single sensor measurement (when zero measurement damping is selected in Configuration Code). Temperature response is 15 seconds maximum. Seven second response for 90% change when used for dual sensor measurement.
Measurement Damping	Choice of 0, 10, 20, or 40 second, additional damping configurable from keypad. Damping affects displayed parameters and analog outputs.

7

Table 1. Standard Specifications (Continued)

Alarms	<ul style="list-style-type: none"> ◆ Two alarms configurable via keypad ◆ Individual set points continuously adjustable 0 to full scale via keypad ◆ Hysteresis selection for both alarms: 0 to 99% of full scale value, configurable via keypad ◆ Three timers for both alarms, adjustable 0 to 99 minutes, configurable via keypad. Allows for trigger timing and on/off control with delay. Timers can be set to allow chemical feed, then delay for chemical concentration control.
Alarm Contacts	Two independent, nonpowered Form C contacts. Rated 5 A noninductive, 125 V ac/30 V dc (minimum current rating 1 A). Inductive loads can be driven with external surge-absorbing devices installed across contact terminations.
Alarm Indication	Alarm status alternately displayed with measurement on LED display
Analog Output (dual outputs on metal units) Isolated, powered outputs	0-10 V (minimum load 1 k Ω) 0-20 mA (800 Ω maximum loop resistance) 4-20 mA (800 Ω maximum loop resistance)
RFI Susceptibility (when all sensor and power cables are enclosed in a grounded conduit)	Plastic General Purpose Enclosure: <0.5 V/m from 27 to 1000 MHz Metal Field Enclosure: >10 V/m from 27 to 1000 MHz
Electromagnetic Compatibility (EMC)	The Model 873RS Electrochemical Analyzer, 220 V ac or 240 V ac systems with metal enclosure, comply with the requirements of the European EMC Directive 89/336/EEC when the sensor cable, power cable, and I/O cables are enclosed in rigid metal conduit. See Table 3 on page 19. The plastic case units are intended for mounting in solid metal consoles or cabinets. The plastic case units will comply with the European EMC Directive 89/336/EEC when mounted in a solid metal enclosure and the I/O cables extending outside the enclosure are enclosed in solid metal conduit. See Table 3 on page 19.

Foxboro 871CC-A2 Contacting Resistivity Sensor

MI 611-151 - June 2006

1. Introduction

Model Code

Description	Model
Contacting Conductivity or Resistivity Sensor ^(a)	871CC
Sensor Mounting and Transducer	
Threaded Bushing, 3/4 NPT (100 k Ω Thermistor)	-A
Universal (100 k Ω Thermistor)	-B
Sanitary (100 k Ω Thermistor)	-C
Insertion (100 k Ω Thermistor)	-D
Twist-Lock (100 k Ω Thermistor)	-E
Threaded Bushing, 3/4 NPT with 1/2 NPT Conduit Connector (100 k Ω Thermistor)	-F
Dip Sensor (100 k Ω Thermistor)	-G
Threaded Bushing, 3/4 NPT, High Temperature (100 Ω RTD) ^(b)	-K
Sanitary, High Temperature (100 Ω RTD) ^(b)	-L
Insertion, High Temperature (100 Ω RTD) ^(b)	-M
Cell Factor and Electrode Material	
0.1 cm ⁻¹ , Titanium	2
10 cm ⁻¹ , Graphite	4
0.1 cm ⁻¹ , Monel (Mounting Codes -A, -G, and -K only)	6
Optional Selections (c)	
Nonstandard Cable Length (Specify Length) ^(d)	-3
No Spade Lug Terminals Attached to End of Cable	-4
Nonstandard Length Integral Cable Terminated in Connector. (For Mounting Codes -A and -G only) ^{(d),(e)}	-5
Integral Connector on Sensor. For Mounting Code -A only. ^{(e),(f)}	-6
Standard Length (6 m [20 ft]) Integral Cable Terminated in Connector. (For Mounting Codes -A and -G only. ^{(e),(f)}	-7
Cell Factor Determined in Foxboro Pure Water Loop	-9
Examples: 871CC-B2; 871CC-A4-34 (40 ft); 871CC-A2-349 (20 m)	

(a) When an 871CC Sensor is used with 873RS, 873ARS, 873CC, 873ACC, or 875CR Analyzer, Option Code -4 must be specified.

(b) The -K, -L, and -M sensors contain an integral 100 Ω RTD for automatic temperature compensation. This RTD is compatible with 873RS, 873ARS, 873CC, 873ACC, and 875CR Analyzers, and 870ITCR Transmitters. No temperature compensation can be applied when used with 870CC Transmitters.

(c) Except for Option Codes -3, -4, and -9 which may be combined (for example, -34, -349), only one Option Code may be specified.

(d) Maximum cable length
 For 870CC and 870ITCR Transmitters: 30 m (100 ft)
 For 873RS, 873ARS, 873CC, 873ACC, and 875CR Analyzers: 150 m (500 ft).

(e) Requires use of Patch Cord
 BS603UA for 3 m (10 ft) length
 BS805UB for other lengths per Sales Order up to 30 m (100 ft).

(f) Not recommended for resistivity measurement.

Standard Specifications

Sensor Type	Electrode Contacting Conductivity or Resistivity Sensor
Cell Factor	0.1 cm ⁻¹ or 10 cm ⁻¹ , as specified
Measurement Range	See Table 1.
Cable Length	
Standard	6 m (20 ft)
Other lengths	
873RS, 873ARS, 873CC,	Up to 150 m (500 ft)
873ACC, 875CR	Up to 30 m (100 ft)
870CC, 870ITCR	
Temperature and Pressure Limits	See Table 1.
Temperature Compensation	See Table 1.
Process-Wetted Materials	See Table 2.

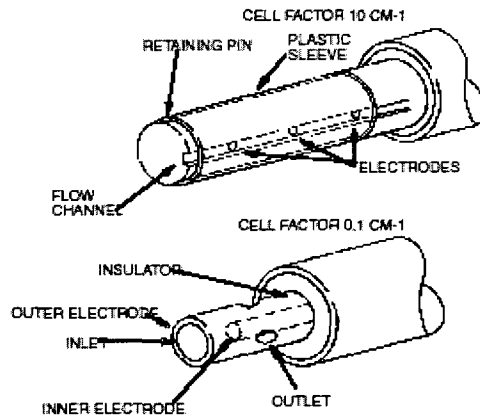


Figure 1. Sensors

Theory of Operation

871CC Sensors are “two electrode contacting conductivity sensors” used to measure conductivity or resistivity of process fluids. These measurement techniques do not measure specific ions; they cannot distinguish one ion type from another, but this technique has been used effectively, for example, to measure water purity or in the analysis of binary mixtures of electrolytes.

Conductance (or its reciprocal, resistance) is an electrical property of solutions that arises from the presence of electrically charged ions in electrolytes. When a conductance cell is placed in this solution and an electrical potential is applied across its electrodes, a current flows as the ions

migrate: the cations to the positively charged anode and the anions to the negatively charged cathode. In practice, a small amplitude alternating voltage is applied to prevent measurement errors due to electrolysis. The magnitude of the resulting alternating current flow is related to the number of charge carriers present and therefore the concentration of the electrolyte may be inferred from the conductance measurement.

Conductivity and resistivity are the more familiar terms used in the measurements of solutions. Specific conductivity, or more commonly conductivity, is the conductance as measured between opposite faces of a 1 cm cube of the solution. Bulk material measurements utilize this “reference state” and conductivity rather than conductance. The conductivity reading shows an almost direct relationship with impurities in the water and is the technique commonly seen in feedwater and pretreatment processes.

For ultrapure and pure water applications, a cell factor of 0.1 cm⁻¹ is selected and measurements are usually expressed as resistivity in units of MΩ•cm or in conductivity in units of uS/cm. Ultrapure water applications benefit from resistivity measurements because it more effectively resolves the range of interest. For more conductive solutions, a cell factor of 10 cm⁻¹ is used and measurements are expressed in mS/cm. When cells are interfaced to Foxboro analyzers or transmitters, effects of temperature on measurements can be compensated and readout in appropriate units can be displayed.

The 0.1 cm⁻¹ cell has two electrodes constructed with concentric cylinders which must be in contact with the solution being measured. The two electrodes are separated by an insulator inside the electrode. The 10 cm⁻¹ cell utilizes two graphite buttons for its measurement electrodes. A third electrode in the sensor eliminates a parallel measurement path that could occur outside of the electrode.

Table 1. Temperature/Pressure Limits, Measurement Ranges, and Temperature Compensation

Sensor Body Code	Temperature Limits	Pressure Limits	Applicable Conductivity and Resistivity Ranges		Temperature Compensator (Integral)
			Cell Factor 0.1 cm ⁻¹ (a)	Cell Factor 10 cm ⁻¹	
-A to -C	0 and 120°C (32 and 250°F)	-0.1 and +1.4 MPa (-15 and +200 psi)	0 to 1 through 0 to 200 μS/cm Conductivity Range	0 to 200 uS/cm through 0 to 20 mS/cm	100 kΩ Thermistor for use with 873RS, 873ARS, 873CC, 873ACC, and 875CR Analyzers; Also 870CC and 870TCR Transmitters.
-K to -M	120°C at 3.4 MPa (250°F at 500 psi) 150°C at 2.5 MPa (300°F at 375 psi) 175°C at 1.7 MPa (350°F at 250 psi)(b)		0 to 2 through 0 to 20 MΩ•cm Resistivity Range	Conductivity Range	100 Ω Platinum RTD for use with 873RS, 873ARS, 873CC, 873ACC, and 875CR Analyzers; Also 870TCR Transmitters.(c)

(a) All 0.1 cm⁻¹ cell factor sensors with Body Codes A through M are labeled with the exact cell factor and temperature cell factor. All 0.1 cm⁻¹ cell factor sensors are constructed and tested for an accuracy of better than ±2%.

(b) Specifications are for 0.1 cm⁻¹ cell factor sensors only. Maximum temperature for 10 cm⁻¹ cell factor is 150°C at 2.5 MPa (300°F at 375 psi).

(c) If -K, -L, or -M sensor is to be used with 870CC Series Transmitters, no automatic temperature compensation can be applied. RTD are not supported on these instruments.

Table 2. Process Wasted Parts

Cell Factor	Sensor Body Code	Seals/O-Rings	Insulator	Removable Sheath	Bushing	Electrodes
Sensors with 3/4 NPT Bushing or Twist-Lock Process Connection						
0.1 cm ⁻¹	-A	EPDM	Ryton (a)	None	Teflon-S Coated 300 Grade ss	Titanium or Monel, as specified by Model Code
	-F	EPDM	Ryton	None		
	-K	EPDM	ptfe (a)	None	None (Twist Lock)	
	-E	EPDM	Ryton	None		
10 cm ⁻¹	-A	EPDM	Noryl	ptfe (a)	Teflon-S Coated 300 Grade ss	High density graphite encapsulated in gold-plated cups
	F	EPDM	Noryl	ptfe		
	K	EPDM	ptfe	ptfe	None (Twist Lock)	
	E	EPDM	Noryl	ptfe		
Universal Mount, Insertion, and Dip Sensors						
0.1 cm ⁻¹	-B	EPDM	Ryton	None	316 ss	Titanium or Monel, as specified by Model Code
	-C	EPDM	Ryton	None	Noryl	
	-D	EPDM	Ryton	None	316 ss (Includes insertion shaft)	
	-M	EPDM	ptfe	None		
10 cm ⁻¹	-B	EPDM	Noryl	ptfe	316 ss	High density graphite encapsulated in gold-plated cups
	-C	EPDM	Noryl	ptfe	Noryl	
	-D	EPDM	Noryl	ptfe	316 ss (Includes insertion shaft)	
	-M	EPDM	ptfe	ptfe		
Sensors with Sanitary Fittings						
0.1 cm ⁻¹	-C	EPDM	Ryton	None	316 ss	Titanium or Monel, as specified by Model Code
	-L	EPDM	ptfe	None	316 ss	
10 cm ⁻¹	-C	EPDM	Noryl	ptfe	316 ss	High density graphite encapsulated in gold-plated cups
	-L	EPDM	ptfe	ptfe	316 ss	

Omega PH-5640 PH Electrode



INDUSTRIAL ELECTRODES

Flat Surface pH/ORP Industrial Electrodes

- ✓ Flat Surface Design
- ✓ 100 psig to 76°C/169°F
50 psig to 100°C/212°F
- ✓ Detachable Design for Easy Replacement
- ✓ Self-Cleaning, Abrasion Free

OMEGA's line of self-cleaning/abrasion-free pH and ORP electrodes are designed for applications in which fouling or coating can present a problem. The electrode has a non-protruding, flat surface design which minimizes coating and helps eliminate electrode breakage. It is this same design which utilizes flow sweeping past the electrode to scrub the electrode clean. The flat glass surface also prevents particles moving past the electrode from impinging upon its surface, thus eliminating abrasion and extending electrode life.

Easy to use and install, the electrodes are compatible with most pH equipment. Designed for such difficult applications as oily waste water, emulsions, lime slurries and flocculant coagulation, they may be the solution to your application problems.

Specifications (General)

Description: CPVC or PVDF gel-filled, double junction combination

pH Range: 0 to 14

Maximum Temperature:

PHE-6510/PHE-4580/PHE-6820

CPVC Body: 65.5°C (150°F)

-ACRYL Option: 87.7°C (190°F)

-ACRYL Option with PVDF

Body: 100°C (212°F)

PHE-5460: 87.7°C (190°F)

Pressure Rating: pH and ORP

Electrodes: 100 PSIG @ 75°C/170°F

85 PSIG @ 81°C/180°F

50 PSIG @ 100°C/212°F

Vacuum: Up to 5 psia

Impedance: Less than 300 megohms @ 25°C/77°F

Response Time: 95% in 5 seconds

Flat Surface Electrode Options

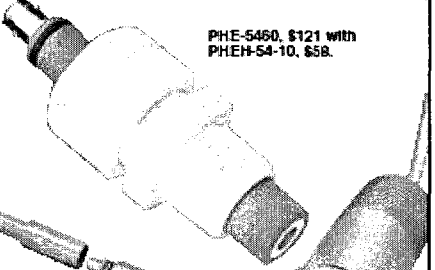
-HF For up to 5% HF Applications. Includes special glass formulation to give longer life in solutions containing acidic fluorides such as Hydrofluoric Acids pH Range: 0 to 12 pH Temp Range: 0 to 50°C (32 to 122°F) Maximum HF concentration is 10%

-LC Low conductivity Gel reference is designed for solutions with low ionic concentrations such as ultrapure or deionized water. LC gels contain 0.1M KCl vs. 3.5 M KCl in standard electrodes.

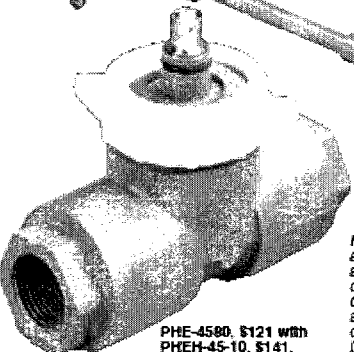
-ACRYL Acrylamide Gel (Acryl gel) is a thicker gel reference recommended for



PHE-6820, \$127 with
PHEH-68-10, \$270.

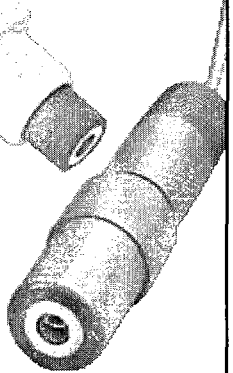


PHE-5460, \$121 with
PHEH-54-10, \$58.



PHE-4580, \$121 with
PHEH-45-10, \$141.

NOTE: Electrode and mounting assembly must be ordered separately. Cable and optional automatic temperature compensation (ATC) included with mounting assembly.



PHE-6510, \$121 with
PHEH-65-10, \$49.

Process flat surface electrodes and electrode holders are available in either Chlorinated Polyvinyl Chloride (CPVC) or in Polyvinylidene Fluoride (PVDF) materials. The material of construction must be the same for the electrode and the mounting assembly. CPVC designs are useful for a broad range of water-based applications. PVDF offers improved organic solvent resistance and longer life in higher temperature applications.

In CPVC designs, materials wetted by the sample include: CPVC, polyethylene, glass, O-rings made of Viton® and, for ORP electrodes, platinum.

Material wetted by the sample in PVDF designs include: PVDF, glass, O-rings made of Viton®, and, for ORP electrodes, platinum. CPVC and PVDF electrodes holders are not interchangeable.

Flat Surface Electrode Type

Series	Type	Applications
PHE-4580	By-Pass	Side stream mount for flows between 3 and 5 GPM
PHE-5460	In Line	½", 1" or 2" pipes or pipe tees
PHE-6510	Submersion	Tanks, flumes, sewer lines
PHE-6820	Insertion	Retractable for pressurized tanks main lines

longer life in operating temperatures above 65°C (150°F). This gel does not liquefy at high temperature, maximum temperature 100°C (212°F). It can also increase life in applications with aggressive chemicals by inhibiting diffusion of the chemicals.

-GL Ground Loop Interrupt Circuit built into the electrode can help eliminate ground loop problems up to potentials of 3 Volts.

Plastic tanks and piping are particularly susceptible because of poor earth grounding.

Dirty motors from pumps or mixers, other

electrical equipment and even conductivity probes leak voltage into the solution which feeds through the pH electrode and electronic circuit. This leads to invalid readings and shortened electrode life.

The DA series electrode combats these problems by utilizing a solution ground and internal battery powered ground interrupt circuit. The battery has an estimated 3 year service life.

Another benefit of this electrode is it will allow for long cable runs (up to 1000') because of the low impedance output of the built-in circuit.

For Sales & Service **1-800-82-66342**
1-800-TC-OMEGA
U.S.A. and Canada

Agilent 3615A DC Power Supply

Specifications and Supplemental Characteristics

INPUT: 115 Vac \pm 10%, 47-63 Hz, 0.8 A, 70 W
 100 Vac \pm 10%, 47-63 Hz, 0.8 A, 70 W
 230 Vac \pm 10%, 47-63 Hz, 0.4 A, 70 W

OUTPUT: E3610A: 0 to 8 V, 0 to 3 A or 0 to 15 V,
 0 to 2 A
 E3611A: 0 to 20 V, 0 to 1.5 A or 0 to 35 V,
 0 to 0.85 A
 E3612A: 0 to 60 V, 0 to 0.5 A or 0 to 120V,
 to 0.25 A

LOAD REGULATION:

Constant Voltage: - Less than 0.01% plus 2 mV for a full load to no load change in output current.
Constant Current: - Less than 0.01% plus 1 mA for a zero to maximum change in output voltage.

LINE REGULATION:

Constant Voltage: - Less than 0.01% plus 2 mV for any line voltage change within the input rating.
Constant Current: - Less than 0.01% plus 1 mA for any line voltage change within the input rating.

RIPPLE AND NOISE:

Constant Voltage: - Less than 200 μ V rms and 2 mV peak to peak (20 Hz - 20 MHz)
Constant Current: - Less than 200 μ A rms and 1 mA peak to peak (20 Hz - 20 MHz)

TEMPERATURE RANGE: 0 to 40°C for full rated output.
 Derate current 1% per degree C between 40°C-55°C

***TEMPERATURE COEFFICIENT:**

Constant Voltage: - Less than 0.02% plus 1 mV per degree C.
Constant Current: - Less than 0.02% plus 2 mA per degree C.

TRANSIENT RESPONSE TIME:

Less than 50 μ sec for output recovery to within 10 mV following a change in output current from full load to half load, or vice versa.

ISOLATION: \pm 240 Vdc

***OUTPUT DRIFT:**

Constant Voltage: - Less than 0.1% plus 5 mV total drift for 8 hours after an initial warm-up of 30 minutes.
Constant Current: - Less than 0.1% plus 10 mA total drift for 8 hours after an initial warm-up of 30 minutes.

METER ACCURACY: \pm 0.5% + 2 counts at 25°C \pm 5°C

***OVERLOAD PROTECTION:**

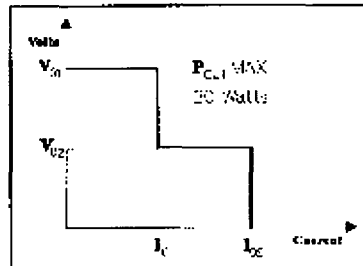
A continuously acting constant current circuit protects the power supply for all overloads including a direct short placed across the terminals. The constant voltage circuit limits the

output voltage in constant current operation.

***OUTPUT TERMINALS:**

Three output terminals are provided on the front panel. They are isolated from the chassis and either the positive or negative terminal may be connected to the ground terminal.

***OUTPUT CHARACTERISTICS**



NOTE: Output voltages higher than V_{02} are possible at low current when the high current range is selected.
 E3610A: $V_{01} = 15$ V $V_{02} = 8$ V $I_{01} = 2$ A $I_{02} = 3$ A
 E3611A: $V_{01} = 35$ V $V_{02} = 20$ V $I_{01} = 0.85$ A $I_{02} = 1.5$ A
 E3612A: $V_{01} = 120$ V $V_{02} = 60$ V $I_{01} = 0.25$ A $I_{02} = 0.5$ A

***METER RESOLUTION**

Voltage: E3610A 10 mV
 E3611A 100 mV
 E3612A 100 mV
 Current: E3610A 10 mA
 E3611A 10 mA
 E3612A 1 mA

***DOWN PROGRAMMING SPEED:** Maximum time for output voltage to change between 100% to 0.1% of maximum rated output voltage at NO LOAD condition.

E3610A: maximum 2.5 sec
 E3611A: maximum 1.0 sec
 E3612A: maximum 1.5 sec

***RESOLUTION:** Minimum output voltage or current change that can be obtained using panel controls.

E3610A: Voltage 10 mV Current 5 mA
 E3611A: Voltage 10 mV Current 5 mA
 E3612A: Voltage 100 mV Current 0.5 mA

COOLING: Convection cooling is employed.

WEIGHT: 8.4 lbs/3.8 Kg net, 8.3 lbs/4.2 Kg shipping.

(NOTE) * SUPPLEMENTAL CHARACTERISTICS

6487 Picoammeter Specifications

RANGE	5% DIGIT DEFAULT RESOLUTION	ACCURACY (1YR) ¹ ±(% RDC. + OFFSET) 18°-28°C, D-70% RH	TYPICAL RMS NOISE ²	TYPICAL ANALOG RISE TIME (10% TO 90%) ³	
				DAMPEN ⁴ OFF	ON
2 nA	10 fA	0.1 % + 400 fA	20 nA	4 ms	60 ms
20 nA	100 fA	0.2 % + 1 pA	20 nA	4 ms	60 ms
200 nA	1 pA	0.15 % + 10 pA	1 pA	500 μs	1 ms
2 μA	10 pA	0.15% + 100 pA	1 pA	300 μs	1 ms
20 μA	100 pA	0.1 % + 1 nA	100 pA	110 μs	110 μs
200 μA	1 nA	0.1 % + 10 nA	100 pA	110 μs	110 μs
2 mA	10 nA	0.1 % + 100 nA	10 nA	110 μs	110 μs
20 mA	100 nA	0.1 % + 1 μA	10 nA	110 μs	110 μs

TEMPERATURE COEFFICIENT: 1P-1°C & 28°-50°C. For each °C, add 0.1 × (% rdg + offset) to accuracy spec.

INPUT VOLTAGE BURDEN: <200V on all ranges except <1mV on 20mA range.

MAXIMUM INPUT CAPACITANCE: Stable to 50nF on all nA ranges and 2pA ranges; 1μF on 20μA and 200μA ranges, and on mA ranges.

MAXIMUM CONTINUOUS INPUT VOLTAGE: 505 VDC.

NWBR: (50 or 60Hz) <50dB.

ISOLATION (Ammeter Common or Voltage Source to chassis): Typically >1x10¹⁰ in parallel with <1nS.

MAXIMUM COMMON MODE VOLTAGE (Between Chassis and Voltage Source or Ammeter): 205 VDC.

MAXIMUM VOLTAGE BETWEEN VOLTAGE SOURCE AND AMMETER: 505 VDC.

ANALOG OUTPUT: Scaled voltage output (Inverting ZV full scale on all ranges); 2.5% ± 2mV.

ANALOG OUTPUT IMPEDANCE: <100Ω, DC-20kHz.

VOLTAGE SOURCE

Range (Max)	Step Size (Typical)	Accuracy ¹ ±(% RDC. + OFFSET) 18°-28°C, D-70% RH	Noise (p-p) 0.1-10 Hz	Temperature Coefficient	Typical Rise Time ² (10%-90%)	Typical Fall Time ³ (90%-10%)
<10.000	200μV	0.1% + 1mV	<5mV	(0.002% + 20pV)/°C	250 μs	150 μs
<10.000	1mV	0.1% + 1mV	<150μV	(0.002% + 200μV)/°C	150 μs	300 μs
<200.00	10mV	0.15% + 10mV	<1.5mV	(0.002% + 2mV)/°C	4.5 ms	1 ms

SELECTABLE CURRENT LIMIT: 2.5mA, 250μA, 25nA for 50V and 500V ranges, 25mA additional limit for 10V range. All current limits are ±20%/-35% of nominal.

WIDEBAND NOISE: <30mV p-p 0.1Hz - 20MHz.

TYPICAL TIME STABILITY: ±(0.002% + 1mV) over 24 hours at constant temperature (within 1°C, between 18°C - 28°C, after 5 minute settling).

OUTPUT RESISTANCE: <2.5Ω.

VOLTAGE SWEEPS: Supports linear voltage sweeps on fixed source range, one current or resistance measurement per step. Maximum sweep rate: 200 steps per second. Maximum step count: 3000. Optional delay between step and measure.

RESISTANCE MEASUREMENT (RV): Used with voltage source; resistance calculated from voltage sensing and measured current. Accuracy is based on voltage source accuracy plus ammeter accuracy. Typical accuracy better than 0.5% for readings between 1kΩ and 1TΩ.

ALTERNATING VOLTAGE RESISTANCE MEASUREMENT: Offers alternating voltage resistance measurements for resistances from 10pΩ to 10¹⁰Ω. Alternates between DV and user-selectable voltage up to ±50V.

¹ At 1 PLC - limited to 60 rds/sec under this condition.

² At 6 PLC, ± standard deviation, 100 readings, filter off, capped input - limited to 10 rds/sec under this condition.

³ Measured at analog output with resistive load >5kΩ.

⁴ Maximum rise time can be up to 25% greater.

⁵ Accuracy does not include output resistance/lead regulation.

⁶ Rise Time is from 10V to ± full-scale voltage (increasing magnitude).

⁷ Fall Time is from ± full-scale voltage to 0V (decreasing magnitude).

⁸ For C_{eq} active loads, add C_{eq}/R_{load} to Rise Time, and C_{eq}/I_{max} to Fall Time.

⁹ Measured with I/O connected to chassis ground.

REMOTE OPERATION

IEEE-488 BUS IMPLEMENTATION: SCPI (IEEE-488.2, SCPI-1996.0) DDC (IEEE-488.1).

LANGUAGE EMULATION: Keithly Model 485/487 emulation via DDC mode.

RS-232C IMPLEMENTATION:

Supports: SCPI 1996.0.

Bit Rates: 300, 600, 1200, 2400, 4800, 9600, 19.2k, 38.4k, 57.6k.

Protocols: Xon/Xoff, 7 or 8 bit ASCII, parity odd/even/none.

Connector: DB-9 TRD/ROD/GND.

GENERAL

AMMETER INPUT CONNECTOR: Three bayonet on rear panel.

ANALOG OUTPUT CONNECTOR: Two banana jacks on rear panel.

VOLTAGE SOURCE OUTPUT CONNECTOR: Two banana jacks on rear panel.

INTERLOCK CONNECTOR: 4 pin DIN.

TRIGGER LINE: Available, see manual for usage.

DISPLAY: 12 character vacuum fluorescent.

DIGITAL FILTER: Median and averaging (selectable from 2 to 100 readings).

RANGING: Automatic or manual.

AUTO-RANGING TIME: <250ms (analog filter off, 1 PLC).

OVERRANGE INDICATION: Display reads "OVERFLOW".

CONVERSION TIME: Selectable 201 PLC to 80 PLC (60PLC under 50Hz operation); (Adjustable from 200 μs to 1s).

READING RATE:

To Internal buffer: 1000 readings/second¹.

To IEEE-488 bus: 900 readings/second².

BUFFER: Stores up to 3000 readings.

PROGRAMS: Provide front panel access to IEEE address, choice of engineering units or scientific notation, and digital calibration.

EMC: Conforms with European Union Directive 89/326/EEC,

EN61326-1.

SAFETY: Conforms with European Union Directive TS/23/VEH,

EN61010-1, CAT 2.

ENVIRONMENT:

Operating: 0°-50°C relative humidity 70% non-condensing, up to

35°C. Above 35°C, derate humidity by 5% for each °C.

Storage: -10°C to +65°C.

WARM-UP: 1 hour to rated accuracy (see manual for recommended

procedure).

POWER: 100-120V or 230-240V, 50-60Hz, (50VA).

PHYSICAL:

Case Dimensions: 90mm high × 214mm wide × 303mm deep (3 1/2" h. × 8 1/2" w. × 11 7/8" d.).

Working Dimensions: From front of case to rear including power cord and IEEE-488 connector: 354mm (13.5 inches).

NET WEIGHT: <4.7 kg (<10.5 lbs).

Notes:

¹ 0.01 PLC, digital filter on E front panel dE, menu item off.

² Binary transfer mode: IEEE-488.1.

³ Measured from trigger to to menu complete.

Specifications are subject to change without notice.

Rev. A
10/25/02

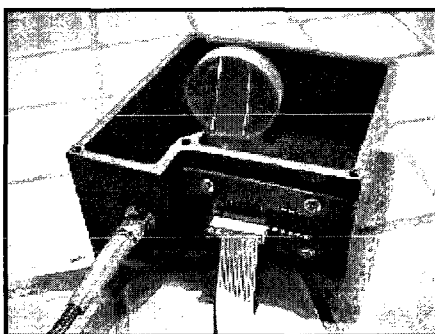
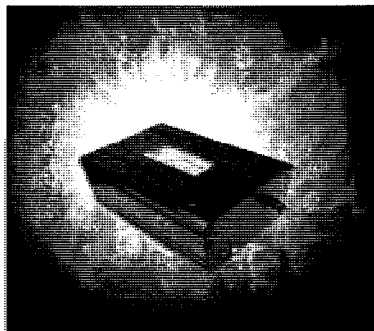
StellarNet EPP200C UV-VIS 100 μ m Slit Spectroradiometer

EPP2000C Concave Grating Spectrometers for UV-VIS & NIR Applications

The StellarNet concave grating spectrometers deliver high optical performance in a small ruggedized package with fiber optic input and a USB-2 & parallel PC interface. The instruments are exceptionally robust with no moving parts and are packaged in small metal enclosures (2.75 x4 x6 inch) for spectroscopy measurements in the Lab, Field, QC areas, or process lines.

Two models for UV-VIS (190-850nm or 280-900nm), and two Super Range models (200-1080nm or 220-1100nm).

The EPP2000C spectrometers utilize a 40mm diameter concave grating with aberration correction to provide superb spectral imaging. This significantly improves spectral shapes by reducing coma and astigmatism found in plane grating spectrograph designs.



The flat field spectrograph architecture does not utilize mirrors and therefore provides the lowest possible stray light in the UV with a holographic grating. A multi-band filter is integrated into the spectrograph to provide order sorting and prevent optical aliasing. The instruments optical input is a standard SMA-905 connector, using single strand fiber optic cable with typical silica core diameters of 400 μ m, 600 μ m, and 1000 μ m.

The SpectraWiz software is included free to accurately measure emissions, reflectance, transmission, absorption, fluorescence, concentrations, & absolute intensities for SpectroRadiometry. TEC cooling optional.

Specifications	EPP2000C \$2750	EPP2000C-SR \$3495
Dynamic range:	2000:1 with 6 decades	Dimensions: 69 x 100 x 150 mm
Optical resolution:	25 μ m slit-1nm, SR-1.5nm	Power consumption: 100 mA @ 5 VDC
Detector type:	2048 pixel CCD	Interface: USB-2 cable and parallel
Pixel size:	14 μ m wide x 200 μ m tall	Digitizer: 16-bit
Standard UV-VIS models:	C=190-850nm, CNR=280-900nm	Detector integration: 1ms to 65s
Super range -SR models:	C-SR=200-1080nm, 220-1100nm	Slit size options: 14, 25, 50, 100, 200 μ m
Concave Grating:	Aberration corrected	Stray light: .02% at 435nm, .3% at 200nm
Grating type:	Holographic, 590g/mm	Fiber optic input: SMA905 0.22na single fiber
Spectrograph:	f/2, Flat field - No mirrors	Operating systems: Win98/Me/00/XP/Vista
Order sorting filter:	Integrated multi-band	Software included: SpectraWiz program & apps
Signal to noise:	1000:1	Also free programs for: LabView/VC/VBA/Delphi



14390 Carlson Circle, Tampa, Florida, 33626 USA
Voice: +1-813-855-8687 Fax: +1-813-855-2279

www.StellarNet-Inc.com
ContactUs@StellarNet-Inc.com

LI-1800 Spectroradiometer

DETECTOR

After emerging from the monochromator, the radiant power is received by the detector which produces a current proportional to the amount of radiation. This current signal is amplified, converted to a voltage, passed through an analog-to-digital converter, and is made available to the internal microcomputer.

The detector in the LI-1800 is a silicon photodiode. Silicon has several advantageous properties: it is mechanically rugged, it does not fatigue, and it has good temperature and long term stability. The temperature stability is best at wavelengths between 400 and 950 nm. Beyond these wavelengths, the silicon's temperature stability degenerates markedly. This is not a problem as long as measurements are taken at about the same temperature at which the instrument was calibrated.

The LI-1800 is calibrated at approximately 25 °C. The temperature dependence of the detector is:

- 0.1% / °C at 350 nm
- 0.05% / °C from 400 - 950 nm
- 0.5% / °C at 1000 nm
- 1.0% / °C at 1100 nm

If the LI-1800 is to be used at temperatures greatly different from 25 °C it is best to calibrate it, or near the operating temperature. This is particularly true if high accuracy is desired in the 1000-1100 nm waveband.

2.3 Instrument Calibration

The LI-1800 has been calibrated by LI-COR and the calibration information is stored as data files in the LI-1800's memory. Calibration of the LI-1800 involves the use of a standard lamp of known spectral power distribution to establish the instrument's response function. The calibration files relate the detector signal (mV) to the irradiance (or radiance) at each wavelength.

When the LI-1800 is calibrated, all elements of the optical path (the radiation receptor, fiber probe (if any), filter wheel, monochromator slits and grating, silicon detector) affect the calibration file. If the radiation receptor or some other optical component is changed, the calibration file becomes invalid for the new optical configuration. Accordingly, each optical receptor used with the LI-1800 requires a unique calibration file. LI-COR has designated the following calibration files for the various optical inputs:

COSC	Calibration file for the standard cosine receptor.
RCOS	Calibration file for the 1800-11 Remote Cosine Receptor.
TELA	Calibration file for 1800-06 Telescope Option A (15° field of view).
TELB	Calibration file for 1800-06 Telescope Option B (3° field of view).
TELE	Calibration file for the combination of 1800-06 options C and E.
TELF	Calibration file for the combination of 1800-06 options C and F.

The presence of these files in the LI-1800 can be verified using the list command (*L). Note that the 1800-12 External Integrating Sphere uses a reference scan as the standard and does not need a unique calibration file (see Section XT).

Absolute calibration of the LI-1800 is derived from lamp standards of spectral irradiance ($W m^{-2} nm^{-1}$), which produce a known output when operated according to prescribed conditions. At LI-COR, working standard lamps are used for all factory calibrations. A working standard is prepared by calibrating against a primary standard supplied by the U.S. National Bureau of Standards (NBS). Both primary and working standards are 1000 watt quartz tungsten halogen lamps operating at a color temperature of 3150 °K. The maximum uncertainty of the spectral irradiance for a working standard is estimated to be 4% at 300 nm and 2% from 500 to 1100 nm.

An absolute calibration file is generated for each LI-1800 receptor by averaging 10 scans of the working standard lamp in 1 nm steps for the full wavelength range (e.g. 300-1100 nm). This generates a detector output file which contains the average photodiode signal (in millivolts) for 10 scans at each wavelength. The calibration file is computed by dividing the detector output file by a lamp file containing the true spectral irradiance ($W m^{-2} nm^{-1}$) of the lamp. LI-COR calibrations are stated as ± 3 to 10% (depending on wavelength) relative to NBS. It is important to note that these values apply only at the time of calibration. Instrument drift with time will add to the uncertainties.

The LI-1800 measures from unknown radiation sources (E_u) following the equation:

$$E_u = \frac{D_u}{K}$$

where $K = \frac{D_s}{E_s}$

and D_u = detector output with unknown source (mV)
 K = calibration file = spectroradiometer's response function ($mV m^2 nm W^{-1}$)
 D_s = detector output with standard source (mV)
 E_s = absolute standard of spectral irradiance ($W m^{-2} nm^{-1}$)

APPENDIX C

MEASUREMENT UNCERTAINTY ANALYSIS

Note: All formal uncertainty analysis were performed using Mathcad version 2001

Thermistor Measurement Uncertainty Analysis

Uncertainty in thermistor resistance measurement

Excitation Voltage

$$V_x := 1.85V$$

Completion Resistor

$$R_c := 200000\text{ohm}$$

From Steinhart worksheet,

At 25 C, V1h and V1l will be 241mV

At 70 C, V1h and V1l will be 48mV

For this analysis it is sufficient to assume that the voltage drop due to the lead resistance is negligible and V1h=V1l

$$V1h := \frac{241}{1000}V$$

$$V1l := V1h$$

Thermistor resistance

$$R_t := \left(\frac{V1h - 2 \cdot V1l}{V1h - V_x} \right) \cdot R_c$$

Uncertainty of measurement (provided by Campbell Sci)
.05% of full scale 250 mv- (250 mv)

Derivative of thermistor resistance W/R to V1h

$$\theta_{V1h} := \frac{d}{dV1h} \left(\frac{V1h - 2 \cdot V1l}{V1h - V_x} \right) \cdot R_c$$

$$u_{V1h} := \frac{250 - (-250)}{1000} \cdot \frac{.05}{100} V$$

Derivative of thermistor resistance W/R to V1l

$$\theta_{V1l} := \frac{d}{dV1l} \left(\frac{V1h - 2 \cdot V1l}{V1h - V_x} \right) \cdot R_c$$

Uncertainty of measurement (provided by Campbell Sci)

$$u_{V1l} := u_{V1h}$$

Derivative of thermistor resistance W/R to Vx

$$\theta_{V_x} := \frac{d}{dV_x} \left(\frac{V1h - 2 \cdot V1l}{V1h - V_x} \right) \cdot R_c$$

Uncertainty of excitation voltage (provided by Campbell Sci)

$$u_{V_x} := \frac{2.5}{1000} V$$

Derivative of thermistor resistance W/R to Rc

$$\theta_{R_c} := \frac{d}{dR_c} \left(\frac{V1h - 2 \cdot V1l}{V1h - V_x} \right) \cdot R_c$$

Uncertainty of resistor value

$$u_{R_c} := 200000 \cdot .001\text{ohm}$$

Uncertainty of thermistor resistance measurement at temperature specified

$$u_R := \sqrt{|\theta_{V1h} \cdot u_{V1h}|^2 + |\theta_{V1l} \cdot u_{V1l}|^2 + |\theta_{V_x} \cdot u_{V_x}|^2 + |\theta_{R_c} \cdot u_{R_c}|^2}$$

$$u_R = 87.319 \Omega$$

Uncertainty in absolute temperature measurement

Steinhart Coefficients as given by YSI

$$A := .000928495705 \quad B := .000222131430 \quad C := .000000123750$$

Temperature (F) as a function of resistance

$$T := \left[\frac{1}{A + B \cdot \ln\left(\frac{R_t}{\Omega}\right) + C \cdot \left(\ln\left(\frac{R_t}{\Omega}\right)\right)^3} \right] \cdot K$$

Derivative of Temperature resistance W/R to R_t

$$\theta_{R_t} := \frac{d}{dR_t} \left[\frac{1}{A + B \cdot \ln\left(\frac{R_t}{\Omega}\right) + C \cdot \left(\ln\left(\frac{R_t}{\Omega}\right)\right)^3} \right] \cdot K$$

Uncertainty of thermistor given by YSI

$$u_t := .1K$$

$$u_T := \sqrt{(\theta_{R_t} \cdot u_R)^2 + (u_t)^2} \quad u_T = 0.121 K$$

The uncertainty in the temperature measurement ranges from .121C @ 25C, and .359 C @ 70C

Uncertainty in resistivity measurement

The resistivity (ohm cm) is calculated from the measured voltage (V) as

Corrected Measurement

Absolute Measurement

$$R_c(V_m) := (.8166876 \cdot V_m - .0013383474) \cdot 10^6 \text{ ohm} \cdot \text{cm} \quad R_a(V_m) := (.8154392 \cdot V_m - .0012565137) \cdot 10^6 \text{ ohm} \cdot \text{cm}$$

The uncertainty of the voltage measurement as given by Campbell is (.05% of full scale 2500mV-(-2500mV))

$$u_V := \frac{.05}{100} \cdot \frac{2500 - (-2500)}{1000} \text{ V}$$

The derivatives of the resistivity with respect to voltage is

Corrected Measurement

Absolute Measurement

$$\theta_{VC} := .8166876 \text{ ohm} \cdot \frac{\text{cm}}{\text{V}}$$

$$\theta_{VA} := .8154392 \text{ ohm} \cdot \frac{\text{cm}}{\text{V}}$$

The uncertainty of the analyzer and sensor as reported by foxboro is given as .5% of the full scale

$$u_s := \frac{.5}{100} \cdot 2.00 \cdot 10^6 \text{ ohm} \cdot \text{cm}$$

The total uncertainties of the resistivity measurements are given by

Corrected Measurement

Absolute Measurement

$$u_{RC} := \sqrt{(u_V \cdot \theta_{VC})^2 + u_s^2}$$

$$u_{RA} := \sqrt{(u_V \cdot \theta_{VA})^2 + u_s^2}$$

$$u_{RC} = 1 \times 10^4 \text{ ohm} \cdot \text{cm}$$

$$u_{RA} = 1 \times 10^4 \text{ ohm} \cdot \text{cm}$$

PH Uncertainty Analysis

Uncertainty in PH measurement

Uncertainty of differential voltage measurement (provided by Campbell Sci) .05% of full scale 250 mv- (-250 mv)

The uncertainty of the sensor itself is estimated as

$$u_{\Delta V} := \frac{250 - (-250)}{1000} \cdot \frac{.05}{100} \text{ V}$$

$$u_s := .05$$

The PH as a function of voltage and temperature is given by

$$\text{PH}(\Delta V, T) := \frac{-0.1755 \cdot 1000 \cdot \Delta V \cdot T}{\text{V} \cdot 298.15 \text{K}} + 7.23199$$

This function estimates the slope of the curve at temperature T using the data from the calibration at 25C

Derivative of PH W/R to ΔV

Derivative of PH W/R to T

$$\theta_{\Delta V}(T) := \frac{-0.1755 \cdot 1000 \cdot T}{\text{V} \cdot 298.15 \text{K}}$$

$$\theta_T(\Delta V) := \frac{-0.1755 \cdot 1000 \cdot \Delta V}{\text{V} \cdot 298.15 \text{K}}$$

The temperature uncertainty is defined as the difference between the calibration temperature and the temperature at which the measurement is made

$$u_T(T) := (T - 298.15 \text{K})$$

The uncertainty in the PH measurement can be expressed as

$$u_{\text{PH}}(\Delta V, T) := \sqrt{(\theta_{\Delta V}(T) \cdot u_{\Delta V})^2 + (\theta_T(\Delta V) \cdot u_T(T))^2 + u_s^2}$$

This can be plotted at the high and low temperatures used for the experiment as a function of ΔV

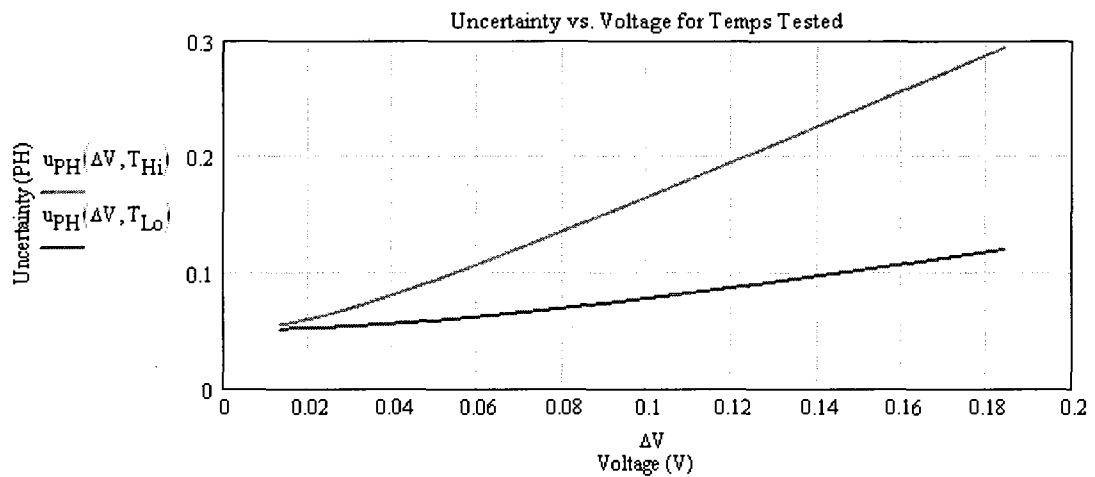
The ΔV measured during calibration is defined

$$\Delta V := \frac{13}{1000} \text{ V}, \frac{13.1}{1000} \text{ V}, \frac{184}{1000} \text{ V}$$

The two temperatures used for the experiment are

$$T_{Hi} := (273.15 + 51.7) \text{ K}$$

$$T_{Lo} := (273.15 + 35.0) \text{ K}$$



The minimum PH observed during the tests was 4.85
This corresponds to a voltage of .135

At the higher temperature, this corresponds to a maximum estimated uncertainty of .22 PH

$$u_{PH}(.135 \text{ V}, T_{Hi}) = 0.218$$

Uncertainty in Cell Voltage measurement

The uncertainty for the cell electrode to ground differential measurement in the highest range used is

$$u_{\Delta V} := \frac{.05}{100} \cdot \frac{2500 - (-2500)}{1000} \text{ V}$$

The uncertainty for the cell reference electrode to ground differential measurement in the highest range used is

$$u_{\Delta VR} := \frac{.05}{100} \cdot \frac{2.5 - (-2.5)}{1000} \text{ V}$$

The maximum uncertainty of the reference cell temperature measurement is estimated as (this estimate is based upon the American National Standards Institute special limits of error for type T thermocouple and the estimated error of the reference junction provided by Campbell Scientific

$$u_T := 1 \text{ K}$$

Electrode potential relative to the SHE is calculated as a function of the two differential voltage measurements and one temperature measurement

$$\Delta V_{\text{SHE}}(\Delta V, \Delta VR, T) := \Delta V - \Delta VR + \frac{\left(-0.001 \cdot \frac{T^2}{\text{K}^2} - .842 \cdot \frac{T}{\text{K}} + 222.9 \right)}{1000} \text{ V}$$

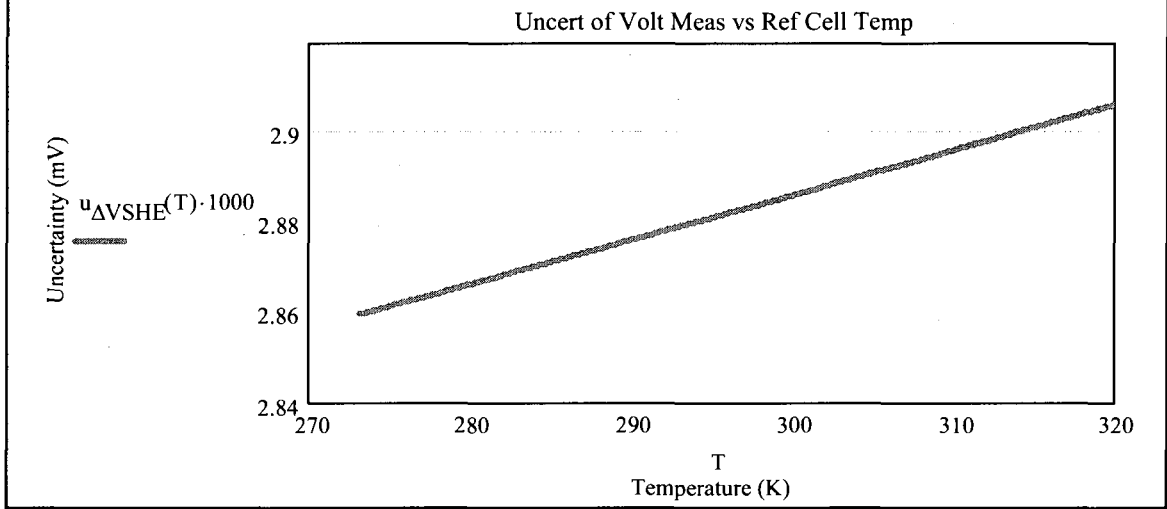
The partial derivatives of the function are

$$\theta_{\Delta V} := 1 \quad \theta_{\Delta VR} := 1 \quad \theta_T(T) := \frac{d}{dT} \frac{\left(-0.001 \cdot \frac{T^2}{\text{K}^2} - .842 \cdot \frac{T}{\text{K}} + 222.9 \right)}{1000} \text{ V}$$

The total uncertainty for the anode or cathode potential measurement relative to the SHE is estimated as

$$u_{\Delta V_{\text{SHE}}(T)} := \sqrt{(\theta_{\Delta V} \cdot u_{\Delta V})^2 + (\theta_{\Delta VR} \cdot u_{\Delta VR})^2 + (\theta_T(T) \cdot u_T)^2}$$

T := 273.15K, 273.26K.. 320K



Uncertainty in current measurement

The current is calculated using Ohms Law

$$I = \frac{\Delta V}{R}$$

The resistance of the precision shunt resistor is

$$R = .715\Omega$$

The uncertainty of the voltage measurements in the two possible measurement ranges (based on current levels observed during tests) as given by Campbell is

$$u_{\Delta V}(\Delta V) := \begin{cases} \left[\frac{.05}{100} \cdot \frac{2.5 - (-2.5)}{1000} \text{ V} \right] & \text{if } \Delta V \leq \frac{2.5}{1000} \text{ V} \\ \left[\frac{.05}{100} \cdot \frac{7.5 - (-7.5)}{1000} \text{ V} \right] & \text{otherwise} \end{cases}$$

Derivative of current W/R to ΔV

$$\theta_{\Delta V} = \frac{1}{R}$$

Derivative of current W/R to R

$$\theta_R(\Delta V) = \frac{-\Delta V}{R^2}$$

Uncertainty of resistor (.1%)

$$u_R = .001 \cdot R$$

The total uncertainty of the current measurement as a function of ΔV is

$$u_I(\Delta V) = \sqrt{(\theta_{\Delta V} \cdot u_{\Delta V}(\Delta V))^2 + (\theta_R(\Delta V) \cdot u_R)^2}$$

Or as a function of the measured current

$$u_I(I) = \sqrt{\left(\theta_{\Delta V} \cdot u_{\Delta V} \left(\frac{I}{R} \right) \right)^2 + \left(\theta_R \left(\frac{I}{R} \right) \cdot u_R \right)^2}$$

For the tests, the measured current was less than 10 ma

$$I := 0\text{A}, \frac{.001}{1000} \text{A} .. \frac{10}{1000} \text{A}$$

REFERENCES

- [1] Licht, S., et al., Over 18% Solar Energy Conversion to Generation of Hydrogen Fuel: Theory and Experiment for Efficient Solar Water Splitting. International Journal of Hydrogen Energy. 26 (2001) 653-659
- [2] Fujishima, A., Honda, K., Electrochemical Photolysis of Water at a Semiconductor Electrode. Nature. 238 (1972) 37-38
- [3] Yoneyama, H., Sakamoto, H., Tamura, H., A Photo-Electrochemical Cell with Production of Hydrogen and Oxygen by a Cell Reaction. Electrochimica. 20 (1975) 341-345
- [4] Mavroides, J., et al., Photoelectrolysis of Water in Cells with TiO₂ Anodes. Mat. Res. Bull. 10 (1975) 1023-1030
- [5] Tamura, H., et al., The Quantum Yields of Photoelectric Decomposition of Water at TiO₂ Anodes and P-Type GaP Cathodes. Journal of Electroanalytical Chemistry. 80 (1977) 357-363
- [6] Rouse, L., Band Bending at the Surface of N-TiO₂ Photoanodes Used to Dissociate Water Under Solar Illumination. Mat. Res. Bull. 13 (1978) 861-868
- [7] Houlihan, J. et al. Doped Polycrystalline TiO₂ Electrodes for the Photo-Assisted Electrolysis of Water. Mat. Res. Bull. 13 (1978) 1205-1212
- [8] Houlihan, J., Walsh, E., Mulay, L., Improved Solar Energy Conversion Efficiencies for the Photocatalytic Production of Hydrogen Via TiO₂ Semiconductor Electrodes. Mat. Res. Bull. 11 (1976) 1191-1198
- [9] Bockris, J., Uosaki, K., Photoproduction of Hydrogen: Potential Dependence of the Quantum Efficiency as a Function of Wavelength. Energy. 1 (1976) 143-145
- [10] Paleocrassas, S., Photocatalytic Hydrogen Production: A Solar Energy Conversion Alternative. Solar Energy. 16 (1974) 45-51
- [11] Salvador, P., The Behaviour of Aluminum-Doped n-TiO₂ Electrodes in the Photoassisted Oxidation of Water. Mat. Res. Bull. 15 (1980) 1287-1294

- [12] Salvador, P., The Influence of Niobium Doping of n-TiO₂ Electrodes in Water Photoelectrolysis. Solar Energy Materials. 2 (1980) 413-421
- [13] Sato, S., White, J., Photodecomposition of Water Over Pt/TiO₂ Catalysts. Chemical Physics Letters 72 (1980) 83-86
- [14] Wrighton, M., et al., Photoelectrolysis of Water by Irradiation of Platinized n-Type Semiconducting Metal Oxides. Journal of Solid State Chemistry 22 (1977) 17-29
- [15] Yazawa, K., et al., Semiconducting TiO₂ Films for Photoelectrolysis of Water. International Journal of Hydrogen Energy. 4 (1978) 205-209
- [16] Saberio, S., et al., Comparisons of the Photoelectric Properties of the System TiO₂-x with the System TiO₂-x-F-x. Mat. Res. Bull. 15 (1980) 1287-1294
- [17] Butler, M., Nasby, R., Quinn, R., Tungsten Trioxide as an Electrode for Photoelectrolysis of Water. Solid State Communications 19 (1976) 1011-1014
- [18] Butler, M., Photoelectrolysis and Physical Properties of the Semiconducting Electrode WO₃. Journal of Applied Physics. 48 (1977) 1914-1920
- [19] Maruthamuthu, P., Ashokkumar, M., Hydrogen Production with Visible Light Using Metal Loaded WO₃ and MV²⁺ in Aqueous Medium. International Journal of Hydrogen Energy. 14 (1989) 275-277
- [20] Milczarek, G., et al., Optimization of a Two-Compartment Photoelectrochemical Cell for Solar Hydrogen Production. International Journal of Hydrogen Energy. 28 (2003) 919-926
- [21] Murphy, A., et al., Efficiency of Solar Water Splitting Using Semiconductor Electrodes. International Journal of Hydrogen Energy. 31 (2006) 1999-2017
- [22] Arouttiounian, V., Arakelyan, V., Shahnazaryan, G., Metal Oxide Photoelectrodes for Hydrogen Generation using Solar Radiation-Driven Water Splitting. Solar Energy. 78 (2005) 581-592
- [23] Bak, T., et al., Photo-Electrochemical Hydrogen Generation from Water Using Solar Energy. Materials Related Aspects. International Journal of Hydrogen Energy. 27 (2002) 991-1022
- [24] Enesca, A., Duta, A., Scoonman, J., Study of Photoactivity of Tungsten Trioxide (WO₃) for Water Splitting. Thin Solid Films. 515 (2007) 6371-6374
- [25] Liu, Y., et al., A Composite Visible-Light Photocatalyst for Hydrogen Production. Journal of Power Sources. 159 (2006) 1300-1304

- [26] Hu, C., Nian, J., Teng, H., Electrodeposited P-Type Cu₂O as Photocatalyst for H₂ Evolution from Water Reduction in the Presence of WO₃. Solar Energy Materials and Solar Cells. 92 (2008) 1071-1076
- [27] Mills, A., Valenzuela, M., Photo-Oxidation of Water Sensitized by TiO₂ and WO₃ in Presence of Different Electron Acceptors. Revista Mexicana De Fisica. 50 (2003) 287-296
- [28]] Maruthamuthu, P., Ashokkumar, M., Hydrogen Generation using Cu(II)/WO₃ and Oxalic Acid by Visible Light. International Journal of Hydrogen Energy. 13 (1988) 677-680
- [29] Maruthamuthu, P., Ashokkumar, M., Doping Effects of Transition Metal Ions on the Photosensitization of WO₃ Particles. Solar Energy Materials. 17 (1988) 433-438
- [30] Maruthamuthu, P., Ashokkumar, M., Hydrogen Evolution from Water with Visible Radiation in Presence of Cu(II)/WO₃ and Electron Relay. International Journal of Hydrogen Energy. 14 (1989) 525-528
- [31] Maruthamuthu, P., Ashokkumar, M., Hydrogen Production with Visible Light using Metal Loaded-WO₃ and MV²⁺ in Aqueous Medium. International Journal of Hydrogen Energy. 14 (1989) 275-277
- [32] Maruthamuthu, P., Ashokkumar, M., Factors Influencing the Photocatalytic Efficiency of WO₃ Particles. Journal of Photochemistry and Photobiology. A: Chemistry, 49 (1989) 249-258
- [33] Maruthamuthu, P., Ashokkumar, M., Photocatalytic Hydrogen Production with Semiconductor Particulate Systems: An Effort to Enhance the Efficiency. International Journal of Hydrogen Energy. 16 (1991) 591-595
- [34] Marsen, B., et al., Progress in Sputtered Tungsten Trioxide for Photoelectrode Applications. International Journal of Hydrogen Energy. 32 (2007) 3110-3115
- [35] Kudo, A., Recent Progress in the Development of Visible Light-Driven Powdered Photocatalysts for Water Splitting. International Journal of Hydrogen Energy. 32 (2007) 2673-2678
- [36] Bamwenda, G., Arakawa, H., The Visible light Induced Photocatalytic Activity of Tungsten Trioxide Powders. Applied Catalysis. 210 (2001) 181-191
- [37] Bamwenda, G., Sayama, K., Arakawa, H., The Effect of Selected Reaction Parameters on the Photoproduction of Oxygen and Hydrogen from a WO₃-Fe²⁺-Fe³⁺ Aqueous Solution. Journal of Photochemistry and Photobiology A: Chemistry 122 (199) 175-183

- [38] Bamwenda, G., Arakawa, H., The Photoinduced Evolution of O₂ and H₂ from a WO₃ Aqueous Suspension in the Presence of Ce⁴⁺/Ce³⁺. Solar Energy Materials & Solar Cells. 70 (2001) 1-14
- [39] Hameed, A., Gondal, M., Yamani, Z., Effect of Metal Doping on Photocatalytic Activity of WO₃ for Water Splitting Under Laser Illumination: Role of 3d-Orbitals. Catalysis Communications. 5 (2004) 715-719
- [40] Kudo, A., et al., Effects of Doping of Metal Cations on Morphology, Activity, and Visible Light Response of Photocatalysts. Chemical Physics. 339 (2007) 104-110
- [41] Sayama, K., et al., Photo-Electrochemical Properties of Oxide Semiconductors on Porous Titanium Metal Electrodes. Solar Energy Materials & Solar Cells. 90 (2006) 2429-2437
- [42] Chatchai, P., et al., Efficient Photocatalytic Activity of Water Oxidation Over WO₃/BiVO₄ Composite Under Visible Light Radiation. Electrochimica Acta. 54 (2009) 1147-1152
- [43] Yang, H., et al., A Novel Composite Photocatalyst for Water Splitting Hydrogen Production. Journal of Power Sources. 159 (2005) 1305-1309
- [44] Georgieva, J., et al., Photoelectrochemical Behaviour of Tungsten Trioxide and Electrosynthesised Titanium Dioxide Single Component and Bilayer Coatings on Stainless Steel Substrates. Journal of Electroanalytical Chemistry. 585 (2005) 35-43
- [45] Radecka, M., et al., Photoelectrochemical Properties of Undoped and Ti-Doped WO₃. Physica B 364 (2005) 85-92
- [46] <http://rredc.nrel.gov/solar/spectra/am1.5>
- [47] Shukla, P., et al., Studies on PV Assisted PEC Solar Cells for Hydrogen Production Through Photoelectrolysis of Water. International Journal of Hydrogen Energy. 27 (2002) 135-141
- [48] Ito, S., et al., Calibration of Solar Simulator for Evaluation of Dye-Sensitized Solar Cells. Solar Energy Materials & Solar Cells. 82 (2004) 421-429
- [49] He, Z., Pong, W., Rate-Determining Step in Photocatalytic Production of Hydrogen. International Journal of Hydrogen Energy. 15 (1990) 99-103
- [50] Mishra, P., Shukla, P., Srinivasta, O., Study of Modular PEC Solar Cells for Photoelectrochemical Splitting of Water Employing Nanostructured TiO₂ Photoelectrodes. International Journal of Hydrogen Energy. 32 (2007) 1680-1685

- [51] Mishra, P., et al., Investigation and Optimization of Nanostructured TiO₂ Photoelectrode in Regard to Hydrogen Production through Photoelectrochemical Process. International Journal of Hydrogen Energy. 28 (2003) 1089-1094
- [52] Karn, R., Misra, M., Srinivasta, O., Semiconductor-Septum Photoelectrochemical Cell for Solar Hydrogen Production. International Journal of Hydrogen Energy. 25 (2000) 407-413
- [53] Srinivasta, O., Karn, R., Misra, M., Semiconductor-Septum Photoelectrochemical Solar Cell for Hydrogen Production. International Journal of Hydrogen Energy. 25 (2000) 495-503
- [54] Misra, M., Pandey, R., Srinivasta, O., Solar Hydrogen Production Employing N-TiO₂/Ti Sc-SEP Photoelectrochemical Solar Cell. International Journal of Hydrogen Energy. 22 (1997) 501-508
- [55] Allam, N., Grimes, C., Effect of Cathode Material on the Morphology and Photoelectrochemical Properties of Vertically Oriented TiO₂ Nanotube Arrays. Solar Energy Materials & Solar Cells. 92 (2008) 1468-1475
- [56] Zhang, Z., et al., Preparation and Photoelectrochemical Properties of a Hybrid Electrode Composed of Polypyrrole Encapsulated in Highly Ordered Titanium Dioxide Nanotube Array. Thin Solid Films. 516 (2008) 2663-8667
- [57] Lu, N., et al., Characterization of Boron-Doped TiO₂ Nanotube Arrays Prepared by Electrochemical Method and Its Visible Light Activity. Separation and Purification Technology 62 (2008) 668-673
- [58] Radecka, M., et al., Importance of the Band Gap Energy and Flat Band Potential for Application of Modified TiO₂ Photoanodes in Water Photolysis. Journal of Power Sources. 181 (2008) 46-55
- [59] Shaban, Y., Khan, S., Visible light Active Carbon Modified N-TiO₂ for Efficient Hydrogen Production by Photoelectrochemical Splitting of Water. International Journal of Hydrogen Energy. 33 (2008) 1118-1126
- [60] Brudnik, A., et al., Thin Film TiO₂ Photoanodes for Water Photolysis Prepared by DC Magnetron Sputtering. Journal of Power Sources. 173 (2007) 774-780
- [61] Shaban, Y., Khan, S., Surface Grooved Visible Light Active Carbon Modified (CM)-N-TiO₂ Thin Films for Efficient Photoelectrochemical Splitting of Water. Chemical Physics. 339 (2007) 73-85
- [62] Zajac, A., Radecka, M., Rekas, M., Photoelectrochemical Properties of Nb Doped Titanium Dioxide. Physica B 399 (2007) 55-59

- [63] Xu, C., et al., Nanotube Enhanced Photoresponse of Carbon Modified (CM)-N-TiO₂ for Efficient Water Splitting. Solar Energy Materials & Solar Cells. 91 (2007) 938-943
- [64] Xu, C., et al., Enhanced Carbon Doping of N-TiO₂ Thin Films for Photoelectrochemical Water Splitting. Electrochemistry Communications. 8 (2006) 1650-1654
- [65] Sobas, A., et al., Visible Photocurrent Response of TiO₂ Anode. Surface Science. 600 (2006) 3964-3970
- [66] Karn, R., Misra, M., Srinivasta, O., On the Structural and Photoelectrochemical Studies of In₂O₃-Admixed Nanostructured TiO₂ With Regard to Hydrogen Production Through Photoelectrolysis. International Journal of Hydrogen Energy. 23 (1998) 439-444
- [67] Prasad, N., Rao, N., Srinivasta, O., On the Photoelectrodes TiO₂ and WSe₂ For Hydrogen Production through Photoelectrolysis. International Journal of Hydrogen Energy. 13 (1988) 399-405
- [68] Ajayi, F., et al., Photocurrent and Photoelectrochemical Hydrogen Production with Tin Porphyrin and Platinum Nanowires Immobilized with Nafion on Glassy Carbon Electrode. International Journal of Hydrogen Energy. 34 (2009) 110-114
- [69] Ichikawa, S., Photoelectrocatalytic Production of Hydrogen From Natural Seawater Under Sunlight. International Journal of Hydrogen Energy. 22 (1997) 675-678
- [70] Steinhart, J., Hart, S., Calibration Curves for Thermistors. Deep-Sea Research. 15 (1968) 497-503
- [71] Sawyer, D., et al., Electrochemistry for Chemists. Second Edition, John Wiley and Sons, New York, NY. 1995
- [72] Kerr, J., et al., An Integrating Pyranometer for Climatological Observer Stations and Mesoscale Networks. Journal of Applied Meteorology. 6 (1967) 688-694
- [73] http://www.nrel.gov/midc/srnl_bms/.

VITA

Graduate College
University of Nevada, Las Vegas

Christopher K. Halford

Home Address:

10201 Deerfield Beach Ave. #202
Las Vegas, Nevada 89129

Degrees:

Bachelor of Science, Mechanical Engineering, 2002
University of Nevada, Las Vegas

Master of Science, Mechanical Engineering, 2004
University of Nevada, Las Vegas

Publications:

C. K. Halford, R. A. Hurt, R. F. Boehm, The UNLV Dish-Stirling Project, Solar 2002 Conference, Reno, Nevada

C. K Halford, R. F. Boehm, Simulation of Concentrated Photovoltaic Cooling System, Solar 2004 Conference, Portland, Oregon.

C. K Halford, R. F. Boehm, Modeling of Phase Change Material Peak Load Shifting, 2005 International Solar Energy Conference, Orlando, Florida

C. K Halford, R. F. Boehm, An On-Sun Evaluation of Photocatalytic Generation of Hydrogen, National Hydrogen Association Annual Hydrogen Conference 2007, San Antonio, Texas

I. Mahderekal, C. Halford , R. F. Boehm. Simulation and Optimization of a Concentrated Photovoltaic System, Journal of Solar Energy Engineering, May 2006

C.K. Halford, R.F. Boehm, Modeling of Phase Change Material Peak Load Shifting, Energy and Buildings, March 2007

S. B. Sadinieni, R. Hurt, C.K Halford , R. F. Boehm. Theory and Experimental Results for Solar Still Operation, Energy-The International Journal, 2008

Thesis Title: An On-Sun Parametric Study of Solar Hydrogen Production Using WO₃ Photoanodes

Thesis Examination Committee:

Chairperson, Robert F. Boehm, Ph. D.

Committee member, Samir F. Moujaes, Ph.D

Committee member, Woosoon Yim, Ph. D.

Committee member, Yitung Chen, Ph. D

Graduate Faculty Representative, Yahia Bahgzouz, Ph. D.